Monitoring Oil Reservoir Deformations by Measuring Ground Surface Movements

by

Kamelia Atefi Monfared

A thesis
presented to the University of Waterloo
in fulfilment of the
thesis requirement for the degree of
Master of Applied Science
in
Civil Engineering

Waterloo, Ontario, Canada, 2009

Author's Declaration

I hereby declare that I am the sole author of this thesis. This is a true copy of the thesis, including any required final revisions, as accepted by the examiners.

I understand that my thesis may be made electronically available to the public.

Abstract

It has long been known that any activity that results in changes in subsurface pressure, such as hydrocarbon production or waste or water reinjection, also causes underground deformations and movement, which can be described in terms of volumetric changes. Such deformations induce surface movement, which has a significant environmental impact. Induced surface deformations are measurable as vertical displacements; horizontal displacements; and tilts, which are the gradient of the surface deformation. The initial component of this study is a numerical model developed in C++ to predict and calculate surface deformations based on assumed subsurface volumetric changes occurring in a reservoir. The model is based on the unidirectional expansion technique using equations from Okada's theory of dislocations (Okada, 1985). A second numerical model calculates subsurface volumetric changes based on surface deformation measurements, commonly referred to as solving for the inverse case. The inverse case is an ill-posed problem because the input is comprised of measured values that contain error. A regularization technique was therefore developed to help solve the ill-posed problem.

A variety of surface deformation data sets were analyzed in order to determine the surface deformation input data that would produce the best solution and the optimum reconstruction of the initial subsurface volumetric changes. Tilt measurements, although very small, were found to be much better input than vertical displacement data for finding the inverse solution. Even in an ideal case with 0 % error, tilts result in a smaller RMSE (about 12 % smaller in the case studied) and thus a better resolution. In realistic cases with error, adding only 0.55 % of the maximum random error in the surface displacement data affects the back-calculated results to a significant extent: the RMSE increased by more than 13 times in the case studied. However, in an identical case using tilt measurements as input, adding 20 % of the maximum surface tilt value as random error increased the RMSE by 7 times, and remodelling the initial distribution of the volumetric changes in the subsurface was still possible. The required area of observation can also be reduced if tilt measurements are used. The optimal input includes tilt measurements in both directions: dz/dx and dz/dy.

With respect to the number of observation points chosen, when tilts are used with an error of 0 %, very good resolution is obtainable using only 0.4 % of the unknowns as the number of benchmarks. For example, using only 10 observation points for a reservoir with 2500 elements, or unknowns resulted in an acceptable reconstruction.

With respect to the sensitivity of the inverse solution to the depth of the reservoir and to the geometry of the observation grid, the deeper the reservoir, the more ill-posed the problem. The geometry of the benchmarks also has a significant effect on the solution of the inverse problem.

Acknowledgements

Dedication

I would like to dedicate this thesis to my dear parents, Mr. Amir Pasha Atefi Monfared and Mrs. Golrokh Tajbakhsh who have always been there for me.

Table of Contents

List of Figures

List of Tables

1. Introduction

Near-surface deformations induced by subsurface movements have been identified as an important operational problem for many years. Subsurface movements can be caused by a number of activities, such as oil production and steam or waste injection. Any activity that causes subsurface pressure changes generates displacement zones and, consequently, surface movements. Hence, the withdrawal or injection of any kind of fluid or material into the subsurface induces subsurface volume changes that cause deformations and displacements at ground level. These surface deformations are typically measured as vertical displacements; horizontal displacements; and tilts, or ground rotations, with respect to the vertical.

Excessive surface deformations can result in significant economic losses because of the failure of underground utility lines, well casings, and pipelines, as well as structural damage generated by seawater intrusions and foundation settlements (Hu et al., 2004). The induced land subsidence can exceed several meters; however, in some cases, even small subsurface deformations can cause significant damage to the surrounding environment (Nagel, 2001). In the Netherlands, for example, where large areas of dry land are below sea level and protected by surrounding dikes, even a small subsidence could result in disaster (Nagel, 2001). Wetland loss is another phenomenon caused by either natural or human-induced subsidence, or, given their complex relationship, by a combination of both.

Extensive research has been performed worldwide in this area because of the wide distribution of regions affected by land deformations, which have a severe impact on the environment. In most studies, the main objective has been to predict surface deformations so that preventive action can be taken as quickly as possible in order to minimize damage, optimize production and injection, and develop better monitoring strategies. Another factor, however, is that surface deformations are measurable and depend on subsurface movements and deformations (Vasco, 2004; Segall, 1985; Geertsma, 1957). Thus, the measurement and monitoring of surface deformations can be used in the modeling and tracking of subsurface deformations. This approach is especially useful in fast-paced projects such as waste or steam injection, in which the continuous monitoring of subsurface deformation is of great value. The evaluation of subsurface deformation using surface deformation data is called an inverse problem. The

1

resulting subsurface deformation data can be used to determine steam concentration zones in steam injection projects, to model deformations and fracture movements in waste injection projects, to manage and optimize injection and production patterns in reservoirs, and to monitor the reaction of a reservoir to production and enhanced recovery processes in the oil and gas industry. In addition, important information can be derived from this subsurface data for tracking the areas of extraction and injection of fluids. Identifying this information is critical in determining whether the reinjected material is remaining in its desired target locations (Dusseault et al., 2002).

Unfortunately, detailed information about subsurface deformations and movements is unavailable for modelling subsurface movements. However, an analog of St. Venant's principle in mechanics applies: if the effect of a force or deformation located at a distance from the point of interest is under study, the details of this force or deformation do not have a significant effect on the induced deformation field. Thus, two approaches are commonly used to reconstruct subsurface deformations:

- Nucleus of strain approach: the subsurface deformations are modeled by representing discontinuities as single points that are expanding or compacting in the subsurface and that represent expansion or compaction, respectively.
- Unidirectional expansion: an approach that is based on equations from the theory of dislocations (Okada, 1985): Okada's solution models concentrated on expansion or compaction that occurs in one direction.

The unidirectional expansion technique is used in this study. This method typically provides better simulations of the behaviour of the reservoir because the thickness of the reservoir is small in comparison to its depth and width. Thus, the induced deformations are primarily in one direction: vertical.

For the first component of this research, a forward numerical model was developed in C++ based on Okada's formulas. This computer program calculates surface deformations from given changes in volume in the subsurface. The main types of input to the program are the geometry of the reservoir (depth, width, length, azimuth and dip angle), the number of observation points, the subsurface volume changes, and the elastic properties of the media

(Lamé's constants). The output of the program is the vertical displacements and ground tilts at each observation point. However, the main focus of this work was to evaluate the subsurface volumetric changes given the field of surface displacements (e.g., the solution of the inverse problem). Like so many other inverse problems, this inverse problem is an ill-posed problem; thus, the solution is significantly affected by minor inaccuracies in the measured data. These inaccuracies are also present in the input data because of the measurement errors, and the solutions of ill-posed problems are therefore not unique. Consequently, the second and main part of this thesis is focused on solving the inverse problem.

Surface deformations computed in the first part of the research for a given set of volume changes are used as input data. The subsurface volume changes are then calculated using the inverse model. For the verification of the model, the results are then compared to the initial assumed volume changes assumed.

Forward and inverse models have been previously studied and reported on in the literature. Some models for the case of extreme uncertainties are based on the nucleus of strain approach, in which subsurface volume changes are modeled at random locations (Dusseault et al., 1993; Kroon et al., 2008; Vasco et al., 2002). The solution in these cases involves minimizing the parameters of these random variables so that the observed deformation field can be reconstructed. The approach in this thesis is based on Okada's unidirectional deformations in well-defined locations. The ground surface displacement data considered in this study include both vertical deformations and tilts. Previous studies were based on measurements of surface displacements only (e.g., Bilak, 1989). The goal of this study was to identify a set of measurements that would result in the best resolution in the solution of the inverse problem. The sensitivity of the inverse solution to the depth of the source of deformation, the locations of the surface measurements, and the measurement error were also studied in detail, and the results are presented in this thesis.

2. Literature Review

Subsurface volumetric change has long been induced by human activities such as oil production, steam reinjection, waste reinjection, and mining. Such types of activities take place all over the world and have a significant environmental impact. In some instances, ground deformations can result in significant structural damage. These phenomena have been the subject of extensive study on the part of oil companies and individual researchers over the past 50 years. The studies have examined aspects of surface deformation, natural and manmade causes of deformation, deformations due to the extraction of fluids or solids, the measurement and monitoring of deformations, the theory and modeling of deformations, the prediction of surface deformations, the social effects of deformations, the environmental consequences of deformations, methods of preventing or controlling induced deformations, the inverse case, and the obtaining of subsurface deformation data based on surface displacement.

Two of the major causes of surface deformation have been oil and gas production, and water withdrawal. Surface deformation due to the withdrawal of water, oil, or gas has been observed and recorded in the literature for more than a decade. The first reported cases related to subsidence caused by underground water withdrawal, one of the earliest cases of which took place in the Osaka field in Japan in 1885. Also caused by water withdrawal was the 3 m of subsidence, with a subsidence bowl of 10 000 Km^2, observed as early as 1906 in the Houston Galveston area. Other early cases were reported in London, England, in 1865 and in Mexico City beginning in 1929 (Gurevich et al., 1993). In the oil industry, one of the earliest cases of subsidence was first noted at the Goose Creek oil field in Texas, USA, in 1918 (Chan et al., 2007). Roadway subsidence due to oil recovery was also observed on Hogg Island and along Tabbs Bay, and surface faulting was first documented in the town of Pelley as early as 1918 (Nagel, 2001).

In the oil and gas industry however, the first major case of surface deformation to be widely recognized was observed at the Wilmington field largely because of the significant amount of land subsidence and the enormous cost of the resulting damage. Wilmington field, located near Los Angeles, California, was first discovered in 1932, with production beginning in 1936. Indications of subsidence were observed in the following years, but the first subsidence due to

production in this field was measured and recorded in 1940. By 1970, more than $100 million had been spent to evaluate the damage due to the subsidence, to protect and compensate for the damages due to subsidence. The total vertical subsidence reached more than 9 m by 1968. It was noted that the oil company was required to maintain a water injection rate of 105 % of the production value in order to prevent further subsidence due to oil withdrawal (Nagel, 2001).

The Ekofisk field in the Norwegian sector of the North Sea, first discovered in 1969, is one of the best known cases in the oil and petroleum industry because of the immense subsidence that has resulted from the oil withdrawal. The reservoir is composed of two fractured chalk horizons from which oil is extracted. Its depth is about 2927 m, and its thickness varies from approximately 107 to 152 m. The porosity of the reservoir ranges from 30 % to a maximum of 48 %. Beneath this chalk reservoir, lies a Tor Formation with a thickness of approximately 77 to 153 m and a porosity of 30 % to 40 % (Hermansen et al., 2000). The first test production at the Ekofisk field began in 1971. Oil production peaked in 1976 at a rate of 350,000 STB/D. Gas injectors were also built, and all the gas produced was reinjected until pipelines were installed in 1977 to transfer the gas to Germany.

Initially, before oil production began, engineers did not expect any subsidence in the seabed. However, this prediction was incorrect, and 3.05 m of seabed subsidence was measured in 1984. Two images that were taken 9 years apart and that show the degree of this deformation are provided in Figure 1.
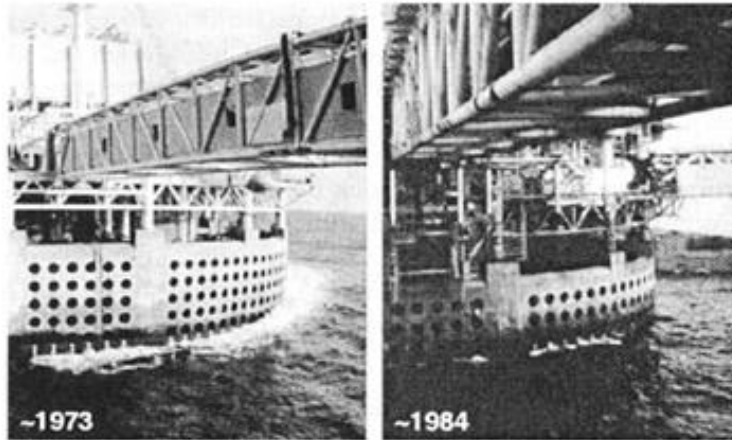
Figure 1: A comparison of the number of holes visible in the outer part of the protective wall in the two photos of the 2/4T platform at the Ekofisk field reveals the extensive vertical subsidence (Hermansen et al., 2000)

Laboratory results indicated that a significant additional amount of oil could be mobilized if high enough gradients existed in the field. In 1983, the company therefore decided to flood the northern Tor formation with water. This massive flooding of the Ekofisk field resulted in a significant increase in oil production and a substantial drop in the gas-to-oil ratio (GOR). The deformation of the reservoir in this chalk formation resulted in casing failures in two-thirds of the wells in Ekofisk (Bruno et al., 1992) and in the failure of a number of them (Du et al., 2001; Nagel, 2001; Hermansen et al., 2000; Bruno et al., 1992).

The vertical displacement rates on the seafloor were also so enormous that in 1987 it was decided to jack up the offshore platforms in order to protect the steel platforms and concrete storage tanks, especially in severe weather; to prevent the structure from sinking beneath sea level; and to maintain a constant platform air gap (Nagel, 2001). In 1989, a concrete protective barrier was designed, and a new phase, the Ekofisk II, was redeveloped as a means of compensating for the huge amounts of subsidence (Nagel, 2001). Also due to the excess tension and compression with respect to the pipelines in the subsiding Ekofisk bowl, 63 km of new pipeline has to be replaced during the Ekofisk II redevelopment. The following actions taken by the company led to an increase in oil recovery: extensive water flooding (a total of 2 billion barrels of water were injected in the first 10 years of the water flooding operations), effective well monitoring, compaction drive energy, the Ekofisk redevelopment, and the overall optimization of field methods and techniques (Hermansen et al., 2000).

The South Belridge field in California is a diatomite reservoir, which is characterized by very high porosity and low permeability, resulting in very high compactions of the reservoir rock. Compaction in this field caused numerous tension fractures on the surface and numerous casing failures (Dusseault et al., 2002). During the 1980s, these failures became so severe that 15 % − 20 % of the well casings failed each year (Nagel, 2001).

The Lost Hills field, located along the west side of the San Joaquin Valley in California, is another diatomite reservoir where petroleum production has led to surface subsidence at rates as high as 30 cm per year and damage to hundreds of wells (Du et al.,2001; Bruno et al., 1992).

More than 20 m of changes in elevation were observed during 30 years of extensive oil and gas production in the Louisiana Coastal Zone area. Land loss in this area has also been reported to be 80% of the total land loss in the United States since the 1930s, which has a major social, economic, environmental, and ecosystem impact. The height of the land loss, which occurred in the 1970s, coincided with the peak of oil and gas production in the area (Chan et al., 2007).

While some reservoirs like the Ekofisk field or the Wilmington field are well known for the large amounts of land deformation induced by hydrocarbon production, in many cases, very small displacements can also present serious challenges and can result in disaster. In Venezuela, for example, induced land subsidence due to reservoir compaction resulted in severe flooding of more than $450 \ km^2$ of land near the coast of Lake Maracaibo. This field is located in an area called the Bolivar Coast where subsidence had occurred due to oil production in several fields as early as 1929. By 1988, the subsidence in these fields exceeded 5 m, and by the following year, 150 km of dikes had been built, for which the annual cost of maintenance was estimated to be $5 million.

The Groningen gas field in the Netherlands is another case in which even small induced land subsidence can be very challenging. The subsidence in this field was reported to be only in the order of tens of centimetres. However, because large areas in the Netherlands are below sea level and are protected by dikes, these induced deformations can cause tension in the surrounding dikes, which could be disastrous (Nagel, 2001). Surface monitoring has thus become very important in this region.

The abovementioned cases are important examples of observed cases of surface deformations induced as a result of oil and gas production. In these cases the intention is usually to predict the deformations and thus solve the problems involved in that specific case. However, as mentioned, in some cases, if water flooding or steam reinjection is applied during production, then keeping track of and controlling the induced volumetric changes in the subsurface would become important. Thus surface monitoring to keep track of induced surface deformations would be required. Based on this surface deformation data, subsurface movements and volumetric changes can be modeled. This is referred to as solving for the inverse case.

Many cases of induced surface deformation that have been observed are due to underground water withdrawal, geysers, geothermal fields, steam reinjection projects, and waste reinjection. The general mechanism and occurrence of induced surface deformations is believed to be similar regardless of the type of the reservoir involved.

The literature contains numerous articles about induced land deformation. Some have focused on specific fields while others have presented a broader and more general analysis.

In 1957 Geertsma conducted extensive research on the similarities between temperature distribution in a thermo elastic material and liquid pressure distribution in a saturated porous medium in two cases of plane strain and plane stress. Plane strain refers to cases in which one dimension is much larger than the other dimension, e.g., a tunnel. Plane stress, however, refers to cases in which one dimension is much smaller than the two other dimensions, such as a plate. The latter case is relevant for reservoirs and how they are modeled for numerical or finite element reconstruction. In both cases, one of the major stresses is equal to zero. Biot (1956) pointed out that in the same way pore compressibility affects the distribution of pore pressure, the dilation of the solid also appears as an interaction term in the temperature distribution equation . Based on this fact, Geertsma (1957) tried to express the constants in pore pressure distribution using the theory of pore and rock bulk volume variations for porous rocks. From a comparison of the completed equation for temperature distribution in thermo elastic materials and the distribution of liquid pressure, it can be seen that liquid mobility in pores is relevant to the heat conductivity, the compressibility replaces specific heat, and the compressibility ratio is replaced by thermal expansion.

A great deal of research has been conducted with respect to the mechanism of surface deformation due to changes in the subsurface volume and focusing on the individual specific cases. The mechanism of and factors in surface subsidence were studied with respect to well-known cases. The following are examples from the literature.

Hermansen et al., (1998) published an article about the experience at the Ekofisk field after 10 years of water flooding the field to prevent large amounts of subsidence due to oil production in the seabed. The main focus of this research was on the water flooding and related challenges. The main difficulty with the water flooding, which was the primary method of compensating for the subsidence, was that uncertainties had to be predicted before massive amounts of water were injected into the highly fractured chalk formation: recovery potential, sweep efficiency, water injectivity, and rock stability. The results of the years of wide water injection were a substantial increase in the oil production of many of the wells and a significant drop in the gas to oil ratio (GOR). Only in wells affected by faults and fracture trends did water breakthrough occur. This study pointed out the importance of detailed mapping of faults and fractures and also of acquiring an understanding of the major stress orientations so that the permeability anisotropy could be determined in order to prevent or minimize water breakthrough.

The same study also examined reservoir compaction and land subsidence. It was initially thought that subsidence is solely the result of an increase in vertical stress due to the depletion of pore pressure as a result of oil withdrawal. However, even after the field was flooded with water and the pore pressure was kept constant, the subsidence rate, although reduced, continued to remain at fair constant. Therefore, another mechanism for the compaction that occurred in the Ekofisk field was sought. The researchers found that areas that experienced increasing water saturation, e.g., due to water breakthrough, even under constant effective stress, also experienced significant amounts of subsidence whereas other areas subjected to constant pressure due to maintenance operations had zero subsidence. Therefore, the weakening of the chalk material due to contact with "non-equilibrium" cold seawater was recognized as another mechanism that caused subsidence in the Ekofisk field. Thus, the subsidence in the Ekofisk field was found to be due to two major factors: an increase in the

effective stress due to a drop in pore pressure and an increase in water saturation in the chalk matrix even in conditions of constant pore pressure.

Also mentioned in this paper were developments suggested and tested for the Ekofisk field as methods of compensating for the induced rates of subsidence caused by the increase in water saturation inside the chalk matrix: injecting gas rather than water, using a water-alternating-gas (WAG) technique, and surfactant injection. In 1996, WAG was applied, and gas injection was tested in one of the wells in which water had previously been injected for about 5 years. The test was unsuccessful, and the injection rate dropped to zero in a matter of hours. The bottom borehole temperatures were found to be $54°F (\approx 12.2°C)$, which is well below the hydrate formation temperature at the reservoir pressure. A temperature contour was then calculated around the well hole, and it was revealed that the hydrate-forming conditions existed at a distance of several hundreds of metres from the well hole. This finding was in accordance with what would be expected after five years of cold water injection into the well. The next solutions suggested were gas injection with heated water.

In 1993 Li Chin considered another mechanism as a cause of the compaction in the Ekofisk reservoir: shear-induced compaction. This suggestion led to a significant effort to predict and model the Ekofisk reservoir compaction and surface subsidence using finite element models. The main mechanism used to simulate reservoir compaction in these models was pore pressure drop due to production. At the time, the results seemed to be in accordance with the observed data, but over time, even after injections were made to slow down the subsidence rate and although the subsidence rate was much less than the previous levels, the observations still indicated larger values than those produced by the models, in which the main mechanism, pore pressure drop, was being controlled by the injections. Another mechanism therefore seemed to be involved.

Uniaxial strain and triaxial stress compaction tests were performed on samples from the Ekofisk reservoir, both on samples from the upper formation, which has a high quartz content, and also on samples from the lower Tor formation, which has a low quartz content. The results showed a K_0 value of 0.2 rather than 0.5. In Mohr-Coulomb cycles, this indicates much greater growth. This low K_0 value shows that as production proceeded, pore pressure dropped, and thus deviatoric stresses increased significantly along with the development of shear stresses,

which caused the rock to fracture. Based on the results and the in-situ stresses calculated, it was deduced that slipping on fractures will also occur because of pressure depletion in the reservoir.

The changes that occur during repressurization were also studied. During repressurization due to water or gas injection, pore pressure increases, causing a decrease in the effective stresses. This effect can also be seen in a Mohr-Coulomb cycle, in which decreasing the effective stresses forces the sample to the left, into the failure zone when $K_0 = 0.2$, whereas for $K_0 = 0.5$, which is the normal case, failure would not be as intense. Measurements from the injection well and the compaction observations showed that a pressure increase resulting from reinjection can cause additional compaction of the affected chalk reservoir formation.

The arch effect of the overburden was also studied, and it was observed that the stresses induced from deformations were greatest on the edges where there is a distinct transition from high- to low-porosity chalk. Based on the observations of the Ekofisk field, since the subsidence was more than predicted, it was determined that the chalk is fractured either naturally or due to the shear stresses that result during injection or production procedures, and thus, in this case, shear stresses are also a cause of compaction mechanism.

Due to the constraints on displacement in the field which are difficult to reproduce in the lab, the actual K_0 value is lower than that of in the lab. For modeling purposes, the most important point determined from this case was that the stress path after the pore pressure drop inside the reservoir should be such that K_0, which is the ratio of change in horizontal effective stress to the change in vertical effective stress, be 0.2 so that field conditions are represented correctly. The stress path in the model was controlled by K_0 as observed in the field. Once the Mohr cycle reaches a critical angle, the coding automatically changes its stress-strain curve to a weaker curve. The model is programmed in such a way that, with the initial conditions (initial vertical and horizontal and pore pressures) under gravitational loads, the K value in the program is set to 0.5. As soon as production is started, K is set to 0.2. This value is then maintained at a constant level as long as the vertical strain is compressive or as long as production is in progress, and thus a decrease in pore pressure and an increase in the effective vertical stress is occurring. As soon as the pore pressure increases, which may be as a result of an injection inside the reservoir, K would be set to 0.5. This value is then maintained until

another change occurs in the direction of the strain. Of course, identifying the *K* value near areas such as injection wells, where pressure increases may be in the order of tens of MPa, is of great importance. The two most important parameters used in this modelling, which were controlled by input data, were the position of the critical envelope and the weakening factor used to determine a weakened stress-strain curve.

To expand oil and gas production development in the Lost Hills field in California, an extensive program was implemented by Bruno et al. (1992): laboratory tests and rock property measurements, monitoring and studying of subsurface compaction and the resulting surface deformations, and analytical and numerical modelling. Surface deformation due to oil production was a problem in this field because of the soft and porous formation of the rock matrix and the thick and shallow nature of the reservoir. Using GPS, data related to surface deformation was gathered at three-month intervals from 1989 to 1991. It was observed that during this period, subsidence was linearly related to the total fluid production in the centre of the field. With respect to the subsurface, approximate measurements of the compaction of the rock matrix were obtained using radioactive bullet logs in one well and gamma logs of natural markers in other wells. These results indicated compaction of about 61 cm from 1990 to 1991. A detailed lithology was recorded for the Lost Hills field, and the layers and formations and their properties were all studied carefully, along with the mechanical properties of the rock.

The two most important factors affecting reservoir compaction mentioned in this research were pore volume compressibility and bulk volume compressibility (Bruno et al., 1992). Although it is said that these compressibility factors are related to other compressibility and elastic constants and can be well defined, in diatomite reservoirs this is not the case. Because the deformation of a diatomite reservoir has been determined to be inelastic at all stress levels, these factors can be measured empirically from lab tests under fully drained conditions. Diatomite samples from Lost Hills showed slightly increased compressibility when the effective stress exceeded 1000-1100 psi. Triaxial tests were carried out on undisturbed diatomite samples. Based on the results, the stress-strain, loading, and unloading graphs were plotted. The slope of the bulk volume strain plotted against that of the hydrostatic stress represents a measure of the bulk compressibility. The unloading curve shows that the material remains stiff when unloaded, thus indicating irreversible damage and deformation. From this

stiffer unloading behaviour, it was determined that water reinjection was needed in order to compensate for irreversible subsidence due to oil withdrawal. These tests revealed that compressibility increased as the effective stress exceeded 1200 Psi.

Core samples were also taken from the overburden material lying over the diatomite reservoir, and triaxial tests were carried out in order to determine the stiffness and failure properties of the overlying material. A finite element model was applied in order to calculate and predict the surface subsidence and well casing failure due to oil withdrawal. For the modelling of the field, several assumptions were made; the field is long and narrow, so a symmetrical line was assumed. This geological model covered up to 1829 m in depth and 305 m in half width up to the symmetrical line, and four materials were modeled: sand and gravels (upper sands), siltstones and shales, diatomite, and shale. The purpose of the model was not provide precise calculation of future subsidence but rather to provide an idea of what might occur, along with an estimate of the damage to a well, areas of potential well failure, potential fault movements, and optimum injection of water to flood the reservoir. The deformations and shear stress induced in the overburden in this model were calculated based on a variety of assumed pressure distributions inside the reservoir. The shale formation underneath the reservoir was modeled as an elastic material. The overlying siltstone and sand layers were modeled based on the Drucker-Prager yield condition.

More than 20 m of change in elevation was observed in the Louisiana Coastal Zone over 30 years, during which extensive gas and oil production was carried out in the area. In 2007, studies were conducted on the role of hydrocarbon production in land deformation and fault reactivation in the Louisiana Coastal Zone by Alvin W. Chan et al. (2007). The values for subsidence due to oil production calculated by the numerical program were below half of those observed in the field. Another factor was therefore suspected of resulting in the subsidence that was occurring in the field, so compaction-induced fault slip along the Golden Meadow fault at the northern edge of the reservoirs was studied as a possibility. The researchers listed the following factors that cause submergence of wetlands: consolidation of the Mississippi River sediment, which might have a first order effect on subsidence; regional subsidence due to the loading of sediments; changes in sea level; movement of faults; hydrocarbon production; and reservoir compaction. The first four mechanisms were mentioned to cause subsidence of up to

3 mm/yr. The data from the observations showed rates ranging from 9 mm/yr to as high as 23 mm/yr, indicating that natural phenomena are not the only cause of land subsidence in the area. It was initially believed that reservoir compaction had very little effect on land subsidence due to the depth of the reservoir. However, based on studies and core samples, the appearance of surface faults and the increase in subsidence during the period of maximum oil and gas production proved this assumption incorrect. In 2007, research was carried out in the area. In-situ stress and pore pressure were analyzed using a Deformation Analysis in Reservoir Space (DARS) to estimate porosity changes due to production. The results combined with the geometry of the reservoir were used to determine compaction (Chan et al, 2007).

Vasco et al (2002) used satellite interferometry to study reservoir monitoring. Using data gathered from InSAR observations, a model was developed for calculating the fractional volume strain of the reservoir. This model was applied to the Coso geothermal field located in California. This field is one of the largest and most highly developed high-temperature Basin and Range hydrothermal systems, with an annual production of 240 MW of electricity. The fluid temperatures in the field have been measured as high as 340° C at depths of less than 2.5 KM.

M.S. Bruno (1990) studied a variety of mechanisms that create the potential for well failures and described the locations of these failures in order to compare the analytical and numerical results with actual field observations. A 2D finite element model was applied for the case of a thick shallow reservoir. Pressure drawdown and field deformations were assumed to be symmetrical around the reservoir centre. The aim was to determine the position of the maximum vertical compression, the maximum shear, and areas with maximum bending stresses. It was found that the maximum vertical compression occurs near the centre of the producing interval and that the areas with maximum shear are located above the producing interval and toward the flanks of the field. The results were in accordance with actual case studies and field observations. At the Wilmington field, for example, several hundred well casings were damaged due to shearing rupture at the flanks of the field at a depth of 488 m, while the production interval started at about 701 m. Another case is the South Belridge field in California: between 1984 and 1987, more than one hundred wells were reported damaged at depths of 229 m, while the producing interval started from about 305 m. In this research, shear

stresses induced in the overburden material were also studied and described using the finite element model. The variation in the induced shear stress with depth and also laterally from the centre of production was calculated and plotted.

Surface deformation data has been proven to contain valuable information about the deformations present in the subsurface. Surface deformation is a measurable quantity that is sensitive to subsurface movement and pressure changes occurring deep in the reservoir. Therefore, by observing and keeping track of surface deformations only, it is possible to actually model the subsurface deformation that results to surface deformation (Dusseault et al., 2002). Figure 2 shows differing surface deformation fields that are due to different subsurface volumetric changes at different depths. It can be seen that modeling the movements in the subsurface would require the deformation to be modeled as discontinuities in the subsurface. The deformation curve at the upper right of the figure shows surface deformation as a result of the presence of two discontinuities. If only the deformation curve is examined, it can be determined that this effect is the result of the presence of two discontinuities of expansion zones under the two peak points of the deformation curve. The curve in the upper left, however, is the result of the presence of two or more sources of expansion points in the subsurface placed very close to each other. Of course, the ability to distinguish each of these sources requires further analysis. The lower deformation curve on the left shows a very small amount of deformation in a very much wider area, which could be the result of the presence of a deformation source located deep in the earth. From an examination of the lower right deformation curve conclusions can be drawn about the shape of the discontinuity and its location at a shallower depth.
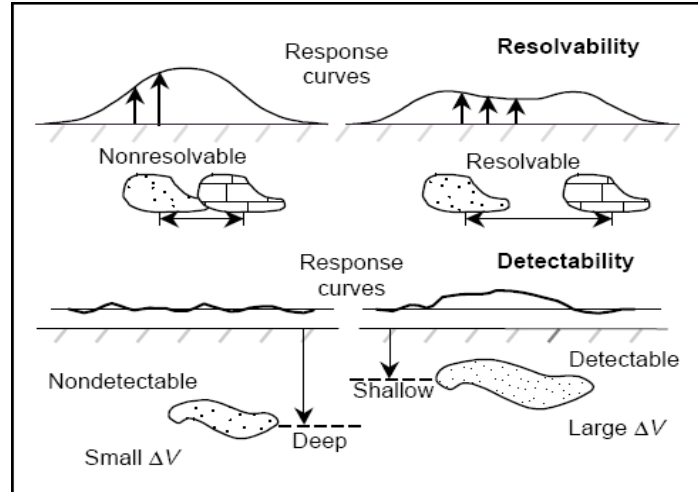
Figure 2 : Illustration of the way in which surface deformation graphs can be used in order to study volumetric changes in the subsurface (Dusseault et al., 2002).

Another example of the use of deformation graphs to analyse events in the subsurface can be seen in Figure 3.
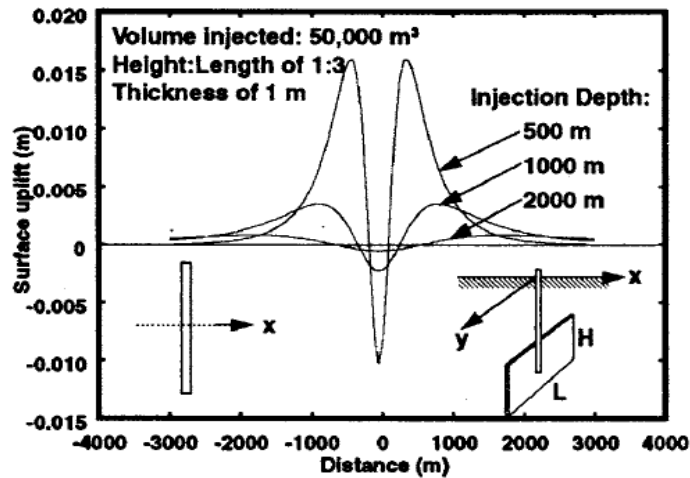
Figure 3: Surface deformation field for a waste injection project (Rothenburg et al., 1994).

The deformation curve shown in Figure 3 was modeled from numerical calculations for a waste disposal monitoring project (Rothenburg et al., 1994). Based only on an examination of the graph, it can be concluded that a fault exists at the centre of the subsidence bowl.

In addition, since the actual values of subsidence are sensitive to subsurface volumetric changes, these observed values can be used for further analysis of the deformations and

pressure changes in the subsurface. For this reason, surface monitoring has become very important and has considerable potential for use in applications in a variety of fields:

- Steam injection projects and the simulation of oil flow, for which the objective is to monitor the concentration of steam zones in the subsurface
- Waste injection projects, in order to track the deformations and fracture movements that occur as a result of the injection process
- Steam-assisted gravity drainage (SAGD)
- General reservoir monitoring, in which it is very important to monitor the behaviour of the reservoir with respect to the production and reinjection processes

As a measurable and sensitive parameter of subsurface deformation, surface deformation data can therefore be used to monitor discontinuities and deformations and fracture modeling, as well as to track the reinjected material in order to determine whether it has been placed correctly and to establish the source of the fluids produced. Using ground deformation data to back-calculate in order to determine the initial movements and volume changes in the subsurface that caused the deformation is referred to as solving for the inverse case.

Rothenburg et al. (1994) used the surface displacement field in order to carry out detailed numerical research with respect to a waste disposal monitoring project. Figure 4 shows the surface deformation as a result of waste reinjection process. A curtain volume of reinjected waste caused volume changes at a depth of 100 m. The discontinuity modeled in the subsurface for the first case was in the shape of a circle, and for the second case, a rectangle. The total volume of discontinuities modeled in these two cases was thus identical, with only the shape of the discontinuity differing. The surface deformation resulting from the two cases was calculated to be almost identical, so it is correct to say that using this deformation curve makes it impossible to remodel the actual shape of the discontinuity or the shape of the initial volume change in the subsurface. This example is a good illustration of the reason inverse cases are referred to as ill-posed problems.

Figure 5 shows induced deformations calculated as the result of waste injection at different depths. The results show that as the depth of the reinjection increases, meaning that volumetric changes are happening at deeper depths, the maximum amplitude of the resulting surface

deformation decreases. However, as can be seen in the graph, the area affected on the surface becomes wider as the induced volume change occurs more deeply into the subsurface.
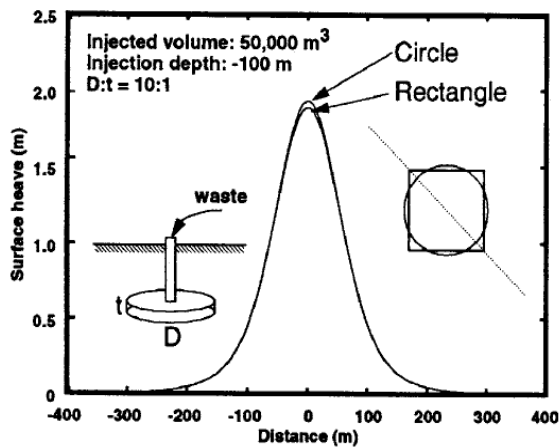
Figure 4: Surface deformation as the result of subsurface volume change (Rothenburg et al., 1994).
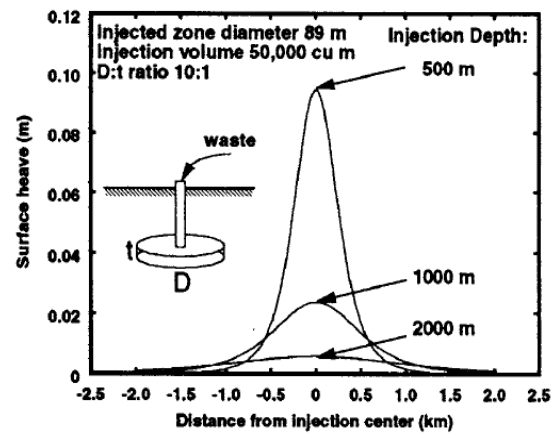
Figure 5: Surface deformation as the result of waste injection at different depths (Rothenburg et al., 1994).

.

Dusseault et al. (2002) conducted detailed research on the data analysis of deformation measurements for reservoir management. They pointed out that if the deformations occurring in the reservoir due to temperature or pressure changes or withdrawal or injection of solids or liquids are transferred linearly to the surface, a unique solution would be available for solving for the location and magnitude of the sources of deformations that occur below the surface. However, the presence of random error along with a limited number of data points would make the solution non unique and ill-posed.

At the Krechba field in Algeria, Ferretti et al., (2008) carried out a study to calculate flow properties and to identify the features that control the flow, e.g., permeability. They investigated the possibility of using measured and observed displacement data gathered from InSAR in order to detect the levels of carbon dioxide CO_2 in the reservoir resulting from CO_2 injection into the surrounding media. One characteristic of the Krechba field was that the concentration of CO_2 in the gas production was 1 % − 9 %, well above the specification for export gas of 0.3 %. The solution that had been employed was to separate the extra CO_2 from the hydrocarbon and to reinject it into the field. The model used in the study was based on the surface deformations caused by the reinjection CO_2. Three benefits of this approach were

18

identified: the cost efficiency of using remotely gathered data, the minor effect on the results and methodology of the heterogeneity of the mechanical properties inside the reservoir, and the ability to solve a linear inverse problem and to calculate the flow properties.

Kroon et al. (2008) investigated a variety of processes that cause land subsidence at different depths; the main focus was to determine the amount each of these processes affected the total land movements observed. This research not only focused on the inverse problem resulting from hydrocarbon extraction, but it also considered all possible parameters from both shallow and deep depths that affected land movement, thus estimating the effect on the entire compaction field. A Bayesian approach was used to estimate the parameters. All the uncertainties and correlations resulting from geological and other considerations were taken into account as prior knowledge. Quantifying variance and covariance for the prior knowledge is therefore essential, which was accomplished using a Monte Carlo simulation.

A forward model was used to describe peat oxidation, which is a shallow compaction that involves both poroelastic and inelastic effects. If the pre-consolidation stress is exceeded, the compactions are irreversible. The results showed that compactions due to peat oxidation or those that occur in clay layers, which are found at shallow depths of less than 50 m, are transferred to the surface instantly. It was also observed that these deformations that occur at shallow depths have a local effect on the surface: they affect areas only at the top of the deformation points.

The second model was developed in order to study the effects of volume changes occurring deep down in depth. They studied a case of a decrease in gas pressure due to the production in the hydrocarbon reservoir. This decrease in pressure, which causes an increase in effective stress, results in the compaction of the rock in the reservoir until a new equilibrium is reached. The behaviour of the overburden was assumed to be elastic, and thus the deformation in the subsurface was transferred almost instantly to the surface. Also because of the elastic behaviour of the overburden, the deformation is extended to a wider range on the surface than the length of the reservoir where the initial deformation took place. The surface deformation field is roughly equal to the depth of the reservoir. The main purpose of the study was to focus on the inverse case: to use the observations of surface deformation in order to determine subsurface movements. The model was validated through tests involving a number of cases. The results clearly indicate that neglecting deformations that occur at shallow depths, if

present, results in much different and incorrect data. If the inversion results based on an observed surface deformation do not make sense or do not agree with prior knowledge, then one or more mechanisms have not been taken into account (Kroon et al., 2008).

Land subsidence due to reservoir compaction has also been a problem in many geothermal fields. The mechanism is generally similar regardless of the type of reservoir. Thus, it is also helpful to study geothermal fields, the deformations that occur in them, and related research. The Cerro Prieto geothermal field in Baja California and the Wairakei geothermal field are two examples mentioned in the literature (Allis, 2000).

Carnec and Fabriol (1999) modeled and analysed the subsidence due to fluid withdrawal in the Cerro Prieto geothermal field, which at the time was one of the largest liquid-dominated fields in the world, supplying three power plants. Part of the waste fluid from the production was reinjected into the west side of the field and part of it was evaporated in the evaporation pond. In order to develop the model, the researchers assumed the deformation to be elastic in a half-space from a point source. Original information was gathered in order to model the subsidence setting. The data was gathered using images selected from InSAR data collected from 1993 to 1997. When analysed, the images revealed the presence of fringes at one corner of the area. The fringes appeared in different combinations, which meant that they could not be present due to atmospheric changes and effects. Moreover, their formation and altitudes indicated that they were also not formed due to topographic effects. The studies and analysis were based on the assumptions that the crust of the Earth is a semi-infinite ideal elastic body and that land surface deformations are due to changes in hydrostatic pressure in a spherical source known as the Mogi source. The best-fit model to represent the phenomena in the area and to locate the compaction/dilation point sources at greater depths was found with trial and error. The results indicated that areas on the surface where uplift was observed matched dilation point sources and, therefore, reinjection areas. The depths of the Mogi sources also showed that the land subsidence was a result of the compaction of the reservoir itself due to a drop in pore pressure that resulted from fluid extraction. Examination of the production pattern showed that during one period, in some local areas, production increased whereas the global withdrawal of natural fluid was maintained at a constant level on the site. Laboratory tests conducted on sandstone core samples taken from the wells indicated that compaction and reduction of permeability had occurred during the production process. Subsidence was recorded both after an earthquake and

20

during an increase in the production and withdrawal of fluid (Glowacka et al., 1999). Only a short interval was identified between events that resulted in changes in the ground water level and the observed subsidence and compaction of sediments.

Aliss (1999) researched the Wairakei geothermal field because of its history of over 45 years of land subsidence, with about 14 ± 0.5 m observed in the subsidence bowl due to production. The main goal was to study the cause of the land deformation and investigate its effects. The distribution of pressure between 1950 and 2000 as well as the mass and rate of heat flow over time during this period were plotted, along with the history of subsidence over time during the same period. By normalizing the subsidence graph, and comparing two benchmarks, it was found that one area had undergone half of its total subsidence by 1963 and that the curve shows a very low rate of subsidence in 1999, indicating that the major cause of subsidence had dissipated and was no longer fully present. However, other areas in the eastern bore field passed the halfway mark of their total subsidence during the mid-1970s. The subsidence in this area caused ponding and cracking. The ponding significantly affected the environment in that area because the roots of the trees around the ponded area were flooded, so the trees died and fell into the expanding pond. The effects of ponding on the environment can be seen in the two photographs in Figure 6.

Figure 6: Evolution of ponding in the Wairakei stream at the centre of the subsidence bowl. The photograph on left was taken in 1981, and the photograph on the right was taken in 1997at almost the same location (Allis, 2000).

As can be seen, the ecosystem in the area has been greatly affected. High rates of tilt recorded in the area indicate high rates of extensional strain, which has resulted in the cracking of the ground at the outer edges of the subsidence bowl. Because of erosion during heavy rainfalls,

these cracks became fissures up to 1 m wide. These vertical and horizontal ground strains have also resulted in casing damage in wells in some areas.

3. Factors Affecting the Movement of the Ground Surface

Generally speaking, volumetric changes in the subsurface result in surface deformations. An increase in the volume of the rock of the reservoir, due, for example, water or steam or waste injection, which results in surface upheaval and compaction in the reservoir due to oil or liquid withdrawal , cause land subsidence. The changes in volume that occur in the subsurface can be caused either by natural causes such as tectonic motion, a rise in sea level (Hu et al., 2004), or earthquakes or by human activities such as ground water withdrawal, oil and gas recovery (petroleum industry), coal mining, sulphur and ore extraction, other mining activities, underground excavations to create tunnels and caverns, and steam or waste reinjection (Nagel, 2001). These changes in the subsurface can occur at shallow depths due to construction work, such as the building of foundations and tunnels; peat oxidation; the compaction of clay layers; ground water withdrawal. They can also occur at much greater depths because of earthquakes, hydrocarbon production, salt production, or waste reinjection. A change in volume at both shallow and deeper depths affects the surface and causes deformations. It has been proven that a surface deformation field created as the result of a point source placed at depth *d* beneath the surface with a volume change of ΔV can be described approximately as an area with a radius *d* above the center of the volume change (Kroon et al., 2008) (Figure 7).
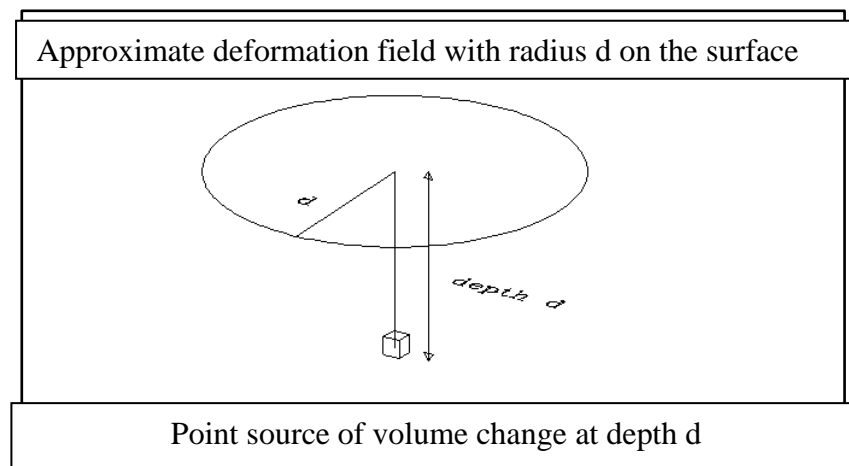
Figure 7: The approximate deformation field as a result of a point source of volume change at depth d.

When discontinuities in volume change are considered as sources of subsurface deformations for modeling purposes, it should be remembered that the principles of the physical occurrence

of compaction or swelling and resulting land deformation are generally the same for all reservoirs, hydrocarbon reservoirs, water reservoirs, geysers, geothermal fields, waste injection fields, etc., regardless of the type of material withdrawn or injected. The major difference lies in the varying geometry, geological settings, and material properties that differ for specific cases and specific reservoirs and that require the application of different models (Gambolati, 1975).

In the oil and gas industry, the causes of surface deformations are usually reservoir compaction or expansion due to fluid withdrawal or reinjection. Thus, the changes in volume that occur in the reservoir depend on many internal factors, such as the properties of the rock in the reservoir, the history of its formation, its geometry, and external factors, such as external loads and the overburden material. The geometry of the reservoir has a sizable impact on the way it will react upon recovery and during injection and has a significant effect on induced deformations that can be monitored on the surface. The most important factors in the geometry of a reservoir are its depth and width, and the ratio between them is critical. If this ratio is larger than 1, meaning that the width is greater than its depth, most of the vertical deformation in the reservoirs is transferred linearly to the surface, and the surface deformation is a function of the change in the reservoir's height (ΔH).

Deformations that occur at significant depths and inside the reservoir are transferred to the surface through the overburden material. The behaviour and properties of the overburden material therefore have a substantial impact on the deformations that occur and can be observed on the surface. Although reservoir deformations may be plastic and irreversible locally, the behaviour of the overburden material also must be elastic in order for its behaviour to be modeled and a solution produced (Dusseault et al., 2002). According to d'Alembert's principle, when a 3D setting of a medium is modelled, a plastic strain at a point can be translated into an elastic strain at a very small distance from the initial source. With respect to the behaviour of overburden material over oil reservoirs, since the strains induced in the overburden are very small, in the order of ($\varepsilon < 10^{-4}$), even in cases where huge vertical deformations are observed on the surface, it is correct to assume that the overburden acts elastically in most cases (Dusseault et al., 2002).

Land deformation due to changes in the volume of the reservoir can be observed as vertical, horizontal, and tilts. However, according to site observations and past studies it has been determined that the maximum values of displacement due to reservoir compaction occur in a vertical direction (Bruno et al., 1990) because of the geometry of reservoirs. The width of a reservoir is far greater than its thickness, which results in vertical surface deformations being much larger than any horizontal movements induced on the surface (Dusseault et al., 2002). Over oil and gas reservoirs, the vertical surface movements have been found to be three to five times larger than the horizontal displacements (Bruno et al., 1990). However, the thousands of well-casing failures observed and recorded in oil fields are not the result of vertical deformation, but are due mostly to shear and bending deformations. Thus, although horizontal displacements and tilts may be small in magnitude, the damage they cause is not insignificant, and they should therefore be studied seriously as well. Tilts also provide important information about the surface deformation field, and their use as input data for investigating changes in the volume of a reservoir is therefore the focus of this thesis.

3.1 Geological terminology

3.1.1 Definition of a reservoir

A reservoir is a formation of one or more subsurface rock formations that contain a natural accumulation of liquid and or gaseous hydrocarbons. A reservoir rock formation itself is porous and permeable. The pores should interconnect to let fluids migrate through the rock and the rock itself should be permeable to have the ability to allow the flow of the fluid through it (Cosse, 1993; Amyx et al., 1960; Calhoun, 1917). This characteristic of the reservoir rock or the subsurface material is the reason that the reservoir or soil compacts because of an increase in effective stress.

How the subsurface reacts under loading, production, and reinjection activities depends strictly on several groups of factors: the characteristics of the subsurface material, the structural features of the reservoir, the characteristics and properties of the reservoir fluid, the pressures present or induced inside the subsurface, the temperatures inside the reservoir, and the operating conditions implicit in the media (Calhoun,1917).

3.1.2 Reservoir materials

One method of classifying the material in a reservoir is to describe it based on the grain types and the type of soil particles that form the reservoir rock.

The rock in a reservoir is composed mainly of sedimentary materials, generally sandstones or limestones. Sandstones and or carbonates, which are sedimentary rocks, comprise 99% of reservoirs (Cosse, 1993; Amyx, 1960).

The best way to describe and study a reservoir and its properties and behaviour under loading, production, or reinjection is to describe the reservoir in terms of measurable engineering quantities, the most useful of which are porosity and permeability (Calhoun, 1917). These two factors are often used to calculate and predict the deformations and compactions that occur inside and above reservoirs.

A soil sample is composed of all three phases of materials: solid (grain particles), liquid (water), and air. Porosity is defined as the ratio of the volume of voids (volume of air + volume of water) in a soil sample to the total volume of the soil sample (Das, 2006):

$$n = \frac{Vv}{Vt} \qquad (3.1)$$

A high porosity indicates a higher volume of voids in a constant volume of soil sample and such a soil would undergo a higher amount of compaction under a load or an increase in the effective stress.

A soil or rock formation is permeable due to the existence of interconnected voids or fractures that provide a path for water to penetrate and move through (Das, 2006).

3.2 Mechanical properties of a reservoir and the compaction subsidence mechanism that occurs due to oil withdrawal

The weight of sediments and any other material that is placed on the soil over a reservoir, otherwise referred to as external loads, is supported by both the rock matrix of the reservoir and the fluid within the rock pore space (Hermansen et al., 2000). The total stress is thus the result of the summation of the effective stress, i.e., the stress carried by the soil skeleton, and the pore pressure, which is the weight carried by the water inside the porous medium.

$$\sigma_v = \sigma' + u \qquad\qquad (3.2)$$

Thus, when fluid is withdrawn from inside the reservoir, the pore pressure drops. If the total stress remains constant, the load that was initially supported by the fluid is now transferred to the solid matrix, and the effective stress increases. Now tolerating a greater load than before, the rock formation is compacted due to the additional stress. The increase in the effective stress can be caused either by an increase in the external loads, such as the addition of facilities and equipment for oil excavation, or by a decrease in the pore pressure inside the soil or rock matrix. A decrease in pore pressure can be due to a decrease in the level of the underground water table in the soil layers or to oil or fluid withdrawal from inside the reservoir. An increase in pore pressure is the result of an increase in the level of the underground water table or of reinjection and water flooding inside reservoirs. Thus, the equilibrium present in the soil prior to any change no longer exists after the change in pore pressure.

Rock or layers of soil react to loading or to an increase in the effective stress, and to unloading or to a decrease in the effective stress differently based on the history of the soil. The consolidation type of the material, which is basically an indication of the load history of the material, is thus of great importance in studying and understanding the behaviour of the material under loading or unloading and also in defining specific qualities of the material, such as compressibility. By performing the oedometer test on a sample of the soil obtained at the depth of study, geotechnical engineers in a laboratory can produce a very important graph: the void ratio plotted against the log of the effective stress (Figure 8). From this graph, the maximum effective stress that has been tolerated by the soil at that specific depth can be calculated. When the effective stress present at the site is compared with this maximum effective stress from the graph, a current effective stress (σ_0') that is lower than the maximum effective stress (σ_c') indicates that the soil has tolerated higher loads during its formation than those present at the time. This soil is referred to as pre-consolidated or over-consolidated. If the effective stress present at the time is larger or equal to the maximum effective stress from the graph, the soil or material is weak and is expected to undergo more deformations and more compaction due to an increase in the effective stress. This soil is referred to as normally consolidated soil.
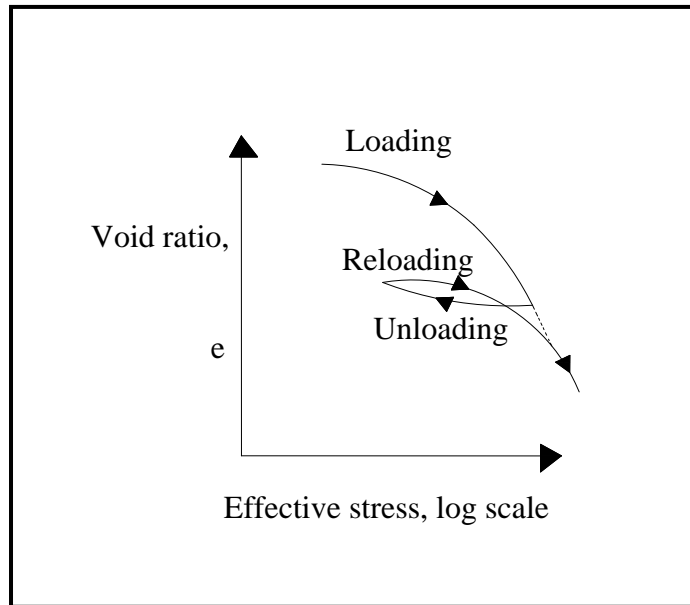
Figure 8: Void ratio of a soil sample plotted against the effective stress from the oedometer test

The slope of the first part of the graph before σ'_c is referred to as the compression index. The slope of the graph from the unloading procedure is referred to the swelling index. These two factors are very important factors for calculating the consolidation and settlement of a soil.

Another important point that can be interpreted from the graph is the deformation after unloading. If, after unloading, the unloading curve rises nearly to the beginning of the graph, it means that most of the deformations have been recovered, and thus, most of the deformations are elastic. If not, then most of the deformation is plastic and irreversible. Elastic deformation in soil is due to elastic deformation in the soil grain particles, meaning that the particle grains compress due to the compression transferred as the result of soil grain contact. Plastic or irreversible deformations, however, are due to the rearrangement or remoulding of the grain structure under loading and also to the soil grain particle breaking into smaller particles under loading. These deformations are therefore irreversible. The deformations in a reservoir have been proven to be primarily of this type.

The main mechanism of the compaction of the reservoir rock in oil and gas reservoirs, as mentioned earlier, is a drop in pore pressure or, more generally, a change in pore pressure due to oil production or reinjection and water flooding, which results in an increase in pore pressure. Other physical mechanisms can also result in reservoir compaction, (Chin et al.,

1993) some of which relate to the reservoir rock and others to the properties and behaviour of the overburden. The following are some of the mechanisms that result in the compaction of a reservoir:

- Pore pressure drops due to oil production.

- Shear induces compaction. Of course, shear does not itself result directly in compaction. However, the stress state due to shear concentrations causes the matrix blocks to displace slightly with respect to one another, these non-equal movements result in concentrated zones of stress that may produce fractures, and thus more displacements under pore pressure changes occur due to this weaker formation (Chin et al., 1993).

- The weakening of some types of reservoir rock material, such as chalk, due to contact with non-equilibrium cold seawater, e.g., in the Ekofisk field (Hermansen et al., 2000).

- Mechanical properties of the overburden material can cause compaction.

These mechanisms cause deformations in the subsurface due to changes in fluid pressure, such as water flooding or oil production. However, in other cases, such as waste injection, when a material is forced into the subsurface, these mechanisms do not apply. The deformations are a result of forcing an external material such as waste into the subsurface area, which then results in surface deformations.

3.2.1 Parameters affecting reservoir compaction

In nature, compaction depends on the overburden load, the amount of this load that is transferred to the reservoir, the tectonic loads applied to the formation, and the strength of the rock. Tectonic movements, although very small, slowly break the contacts between grains in different areas, thus resulting in the rearrangement and compaction of the grains even without any additional load (Gurevich et al., 1993). Periodic temperature changes cause the same damage and rearrangement of grain particles, thus creating compaction. Generally, disregarding thermal and chemical effects such as dissolution, reservoir compaction can be considered a function of three parameters: increases in the effective stress, the thickness of the reservoir, and the compressibility of the reservoir rock (Nagel, 2001).

3.2.1.1 Increases in the effective stress

Originally, prior to the production and withdrawal of oil, the reservoir rock and the overburden are both in equilibrium conditions. The rock has been consolidated and compacted by the effective stress present due to the overburden material and the loads placed on it. As oil production starts, the pore pressure drops because of fluid withdrawal. The total stress remains constant, so the effective stress increases. As the effective stress increases, the pressure on the reservoir rock matrix increases, causing it to compact. The reservoir rock compacts up to the point at which the matrix re-establishes new equilibrium states (Nagel, 2001).

If the compaction of the reservoir rock is the result of an increase in the effective stress due to fluid withdrawal, it can be controlled by controlling the pressure of the pore water (Nagel, 2001), either by managing the production rate or by reinjecting water into the reservoir to compensate for the loss in pressure. The principle is that after fluid withdrawal has stopped, if the pore pressure has remained constant or has increased, e.g., because of injection, then some part of the subsidence is recoverable and even a measure of uplift on the surface can be observed in some cases. This phenomenon is known to be due to the relaxation of the elastically compressed overburden materials after the pore pressure has been increased and is commonly known as elastic rebound. A good example of elastic rebound in the literature is the extensive research on reinjection experiments carried out at the Wilmington oilfield in California (Chen et al., 2007).

3.2.1.2 Thickness of the reservoir

Unlike changes in effective stress, reservoir thickness is an intrinsic characteristic of the reservoir that cannot be changed (Nagel, 2001). Most well-known compacting reservoirs are relatively thick, with measurements greater than 100 m. Generally, the greater the thickness of a reservoir, the more compaction is expected to undergo. Thus, the thickness of a reservoir has a direct relationship to its compaction (Nagel, 2001). In Table 1 lists the thickness and other properties of the most common oil reservoirs.

Table 1: Properties of common subsiding oil reservoirs (Nagel, 2001).

Place	Thickness, m	Depth, m	Porosity, %	Pressure, MPa
Belridge	Up to 800	250-900	Up to 70	
Bolivar Coast	Up to 180	>300	Up to 40	~6-10 (change)
Ekofisk	Up to 300	>3000	Up to 45	50 (initial)
Groningen	120-270	~ 3000		35 (initial)
Po Delta	Up to 600	100-600	Up to 30	
Valhall	Up to 280	>2400	Up to 50	45 (initial)
Wilmington	800-2000	700-1800	Up to 45	~10 (change)

3.2.1.3 Compressibility of the reservoir rock

The compressibility of the reservoir rock is another factor that affects its compaction. Like thickness, compressibility is an intrinsic characteristic of the reservoir, but these two parameters work in opposition to each other, meaning that a thin but highly compressible reservoir and a thick but less compressible reservoir may have the same amount of compaction under the same pore pressure drop and similar conditions. Although compressibility is an intrinsic characterization of the reservoir, unlike thickness, in some cases, it can be altered. Thermal or geochemical effects can change compressibility, and it has been proven that changes in water saturation also lead to significant changes in the compressibility of a reservoir (Nagel, 2001).

Of the three parameters that affect the compaction of a reservoir, compressibility is the hardest to measure accurately. Compressibility is itself a function of other parameters, such as the mineral composition of the rock matrix, the degree of mineral decomposition or alteration, the cementation and porosity of the rock, and the degree of sorting. Well sorted refers a soil formation in which the sediment sizes are similar whereas poor sorted refers to mixed sediment sizes. Of these factors, porosity is the critical parameter that defines the compressibility of a rock or soil. Table 1 shows that the majority of highly compactable reservoirs have a porosity level greater than 30 %.

According to Bruno (1990), who conducted detailed research with respect to the compressibility of reservoir rock, rock compressibility itself depends on two important factors:

- Material pore volume compressibility C_p
- Bulk compressibility C_b

These two factors are defined as follows:

$$C_p = \frac{1}{V_p} * \frac{\Delta V_p}{\Delta P_p} \qquad (3.3)$$

$$C_b = \frac{1}{V_b} * \frac{\Delta V_p}{\Delta P_p} \qquad (3.4)$$

where V_p = pore volume

V_b = bulk volume

P_p = pore pressure

C_p and C_b are defined as the change in pore volume and bulk volume, respectively, with respect to pore pressure change, ΔP_p at a constant confining pressure. These two factors are well defined in theory, but in some cases, such as in diatomite reservoirs, where the deformations are inelastic at almost all stress levels, these factors can be defined only empirically through laboratory measurements.

3.3 Methods of monitoring reservoir compaction (subsurface monitoring)

The casing collar locator log method is one of the earliest methods of monitoring reservoir compaction. Using this method, the change in the distance between casing collars is measured in order to determine and monitor the compaction of a reservoir. The accuracy of the data gained from this method is ± 0.012 m per casing joint. This method is very dependent on the coupling of the reservoir rock and the casing, and the results are therefore questionable in the majority of cases (Nagel, 2001).

Compaction monitoring with radioactive bullets shot into the formation is another method that is not sensitive to the interaction between the casing and the reservoir. Radioactive bullets are shot into the formation at regular intervals. After statistically analysing the data and with the use of accelerometer corrections to account for errors due to any irregular movements of the tool, changes in the distance between two bullets can be measured even up to 1 cm. If the bullets are shot into the overburden, it would be possible to obtain the ratio between the compaction of the reservoir and the surface subsidence that results from the transfer of the subsurface compaction.

This method also has limitations. If the bullet does not penetrate to the desired extent, the results are neither accurate nor useful (Nagel, 2001).

Monitoring porosity over time is an indirect way of monitoring the compaction of a reservoir. Since compaction results in a decrease in pore volume, compaction can be monitored by logging the porosity. Changes in the porosity in the reservoir rock can then be linked to the compression of the reservoir by comparing the results to the behaviour measured through laboratory testing and changes in the porosity due, for example, to a given strain in the uniaxial test. The results produced by this method can be inaccurate because of the heterogeneity of the distribution of the porosity inside the entire reservoir and also because of the limitations of the accuracy of porosity logging (Nagel, 2001).

Micro seismic surveys and the use of 4D seismic technology are other methods of monitoring the compaction of a reservoir. These methods are limited because of the presence of gas in the overburden material, the effects of changes in the degree of water saturation on rock velocity, and their level of accuracy (Nagel, 2001).

Reservoir compaction monitoring is carried out in order to determine the conditions and changes inside the reservoir. This data is needed in order to determine and predict the motion of the ground and the surface subsidence as a result of oil production. However, as can be seen, these procedures are time consuming, and the results can be inaccurate if the set-up is not precise. Deformations induced in the subsurface due to injections, e.g., waste injection are not easy to monitor, which explains why the inverse case has become of great interest to researchers.

3.4 Overburden material and the degree to which subsurface compaction is transferred to the surface

The degree to which the induced subsurface deformations are transferred to the surface and thus the amount and shape of the resulting surface deformation are dependent on the following factors: the geometry and areal extent of the reservoir, the depth of the reservoir burial, the stiffness properties of the material surrounding the pressure-depleted zone (Bruno, 1990), and the mechanical properties of the overburden material (Chin et al., 1993).

Deformations in the subsurface occur primarily in the central portion of the reservoir, usually where the porosity is the highest. Once the reservoir deforms, the overburden on top deforms as well. If a compaction zone is induced in the subsurface, the overburden moves downward as well. However, it also resists the deformation and attempts to remain rigid over the reservoir, flexing down over the crest of the reservoir but pinned on the exterior of the flanks of the reservoir. Thus, a portion of the load which was supported by the centre of the reservoir rock is transferred to the regions at the edges. This phenomenon is referred to as the arch effect. When the load is transferred to the edges, less of the load is supported by the reservoir rock, which results in less deformation. The effect of the overburden resisting deformation depends on the mechanical properties of the overburden, and the arching effect results in the development of shear stresses. The maximum values of these stresses are found primarily on the edges, where transition occurs between layers of material. If the shear stresses become large enough that the overburden loses its ability to resist deformation, the arching is no longer effective and the load transfer characteristics become less effective as well (Chin et al., 1993).

The presence of vertical tensile strains and elongations above a compacting reservoir is evidence of the bridging effect and indicates that all of the overburden weight has not been fully transmitted to the reservoir. The result is that the reservoir compacts much faster than the overlying material and layers (Gurevich et al., 1993).

3.5 Surface deformation monitoring

The deformations induced in the subsurface are transferred to the surface through the overburden material, and the surface deforms as a result. If the reservoir is horizontal and homogeneous, the displacement contour observed on the surface appears as displaced points positioned around the centre of the volume change (injection or production wells) (Vasco et al., 2002). However, in most cases, a fault zone is inside or close to the reservoir and causes skewing of the distribution of the volume change and the resulting surface deformations. Thus, it can be seen that observing only the pattern of the surface deformations can provide an idea of the distribution of the changes in volume inside the reservoir, and since the distribution of the changes in volume is related mainly to reservoir permeability and compressibility, from the discontinuities found in the distribution of the changes in volume in the reservoir, these two parameters can be solved for as well (Vasco et al., 2002). Surface monitoring is also an

effective method of checking for validation of the models used to predict future subsidence or upheaval and can thus be used to solve the direct problem.

Monitoring surface deformations is therefore a very important part of the production operation. The most common techniques for measuring and monitoring deformations in the petroleum industry, steam reinjection projects, and waste reinjection are as follows:

3.5.1 Global positioning system (GPS)

Using this method, data can be collected periodically, and the elevation of each given observation point in the field can be determined with centimetre-level accuracy. Global positioning satellites are used to monitor the vertical and horizontal movement of receiver stations, each of which must contain a receiver and a data collection system.

3.5.2 Interferometric synthetic aperture radar (InSAR)

This method also uses satellites that can map and document surface displacements at both a large and small scale but with less accuracy than GPS. In this method, the changes in phase between satellite radar images are used to determine changes in elevation. This method is used for mapping topography, for monitoring and recording displacements induced by earthquakes and displacements in magnetic fields, for producing images of ice dynamics, and for monitoring subsidence induced by mining and geothermal production (Nagel, 2001; Du et al., 2001; Vasco et al., 2002).

3.5.3 Tilt meter monitoring

Tilt meter monitoring is currently one of the most popular methods of observing and monitoring land subsidence, especially in the oil and gas industry. This technology uses highly precise levels placed near the surface in order to measure deformations that occur due to field operations such as oil production, fluid withdrawal, fluid injection, and hydraulic fracturing. Tilt meters measure what are called tilts, which are displacement gradients.

The common use of the tilt meter has resulted from its advantages over other methods: its very high precision and ability to detect motion in the order of 10^{-5} m and its continuous data collection capability that permits deformations due to production, injection, or any other type of field operations to be closely monitored.

3.5.4 Levelling and distance survey data

The use of levelling and distance survey data is one of the oldest methods of monitoring subsidence. A network of stations is established in the area, and motion in each is monitored over time. This method is costly and time consuming and its application is usually limited to onshore sites (Ferretti et al., 2008; Nagel, 2001).

The usual purpose of monitoring is to solve the inverse case, which requires a large number of observation points. Obtaining data by means of one of the above methods is much less costly and faster than having to drill deep wells into the reservoir and using pressure gauges and sensors to record changes in pressure. It is for this reason that solving the inverse case is of interest.

The data recorded from surface monitoring is used for the following purposes:

- monitoring of hydraulic fracturing
- monitoring of fluid migration in volcanic areas
- steam injection
- well testing
- petroleum production
- monitoring of waste reinjection and fracture and the resulting subsurface deformation

4. Mathematical Approach

4.1 Direct case

The direct case to be solved involves the calculation or prediction of surface deformations due to subsurface movements, based on measured reservoir compaction and changes in volume in the reservoir rock or in the subsurface, using data gathered from the methods mentioned in section 3.3 or using the distribution of changes in volume assumed to be occurring within the reservoir to further predict the induced surface movements. All calculations in this thesis are based on Okada's formulas (Okada, 1985). Okada's solution models concentrated on the expansion or compaction that occurs in one direction, which is certainly not an exact representation of what is actually taking place but is a very good approximation. The approach used in previous models for similar inverse cases was to use the nucleus of strain approach (e.g., Bilak, 1989). Nucleus of strain is a model that describes deformation as expansion or compaction points being deformed into the space of the subsurface in all directions. Figure 9 shows a point source representing expansion in volume in the subsurface using the nucleus of strain approach.
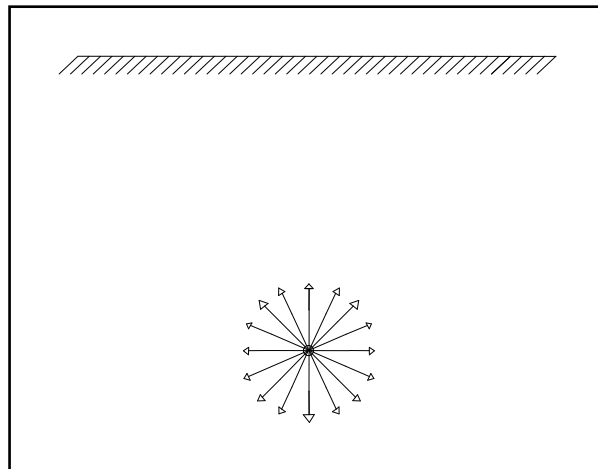
Figure 9: Change in volume modeled as a point of expansion in the subsurface: nucleus of strain approach.

Since the reservoir elements are much smaller than the geometry of the reservoir and its depth, it is correct to assume that the volume changes that occur in each reservoir element can be remodelled as point sources. These point sources that represent volume changes in each

37

element and are assumed to be at the centre of each cubic element are referred to as nucleus of strain points (Figure 10).
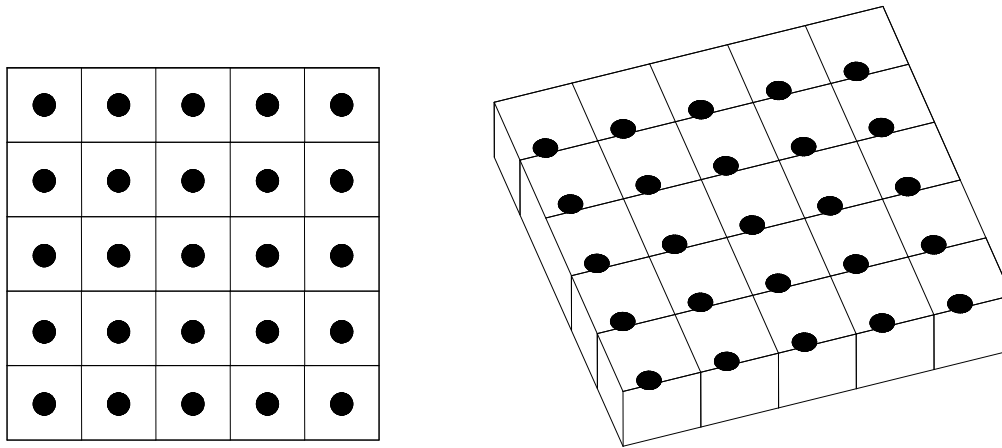
Figure 10: Nucleus of strain points in reservoir elements.

The concept of nucleus of strain was first introduced by Geertsma (1973) in the field of continuum mechanics. According to this concept, it is assumed that the volumetric strain at an element caused by local reduction or a change in pore pressure can be treated as a compression point, or, an expansion point, in the centre of an elastic half-space. This assumption would result in deformations induced in the free space. Thus the deformation at a given point on the surface is the result of the contribution of these compression or dilation nucleolus of strain points in the reservoir elements using the nucleus of strain approach.

Modelling an actual deformation in all directions using Okada's method requires the addition of three Okada solutions in three directions. The results would of course differ slightly from those produced by the nucleus of strain approach which represents deformations as a series of nucleus of strains, and are integrated over the reservoir.

It is difficult to say which approach is closest to reality; however, in the reservoirs that are the main focus of this research, the thickness is much smaller than depth or width so the majority of deformations occur vertically. Because deformations induced in these cases are mostly one dimensional, displacement discontinuity provides a better model for these applications.

A number of assumptions were made in modeling and solving for the direct case. The media was assumed to be an isotropic homogenous semi-infinite medium (Okada, 1985) and the only

source of subsurface volumetric change was assumed to be that of the reservoir. Since the length of a reservoir is normally much larger than its thickness, for the purposes of this thesis, the shape of the reservoir was assumed to be a thin rectangular plate (Figure 11).
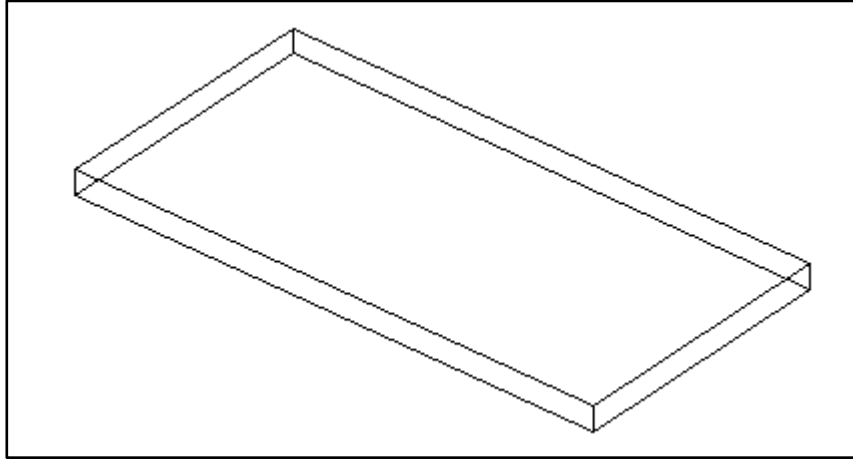
Figure 11: Shape of the reservoir assumed for modeling.

Although many factors that affect the land and surface deformations in reality were neglected, such as the curvature of the Earth, the surface topography, crustal layering, inhomogeneity or vertical layering, and angled layered medium, the results are still acceptable. Previous studies have shown that the curvature of the Earth can be negligible in events happening at shallow depths and at distances of less than 20 degrees. However, vertical layering has a significant effect on deformations and the results of modeling (Okada, 1985). Despite this factor and the many others that can be involved in an actual modeling of the Earth, the assumption of a simple isotropic homogenous half-space was used for this study. The assumptions made can be considered acceptable because the theoretical models based on these assumptions have been proven to be good approximations of actual cases (Okada, 1985).

The subsurface source that causes induced surface deformations was modeled as a finite rectangular source (Okada, 1985).

Finite rectangular source

The source of subsurface deformation can be described as a finite rectangular source that causes deformations. To model the deformations, the reservoir was divided into smaller rectangular elements. Each element was considered to undergo a change in volume due to

activities such as oil production, steam reinjection, and waste injection. The source resulting in subsurface deformation was thus considered to be a finite rectangular source.

Based on Figure 12 from Okada (1985), the total force is the source of deformation. Thus the volumetric deformations resulting from the total force can be described as the combination of three forces or changes in dimension in three directions, as follows:

- x direction: the change would be along the x axis in the Cartesian coordinate system,
- y direction: the change would be along the y axis in the Cartesian coordinate system.
- z direction: the change would be along the z axis in the Cartesian coordinate system.
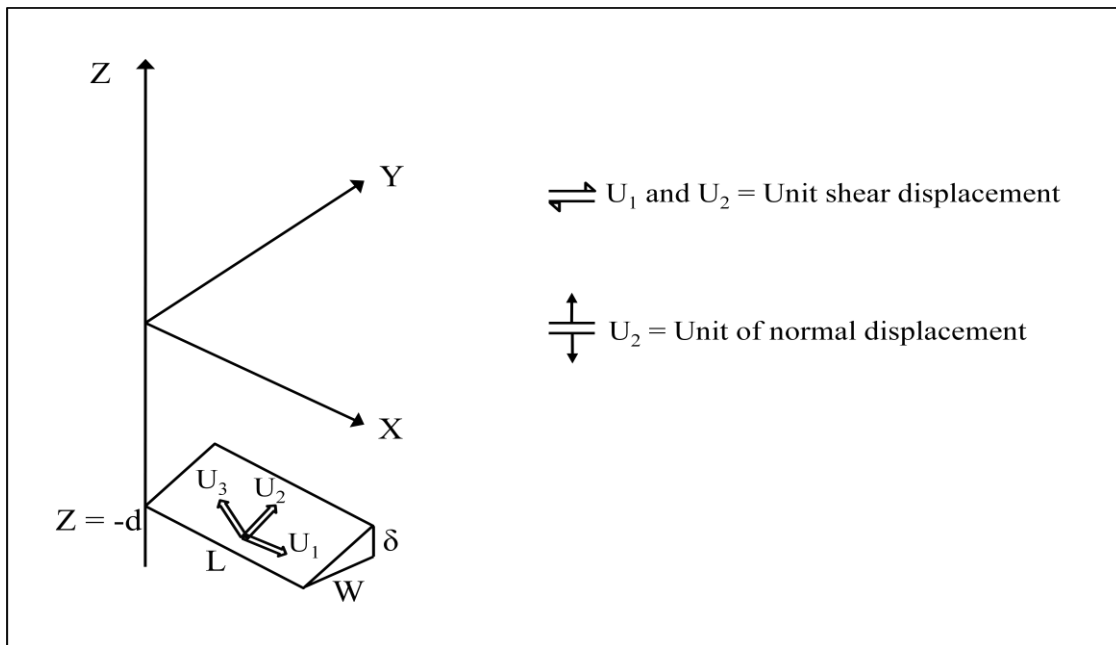
Figure 12: A general form of reservoir plate with a dip angle of δ, a length of L, a width of W, a depth of –d, and an Azimuth of 0° (Okada, 1985).

As can be seen in Figure 12, the elastic medium occupies the area of z<=0 in the selected coordinate system. This research was focused on the dislocations caused by the finite rectangular source rather than on the force itself. As mentioned above, the dislocation can be described as the combination of the dislocations in the three major directions in the Cartesian system. U_1, the vector in the x direction corresponds to strike-slip; U_2, which is the vector of dislocation parallel to the y axis, is referred to as dip-slip; and U_3, which is the vector of dislocation parallel to the z axis, is referred to as the tensile component of a general

dislocation. The fault, which in this case represents the reservoir, or to be more precise, a rectangular element of the reservoir with a length L and a width W, is modeled for a general case with an angle of rotation of δ from the XY plane (dip angle) and an azimuth (the rotation angle of the reservoir from the X axis).

Due to the subsurface dislocations, which are assumed to be the result of a rectangular finite force, the induced surface deformations occur on the surface in all three directions (x, y, and z). The first two induced surface deformations are referred to as horizontal deformations, and the third is called the vertical displacement or deformation. Based on Okada (1985), the resulting deformations on the surface can be calculated using the following formulas:

- **Displacements**

  <u>For strike-slip</u>   (4.2)

$$
\begin{cases}
u_x = -\dfrac{U_1}{2\pi}\left[\dfrac{\zeta q}{R(R+\eta)} + tan^{-1}\dfrac{\zeta\eta}{qR} + I_1 sin\delta\right] \|\\[2ex]
u_y = -\dfrac{U_1}{2\pi}\left[\dfrac{\ddot Y q}{R(R+\eta)} + \dfrac{q cos\delta}{R+\eta} + I_2 sin\delta\right] \|\\[2ex]
u_z = -\dfrac{U_1}{2\pi}\left[\dfrac{\ddot I q}{R(R+\eta)} + \dfrac{q sin\delta}{R+\eta} + I_4 sin\delta\right] \|
\end{cases}
$$

where

u_x = surface displacement in the x direction due to the strike-slip dislocation U_1

u_y = surface displacement in the y direction due to the strike-slip dislocation U_1

u_z = surface displacement in the z direction due to the strike-slip dislocation U_1

$$\zeta = XL - 0.5fl$$

$$\eta = YL.\cos(dip) + d.\sin(dip)$$

where

$$XL = Dx.\cos(dip) + Dy.\sin(dip)$$

$$YL = -Dx.\sin(dip) + Dy.\cos(dip)$$

$$Dx = x_0 - x_f$$

$$Dy = y_0 - y_f$$

Where

$$x_0 \& y_0 = coordinates\ of\ the\ observation\ point$$

$$x_f \& y_f = coordinates\ of\ the\ reservoir\ element$$

<u>For dip-slip</u> (4.3)

$$
\begin{cases}
u_x = -\dfrac{U_2}{2\pi}\left[\dfrac{q}{R} - I_3 sin\delta cos\delta\right] \| \\[2ex]
u_y = -\dfrac{U_2}{2\pi}\left[\dfrac{\ddot{Y}q}{R(R+\zeta)} + cos\delta tan^{-1}\dfrac{\zeta\eta}{qR} - I_1 sin\delta cos\delta\right] \| \\[2ex]
u_z = -\dfrac{U_2}{2\pi}\left[\dfrac{\ddot{I}q}{R(R+\zeta)} + sin\delta tan^{-1}\dfrac{\zeta\eta}{qR} - I_5 sin\delta cos\delta\right] \|
\end{cases}
$$

where

u_x = surface displacement in the x direction due to the dip-slip dislocation U_2

u_y = surface displacement in the y direction due to the dip-slip dislocation U_2

u_z = surface displacement in the z direction due to the dip-slip dislocation U_2

<u>For tensile fault</u> (4.4)

$$
\begin{cases}
u_x = -\dfrac{U_3}{2\pi}\left[\dfrac{q^2}{R(R+\eta)} - I_3 sin\delta^2\right] \| \\[2ex]
u_y = -\dfrac{U_3}{2\pi}\left[\dfrac{-\ddot{I}q}{R(R+\zeta)} - sin\delta\{\dfrac{\zeta q}{R(R+\eta)} - tan^{-1}\dfrac{\zeta\eta}{qR}\} - I_1 sin\delta^2\right] \| \\[2ex]
u_z = -\dfrac{U_3}{2\pi}\left[\dfrac{\ddot{Y}q}{R(R+\zeta)} + cos\delta\{\dfrac{\zeta q}{R(R+\eta)} - tan^{-1}\dfrac{\zeta\eta}{qR}\} - I_5 sin\delta^2\right] \|
\end{cases}
$$

In the above formulas,

$$I_1 = \frac{\mu}{\mu + \lambda}\left[\frac{-1}{\cos\delta}\frac{\zeta}{R + \ddot{I}}\right] - \frac{\sin\delta}{\cos\delta}I_5$$

$$I_2 = \frac{\mu}{\mu + \lambda}[\ln(R + \eta)] - I_3$$

$$I_3 = \frac{\mu}{\mu + \lambda}\left[\frac{1}{\cos\delta}\frac{\ddot{Y}}{R + \ddot{I}} - \ln(R + \eta)\right] + \frac{\sin\delta}{\cos\delta}I_4$$

$$I_4 = \frac{\mu}{\mu + \lambda}\frac{1}{\cos\delta}[\ln(R + \ddot{I}) - \sin\delta\ln(R + \eta)]$$

$$I_5 = \frac{\mu}{\mu + \lambda}\frac{2}{\cos\delta}\tan^{-1}\frac{\eta(X + q\cos\delta) + X(R + X)\sin\delta}{\zeta(R + X)\cos\delta}$$

where

- μ and λ are Lame's constants
- μ = shear modulus = $\frac{\Delta F/A}{\Delta L/L}$ where
  - F = shear stress
  - A = area
  - ΔL = distance between shearing planes
  - L = shear distance
- λ = k-2/3*μ where
  - k = bulk modulus

If $\cos\delta = 0$,

$$I_1 = -\frac{\mu}{2(\mu + \lambda)}\frac{\zeta q}{(R + \ddot{I})^2}$$

$$I_3 = \frac{\mu}{2(\mu + \lambda)}\left[\frac{\eta}{R + \ddot{I}} + \frac{\ddot{Y}q}{(R + \ddot{I})^2} - \ln(R + \eta)\right]$$

$$I_4 = -\frac{\mu}{\mu + \lambda} \frac{q}{R + \ddot{I}}$$

$$I_5 = -\frac{\mu}{\mu + \lambda} \frac{\zeta \sin\delta}{R + \ddot{I}}$$

(4.7)

$$p = y.\cos\delta + d.\sin\delta$$

$$q = y.\sin\delta - d.\cos\delta$$

$$\ddot{Y} = \eta.\cos\delta + q.\sin\delta$$

$$\ddot{I} = \eta.\sin\delta - q.\cos\delta$$

$$R^2 = \zeta^2 + \eta^2 + q^2 = \zeta^2 + \ddot{Y}^2 + \ddot{I}^2$$

$$X^2 = \zeta^2 + q^2$$

- **Strains**

  For strike-slip   (4.8)

$$\frac{\partial u_x{}^0}{\partial x} = \frac{U_1}{2\pi} \left[\zeta^2 q A_\eta - J_1 \sin\delta \right] ||$$

$$\frac{\partial u_x{}^0}{\partial y} = \frac{U_1}{2\pi} \left[\frac{\zeta^3 \ddot{I}}{R^3(\eta^2 + q^2)} - (\zeta^3 A_\eta + J_2)\sin\delta \right] ||$$

$$\frac{\partial u_y{}^0}{\partial x} = \frac{U_1}{2\pi} \left[\frac{\zeta q}{R^3} \cos\delta + (\zeta q^2 A_\eta - J_2)\sin\delta \right] ||$$

$$\frac{\partial u_y{}^2}{\partial y} = \frac{U_1}{2\pi} \left[\frac{\ddot{Y}q}{R^3} \cos\delta + \{(q^3 A_\eta)\sin\delta - \frac{2q\sin\delta}{R(R + \eta)} - \frac{\zeta^2 + \eta^2}{R^3} \cos\delta - J_4\}\sin\delta \right] ||$$

  For dip-slip   (4.9)

$$\frac{\partial u_x{}^0}{\partial x} = \frac{U_2}{2\pi} \left[\frac{\zeta q}{R^3} + J_3 \sin\delta\cos\delta \right] ||$$

$$\frac{\partial u_x{}^0}{\partial y} = \frac{U_2}{2\pi}\left[\frac{q\ddot{Y}}{R^3} - \frac{sin\delta}{R} + (J_1)sin\delta cos\delta\right]||$$

$$\frac{\partial u_y{}^0}{\partial x} = \frac{U_2}{2\pi}\left[\frac{\ddot{Y}q}{R^3} + \frac{qcos\delta}{R(R+\eta)} + J_1 cos\delta sin\delta\right]||$$

$$\frac{\partial u_y{}^0}{\partial y} = \frac{U_2}{2\pi}\left[\ddot{Y}^2 qA_\zeta - \left\{\left(\frac{2\ddot{Y}}{R(R+\zeta)}\right) + \frac{\zeta cos\delta}{R(R+\eta)}\right\}sin\delta + J_2 sin\delta cos\delta\right]||$$

<u>For tensile fault</u> (4.10)

$$\frac{\partial u_x}{\partial x} = -\frac{U_3}{2\pi}\left[q^2\zeta A_\eta + J_3 sin^2\delta\right]||$$

$$\frac{\partial u_x}{\partial y} = -\frac{U_3}{2\pi}\left[-\frac{\ddot{I}q}{R^3} - \zeta^2 qA_\eta sin\delta + J_1 sin^2\delta\right]||$$

$$\frac{\partial u_y}{\partial x} = -\frac{U_3}{2\pi}\left[\frac{q^2}{R^3}cos\delta + q^3 A_\eta sin\delta + J_1 sin^2\delta\right]||$$

$$\frac{\partial u_y}{\partial y} = -\frac{U_3}{2\pi}\left[(\ddot{Y}cos\delta - \ddot{I}sin\delta)q^2 A_\eta - \frac{qsin2\delta}{R(R+\zeta)} - (\zeta q^2 A_\eta - J_2)sin^2\delta\right]||$$

where (4.11)

$$J_1 = \frac{\mu}{(\mu+\lambda)}\frac{1}{cos\delta}\left[\frac{\zeta^2}{R(R+\ddot{I})^2} - \frac{1}{R+\ddot{I}}\right] - \frac{sin\delta}{cos\delta}K_3$$

$$J_2 = \frac{\mu}{(\mu+\lambda)}\frac{1}{cos\delta}\left[\frac{\zeta*\ddot{Y}}{R(R+\ddot{I})^2}\right] - \frac{sin\delta}{cos\delta}K_1$$

$$J_3 = \frac{\mu}{\mu+\lambda}\left[-\frac{\zeta}{R(R+\eta)}\right] - J_2$$

$$J_4 = \frac{\mu}{\mu+\lambda}\left[-\frac{cos\delta}{R} - \frac{q*sin\delta}{R(R+\eta)}\right] - J_1$$

K_1 and K_3 are given in equations (4.17) or (4.18)

If $cos\delta = 0$, (4.12)

45

$$J_1 = \frac{\mu}{2(\mu + \lambda)} \frac{q}{(R + \tilde{\imath})^2} \left[\frac{2\zeta^2}{R(R + \tilde{\imath})} - 1 \right]$$

$$J_2 = \frac{\mu}{2(\mu + \lambda)} \frac{\zeta \sin\delta}{R(R + \tilde{\imath})^2} \left[\frac{2q^2}{R(R + \tilde{\imath})} - 1 \right]$$

$$\begin{cases} A_\zeta = \frac{2R + \zeta}{R^3 (R + \zeta)^2} \\ A_\eta = \frac{2R + \eta}{R^3 (R + \eta)^2} \end{cases} \tag{4.13}$$

- **Tilts**

  For strike-slip $\hspace{8cm}$ (4.14)

$$\frac{\partial u_z}{\partial x} = \frac{U_1}{2\pi} \left[-q^2 \zeta A_\eta \cos\delta + (\frac{\zeta q}{R^3} - K_1)\sin\delta \right] \|$$

$$\frac{\partial u_z}{\partial y} = \frac{U_1}{2\pi} \left[\frac{\ddot{\imath}q}{R^3} \cos\delta + (\zeta^2 q A_\eta \cos\delta - \frac{\sin\delta}{R} + \frac{\ddot{Y}q}{R^3} K_1)\sin\delta \right] \|$$

  For dip-slip $\hspace{8cm}$ (4.15)

$$\frac{\partial u_z}{\partial x} = \frac{U_2}{2\pi} \left[\frac{\ddot{\imath}q}{R^3} + \frac{q\sin\delta}{R(R + \eta)} + K_3 \sin\delta\cos\delta \right] \|$$

$$\frac{\partial u_z}{\partial y} = \frac{U_2}{2\pi} \left[\ddot{Y}\ddot{\imath}q A_\zeta - \left\{ \frac{2\ddot{\imath}}{R(R + \zeta)} + \frac{\zeta\sin\delta}{R(R + \eta)} \right\} \sin\delta + K_1 \sin\delta\cos\delta \right] \|$$

  For tensile fault $\hspace{7cm}$ (4.16)

$$\frac{\partial u_z}{\partial x} = -\frac{U_3}{2\pi} \left[\frac{q^2}{R^3} \sin\delta - q^3 A_\eta \cos\delta + K_3 \sin^2\delta \right] \|$$

$$\frac{\partial u_z}{\partial y} = -\frac{U_3}{2\pi} \left[(\ddot{Y}\sin\delta + \ddot{\imath}\cos\delta)q^2 A_\zeta + \zeta q^2 A_\eta \sin\delta\cos\delta - \left\{ \frac{2q}{R(R + \zeta)} - K_1 \right\} \sin^2\delta \right] \|$$

  where $\hspace{9cm}$ (4.17)

$$K_1 = \frac{\mu}{(\mu + \lambda)} \frac{\zeta}{\cos\delta} \left[\frac{1}{R(R + \tilde{\imath})} - \frac{\sin\delta}{R(R + \eta)} \right]$$

$$K_2 = \frac{\mu}{(\mu + \lambda)}\left[-\frac{sin\delta}{R} + \frac{qcos\delta}{R(R + \eta)}\right] - K_3$$

$$K_3 = \frac{\mu}{(\mu + \lambda)}\frac{1}{cos\delta}\left[\frac{q}{R(R + \eta)} - \frac{\ddot{Y}}{R(R + \ddot{I})}\right]$$

If $cos\delta = 0$ (4.18)

$$K_1 = \frac{\mu}{(\mu + \lambda)}\frac{\zeta q}{R(R + \ddot{I})^2}$$

$$K_3 = \frac{\mu}{(\mu + \lambda)}\frac{sin\delta}{R + \ddot{I}}[\frac{\zeta^2}{R(R + \ddot{I})} - 1]$$

To avoid singularity in the above integrals,

if q=0, set $tan^{-1}\frac{\zeta\eta}{qR}$ to 0;

when $\zeta = 0$ set I_5 to 0;

when R+η=0, which occurs when $sin\delta < 0$ and $\zeta = q = 0$,

- set all terms containing R+η to 0
- and replace ln(R+η) to -ln(R-η)

From the above integrals, surface displacements, strains, and tilts can be calculated as the result of subsurface deformations being expressed as a combination of strike-slip, dip-slip, and tensile fault deformations.

4.2 Inverse case

The main purpose of this research is to focus on solving the inverse case, which uses the observation data obtained from the surface monitoring methods mentioned in section 3.5 and reconstructs the distribution of the changes in volume that occur within the subsurface that have resulted in the induced surface deformations. Measuring and recording surface deformation data have become very fast and easy, with many methods available for monitoring deformations. On the other hand, keeping track of the volume changes and the deformations that occur within the reservoir rock, along with the changes in pressure, is very important

47

because these data help with the modeling and understanding of what is actually happening within the reservoir and how it is responding to production. This data will also help in reservoir management and in arranging the timing and quantity of production or water reinjection for optimum results, in modeling deformation and fracture movements in waste injection projects, and in studying subsurface displacements as a result of steam injection. Using surface data observation points for back-calculating and determining reservoir compaction has therefore become of great interest.

The approach for this thesis was to divide the reservoir into small rectangular elements. Based on Geertsma (1973), volumetric changes inside the reservoir can be modeled as volume change distribution in each element that occur in one direction. The surrounding medium, which is the overburden material, is assumed to be a porous, elastic half-space, and the surface is assumed to be stress free. Any observation point chosen on the surface thus has a deformation due to the effect of volume changes occurring in each reservoir element. Of course this approach is correct if the only source of deformation is the volume change in the reservoir. If not, the deformations taking place at each observation point are the result of the effect of all sources of deformation at different depths. In this study, as previously mentioned, it was assumed that the changes in volume in the reservoir are the only source of deformation. Thus displacements and tilts occurring at an observation point can be written as the summation of the effects of the volume changes, either through expansion or compaction, that occur in each reservoir element. Integrating these points in this way over the reservoir volume permits the calculation of the deformations on the surface. From the equations mentioned in section 4.1 for calculating the induced subsidence, it can be seen that the surface deformation can be described generally as the following (Bilak, 1989):

$$U_x(r') = \int_v U(r,r').E_v(r).dV_r \qquad (4.19)$$

The mathematical approach used in this thesis is based on equation (4.19). $U_x(r')$ is the surface deformation or the induced subsidence at point r' from the origin in a polar coordinate system. $U(r,r')$ represents Green's function of the deformation (vertical deformation or tilts or horizontal deformations, depending on the formula used) at a point r' as a result of the volumetric strain (E_v)of a point source of r' in the polar system in dV_r (Figure 13).
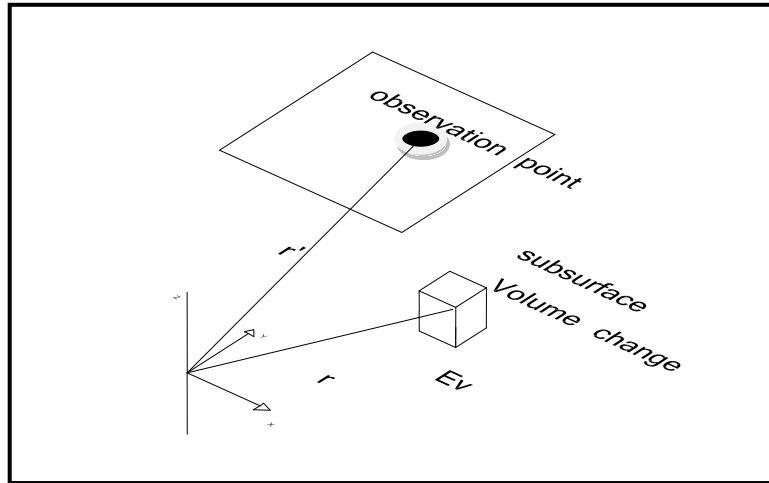
Figure 13: Illustration of the mathematical approach of the surface deformation that occurs due to a subsurface volume change (Bilak, 1989).

As mentioned, based on Geertsma (1973), the integral can be rewritten as a summation, and thus the surface deformation at a chosen observation point can be described as the summation of the effects of the volume changes occurring in each element, as follows:

$$U_x(r^{'}) = \sum_{i=1}^{N} U_i(r, r^{'}).E_{vi}(r).dV_{ri} \tag{4.20}$$

where N is the total number of reservoir elements.

The formulas mentioned so far are all used for solving the direct case, in which the volumetric changes in the reservoir are known, either from an assumed distribution or from actual measurements of the reservoir compaction, and the surface deformation is then calculated accordingly. However, in the inverse case, which is the main focus of this thesis, volume distribution is the unknown factor to be solved for based on the measured surface subsidence. Solving for the inverse case is not as easy as the direct case because it is an ill-posed problem.

4.3 Ill-posed problem

Inverse problems are generally referred to as problems in mathematical physics in which the aim is to solve for or determine an internal structural property or the past state of a system using indirect measurements (Engl et al., 1987). Calculating the position and size of a heating

source based on knowledge of the properties of the medium and the spatial distribution of the surface temperature (Vasco, 2004) is an example of an ill-posed problem.

Many inverse problems can be described as a general form of

$$A * Z = u \quad (4.21)$$

where

- u = the "external parameter" which is measured and known.
- Z = the "internal parameter" which cannot be measured or is very hard to measure directly.
- A = in this case a given operator between u and Z.

In this thesis, u is the measured surface deformation, and Z, the internal parameter, is the volume change occurring in the reservoir. A is the matrix relating volume changes to surface deformations.

Equation (4.20), which is the general form for calculating surface subsidence from volume changes is a form of Fredholm integral equation of the first kind with a kernel $K(x,s)$ (Tikhonov et al., 1977):

$$u(x) = \int_a^b K(x,s)Z(s)ds \qquad c \leq x \leq d \qquad (4.22)$$

$Z(s)$ is the internal parameter or the unknown function in a space F. $u(x)$ is the external parameter or known function in a space U. The kernel $K(x,s)$ is assumed to be continuous with respect to variable x and also has a continuous partial derivative with respect to x ($\partial K / \partial x$).

Tikhonov and Arsenin (1977) rewrote the above integral using an operator of A:

$$A * Z = \int_a^b K(x,s)Z(s)ds \qquad (4.23)$$

The aim now is to solve for $Z(s)$, the internal parameter. Assume that in an actual case of $u(x) = u_1(x)$ there is a solution of $Z_1(s)$ in equation (4.22). This assumption means that, in this case, a volume change of $Z_1(s)$ in the reservoir element has resulted in a surface deformation of $u_1(x)$:

$$u_1(x) = \int_a^b K(x,s)Z_1(s)ds \qquad (4.23.1)$$

However, in real and actual cases, the external parameter or the known factor, which is measured and recorded experimentally by tools and engineering devices, would always contain an error, no matter how exact and accurate the device is. This inaccuracy might be due to error in the equipment itself, or in the set up, or in the reading of the data. Thus, rather than an exact value or function for $u_1(x)$, only an approximation of the actual data $u(x)$, that is slightly different from $u_1(x)$, would be possible.

So now the approximate solution of the equation can be solved for, and the answer will be close to $Z_1(s)$ and not exactly $Z(x)$. However, Tikhonov et al. (1977) showed that since approximate data are used for $u_1(x)$, and $u_1(x) \neq u(x)$, the exact function of $Z_1(s)$ cannot be used for the approximate solution of equation (4.22), since the solution might not exist because the kernel $K(x, s)$ has a continuous derivative with respect to x, so $u(x)$ must also have a continuous derivative with respect to x as well. If $u(x)$ does not have a continuous derivative with respect to x, the solution to equation (4.22) will no longer exist. Furthermore, equation (4.22) has a solution only if the approximate members of $u(x)$ that belong to the image AF of the set F of the function $Z(s)$ under the mapping executed by the operator A, as mentioned, is as follows:

$$u = A * Z \equiv \int_a^b K(x,s)Z(s)ds \quad , z(s) \in F \qquad (4.24)$$

According to Tikhonov et al. (1977), the solution to equation (4.22) can be described in a classic form based on equation (4.21). The solution to the equation would thus be written as

$$Z = A^{-1} * u \qquad (4.25)$$

In the equation (4.25), A^{-1} is not stable under small changes in the initial data (u in this case). The problem is therefore referred to as ill-posed, and its solution is not straightforward, as is usually the case for inverse cases. The known data is almost never the exact value and always contains small error. This very small noise or slight discrepancies from the absolute exact values in the initial observed data, which is the known data in the equation, would result in large random variations in the solution for $Z(s)$. In other words, small variations in the

51

observed data would result in large changes in the solution, thus making the solution unstable even under very small changes in the input. The following example is a good illustration of the effect of error in the known observation data on the solution (Bilak, 1989):

$$\begin{cases} 0.9999x + 1.0001y = 1 \\ x - y = 1 \end{cases}$$

Thus
$$x = 0.5 \text{ and } y = -0.5$$

If an error of $\delta \ll 1$ is now added to the known part the result would be as follows:

$$\begin{cases} 0.9999x + 1.0001y = 1 \\ x - y = 1 + \delta \end{cases}$$

Thus
$$x = 0.5 + 5000\delta \quad y = -0.5 + 4999.5\delta$$

If equation 4.21 is non-singular, meaning that the determinant of A is not zero (det $A \neq 0$), based on Cramer's rule, it would have a unique solution. This result will be explained in more detail in the following section. However, if the determinant of A is equal to zero (det $A = 0$) and the equation is thus singular, a solution would be found (but would not be unique), only if the condition for the existence of a solution is satisfied: vanishing of the relevant determinants. The existence of the solution is then dependent only on the initial data set or the external factor (Tikhonov et al., 1977).

As mentioned above, since exact values are not available, rather than dealing with equation 4.21, the following approximation equation would be used:

$$\tilde{A} * Z = \hat{u} \qquad\qquad (4.26)$$

where

$$\|\tilde{A} - A\| < \delta \quad \text{and} \quad \|\hat{u} - u\| < \delta$$

Therefore the approximate matrix $\tilde{A}$ must be considered rather than A, and it is thus more difficult to determine whether the system is singular (Tikhonov et al., 1977). Since only the approximate system $\tilde{A} * Z = \hat{u}$ can be used, rather than the exact system $(A * Z = u)$, only an

approximate solution can be found. It should be remembered that this system must be stable under small changes in the initial data in order for the equation to have a solution

For defining and providing a clear understanding of the concept and conditions of ill-posed problems, describeing the conditions of a well-posed problem is helpful. In determining the solution Z in space F from an initial observed data set of u in space U, the problem is well posed on the pair of metric spaces (F,U) if the following conditions are satisfied (Tikhonov et al., 1977):

- For every element $u \in U$ there exists a solution Z in the space F.
- The solution is unique.
- The problem is stable on the spaces (F,U).

Problems that do not satisfy these three conditions are known as ill-posed problems. It should be pointed out that the term ill-posed is used with respect to a given pair of metric spaces (Tikhonov et al., 1977), meaning that the same problem can be well posed in other matrixes while being ill posed in (F, U).

With respect to the above conditions for a well-posed problem, the first two conditions characterize the mathematical determinacy of a problem. The third condition, however, is related to the physical determinacy of the problem and also implies the possibility of applying numerical methods to solve it on the basis of approximate observation data (Tikhonov et al., 1977).

The problem of solving a Fredholm integral equation of the first kind was proven by Tikhonov et al. (1977) to be an ill-posed problem, and it was pointed out that the solution is unstable under small changes in the observation data or in the known external parameter of *u(x).*

4.4 Ill-posed problems: the inverse case

Inverse cases make up a broad class of ill-posed problems in fields such as engineering, physics, and technology. Observation data is gathered and processed as the external parameter in the equation (4.21).The data processing is generally carried out in three steps (Tikhonov et al., 1977):

- Data are gathered or read from a measurement device.

- The results are processed statistically with an estimate of the degree of reliability.

- The results from step two are interpreted.

The goal is now to use the final data as *u(x)* to solve equation (4.21).

Suppose that the phenomenon has occurred and can be characterized by an element of Z_T belonging to a set F. The result would be $A * Z_T = u_T$. Here $u_T \in AF$, and AF is the image of the set F under the mapping executed by the operator A. Z_T can not be measured or it is hard to measure, and thus only the resulting effect of it, u_T, is measured and known. It can thus be described as an inverse case. Equation (4.21) has a solution on F only for observed data points that belong to the set of AF. The value of u_T is obtained from observation and measured data, and thus only the approximate value is known. Thus only an approximate solution can be used to solve for a value close to Z_T (Tikhonov et al., 1977).

$$A * Z = û \qquad\qquad\qquad (4.27)$$

û, the approximate external parameter, does not usually belong to the set of AF. Moreover, the operator A is usually defined in such a way that it's inverse, A^{-1}, is not continuous. Thus, it might not have a solution for two reasons (Tikhonov et al., 1977):

- The approximate solution might not exist on the set of F since û might not belong to the set of AF, and the first requirement of well-posed problems is not satisfied.

- Even if the solution does exist, the stability requirement is not satisfied. That is, the solution would not be stable under small changes in the external parameter because the inverse matrix A^{-1} is not continuous. The third requirement of well-posed problems is therefore not met.

Thus, inverse problems in which the input is measured data, and therefore only an approximation of the actual value is available, are ill-posed problems. Therefore, the inverse case that is the focus of this thesis, which is the calculation of the changes in volume based on surface observation data, is an ill-posed problem. To solve and model the volume changes, the reservoir is divided into small elements. Each element represents the volume changes that cause deformations. This assumption is correct since the depth of the reservoir is much larger

than the dimensions of each element (Bilak, 1989). Thus, the deformation at each observation point is the summation of the effects of the volume changes occurring in each element:

$$u_m = \sum_{n=1}^{N} K_{m,n} * \Delta v_n \qquad (4.28)$$

u_m= surface observation data from the mth observation point, which in this thesis can be the vertical displacement or tilt1 or tilt2

N = number of reservoir elements

Δv_n= volume change in the nth reservoir element

Equation (4.28) can be written in the form of a matrix, as follows:

$$[K]_{m*n} * [\Delta v]_{n*1} = [u]_{m*1} \qquad (4.29)$$

To solve for the unknown matrix $[\Delta v]_{n*1}$,

$$[\Delta v]_{n*1} = [u]_{m*1} * [K]_{m*n}^{-1} \qquad (4.30)$$

A straightforward solution for a well-posed inverse linear problem would be to use Cramer's rule to solve for Δv. The following is a general example for a reservoir with two elements and three observation points on the surface:

A reservoir of two elements is assumed with three observation points on the surface. The unknowns are the volume changes in each element, so two unknowns are present. The format of the equation to be solved is as follows:

$$\begin{vmatrix} K_{11} & K_{12} \\ K_{21} & K_{22} \\ K_{31} & K_{32} \end{vmatrix} * \begin{vmatrix} \Delta v_1 \\ \Delta v_2 \end{vmatrix} = \begin{vmatrix} U_1 \\ U_2 \\ U_3 \end{vmatrix}$$

where Δv_1 and Δv_2 are the unknowns.

Using Cramer's rule would result in

$$\Delta v_1 = \frac{\det K_1}{\det K}$$

$$\Delta v_2 = \frac{\det K_2}{\det K}$$

where

$$K = \begin{vmatrix} K_{11} & K_{12} \\ K_{21} & K_{22} \\ K_{31} & K_{32} \end{vmatrix}$$

and

$$K_1 = \begin{vmatrix} U_1 & K_{12} \\ U_2 & K_{22} \\ U_3 & K_{32} \end{vmatrix} \quad \text{and} \quad K_2 = \begin{vmatrix} K_{11} & U_1 \\ K_{21} & U_2 \\ K_{31} & U_3 \end{vmatrix}$$

The general form for K_1 and K_2 is as follows:

$$K_1 = \begin{vmatrix} U_1 & K_{12} & K_{13} & \cdots \\ U_2 & K_{22} & K_{23} & \cdots \\ U_3 & K_{32} & K_{33} & \cdots \end{vmatrix}$$

$$K_2 = \begin{vmatrix} K_{11} & U_1 & K_{13} & \cdots \\ K_{21} & U_2 & K_{23} & \cdots \\ K_{31} & U_3 & K_{33} & \cdots \end{vmatrix}$$

$$K_3 = \begin{vmatrix} K_{11} & K_{12} & U_1 & \cdots \\ K_{21} & K_{22} & U_2 & \cdots \\ K_{31} & K_{32} & U_3 & \cdots \end{vmatrix}$$

$$\Delta v_1 = \frac{\det K_1}{\det K} \quad \Delta v_2 = \frac{\det K_2}{\det K} \quad \Delta v_3 = \frac{\det K_3}{\det K} \cdots \Delta v_n = \frac{\det K_n}{\det K}$$

As can be seen for the solution of the volume changes, if the determinant of the K matrix is zero or close to zero, the result of Δv would go to infinity and thus there would be no solution, meaning that the problem would be ill-posed.

$$\det k = |k|$$

$$\text{If} \ \ |k| \to 0$$

$$\Delta v_n = \frac{|K_n|}{|K|} \to \infty$$

The elements of the K matrix can be described as

$$\begin{vmatrix} K(x_1, S_1) & K(x_1, S_2) & ... \\ K(x_2, S_1) & K(x_2, S_2) & ... \\ ... & ... & ... \end{vmatrix}$$

As the number of reservoir elements increases, the size of the elements decreases, and the distance between each point would become too small. As a result, the two columns in the K matrix would be very similar, and as the number of elements increases, the columns in the K matrix would become close to identical. Thus, in a reservoir that has a large number of elements, $|k| \rightarrow 0$ as the number of reservoir elements increases (Rothenburg, 2009, personal communication). Therefore, the problem is ill-posed, and in order to solve for the volume changes the system must be changed into a well-posed system that is not singular and is stable under small changes in the input.

4.5 Regularization technique

As mentioned in previous sections, this thesis deals with an ill-posed problem. The major factor that causes the problem to be characterized as ill-posed is the approximate nature of the observation data points available and the known information, which thus results in u being outside the set of AF. Tikhonov et al. (1977) called these types of problems genuinely ill-posed problems. A method of dealing with such problems is to construct approximate solutions for the following equation:

$$A * Z = u \tag{4.21}$$

Tikhonov et al. (1977) introduced the concept of the regularization as an approach for finding an approximate solution for these types of problems. The solution being constructed must be stable under small changes in the initial observed data. As approximate data u_δ, and not the exact value u_T, observation points might be outside AF. Thus A^{-1} would not be continuous, and the solution would not exist. If the approximate and the exact values differ from each other by no greater than δ, $| u_\delta - u_T | < \delta$, δ being the difference between the exact value and the observed value, the data used as input would basically be the error present in the observation point. Since $u_\delta \neq u_T$, the above exact equation cannot be used to solve for the approximate volume change of Z_δ. That is,

$$Z_\delta = A^{-1} * u_\delta \qquad\qquad (4.31)$$

Calculation of Z_δ requires the use of an operator that is dependent on or in accordance with the error, which means that when the error is too small and $\delta \to 0$, the approximate solution must approach the exact solution ($Z_\delta \to Z_T$) (Tikhonov et al., 1977).

Suppose that elements of $Z_T \in F$ and $u_T \in U$ and that Z_T and u_T are connected by A matrix as $A * Z_T = u_T$, Thus:

An operator of $R(u, \beta)$ is defined by Tikhonov et al. (1977) as a ***regularizing operator*** for the general form of the above equation (A*Z=u) in the neighbourhood of $u = u_T$ if an approximate solution for $Z_\beta = R(u_\delta, \beta)$ can be found using the approximate known data of u_δ and with the aid of the regularization operator ($R(u, \beta)$). Here $\beta=\beta(\delta, u_\delta)$, which is in accordance with the error present in the observed data(δ). The solution is referred to as the ***regularized solution*** and the numerical parameter β is called the ***regularization parameter.***

There may be many operators $R(u,\beta)$ from U into F that are dependent on parameter β and are defined for every element of U and every positive value of β. However, another characteristic of the regularizing operator is that it should be continuous with respect to u as well. Tikhonov et al. (1977) proved the following theorem*:*

<u>Theorem:</u> Let *A* denote an operator from F into U, and let R(*u*,β) denote an operator from U into F that is defined for every element *u* of U and every positive value of β and that is continuous with respect to *u*. If

$$\lim_{\beta \to 0} R(AZ, \beta) = Z$$

for every element Z of F, then the operator R(*u*,β) is a regularizing operator for the equation

$$A * Z = u.$$

To summarize, every regularizing operator of R characterizes approximate construction of stable solution provided that the value of β is in accordance with and consistent with the accuracy δ of the observed data (β=(δ)). Since $|u_\delta - u_T| < \delta$, the regularization parameter

58

can be chosen in such a way that as the error moves toward zero $(\delta \rightarrow 0)$, meaning that the approximate value of the input data approaches the absolute actual value, the regularized solution of $Z_\beta = R(u_\delta, \beta(\delta))$ would approach the exact solution of Z_T, and thus,

$$|Z_T - Z_\beta| \rightarrow 0$$

Thus, to find an approximate solution for the equation (4.21) that is stable under small changes in the initial observed data points requires the following:

1. Define a regularizing operator R.
2. Verify the regularization parameter β using supplementary information related to the problem, for example, pertaining to the size of the error present in the input observed data.

As mentioned in previous sections, the problem this thesis deals with, which is calculating reservoir deformations and volume changes using surface deformation data, is a Fredholm integral of the first type. Due to the ill-posed nature of the integral, a solution might not exist, and thus, to solve the problem, an approximate solution should be used. Based on Tikhonov et al. (1977), the solution of another problem that is stable and is close to the original problem can be used for small values of error in the observed input data. Rather than the initial equation having to be solved, another problem is thus chosen, and the solution to that equation would be the approximate solution of the initial ill-posed problem. The problem now to be solved would be

$$u(x) = \int \{U * E_v * dv + \beta * R(E_v)\} \qquad (4.32)$$

The next steps would then be to find the suitable regularization operator for the Fredholm integral and to define the regularization parameter of β.

4.5.1 Defining β

β is a number between zero and one, which is obtained through trial and error. If the value of β used is a very small value or zero, the second term added to the initial ill-posed equation to make it stable would be omitted, and the equation would still be the same initial ill-posed problem, with a large amount of noise observable in the results. However, using a very large

value of β would significantly affect the solution and would result in a smooth solution that is not correct (Figure 14).
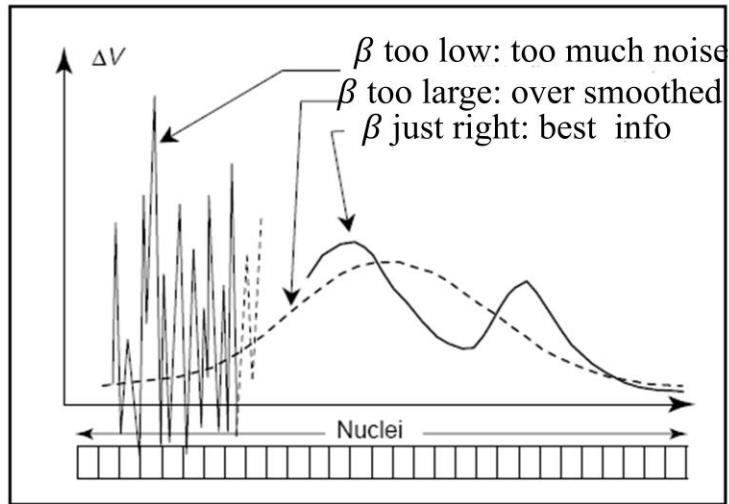

Figure 14: The effect of the value of β on the solution of the inverse problem (Dusseault et al., 2002).

4.5.2 Construction of the regularization operator

One possible approach to the construction of a regularization operator that is suitable for the Fredholm integral is using the least square approach. If the functional referred to as the *smoothing functional* is minimized, the regularization operator can be defined. The procedure is described in detail as follows.

If $\delta=0$ and thus no error is present in the observed data points, the following is correct:

$$u(x) = \int U * E_v * dv$$

As mentioned, the above equation can be described as a general form of the Fredholm integral:

$$u(x) = \int k(x,s) * Z(s) * ds$$

However, the measured observation data are not the actual exact values. If the right-hand side of the equation is the exact solution resulting in the precise value of Z, thus different from the observation point:

$$u(x) - \int k(x,s) * Z(s) * ds$$

where

- $u(x)$ = the data with error
- $\int k(x,s) * Z(s) * ds$ = the exact surface deformation

As indicated above, this approach can be used in the construction of the regularization operator. A functional is written based on the integral or summation of the square differences between the observation points and the actual values from the solutions:

$$M(u,z) = \int [u(x) - \int k(x,s) * Z(s) * ds]^2 * dx \qquad (4.33)$$

The solution involves finding the minimum value from the above equation. This value is unique and equal to Z_T for u_T as the input observation point. However, since the problem is ill-posed due to variations in the observation data, the values available are only approximate values, and the solution therefore might not lead to a smoothing function.

Due to the ill-posed nature of the problem, the approximate solution should be sought. Based on Tikhonov et al. (1977), the solution of another problem that is close to the initial problem with respect to small errors in the values of the input and observed data can be used, and both solutions would approach the same results as the error→ 0. The following equation is used as the approximate equation for the approximate solution for the smoothing function:

$$M(u,z) = \int [u(x) - \int k(x,s) * Z(s) * ds]^2 * dx + \beta * \Omega(z) \qquad (4.34)$$

Unlike the initial problem that was not stable under small changes, the problem of minimizing the above equation has been shown to be stable by Tikhonov et al. (1977). Stability was reached by eliminating and narrowing the class of possible solutions through the use of the functional $\Omega(z)$. Thus, in the above equation, $\Omega(z)$ plays a stabilizing role. Therefore, $\Omega(z)$ is called the *stabilizing function*, and M(u,Z) in equation (4.34) is called the **smoothing function.** The regularizing operator is basically constructed by minimizing the smoothing functional.

If F, which is a set of possible solutions of the equation $A*Z=u$, is assumed to be a matrix space and $\Omega(z)$ is a stabilizing functional defined on a set $F_1 \subset F$, then the following would apply (Tikhonov et al., 1977):

Theorem: Let A denote a continuous operator from F into U for every element u of U and every positive parameter β, there exists an element $Z_\beta \in F_1$ for which the functional

$$M(u,z) = \int [u(x) - \int k(x,s)*Z(s)*ds]^2 * dx + \beta * \Omega(z)$$

attains its greatest lower bound.

Tikhonov et al. (1977) introduced the following stabilizing functional:

$$\Omega(z) = \int_a^b \sum_{r=0}^p q_r(x) * (\frac{d^r z}{dx^r})^2 dx \tag{4.35}$$

They proved that it is the smoothest function up to the order of p for which $|AZ-u|=\delta$. Thus, the general form of the smoothing function using the above stabilizing function of the first order, p=1, would be

$$M(u,z) = \int_c^d [u(x) - \int_a^b [k(x,s)*Z(s)*ds]]^2 * dx + \beta * \int_a^b \sum_{r=0}^1 q_r(x) * (\frac{d^r z}{dx^r})^2 dx$$

$$c \leq x \leq d$$

In the above equation, q(s) is a continuous function, is defined randomly, and can be used to modify the solution functions of Z(s). The result would be the following:

$$M(u,z) = \int_c^d [u(x) - \int_a^b [k(x,s)*Z(s)*ds]]^2 * dx + \beta$$

$$* \int_a^b q_0(x)*Z^2(s) + q_1(x)*(\frac{dz}{dx})^2 * dx$$

The graph in Figure 15 shows the results of the solution of an ill-posed problem along with the actual expected values at $\beta=0$.
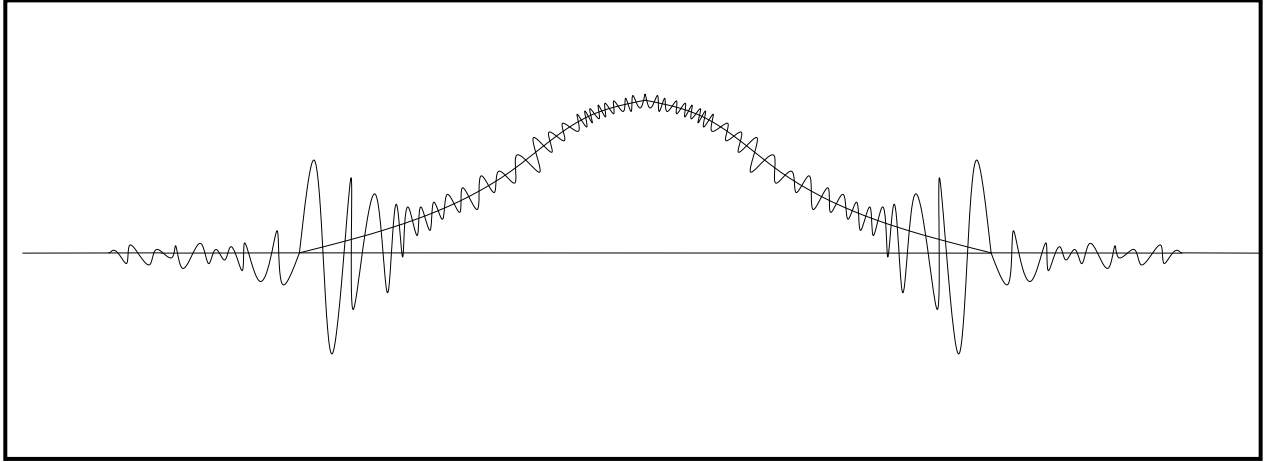

Figure 15: Results of the inverse calculations, showing a large number of jumps, especially at the corner points; the solution is therefore not smooth (Rothenburg, 2009, personal communication).

The smooth curve represents the actual subsurface deformation, and the graph with noise illustrates the result of the ill-posed solution when $\beta=0$. The goal is thus to smoothen the solution. As can be seen, the corner points contain a greater degree of inaccuracy and therefore more noise in the results than the middle points. A value of q must be chosen that will smoothen the entire solution. On the other hand, outside the range of the actual values, there will still be noise while the expected value is supposed to be zero. However, it is not desirable to force the solution to be zero outside the range. Therefore, $q=1$ and $q_0 = 0$ were chosen for smoothening the solution (Rothenburg, 2009, personal communication)

$$M(u,z) = \int_{c}^{d} [u(x) - \int_{a}^{b} [k(x,s) * Z(s) * ds]]^{2} * dx + \beta * \int_{a}^{b} 0 * Z^{2}(s) + 1 * (\frac{dZ}{dx})^{2} * dx$$

For the Fredholm integral of the first kind, Tikhonov defined the stabilizing function to be used in the above equation as follows:

$$\Omega(z) = \int q(s) * (\frac{dZ(s)}{ds})^{2} ds$$

This format is basically the general form of the function used in the previous equation.

As mentioned, the initial aim in solving for the ill-posed problem was to determine the regularization operator, $Z_\beta = R(u_\delta, \beta)$. The approach used is to minimize the smoothest function. Thus, taking the first derivative of equation (4.34) with respect to x would result in the following:

$$\frac{\partial M(Z,u)}{\partial x} = [u(x) - \int K(x,s) * Z(s) * ds]^2 + \beta \int (\frac{dZ}{ds})^2 * ds$$

For the minimum to exist, the derivative must be set to zero. Thus,

$$\frac{\partial M(Z,u)}{\partial x} = [u(x) - \int K(x,s) * Z(s) * ds]^2 + \beta \int \left(\frac{dZ}{ds}\right)^2 * ds = 0$$

The first part of the equation, $[u(x) - \int K(x,s) * Z(s) * ds]^2$, is always nonnegative. As for the second part, $\beta \int \left(\frac{dZ}{ds}\right)^2 * ds$, β being always positive and the integral a power of two, thus always nonnegative. Therefore, for the entire derivative to be equal to zero and for a minimum to exist, both sentences must be zero.

Since, as previously mentioned, the thickness of a reservoir is much smaller than its width and length, it can be modeled as a thin plate. It is thus correct to assume that we are dealing with a two dimensional. Thus, $(\frac{dZ}{ds})^2$ can be written as $(\frac{d^2 Ev}{dx^2} + \frac{d^2 Ev}{dy^2})$, so in the problem of surface deformation analysis, the derivative of the Fredholm integral would be defined as follows:

$$u(x) - \int_v u.E_v.dv + \beta \left(\frac{d^2 Ev}{dx^2} + \frac{d^2 Ev}{dy^2}\right) = 0 \qquad (4.36)$$

As can be seen, the parameter is a function of the two variables x and y. The regularization operator that would result in the best approximate solution to the ill-posed problem of solving for the reservoir's volume changes using surface deformation data would be the Laplacian operator:

$$(\frac{d^2 Ev}{dx^2} + \frac{d^2 Ev}{dy^2})$$

in which Ev_β is the set of back-calculated volume changes with respect to the initial error in the input observation data. For $Ev_\beta = R(u_\delta, \beta)$ to satisfy the existence of the solution for the minimum of equation (4.34) to be obtainable, the following must apply:

$$\left(\frac{d^2 Ev}{dx^2} + \frac{d^2 Ev}{dy^2}\right) = 0$$

Tikhonov et al. (1977) showed that for the Laplacian operator, the equation (4.36) has a unique solution for Ev_β that is continuous for all values of β. If $\beta=0$,

$$M(u,z) = \int_c^d [u(\mathrm{x}) - \int_a^b [k(x,s) * Z(s) * ds]]^2 * dx + 0 * \int_a^b 0 * Z^2(s) + 1 * (\frac{dZ}{dx})^2 * dx$$

and

$$M(u,z) = \int_c^d [u(\mathrm{x}) - \int_a^b [k(x,s) * Z(s) * ds]]^2 * dx$$

This equation would be the initial ill-posed problem. The solution would thus be the solution of the original equation which might not exist. For small values of β, the solution would be an approximate solution of the original equation.

The initial matrix form of the problem, which was

$$[K]_{m*n} * [\Delta v]_{n*1} = [U]_{m*1}$$

is rewritten, and if the Lapacian operator and the regularization coefficient are added to the original equation, the following would be obtained

$$[K]_{M*N} * [\Delta v]_{N*1} - \beta * [Laplace]_{N*N} * [\Delta v]_{N*1} = [U]_{m*1} \qquad (4.37)$$

Thus,

$$([K]_{M*N} - \beta * [Laplace]_{N*N}) * [\Delta v]_{N*1} = [U]_{m*1} \qquad (4.37.1)$$

As mentioned previously, the reservoir can be assumed to be divided into small elements and the changes in volume in the reservoir thus be described as the summation of the changes in volume that occur in each element. The initial smoothing function, which was an integrated formula, can therefore be written as a series of summations.

$$\emptyset = \sum_{m=1}^{M}(U_m - \sum_{n=1}^{N} K_{mn} * \Delta v_n)^2 \quad (4.38)$$

This equation therefore represents the initial problem, where

- M = total number of observation points on the surface
- N = total number of reservoir elements
- K_{mn} = matrix relating volume changes in the nth reservoir element to surface deformations occurring in the mth point on the surface grid
- Δv_n = volume change in the nth reservoir element
- U_m = observation data (deformation, i.e., vertical displacement, tilts) in the mth observation point

However, due to the noise in the observation data, U_m, the problem of minimizing the equation and solving it would not have a solution since it is not stable under small changes. Thus, the stabilizing function, which in the case of a Fredholm integral of the first type is a Laplacian operator, should be added to the equation as proven above. The summation form of the problem to be solved would thus be

$$\emptyset = \sum_{m=1}^{M}(U_m - \sum_{n=1}^{N} K_{mn} * \Delta v_n)^2 + \beta * \sum_{n=1}^{N}(0 - \sum_{j=1}^{N} L_{nj} * \Delta v_j)^2 \quad (4.39)$$

The goal is to find solutions that will minimize $\emptyset$.

4.6 Calculating the general matrix equation form of the problem

The inverse problem of solving for the reservoir volumetric changes using surface data was reduced to minimizing the following equation:

$$\emptyset = \sum_{m=1}^{M}(U_m - \sum_{n=1}^{N} K_{mn} * \Delta v_n)^2 + \beta * \sum_{n=1}^{N}(0 - \sum_{j=1}^{N} L_{nj} * \Delta v_j)^2 \quad (4.39)$$

This equation can be written in two main parts:

$$\emptyset = I + II$$

where

$$I = \sum_{m=1}^{M} \left(U_m - \sum_{n=1}^{N} K_{mn} * \Delta v_n\right)^2$$

$$II = \beta * \sum_{n=1}^{N} \left(0 - \sum_{j=1}^{N} L_{nj} * \Delta v_j\right)^2$$

To minimize the equation,

$$\frac{\partial \emptyset}{\partial v_i} = \frac{\partial I}{\partial v_i} + \frac{\partial II}{\partial v_i}$$

where ∂v_i is the volume change in the ith reservoir element. Thus, for the general case of a reservoir with N number of elements and M, *being* the total number of observation points the following would result:

Part I:

$$I = \sum_{m=1}^{M} \left(U_m - \sum_{n=1}^{N} k_{mn} * \Delta v_n\right)^2$$

$I = (U_1 - (k_{11} * \Delta v_1 + k_{12} * \Delta v_2 + k_{13} * \Delta v_3 + \cdots + k_{1N} * \Delta v_N))^2 + (U_2 - (k_{21} * \Delta v_1 + k_{22} * \Delta v2 + k23*\Delta v3 + \ldots + k2N*\Delta vN)2 + \ldots + (UM - kM1*\Delta v1 + kM2*\Delta v2 + kM3*\Delta v3 + \ldots + kMN*\Delta vN)2$

$\frac{\partial I}{\partial v_1} = 2 * [U_1 - (k_{11} * \Delta v_1 + k_{12} * \Delta v_2 + k_{13} * \Delta v_3 + \cdots + k_{1N} * \Delta v_N)] * k_{11} + 2 * [U_2 - (k_{21} * \Delta v_1 + k_{22} * \Delta v_2 + k_{23} * \Delta v_3 + \cdots + k_{2N} * \Delta v_N) * k_{21}] + \cdots + 2 * [U_M - (k_{M1} * \Delta v_1 + k_{M2} * \Delta v_2 + k_{M3} * \Delta v_3 + \cdots + k_{MN} * \Delta v_N) * k_{M1}] = 0$

$\frac{\partial I}{\partial v_2} = 2 * [U_1 - (K_{11} * \Delta v_1 + K_{12} * \Delta v_2 + K_{13} * \Delta v_3 + \cdots + K_{1N} * \Delta v_N)] * K_{12} + 2 * [U_2 - (K_{21} * \Delta v_1 + K_{22} * \Delta v_2 + K_{23} * \Delta v_3 + \cdots + K_{2N} * \Delta v_N) * K_{22}] + \cdots + 2 * [U_M - (K_{M1} * \Delta v_1 + K_{M2} * \Delta v_2 + K_{M3} * \Delta v_3 + \cdots + K_{MN} * \Delta v_N) * K_{M2}] = 0$

...

The general matrix form of the above equations would be

$$[K]_{N*N} * [\Delta v \text{ or the unknown}]_{N*1} = [U \text{ or The Answer matrix}]_{N*1}$$

where

- $K = \begin{vmatrix} \sum_{i=1}^{M}(k_{i1})^2 & \sum_{i=1}^{M} k_{i1} * k_{i2} & \sum_{i=1}^{M} k_{i1} * k_{i3} & \cdots \\ \sum_{i=1}^{M} k_{i1} * k_{i2} & \sum_{i=1}^{M}(k_{i2})^2 & \sum_{i=1}^{M} k_{i2} * k_{i3} & \cdots \\ \sum_{i=1}^{M} k_{i1} * k_{i3} & \sum_{i=1}^{M} k_{i2} * k_{i3} & \sum_{i=1}^{M}(k_{i3})^2 & \cdots \\ & & \vdots & \end{vmatrix}_{N*N}$

  As can be seen, K matrix is a symmetric matrix.

- $\Delta v_i = \begin{vmatrix} \Delta v_1 \\ \cdots \\ \Delta v_N \end{vmatrix}$

- $U = \begin{vmatrix} \sum_{i=1}^{M} k_{i1} * u_i \\ \vdots \\ \sum_{i=1}^{M} k_{1N} * u_i \end{vmatrix}$

  where u_i is the observation data from the ith observation point.

For the second part,

$$II = \beta * \sum_{n=1}^{N}\left(0 - \sum_{j=1}^{N} L_{nj} * \Delta v_j\right)^2$$

Part II:

$$\frac{\partial II}{\partial v_1} = 2\beta * [0 - (L_{11} * \Delta v_1 + L_{12} * \Delta v_2 + L_{13} * \Delta v_3 + \cdots + L_{1N} * \Delta v_N)] * L_{11} + 2\beta$$
$$* [0 - (L_{21} * \Delta v_1 + L_{22} * \Delta v_2 + L_{23} * \Delta v_3 + \cdots + L_{2N} * \Delta v_N) * L_{21}] + \cdots + 2\beta$$
$$* [0 - (L_{N1} * \Delta v_1 + L_{N2} * \Delta v_2 + L_{N3} * \Delta v_3 + \cdots + L_{NN} * \Delta v_N) * L_{N1}] = 0$$

$$\frac{\partial II}{\partial v_2} = \cdots$$

The general matrix of L from the above equations would thus be as follows:

$$L = \beta * \begin{vmatrix} \sum_{i=1}^{N}(L_{i1})^2 & \sum_{i=1}^{N}L_{i1}*L_{i2} & \sum_{i=1}^{N}L_{i1}*L_{i3} & \cdots \\ \sum_{i=1}^{N}L_{i1}*L_{i2} & \sum_{i=1}^{N}(L_{i2})^2 & \sum_{i=1}^{N}L_{i2}*L_{i3} & \cdots \\ \sum_{i=1}^{N}L_{i1}*L_{i3} & \sum_{i=1}^{N}L_{i2}*L_{i3} & \sum_{i=1}^{N}(L_{i3})^2 & \cdots \\ & \vdots & & \end{vmatrix}$$

The general form of the second part in matrix form would then be

$$-\beta * [L]_{N*N} * [\Delta v \text{ or the unknown }]_{N*1} = 0$$

To summarize, the initial problem, which was $\frac{\partial \emptyset}{\partial v_i} = 0$, would be written in the form of the following matrix problem:

$$[K]_{N*N} * [\Delta v \text{ or the unknown }]_{N*1} - \beta * [L]_{N*N} * [\Delta v \text{ or the unknown }]_{N*1}$$
$$= [U \text{ or The Answer matrix}]_{N*1}$$

$$[K - \beta L]_{N*N} * [\Delta v \text{ or the unknown }]_{N*1} = [U \text{ or The Answer matrix}]_{N*1} \qquad (4.40)$$

This would be the matrix to solve.

4.7 Solving the matrix equation

4.7.1 Singular value decomposition method

To solve the matrix equation, the singular value decomposition (SVD) method was used. This method is used for solving or dealing with sets of equations or matrix systems that are either singular or numerically very close to being singular. Unlike some other techniques used for dealing with a set of equations, SVD not only diagnoses the problem but also solves it.

The SVD method is based on the theorem of linear algebra. Any A matrix of M*N that M≥N can be written as the product of three metrics as follows:

$$[A]_{M*N} = [U]_{M*N} * \begin{vmatrix} w_1 & 0 & 0 & 0 & 0 \\ 0 & w_2 & 0 & 0 & 0 \\ 0 & 0 & w_3 & 0 & 0 \\ 0 & 0 & 0 & \ddots & 0 \\ 0 & 0 & 0 & 0 & w_N \end{vmatrix}_{N*N} * [V^T]_{N*N}$$

Alternatively, each element of A matrix can be written as

$$A_{ij} = \sum_{K=1}^{N} w_k * U_{ik} * V_{jk}$$

where

- $[U]_{M*N}$ is a column-orthogonal matrix.
- $[W]_{N*N}$ is a diagonal matrix with positive or zero elements. These elements are the singular values.
- $[V^T]_{N*N}$ is the transpose of an N*N orthogonal matrix of V.

The SVD method can also be applied for cases when M<N but the decomposition matrixes are slightly different from what mentioned above. Details can be found in Press et al. (1988) .

As mentioned, the general form of an inverse problem would be

$$A * Z = U$$

The issues with ill-posed problems are as follows:

- They are not stable under small changes in the input data u due to errors caused by measurement devices. Regularization technique was used to deal with this problem.
- After the equation is stabilized, when solving for the unknown, the A matrix might be singular or the resolution might be close to being singular. Thus, the inverse of A might not exist. The SVD method was used in this study in order to deal with this problem. Using SVD, matrix A is written as the product of the three following matrixes:

$$A = U * [w_i] * V^T$$

70

$$Z = u * A^{-1}$$

In the case of a square matrix, which is the case in this thesis and has been represented by $([A]_{N*N})$ in previous sections, the inverse of the original matrix can be written as the inverse of the product of the three matrixes. Thus, since U and V are orthogonal matrixes, their inverse matrixes would be their transpose. As for the w matrix, since it is a diagonal matrix, the inverse would also be a diagonal matrix, with the elements being $1/w_i$.

$$A^{-1} = V * \left[diag\left(\frac{1}{w_i} \right) \right] * U^T$$

Thus, calculating the inverse would become simple and straightforward except when any element of the w matrix is equal to zero ($w_i = 0$) or is very small, this is, so small that the value would be dominated by the round-off error and thus be inaccurate. The more elements of w satisfy the above condition, the more singular matrix A would be. To be more specific, a factor named the condition number of a matrix was used by Press et al. (1988) to define the singularity of a matrix. The condition number of a matrix is defined as the ratio of the largest magnitude of w_i to the smallest magnitude of w_i .

$$Condition\ number = \frac{w_{max}}{w_{min}}$$

If the condition number of a matrix is infinite, then the matrix would be singular. If the condition number is too large, then the matrix is referred to as ill-posed.

The decomposition of the A matrix can always be done regardless of how singular it is.

To deal with singular matrixes where w_i is zero or very small, the SVD method simply replaces the elements of the inverse diagonal matrix that are too large or are infinite with zero:

$$\frac{1}{w_i} \rightarrow replace\ with\ 0\ if\ w_i \cong 0$$

The details and procedures are mentioned in detail in Press et al. (1988).

5.0 Modeling Technique

Mathematical and numerical models are among the most powerful methods used in the hydrocarbon industry. Although simple to use, the analytical solution that uses the formulas presented in Chapter 4.0 has the disadvantage that the deformations can be calculated only for the surface and not throughout an entire vertical section (Bruno et al., 1992).

The overburden material was modeled based on the assumption of its being an isotropic homogeneous half-space. As mentioned, the reservoir is divided into assumable elements, and a volume change is then assigned to each element in such a way that the total change in volume in a reservoir is the result of the summation of the individual changes in volume in each element. The source of deformation, that is, the change in volume, is treated as a finite rectangular source, and thus a source of deformation is assigned to each element.

The programming was written in C++ coding. The steps in the procedure are described in sequence in the following sections.

The first step, which is to solve the direct case, was to calculate the displacements in given observation points based on an assumed volume change distribution in the reservoir, using Okada's formulas for a finite rectangular source.

5.1 The direct case

It was assumed that the geometry of the reservoir is measured and known and thus the general inputs are the width, length, depth, azimuth, and dip angle of the reservoir. A grid of the observation points relevant for calculating the displacements was generated based on the number of observation points that extended in each direction, x and y, and also the distance between the observation points, all given as inputs. The reservoir was next divided into rectangular elements with given length and width as input. An assumable volume change in either one of the directions or in all three directions, i.e., Δv_x, Δv_y, and Δv_z, was assigned to each reservoir element.

Three subroutines where written: Calculation, Okadadisp, and Okadatilt. Thus, displacement in the three directions of strike-slip, dip-slip, and tensile fault; strains in three directions; and tilts

were all calculated for each observation grid point, based on the given input and Okada's formulas for a finite rectangular source.

5.2 The inverse case

With respect to solving the inverse case, for which surface deformation data points were used to back-calculate and to solve for the change in the volume of the reservoir, the deformation data, i.e., vertical displacement and tilts in two directions, $\frac{\partial U_z}{\partial x}$ and $\frac{\partial U_z}{\partial y}$, as calculated from the previous part (the direct case) based on the assumed volume change distribution were used as input data. Thus the back-calculated volume change distribution was then compared to the initial volume change assumed to verify the solution. The procedure was as follows:

Data from each observation point, which are basically the vertical displacement and or tilts calculated from the previous part, are used as input for the inverse program.

5.2.1 Using only one data set from each observation point as input

The objective of the inverse case was to solve the following equation:

$$[K - \beta L]_{N*N} * [\Delta v \text{ or the unknown }]_{N*1} = [U \text{ or The Answer matrix}]_{N*1}$$

The first step is to form k matrix elements using the related Okada formulas. The k matrix is as follows:

$$k = \begin{vmatrix} k_{11} & k_{12} & ... \\ k_{21} & k_{22} & ... \\ ... & ... & ... \end{vmatrix}_{m*n}$$

where

- m is the total number of observation points.
- n is the total number of reservoir elements.
- The element of k_{mn} is the mth number of observation node and the nth number of reservoir element.

As mentioned, the direct case could be written as

$$u = \Delta v * k$$

73

Therefore, if $\Delta v = 1$, the following would result:

$$\sum_{n=1}^{N} k_{mn} = displacement\ in\ m^{th}\ node$$

After the k matrix is arranged, the *K* matrix should be formed. The *K* matrix is an *N*N* matrix where *N* is the total number of reservoir elements. As shown in the previous section, the *K* matrix is formed using elements of the k matrix, and the general format is as follows:

$$K = \begin{vmatrix} \sum_{i=1}^{M}(k_{i1})^2 & \sum_{i=1}^{M}k_{i1}*k_{i2} & \sum_{i=1}^{M}k_{i1}*k_{i3} & \cdots \\ \sum_{i=1}^{M}k_{i1}*k_{i2} & \sum_{i=1}^{M}(k_{i2})^2 & \sum_{i=1}^{M}k_{i2}*k_{i3} & \cdots \\ \sum_{i=1}^{M}k_{i1}*k_{i3} & \sum_{i=1}^{M}k_{i2}*k_{i3} & \sum_{i=1}^{M}(k_{i3})^2 & \cdots \\ & & \vdots & \end{vmatrix}_{N*N}$$

The next step was to calculate the answer matrix based on the observation data points, which are calculated from the direct case and elements of the k matrix.

5.2.2 Using two or more data sets from each observation point

As mentioned, either vertical displacement or the tilts from each observation point can be used as input to back-calculate and solve for the reservoir volume change. If only one of the abovementioned data is used, the u_i that forms the *U* matrix would be either the displacement or the tilts used. More than one data thus can be used from each point in order to back-calculate and solve for the volume change. Since the magnitude of the values of the displacements and tilts are in totally different ranges, if all three types of data are used together, the tilt values would fade away as noise in comparison to the displacement values. Thus for all three data sets to be useful for back-calculations, they must be converted into the same range. Each data set was therefore normalized, meaning that values of each set were divided by the absolute maximum value of the related data set so that they were in the range of zero and one, 0<data<1. Maximum displacements are measured directly. As With respect to the tilts, either

tilt meters can be used directly and thus recording the maximum values for calculations, or, as in this thesis, the tilts can be obtained directly from the calculations of the direct case. Alternatively maximum tilts can be calculated using displacement graphs on the surface by obtaining the slope of the displacement graph at the point where the bulge of the graph changes to a concave curve. The first method is much faster and easier, and thus for this study, values for the tilts calculated from the direct case, which represents the data from tilt meters, were used as input for the inverse case.

In the case of all three displacement data being used, the procedure was as follows:

The objective was to minimize the following:

$$\emptyset = \frac{1}{|U_{max}|}\sum_{m=1}^{M}\left(u_m - \sum_{n=1}^{N}k_{mn}*\Delta v_n\right)^2 + \frac{1}{|Tilt\,1_{max}|}\sum_{m=1}^{M}\left(Tilt1_m - \sum_{n=1}^{N}k1_{mn}*\Delta v_n\right)^2 +$$

$$1/Tilt2max|m=1M(Tilt2m-n=1Nk2mn*\Delta vn)2+\beta*n=1N(0-j=1NLnj*\Delta vj)2 \qquad (5.1)$$

where

- $k1_{mn}$ is calculated based on data from tilt1,
- $k2_{mn}$ is calculated based on data from tilt2,
- k_{mn} is calculated based on data from vertical displacement,
- u_m is the vertical displacement at point m.

To minimize the above formula, $\frac{\partial\emptyset}{\partial v_i} = 0$

As can be seen, the calculations involve four nonnegative parts with the power of two. Therefore, for a minimum to exist, all sentences must be set to zero. The last part has not changed, and thus, the Laplacian matrix and the resulting solution would not change compared to the case of using only one set of data as input. With respect to the first three parts, the solution would result in the following:

$$
\left|\begin{array}{cc}
\dfrac{1}{u_{max}}\displaystyle\sum_{i=1}^{M}(k_{i1})^2 + \dfrac{1}{Tilt1_{max}}\displaystyle\sum_{i=1}^{M}(k1_{i1})^2 + \dfrac{1}{Tilt2_{max}}\displaystyle\sum_{i=1}^{M}(k2_{i1})^2 & \cdots \\[2ex]
\dfrac{1}{u_{max}}\displaystyle\sum_{i=1}^{M}k_{i1}*k_{i2} + \dfrac{1}{Tilt1_{max}}\displaystyle\sum_{i=1}^{M}k1_{i1}*k1_{i2} + \dfrac{1}{Tilt2_{max}}\displaystyle\sum_{i=1}^{M}k2_{i1}*k2_{i2} & \cdots \\[2ex]
\vdots & \vdots
\end{array}\right|_{N*N} * \left|\begin{array}{c}\Delta v_1 \\ \vdots \\ \Delta v_N\end{array}\right| =
$$

$$
\left|\begin{array}{c}
\dfrac{1}{u_{max}}\displaystyle\sum_{i=1}^{M}k_{i1}*u_i + \dfrac{1}{Tilt1_{max}}\displaystyle\sum_{i=1}^{M}k1_{i1}*Tilt1_i + \dfrac{1}{Tilt2_{max}}\displaystyle\sum_{i=1}^{M}k2_{i1}*Tilt2_i \\[2ex]
\vdots \\[2ex]
\dfrac{1}{u_{max}}\displaystyle\sum_{i=1}^{M}k_{1N}*u_i + \dfrac{1}{Tilt1_{max}}\displaystyle\sum_{i=1}^{M}k1_{iN}*Tilt1_i + \dfrac{1}{Tilt2_{max}}\displaystyle\sum_{i=1}^{M}k2_{iN}*Tilt2_i
\end{array}\right|
$$

Only the first column is written for the *K* matrix, and as can be seen, the terms related to tilts have been added to the initial matrix.

When the above matrix is compared to the same matrix equation that uses only one set of known data, e.g., vertical displacement, it can be seen that the general format is the same and that the *K* matrix is still symmetric. The only difference is that the elements of each matrix are the summation of sentences from the displacement, tilt1, and tilt2 data (if all three data sets are used). The final *K* matrix is also a symmetric *N*N* matrix, *N* being the number of reservoir elements.

The next step was to calculate the Laplace matrix. The calculations and procedures to form this matrix are included in Appendix I. This step required the writing of a subroutine named *laplace*.

After the *K* matrix and Laplace matrix were formed, the next step was to form $[K - \beta L]_{N*N}$. β is a number between zero and one. Its value was assumed and chosen as the input at the beginning of the program. A final and suitable value of β was obtained using trial and error. The optimum β is the β that would minimize equation (5.1) and thus result in back-calculated values closest to the initial values. When the value of β is changed, the solution for some reservoir elements would improve; however, for other elements, the results would deteriorate

(Rothenburg, 2009; personal communication). Therefore to be able to get the optimum β and use it in the solution, parameters such as mean square error (MSE) and root of mean square error (RMSE) were used. Plotting MSE or RMSE versus β, it was seen from previous research that increasing β from zero to one, would result to a decrease in MSE and RMSE up to a point after which it will generally increase (Bilak, 1989). Thus, the minimum point is the solution. However, finding this minimum point is not easy and in some cases there might be several minimums between zero and one. Thus the trial and error procedure should be done many times.

Once K and L and the initial value for β were defined, the following could be calculated

$$A = [K - \beta L]_{N*N}$$

where

$$[K - \beta L]_{N*N} * [\Delta v \text{ or the unknown }]_{N*1} = [U \text{ or The Answer matrix}]_{N*1}$$

Thus,

$$[A]_{N*N} * [\Delta v \text{ or the unknown }]_{N*1} = [U \text{ or The Answer matrix}]_{N*1}$$

$$[\Delta v \text{ or the unknown }]_{N*1} = [A]^{-1}{}_{N*N} [U \text{ or The Answer matrix}]_{N*1}$$

To solve for Δv, the inverse of A matrix must be calculated, but due to the previously mentioned factors inherent in an ill-posed problem, the singular value decomposition method was used and the initial A matrix was broken up into three matrixes in such a way that the product of the three matrixes would result in the initial A matrix:

$$A = U * [w_i] * V^T$$

For this step, a *SVDcmp* subroutine was used to generate the three products of the A matrix.

To solve the final matrix equation and to calculate Δv_i, a svbksb subroutine was used.

The back-calculated results were then compared to the initial assumed volume changes by calculating three parameters as follows:

$$Error_n\% = \frac{(\varDelta V_{initial} - \varDelta V_{back\ calculated}) * 100}{\varDelta V_{initial}}$$

$$MSE = \frac{\sum_{n=1}^{N}(\varDelta V_{initial} - \varDelta V_{back\ calculated})^2}{N}$$

$$RMSE = \sqrt{MSE}$$

Plotting the back-calculated volume change distribution for each row of the reservoir along with the initial assumed volume change also provided a very good understanding of the solution. Through trial and error, different values of β from zero to one were chosen, and the RMSE and the shape of the volume change distribution were compared to the initial values assumed. The result was the determination of a suitable value for β and, thus, the solution of the inverse ill-posed problem mentioned above.

In this thesis, an initial volume change was assumed. Based on that assumption, surface data were calculated and back-calculations were performed in order to solve for the initial changes in volume. This procedure was chosen in order to find an actual mean to verify the method being applied. In actual cases, however, the volume changes are unknown. Therefore, surface deformation data (measurements of vertical deformation and tilts) from observation points and benchmarks, are the known set of data. Based on the assumptions made and on an assumed value of β between zero and one, volume change distribution can be calculated. Using this volume change and direct formulas in order to calculate surface deformations, the surface displacements and tilts are recalculated. The results are then compared with the initial data available, and changing the value of β according to trial and error, an acceptable answer is finally determined for the volume change distribution in the reservoir, which would result in surface deformation close to what has been observed.

The following flowchart summarizes the procedure for the numerical coding;

```
        ┌─────────────┐   ┌─────────────┐   ┌─────────────┐   ┌─────────────┐
        │  Reservoir  │   │ Overburden  │   │ Observation │   │  Reservoir  │
        │             │   │             │   │    grid     │   │volume change│
        └─────────────┘   └─────────────┘   └─────────────┘   └─────────────┘
```

Width, Length, Depth, Azimuth, Dip angle, Number of reservoir elements in each direction of X & Y	Material property: Poisson ratio	Defining number of observation points and their distance in each direction of X & Y	Defining Δv distribution as a function of X & Y in the reservoir (can be in all 3 directions)

Input for the direct case of the program

Grid generation

Assign volume change to each reservoir element

Okadatilt subroutine: tilt calculations	Okadadisp subroutine: displacement calculations

Calculation subroutine: integrates and does the summation of deformations due to volume changes of all elements in the reservoir

Calculating displacement and tilt in both directions for each observation point

1

Output of the direct case

Input for the inverse case: Vertical displacement, Tilt1, Tilt2

```
     ┌───┐        ┌──────────────────────────────┐
     │ 1 │───────▶│  Produce random error to add to │
     └───┘        │  the absolute input values     │
                  └──────────────────────────────┘
                              │
                              ▼
```

$$Displacement_{i_{error}} = Displcament_i + Random\ error$$

$$Tilt1_{i_{error}} = Tilt1_i + Random\ error$$

$$Tilt2_{i_{error}} = Tilt2_i + Random\ error$$

Choose β,

$0 < \beta < 1$

Form U matrix, from the observation data with error

Get k_{mn} from the direct calculations for each input data

Form Okada coefficient matrix for each of the observation data sets used as input

Form **K** matrix

Form Laplace matrix

Form A matrix: $[A] = [K - \beta L]$

Using SVD method and SVDcmp subroutine:

$A = U * [w_i] * V^T$

Error%

MSE

RMSE

Using svbksb, solve for Δv_i

Comparing the back-calculated results with the initial assigned volume

6.0 Cases considered and results

A variety of case scenarios were considered in order to determine the effect of different variables on the solution to the numerical inverse ill-posed problem. The factors and variables studied were

- the effect of the depth of the reservoir on the solution of the ill-posed inverse problem,
- the number of observation points chosen and the definition of the minimum number needed in order to obtain a reasonable resolution,
- the geometry and distribution of the benchmark grid chosen and its effect on the results of the inverse solution,
- the distance between observation points,
- the error present in the observation data obtained from the surface and the range of the maximum error that could be present in the data but still not significantly affect the results.

The main focus was to assume a volume change distribution in the subsurface and then regenerate it with the highest resolution possible from the measurable data. Until now, there has been little attention paid to tilts as deformation data because the induced tilts observed and recorded above oil reservoirs that have occurred due to volume change as the oil production are very small compared to induced vertical displacements. The goal of this study was to find the best surface deformation data, including tilts, which would provide the best resolution and reconstruction closest to the volume changes in a reservoir.

6.1 Verifying the code

To verify the numerical calculations for the first part of the code, which is for the direct case, one of the cases used in Okada's checklist of numerical calculations was modeled, and the results were compared to Okada's checklist.

The input data used are as follows:

1. Finite rectangular source with $width = 2m$ and $length = 3m$
2. One observation point with coordinates of $x = 0, y = 0$

3. $depth = 4m, \delta = dip = 90°, \; Azim = 0°$

Both the surface deformations as calculated for this study and the reference surface deformations provided by Okada are summarized in Table 2.

Table 2: Verifying the results using Okada's numerical checklist

	Uz	dz/dx	dz/dy	
	Tensile (E-02)	Tensile (E-03)	Strike (E-02)	Dip (E-02)
Okada table	-1.606	-9.146	2.289	-7.166
Results	1.60627	-9.1461	2.2885	7.1664
% Error	1.681	1.093	2.184	6.837

It can be seen that the absolute values of the results are in excellent agreement with the numerical checklist provided by Okada. The differences in signs observed are due to the differences between this and Okada's study with respect to the assumed positive and negative directions for the coordinate systems.

The second check used for verifying the code and the generated results involved the modeling of a simple case of volume change at a very shallow depth. Thus, a single horizontal reservoir element, $dip = 0°$, with volume change of $1m^3$ at a depth=0.1 m was chosen. At very shallow depths, the displacement field should be very similar to the subsurface deformation field in the same range of area because the extension of the deformation field is related directly to the depth of the reservoir. The deformation field was regenerated using the model developed, and Figure 16 shows a plot of the results prepared with SURFER.
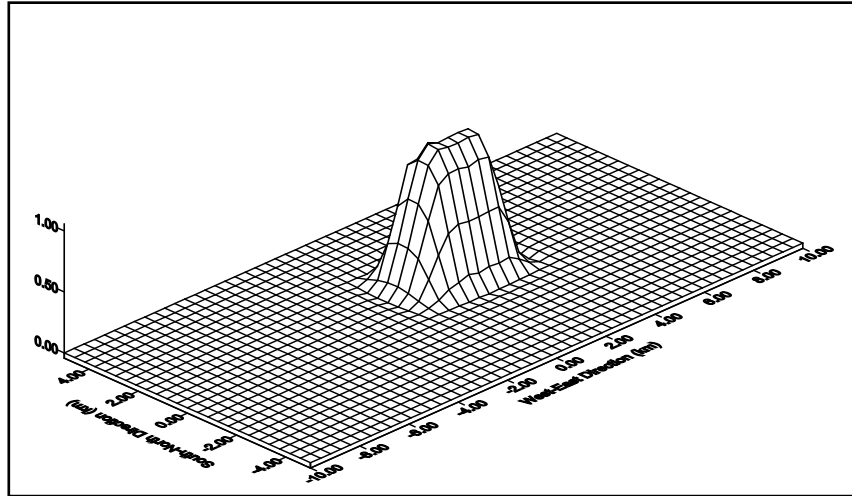
Figure 16: Surface deformation due to volume change at a very shallow depth.

As can be seen, the field is very much in agreement with the assumed volume change. The maximum magnitude of the displacement is in accordance with the volume change which was $1m^3$.

6.2 Studying the effect of depth on the ill-posed nature of the problem

6.2.1 Case 1

A simple case of a 4*4 reservoir element was chosen. Observation points were chosen so that they were above and on the midpoint of each reservoir element. An initial volume change of $\Delta v = -1m^3$ was assigned to each reservoir element to be regenerated, using the induced deformation data. The input was as follows:

- Range of x: 0<x<4
- Number of elements in x direction=4
- Range of y: 0<y<4
- Number of elements in y direction=4
- Range of observation grid points: -1<x<9, -1<y<9

The results for β=0 and for different depths are listed in Table 3.

For $\beta=0$:

Table 3: Results of back-calculations when $\beta=0$ for various depths.

Depth (m)	0.01	5	10	15	20
Volume (m^3)	-1	-0.999312	-1.42457	-2.23591	18.3232
	-1	-1.00146	0.00315068	1.6957	98.7587
	-1	-0.998346	-1.90729	-6.01317	-113.856
	-1	-1.00079	-0.691937	2.54732	19.0956
	-1	-1.00154	-0.580117	-0.466824	-132.531
	-1	-0.996606	-1.93339	-0.876705	-26.3254
	-1	-1.00397	-0.26122	5.15316	18.6178
	-1	-0.998062	-1.17876	-7.80237	64.1858
	-1	-0.998302	-0.73372	1.10679	114.868
	-1	-1.00386	-1.74241	-7.92793	21.3669
	-1	-0.995501	-0.11267	-0.475223	32.3009
	-1	-1.0022	-1.45046	3.31107	-103.568
	-1	-1.00089	-1.37462	-2.52585	12.6821
	-1	-0.997956	-0.0443029	3.40919	-144.059
	-1	-1.00235	-1.99475	-2.94857	102.042
	-1	-0.998863	-0.573784	-1.95243	2.24501

It can be seen that for $\beta=0$, which would result in the initial ill-posed problem as mentioned in the previous sections, as the depth increases, the problem becomes increasingly more ill conditioned. Thus, for very shallow depths, the solution starts to become well posed.

The actual solution of the above problem was then generated using different non-zero β values in order to obtain the best resolution for this reservoir for different depths. The resulting volume changes for the values of β considered are summarized in Table 4 to 7.

Table 4: Results of back-calculations for a depth=5 m.

Depth	5m		
β	0.0001	0.001	0.01
Volume (m³)	-0.999888	-1.00001	-1
	-1.00001	-1	-1
	-1.0001	-1	-1
	-1.00002	-1.00001	-1
	-1	-0.999998	-1
	-1.00003	-0.999994	-1
	-0.999977	-0.999994	-1
	-0.999896	-0.999998	-1
	-1.00011	-0.999999	-1
	-1.00003	-0.999998	-1
	-0.999968	-0.999998	-1
	-0.999992	-0.999999	-1
	-0.999974	-1	-1
	-0.999915	-1	-0.999999
	-0.99998	-1	-1
	-1.00012	-0.999999	-1

Table 5: Results of back-calculations for a depth=10 m.

Depth	10m			
β	0.0001	0.001	0.01	0.1
Volume (m³)	-0.999911	-0.999996	-1	-1
	-0.999962	-0.999999	-1	-1
	-1.00005	-1	-1	-1
	-1.00008	-1	-1	-0.999999
	-0.999958	-0.999999	-1	-1
	-0.999976	-1	-1	-1
	-1.00003	-1	-1	-0.999999
	-1.00005	-1	-1	-0.999999
	-1.00005	-1	-0.999999	-1
	-1.00002	-1	-0.999999	-1
	-0.999961	-1	-0.999998	-1
	-0.999955	-1	-0.999998	-1
	-1.00009	-1	-0.999998	-1
	-1.00005	-1	-0.999998	-1
	-0.999945	-1	-0.999997	-1
	-0.999923	-0.999999	-0.999997	-1

Table 6: Results of back-calculations for a depth=15 m.

Depth	15m				
β	0	0.0001	0.001	0.01	0.1
Volume (m³)	-2.23591	-0.999999	-0.999995	-0.999998	-1.00001
	1.6957	-0.999999	-0.999996	-0.999999	-1.00001
	-6.01317	-1	-0.999998	-1	-1
	2.54732	-0.999998	-0.999998	-1	-1
	-0.466824	-0.999998	-0.999998	-0.999999	-1
	-0.876705	-0.999999	-0.999999	-0.999999	-1
	5.15316	-1	-1	-1	-1
	-7.80237	-1	-1	-1	-1
	1.10679	-1	-1	-0.999999	-1
	-7.92793	-1	-1	-1	-1
	-0.475223	-1	-1	-1	-1
	3.31107	-0.999998	-1	-1	-1
	-2.52585	-1	-1	-1	-1
	3.40919	-1	-1	-1	-1
	-2.94857	-0.999999	-1	-1	-1
	-1.95243	-0.999992	-1	-1	-1

Table 7: Results of back-calculations for a depth=20 m.

Depth	20m				
β	0	0.0001	0.001	0.01	0.1
Volume (m³)	18.3232	-0.999952	-1	-1	-0.999972
	98.7587	-0.999959	-0.999999	-1	-0.999972
	-113.856	-0.999982	-1	-0.999998	-0.999971
	19.0956	-0.999993	-1	-0.999997	-0.99997
	-132.531	-0.999966	-1	-1	-0.999974
	-26.3254	-0.999972	-1	-0.999999	-0.999973
	18.6178	-0.999995	-1	-0.999998	-0.999971
	64.1858	-1.00001	-1	-0.999998	-0.999971
	114.868	-0.999997	-1	-0.999999	-0.999978
	21.3669	-1.00001	-1	-0.999999	-0.999978
	32.3009	-1.00003	-1	-0.999998	-0.999974
	-103.568	-1.00003	-1	-0.999998	-0.999973
	12.6821	-1.00001	-1	-0.999998	-0.99998
	-144.059	-1.00002	-1	-0.999998	-0.999979
	102.042	-1.00004	-1	-0.999998	-0.999976
	2.24501	-1.00004	-1	-0.999998	-0.999975

It is apparent from the above results that, as the depth of the reservoir increases, meaning that the depth of the source of the changes in volume increases, the problem becomes more ill-posed. The optimum value of β that would result in the minimum RMSE of the volume change distribution was observed to increase with depth as well.

In reality and in actual cases, however, an oil reservoir spans a very large underground area. The volume changes occurring in a reservoir due to production or reinjection also vary in different parts of the reservoir. Consequently, to model and study a case that can be considered an actual reservoir case, the following reservoir was modeled:

Reservoir: $width = 500m,\ length = 500m,\ depth = 500m,\ Azimuth = 0°,\ dip = 0°(horizontal\ reservoir)$

The following volume was assigned to the reservoir:

$$Volume\ change_i = -e^{\left(-\frac{\left(Xreservoir_i - \frac{lengt\ h_{reservoir}}{2}\right)^2 + (Yreservoir_i - \frac{widt\ h_{reservoir}}{2})^2}{100*Leng\ ht\ Reservoir}\right)}$$

To simplify the procedure for modeling purposes, only volume changes in vertical direction were assigned to each reservoir element.

A 3D plan of the reservoir compaction (volume change) assigned for modeling and studying the cases was plotted, as shown in Figure 17.
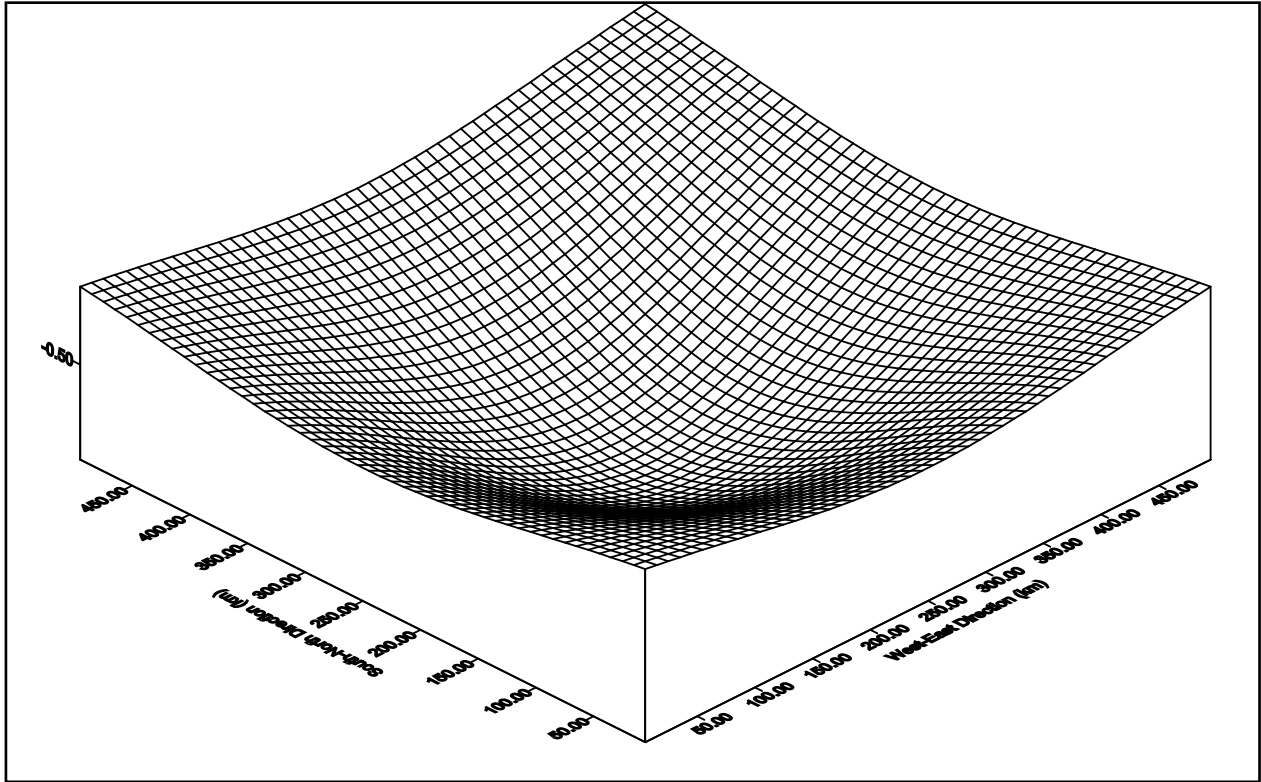
Figure 17: Distribution of volume change assigned to the test reservoir.

The result of the surface deformations due to this volume change distribution in the subsurface was plotted for the following range, as shown in Figure 18:

$$-500 \leq x, y \leq 1000$$

It should be noted that only the vertical deformations were plotted since tilt values are much smaller than vertical displacement values. To increase the accuracy, all the deformations, including vertical displacements and tilts, should be plotted together. The maximum tilt calculated in the deformation field in this case was $3.73 * 10^{-4}$, and the maximum vertical displacement calculated in the deformation field was 0.182285 m. As can be seen, the vertical deformation is much larger than the tilts induced by the reservoir volume change.
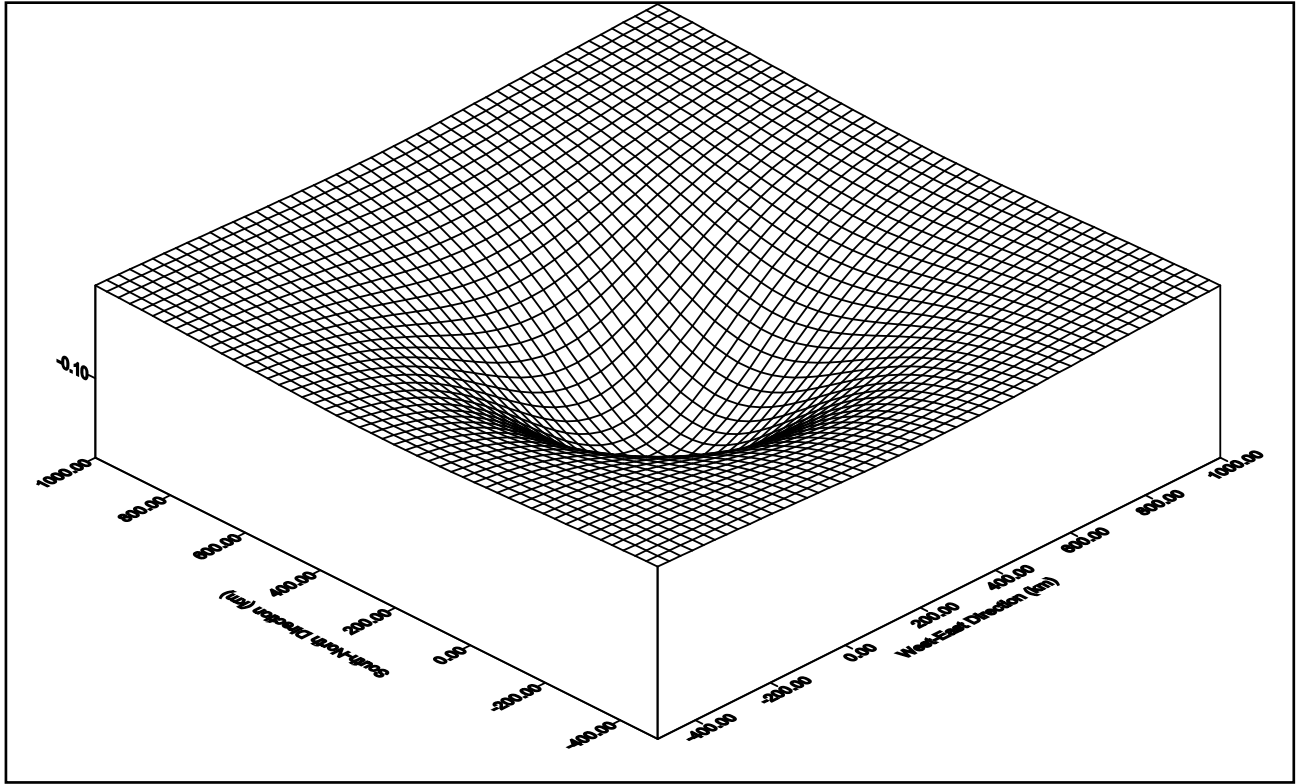
Figure 18: Induced vertical deformations due to reservoir's volume change

6.3 Finding the best surface deformation data as input that results in the best resolution

6.3.1 Comparing results from displacement and tilts assuming no error present

A reservoir with the geometry specified in the previous section was assumed. It was divided into 50*50 elements in each direction (totalling 2500 elements). Each element or volume change source was thus defined to be 10*10 m^2. Consequently, for the inverse problem of 2500 unknowns, i.e., volume changes, are to be solved for. The reservoir geometry that was applied is

$$0 \le x, y \le 500$$

With respect to the observation points, 2704 points were chosen in a 52*52 grid with a range of

$$-500 \le x, y \le 1000$$

The geometry of the reservoir and the resulting deformation field are shown in Figure 19.
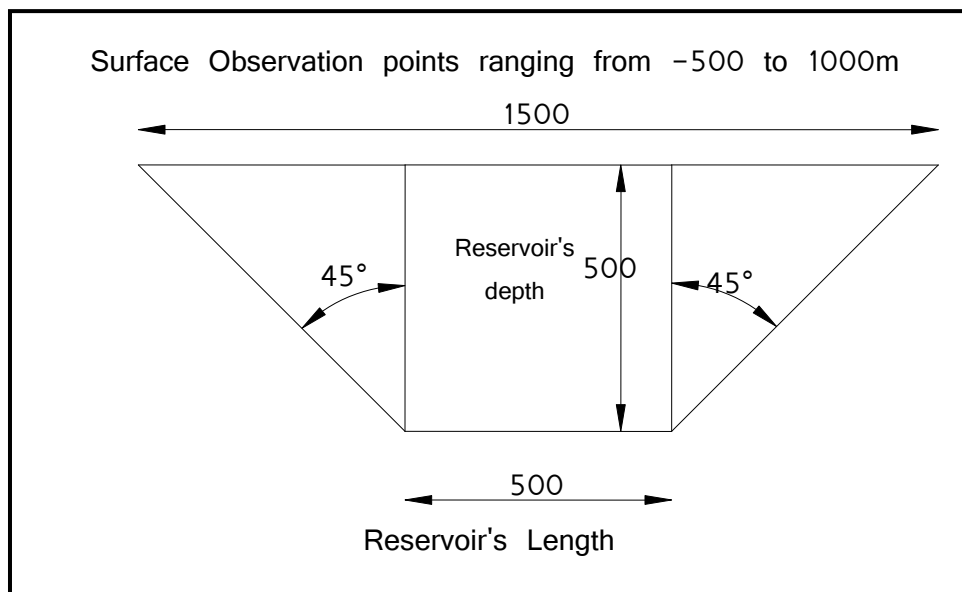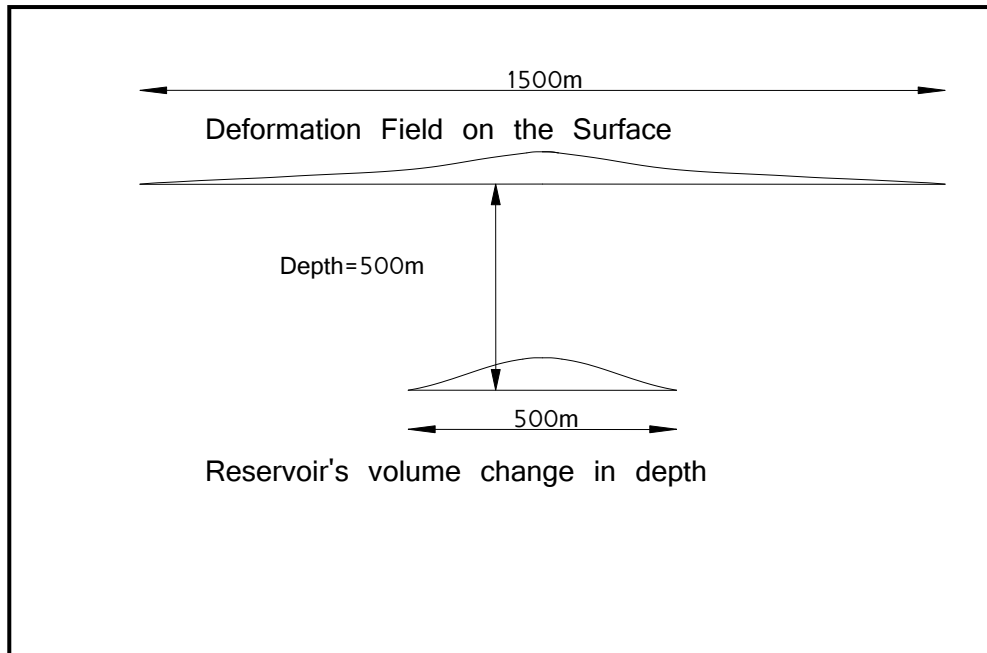
Figure 19: The reservoir to be modeled and the resulting induced deformation field on the surface due to reservoir volume change

After each ill-posed case was solved and the optimum value of β that results in the minimum RMSE of the solution was found, the calculated changes in volume for each element was plotted along with the initial assigned changes in volume against the block of the reservoir for

each reservoir row. A good understanding of the distribution and variations in the solution was now possible.

6.3.1.1 Case 2: employing displacement as input data

In case 2, vertical displacements from each observation points calculated based on the assumed volume change distribution were used as input for the inverse ill-posed problem. The MSE and RMSE for verifying and comparing the results with the initial assumed volume change distribution were calculated and plotted against β (Figure 20). It can be seen that when $\beta=0$, which is the initial ill-posed problem, the MSE is very high ($MSE = 1.93007 * 10^{21}$), and the solution is thus unacceptable. If the value of β is increased, the MSE and RMSE decrease until a minimum is reached, as can be seen in the graphs. The value of β that results in the minimum MSE or RMSE is referred to as the optimum β.
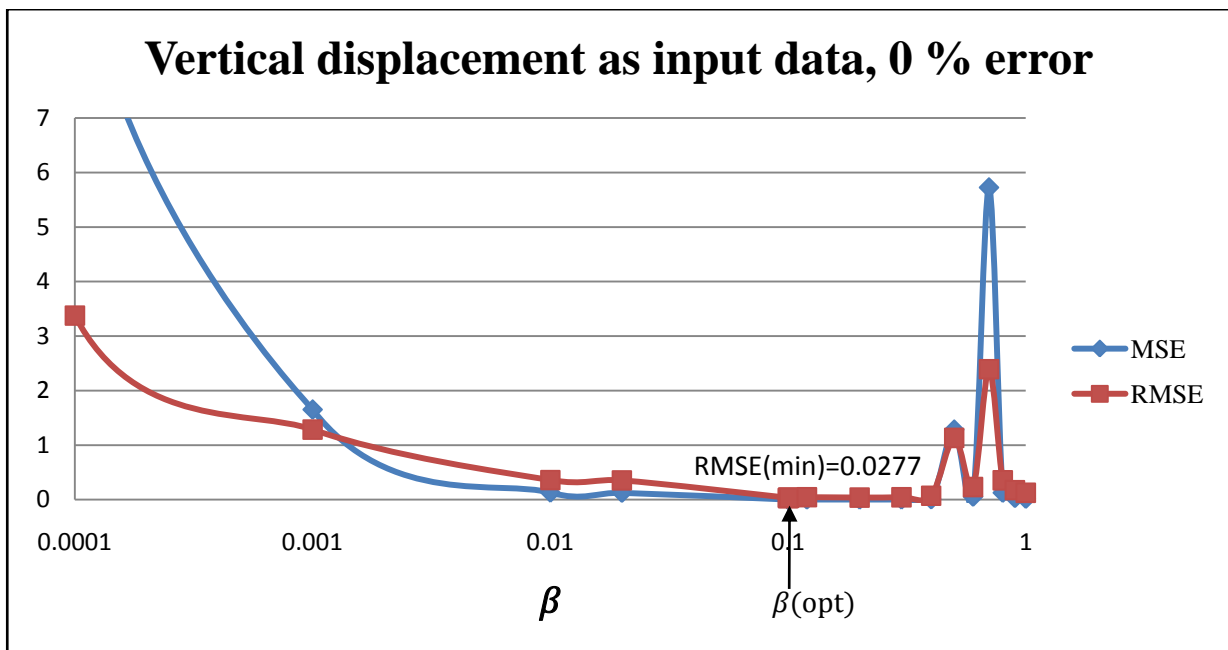
Figure 20: MSE and RMSE plotted against β: Case 2

As can be observed in **Figure 20**, the general response of both factors to the change in the value of β is very similar.

The optimum value of β resulting in the minimum MSE in this case was found to be

$$\beta_{opt} = 0.1000001$$

$$MSE_{min} = 0.000767697 \,\&\, RMSE_{min} = 0.0277073,$$

For all cases, the results of the back-calculated values for the corner elements of the reservoir had the greatest error due to the effects of boundary conditions on the calculations. However, as for the reservoir elements close to the centre, the results had smaller errors and thus were a better reconstruction than that for the corner elements. Consequently, in each case used for comparison, this thesis includes the worst cases, which were the corner elements, and the best reconstruction for each model, which was associated with the centre elements.

The back-calculated results, which were plotted along with the initial distribution of the volume changes against the reservoir block in each row. The results, shown in Figure 21, were plotted for the first six rows, which include the worst results, and also for the mid-rows in Figure 22, which provided the best and closest reconstruction in each model.
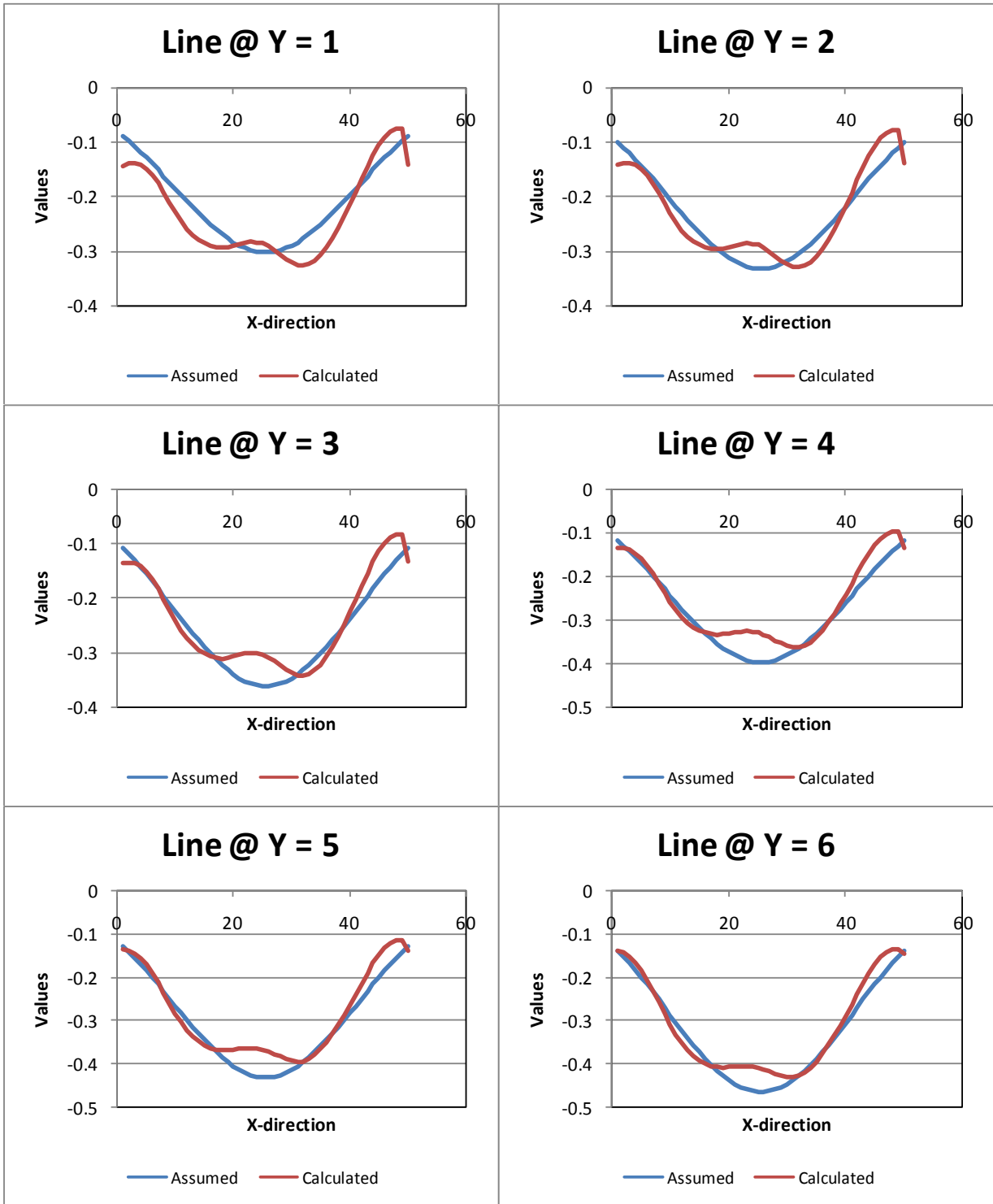
Figure 21: Δv for the first six rows of the reservoir; Case2.
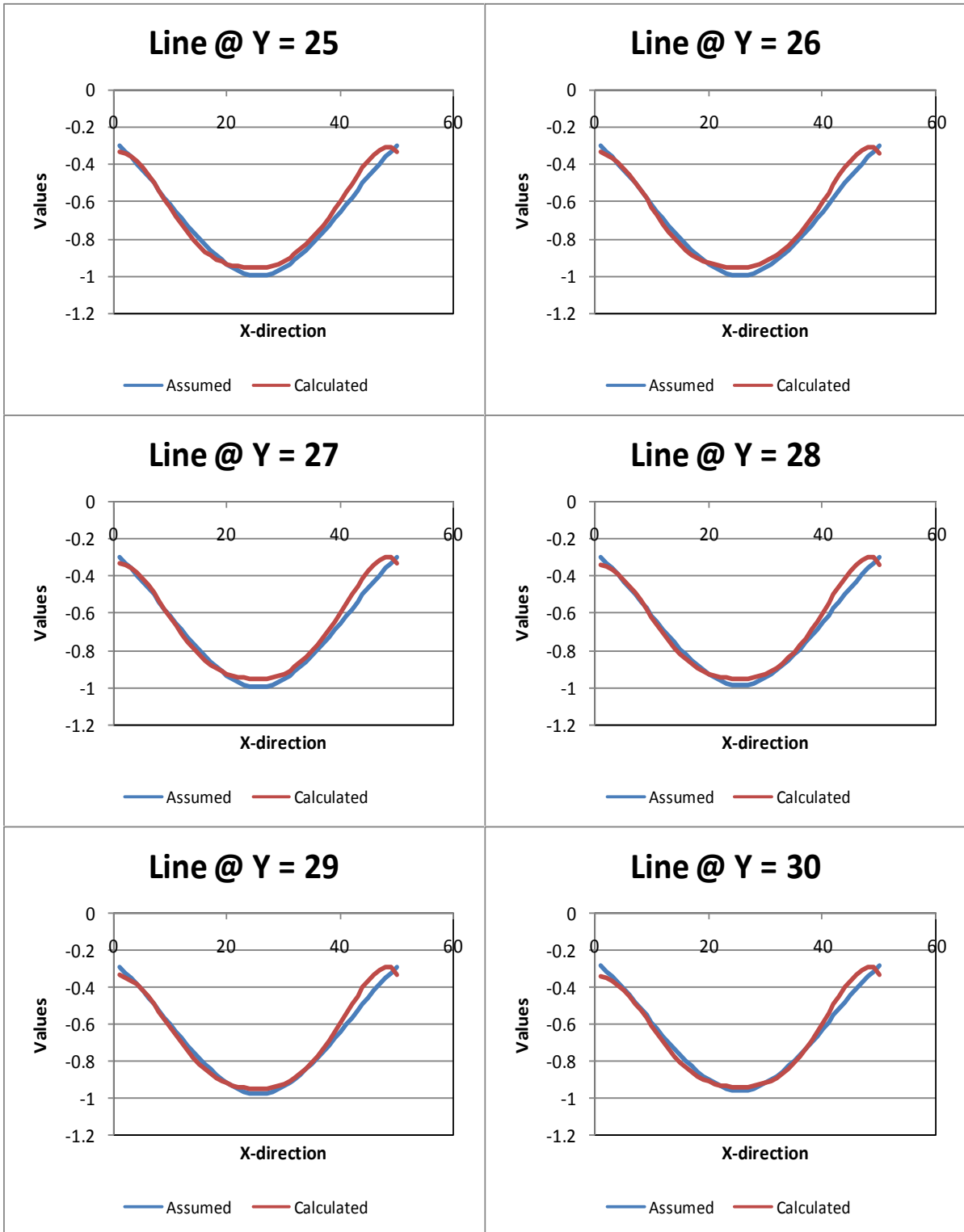
Figure 22: Δv for the rows 25 to 30 of the reservoir; Case2.

6.3.1.2 Case 3: using tilt1 as input data

The same reservoir geometry and observation points used in case 2 were applied in case 3 as well. The only difference was that for the inverse case, tilt1, which is $\frac{\partial U_z}{\partial x}$, was used rather than the vertical displacements as the input data for the back-calculations and the solving of the inverse case. The results of the MSE and RMSE plotted against β can be seen in Figure 23.
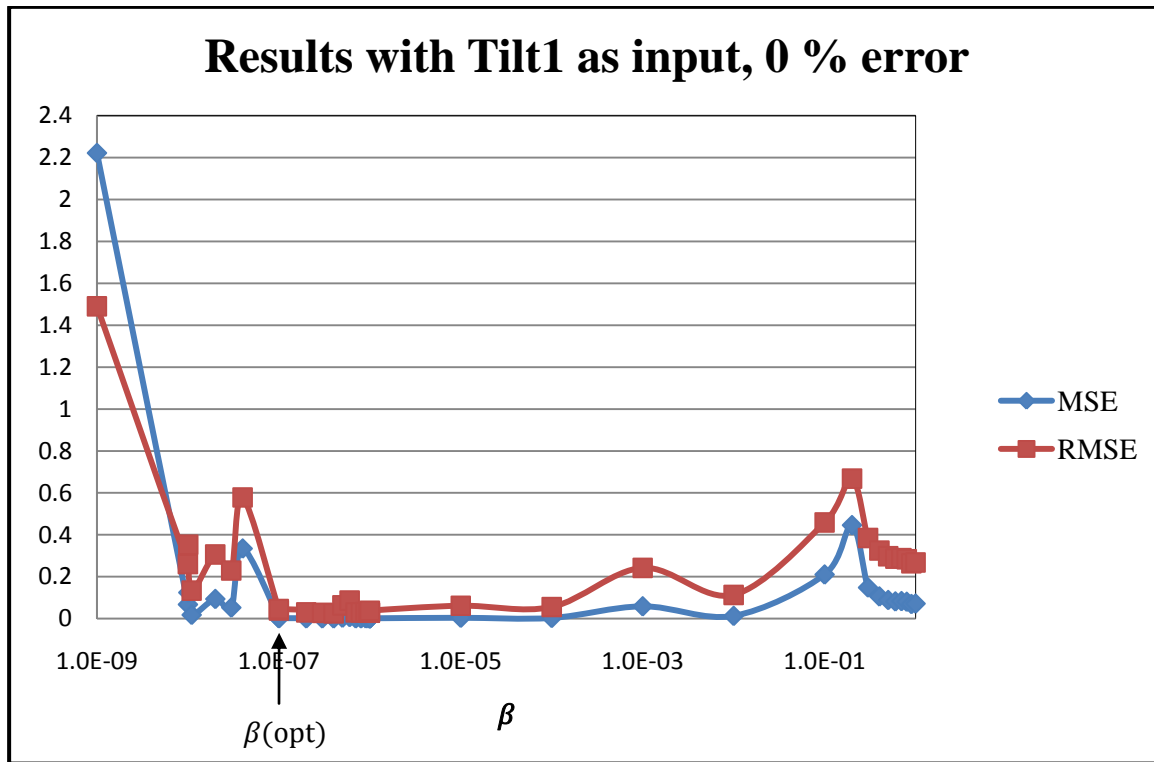
Figure 23: MSE and RMSE plotted against β: Case 3

As can be seen from a comparison of Figure 20 and Figure 23, the range of β that results in an acceptable resolution is wider when tilt1 is used as input.

The minimum RMSE, and thus the best result, is achieved with β_{opt} = 0.0000004. In this case, the best result is as follows:

$$MSE_{min} = 0.000605308, \qquad RMSE_{min} = 0.024603$$

The resulting volume changes compared to the initial assumed volume changes across each row in the reservoir for the first six rows and also for rows 25 to 30 are illustrated in Figure 24 and Figure 25.
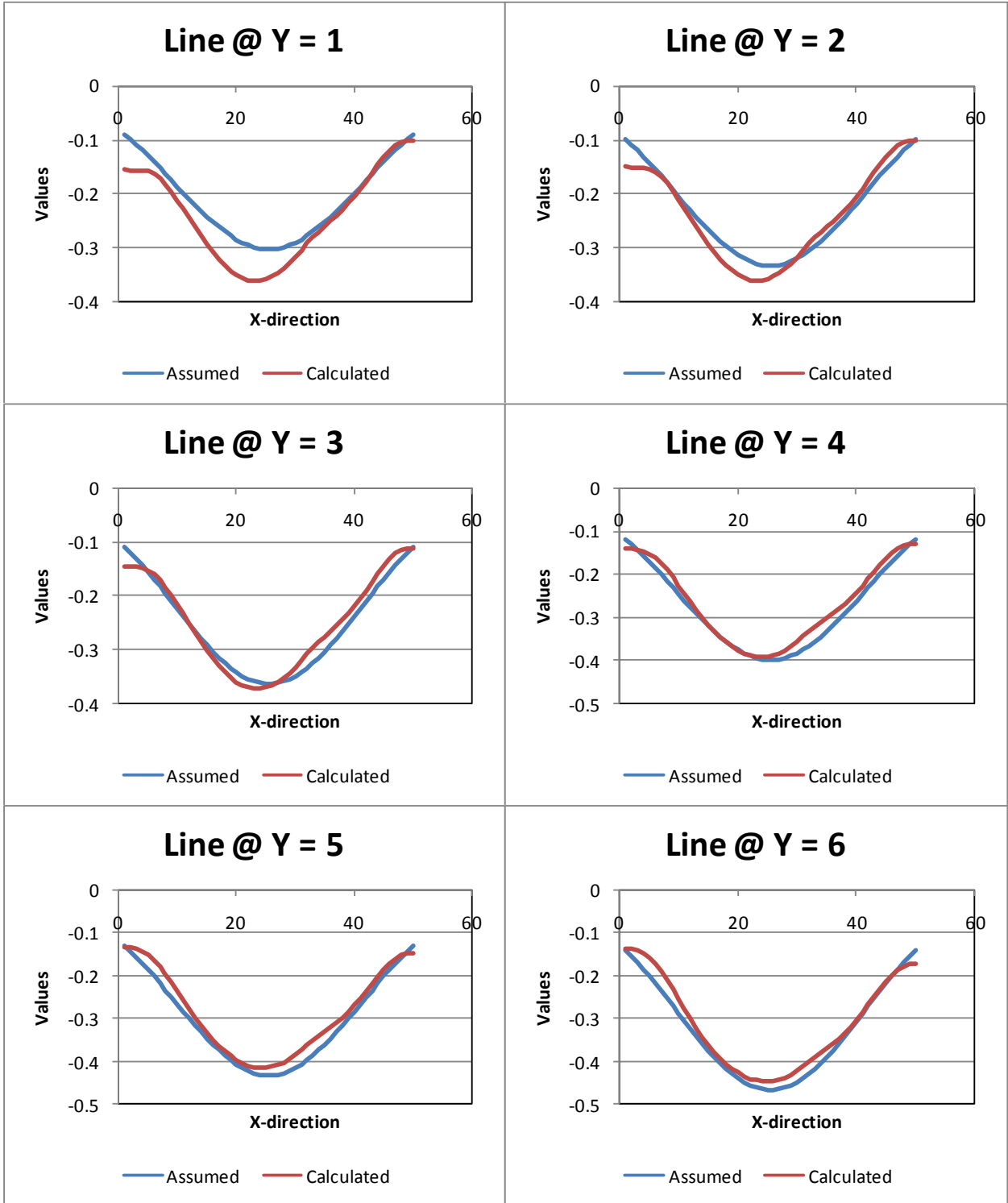
Figure 24: Δv for the first six rows; Case 3.
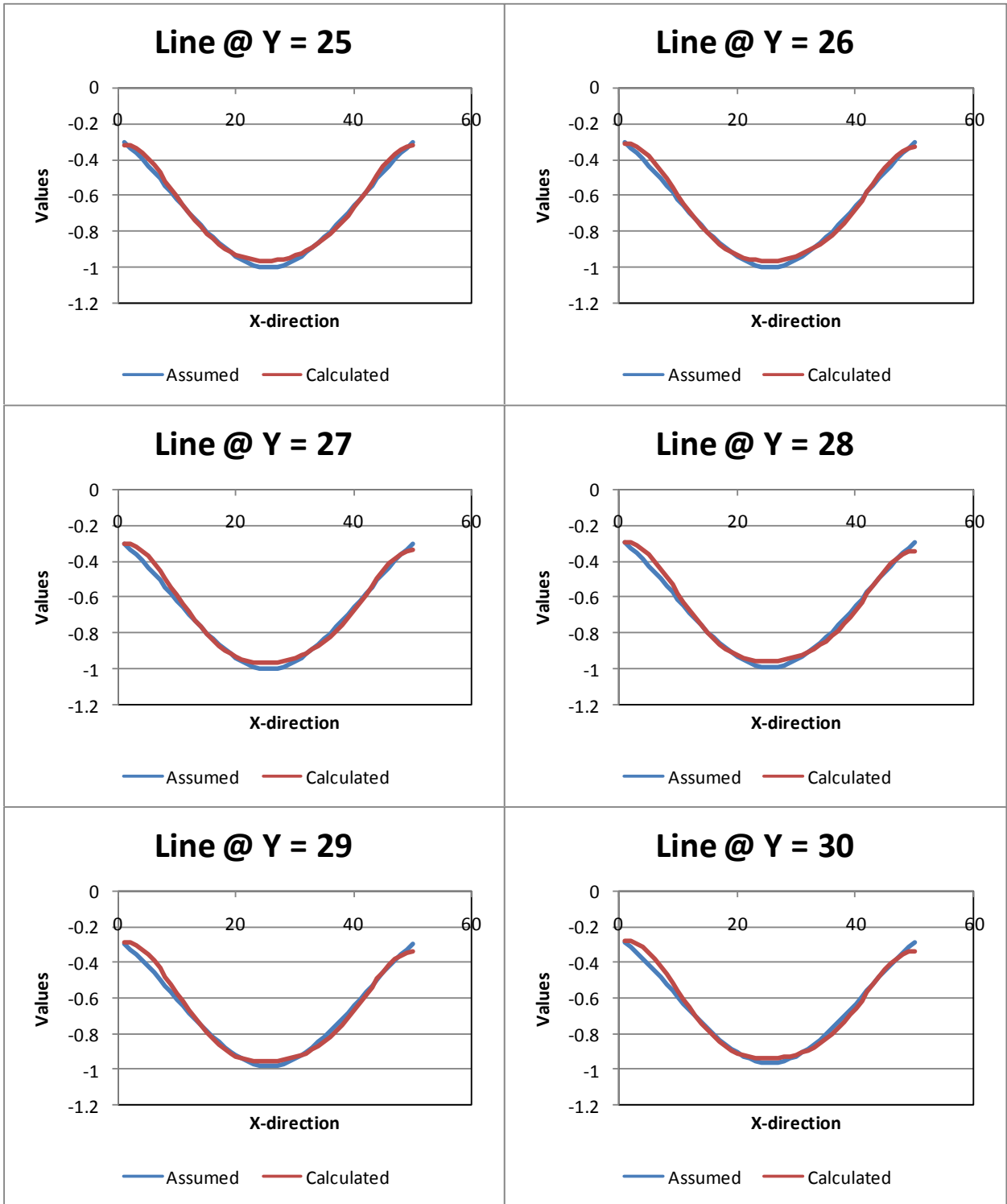
Figure 25: Δv for rows 25 to 30 of the reservoir; Case 3.

6.3.1.3 Case 4: using tilt2 as input data

The same reservoir geometry and distribution of volume changes and observation points used in the previous two cases were used in this case as well. The only difference is that tilt2 at each observation point, which is $\frac{\partial u_z}{\partial y}$, was used as input for the back-calculations. The results of the MSE and RMSE plotted against β were as shown in Figure 26.
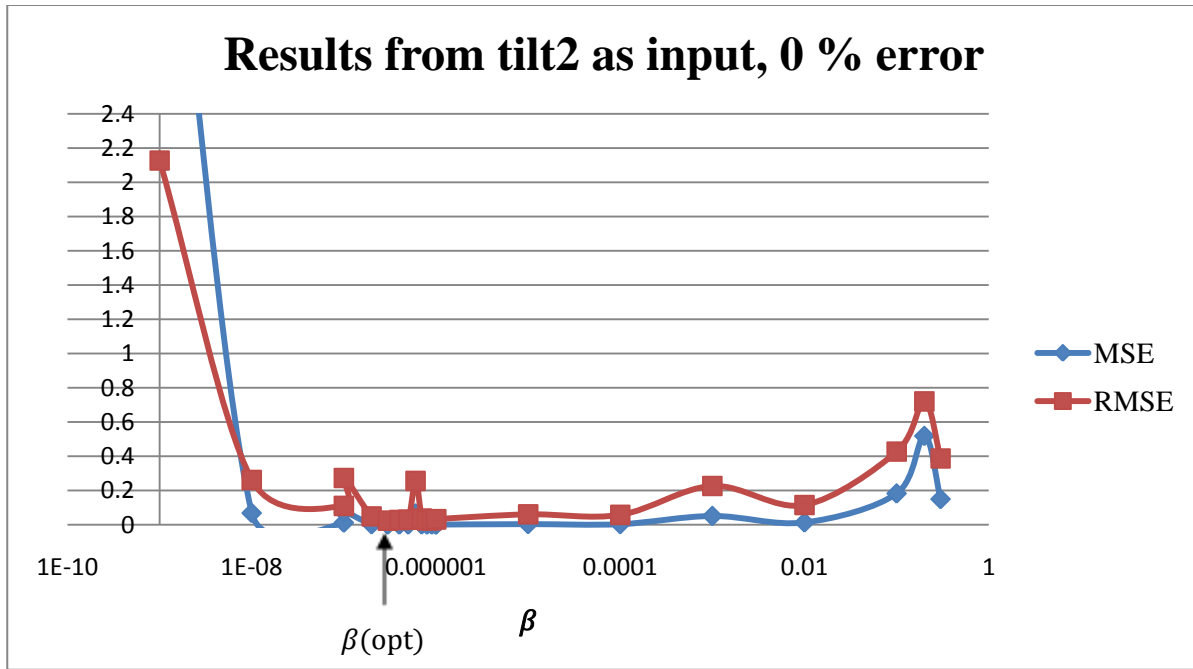
Figure 26: MSE and RMSE plotted against β: Case 4

From the graph in Figure 26, it can be determined that the optimum solution occurs at

$$\beta_{opt} = 0.0000003, \ MSE_{min} = 0.0005932, \ RMSE_{min} = 0.0243557$$

The graphs of the distribution of the volume changes can be found in Appendix II.

6.3.1.4 Case 5: using tilt1+2

In case 5, a combination of tilt1+2 from each observation point was used as input for the inverse case. The results obtained are summarized in Figure 27.
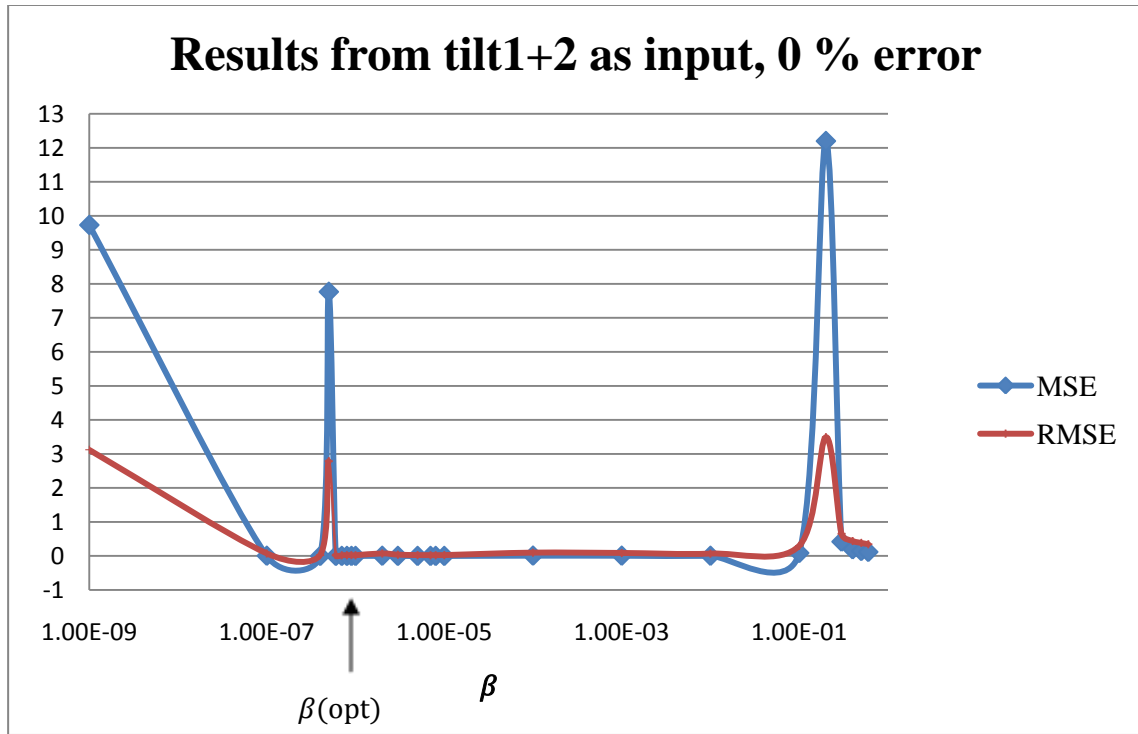
Figure 27: MSE and RMSE and the third factor used plotted against β, Case 5

It should be noted that the optimal solution occurs at

$$\beta_{opt} = 1.\text{E-}06, \ MSE_{min} = 0.000408, \ RMSE_{min} = 0.02021$$

The resulting volume changes compared to the initial assumed volume changes across each row in the reservoir for the first six rows and also for rows 25 to 30 are illustrated in Figure 28 and 29.
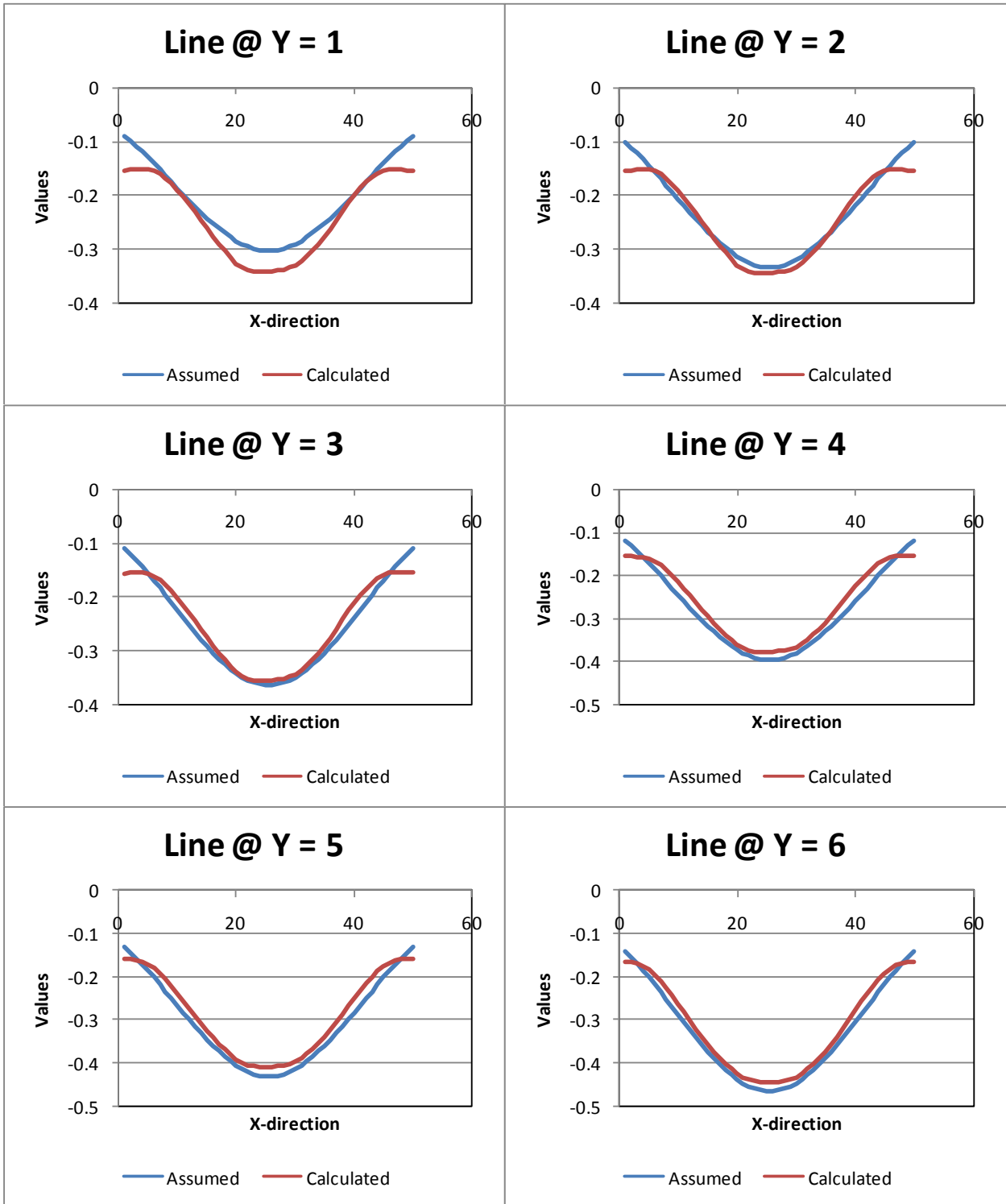
Figure 28: Δv for the first six of the reservoir; Case 5.
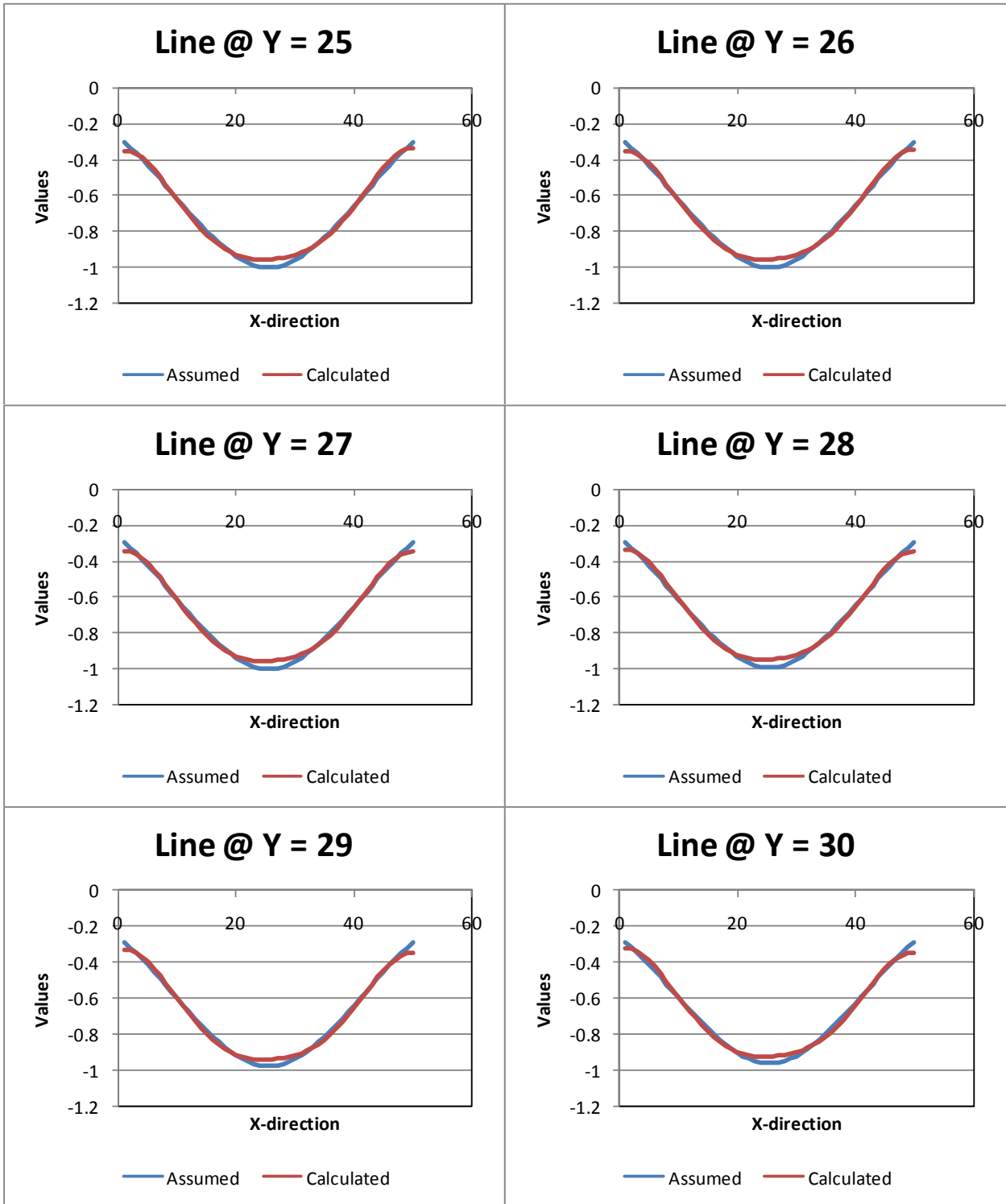
Figure 29: Δv for the rows 25 to 30 of the reservoir; Case 5.

6.3.1.5 Case 6 Tilt1+2 + displacements

In case 6, all three sets of data from each observation point were used as input data for solving the inverse case. The geometry of the reservoir, the number and arrangement of observation points, and the initial assumed distribution of the volume changes are identical to those of the previous four cases. The optimum β and the minimum RMSE were found to be

$$\beta_{opt} = 0.38, \text{ RMSE}=0.0208086$$

The resulting volume changes compared to the initial assumed volume changes across each row in the reservoir for the first six rows and also for rows 25 to 30 are illustrated in Figure 30 and 31.
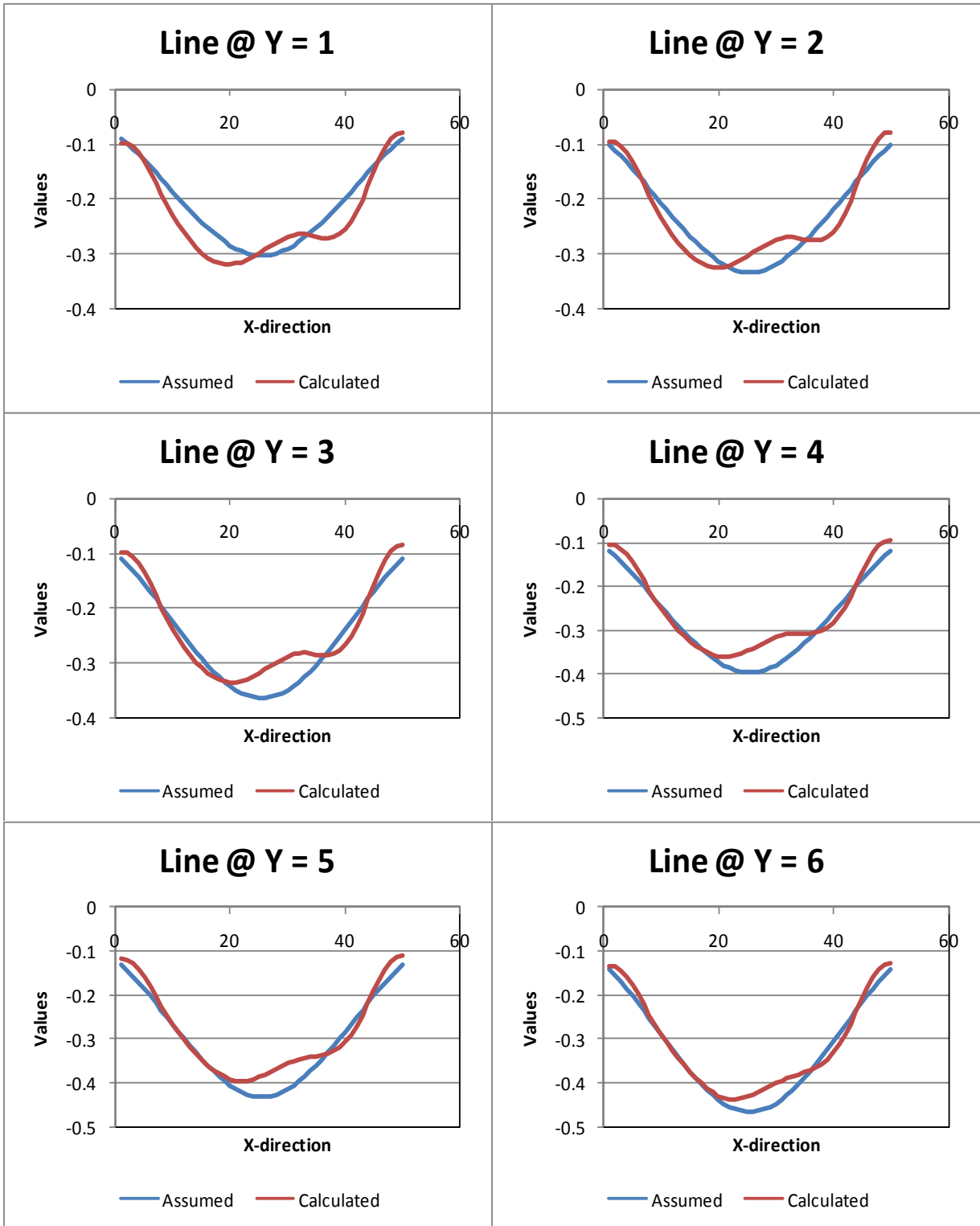
Figure 30: Δv for the first six rows of the reservoir; Case 6.
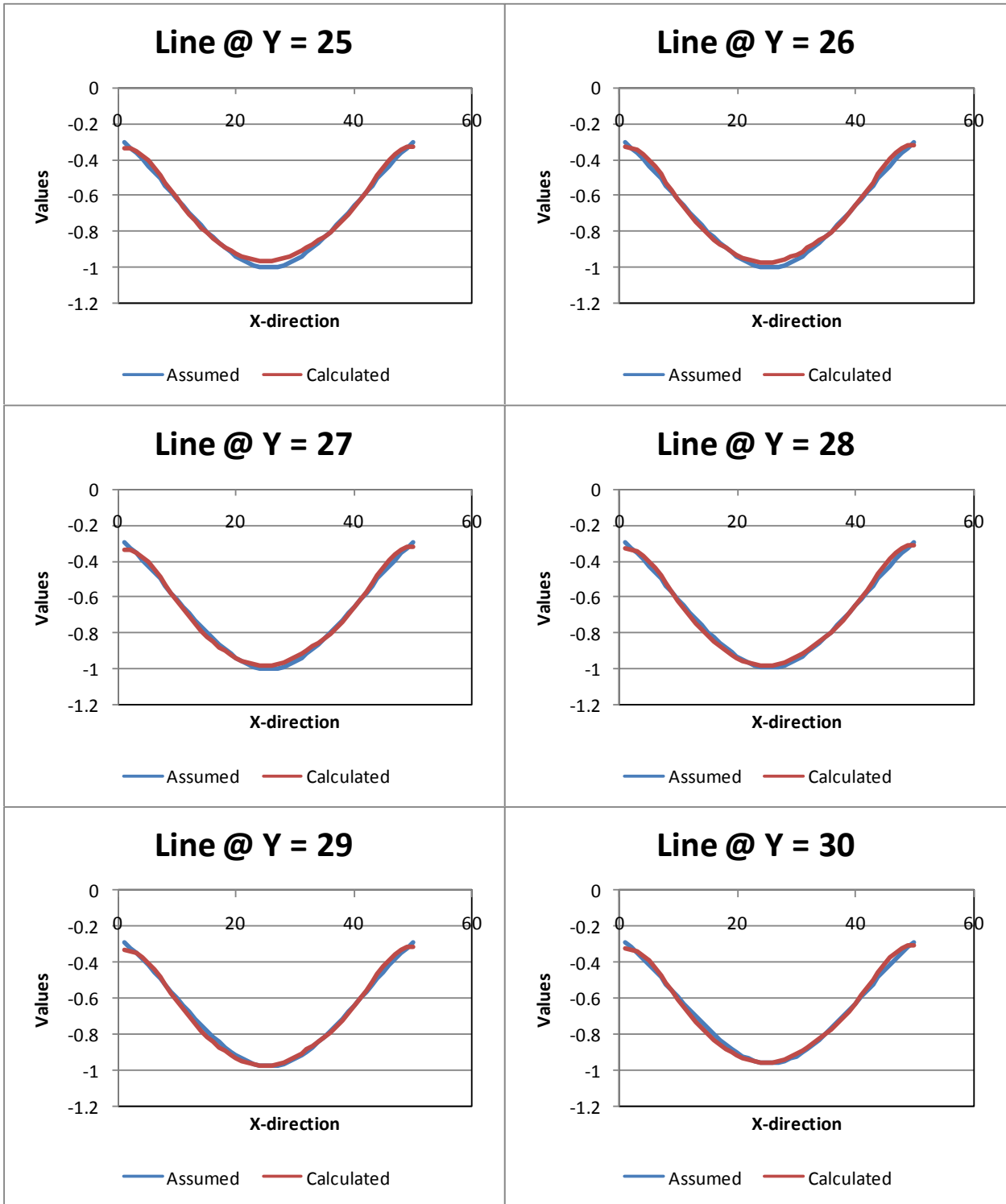
Figure 31: Δv for the rows 25 to 30 of the reservoir; Case 6.

6.3.2 Results of a comparison of cases 2 -- 6

The five cases are identical with respect to the geometry of the reservoir, the distribution of the volume changes, and the number and distribution of the observation points; the only difference was the input used for the back-calculation. Table 8 provides a summary and comparison of the results.

Table 8: Comparison of results from identical cases for which input deformation data varied.

Case No	Input data used with 0 % error	β_{Opt}	MSE_{min}	$RMSE_{min}$
2	Displacements	0.1000001	0.000767697	0.027707
3	Tilt1	0.0000004	0.0006053	0.024603
4	Tilt2	0.0000003	0.000593	0.024352
5	Tilt1+Tilt2	0.000001	0.000408	0.020199
6	displacements+Tilt1+2	0.38	0.000433	0.020809

Thus, with 0 % error in the input data, which is not a realistic case but rather an ideal case, using both tilts as input data results in the best resolution. However, it should be noted that using all three sets of data recorded at each observation point also results in a resolution very close to that obtained with only two tilts.

As can be seen, although unlike the results expected and contrary to those obtained with commonly applied techniques, using vertical deformation data for the inverse solution does not result in the best resolution. Table 8 shows that using observed tilts from each benchmark as input data for solving the distribution of the volume changes that occur inside a reservoir results in a much better resolution than using vertical displacements. Moreover, the optimum β that results in the best resolution for tilt1 and for tilt 2 is almost identical, and accordingly, the MSE from the solution of the two cases is almost identical. It can thus be concluded that using either of the two tilts results in the same resolution with the same optimum β and that this resolution is a much better result than that obtained using displacements as input data as well. Furthermore, based on Figure 20 and 23, a comparison of the variations in the MSE and RMSE of the solutions as a function of β reveals that the range of β that results in an acceptable resolution is much wider when tilt1 is used as input than when vertical displacements are used.

6.4 Limiting the area range for observation points using tilts

As mentioned previously, it has been shown that a volume change that occurs in the subsurface at depth d would affect and cause displacement and surface deformations mostly in an area with a radius of d around the centre of the subsurface deformation. Thus, to be able to back-calculate and reconstruct the initial volume, data from all areas affected should be gathered and employed for the back-calculation. In other words, observation points are best chosen throughout the entire area affected by the volume change, in order to enable the reconstruction of the actual value of the volume change. However, in actual reservoir cases, the reservoir itself is a huge body, and the area affected by a change in volume in the subsurface is manifested in a larger area at ground level. As well, oil reservoirs are usually located at substantial depths, thus affecting an even wider range of area at the surface level. It might not be convenient to choose benchmarks over the very vast area that is affected and deformed because there might be limitations caused by the presence of structures or other natural barriers. It is thus of interest to determine whether using tilts as input data for back-calculations will allow the limitation of the area of measurements and the investigation of the possibility of omitting some of the data points, while still resulting in the reconstruction of the initial volume change with an acceptable degree of accuracy.

6.4.1 Case 7

In case 7, the geometry of the reservoir and initial distribution of the volume changes are identical to those in the previous cases. The number of observation points is also the same: 2704. The only difference incorporated is that the points were chosen from a limited area:

$$-5 \leq X_{obser} , Y_{obser} \leq 505$$

The area chosen for the observation grid, as shown in Figure 32 is located directly above the area of the reservoir (the area indicated by hatch marks).
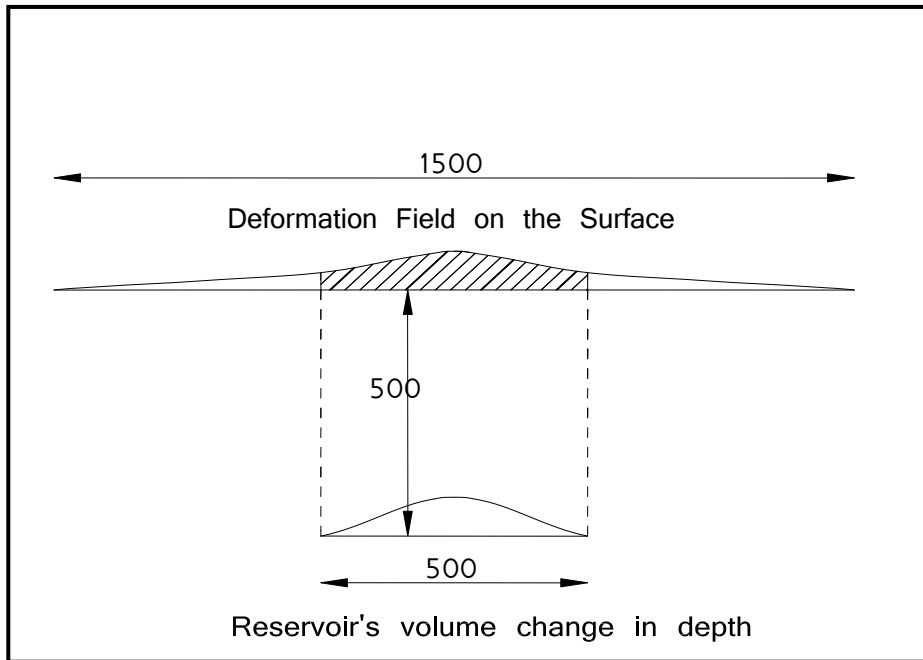
Figure 32: Cutting out a part of data by limiting the observation area on the surface and thus using only data from part of the observation field

Tilt 1 and tilt2 at each observation point were used separately as input data for the back-calculations. The results for these two cases are summarized in Table 9.

Table 9: MSE and RMSE for different βs: tilt1 and tilt2

Results from tilt1				Results from tilt2		
β	MSE	RMSE		β	MSE	RMSE
0	1.35E+21	3.67E+10		0	2.19E+21	4.68E+10
1E-09	16.5416	4.06714		1.00E-09	44.4929	6.6703
1E-08	0.794137	0.891143		1.00E-08	1.61051	1.26906
1E-08	0.874255	0.935016		1.00E-07	0.539316	0.734381
1.01E-08	0.707968	0.841408		0.000001	0.001949	0.044149
1.02E-08	1.78159	1.33476		0.00001	0.00506	0.071132
1.1E-08	0.972188	0.985996		0.0001	0.001314	0.036246
2E-08	0.750146	0.86611		0.001	0.002542	0.050415
3E-08	0.214924	0.463599		0.01	0.015098	0.122873
4E-08	0.0562546	0.237181		0.1	88.4328	9.40387
4.01E-08	0.24359	493548		0.2	0.186553	0.431918
4.1E-08	0.110251	0.332041				
4.2E-08	0.714769	0.84544				
5E-08	1.77428	1.33202				
1E-07	1.00122	1.00061				
0.000001	0.005576	0.074673				
0.00001	0.0046435	0.068144				
0.0001	0.0013079	0.036164				
0.001	0.0027544	0.052483				
0.01	0.0300482	0.173344				
0.1	73.4291	8.56908				
0.2	0.1891	0.434856				
1	0.0758763	0.275457				

It can be observed from Table 9 that the results from tilts 1 and 2 are very similar, meaning that the optimum β in both cases is the same, as is the minimum MSE or RMSE.

As can be seen, the RMSE is small. Plots of the volume changes calculated based on tilt2 as input, along with the initial assumed volume changes are summarized in one graph, for the first five rows of the reservoir (Figure 33).
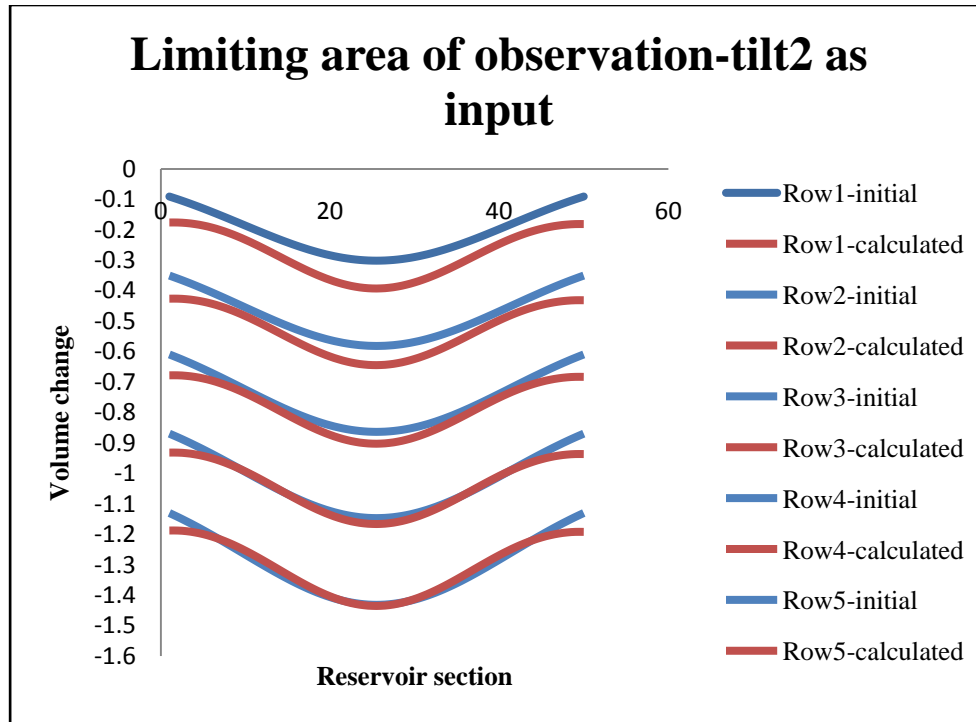
Figure 33: Volume changes in volume in the first five rows of the reservoir, with the observation field limited

Table 10 provides a summary and comparison of the results of case 7 and case 4, which is a similar case but with observation points scattered over an area of $-500 \leq X, Y \leq 1000$.

Table 10: Comparison of results for a limited area of observation points

case	range of observation points	MSE	RMSE
4	-500<X,Y<1000	0.000593	0.024351591
7	-5<X,Y<505	0.001314	0.0362455

As expected, the results from case 4 are better, and the RMSE of the calculated results is lower because the input data used in case 4 are taken from the entire deformation field. However, an examination of the plots of the calculated volumes and the initial assumed volume changes (Figure 33) shows that case 7 also results in an acceptable resolution. Therefore if tilts are used as input data, the area of observation can be limited, which would be more convenient for obtaining experimental observation data.

6.5 Error in the input data

In the cases studied, it was assumed that the observation data recorded from the observation points does not contain errors and that the values recorded are the exact actual values of deformations caused due to the volume change occurring in the reservoir. In reality, however, error is always present in recorded experimental data. Consequently, an engineer cannot expect to have precise measurements of deformations. This section presents the effect of the error present in the measurements of the displacements and tilts, which are used as input for the inverse case, on the resolution of the ill-posed problem. A random number generator was used to generate random errors within a given range. With respect to the maximum of the random error generated, a percentage of the maximum observation data gathered from the entire observation grid was used to render the results more practical and applicable for general cases. Thus, based on a percentage of the maximum amount of observation data recorded, the maximum error that would not affect the results to a significant extent is to be found. This random error was then added to each observation data point used as input for the back-calculations. For example, if vertical displacement is used as input, a random error that is 10% of the maximum value of the vertical displacement is incorporated, as follows:

$$0 \leq Random\ error$$
$$\leq maximum\ value\ of\ displacement\ recorded\ in\ observation\ points$$
$$* 10\%$$

$$dsiplacement_{error\ i} = displacement_i + Random\ error$$

Thus, $dsiplacement_{error\ i}$ is substituted as input data for the back-calculations.

6.5.1 The effect of the error present in vertical displacement measurements on the resolution of the ill-posed problem

For these cases, the geometry of the reservoir, the distribution of volume changes and the observation points are all identical to those of the previous cases.

6.5.1.1 Case 8: random error of 0-1 mm, which is 0.55 % of the maximum value recorded

The maximum displacement calculated due to the assumed distribution of the volume changes was found to be

$$displacement_{max} = 0.182285\ m$$

Therefore, for the first case, a random error with the following range was generated:

$$0 \leq random\ error \leq 1mm$$

This amount of error would be 0.5486 % of the maximum displacement value measured. This error was added to the displacements calculated for each observation point, and the resulting value then was used as input for the back-calculations.
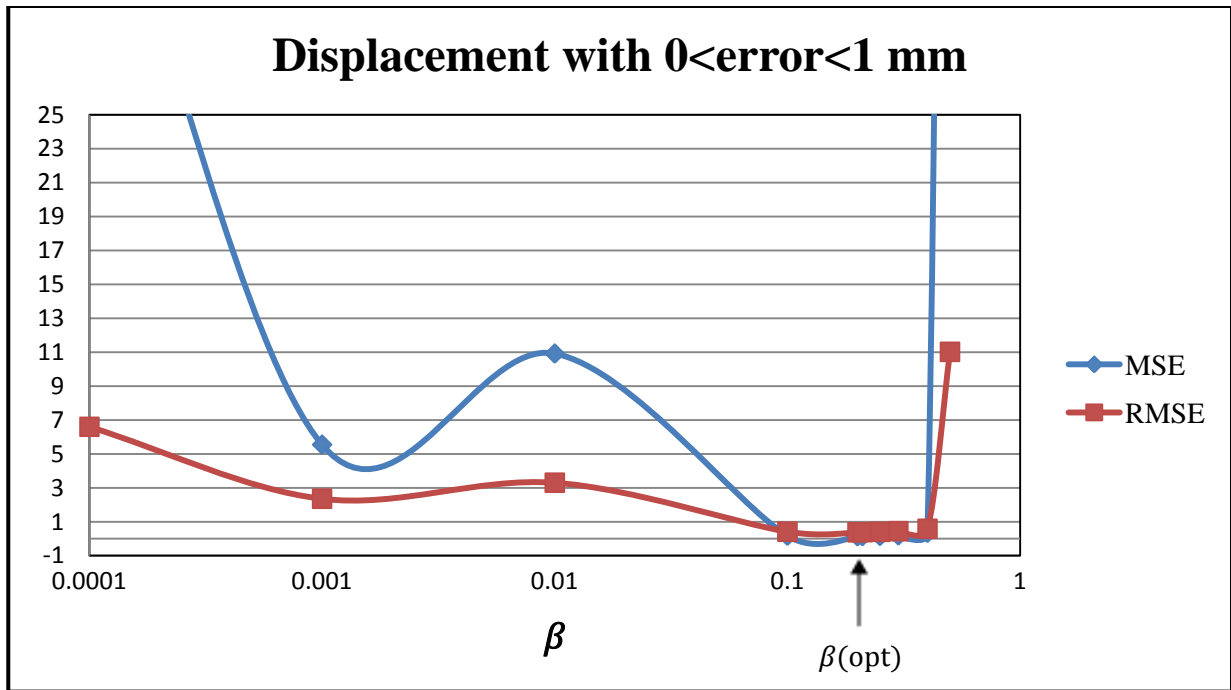
Figure 34: MSE and RMSE plotted against β: Case 8

The optimum β resulting in the minimum MSE in this case was β=0.2, MSE_{min} =0.141099

The resulting volume changes compared to the initial assumed volume changes across each row in the reservoir for the first six rows and also for rows 25 to 30 are illustrated in Figure 35 and 36.
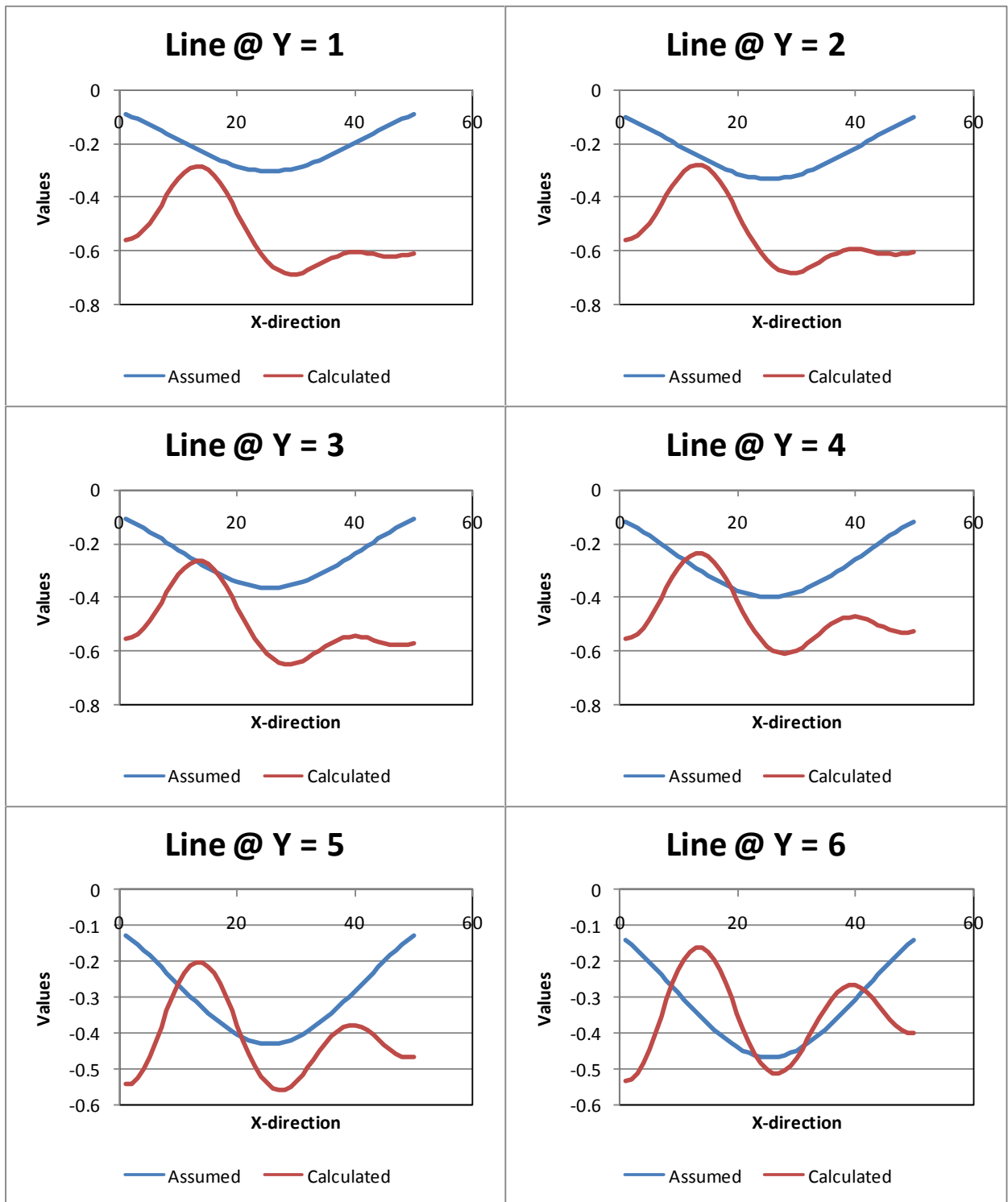
Figure 35: Δv for the first six rows of the reservoir; Case 8.
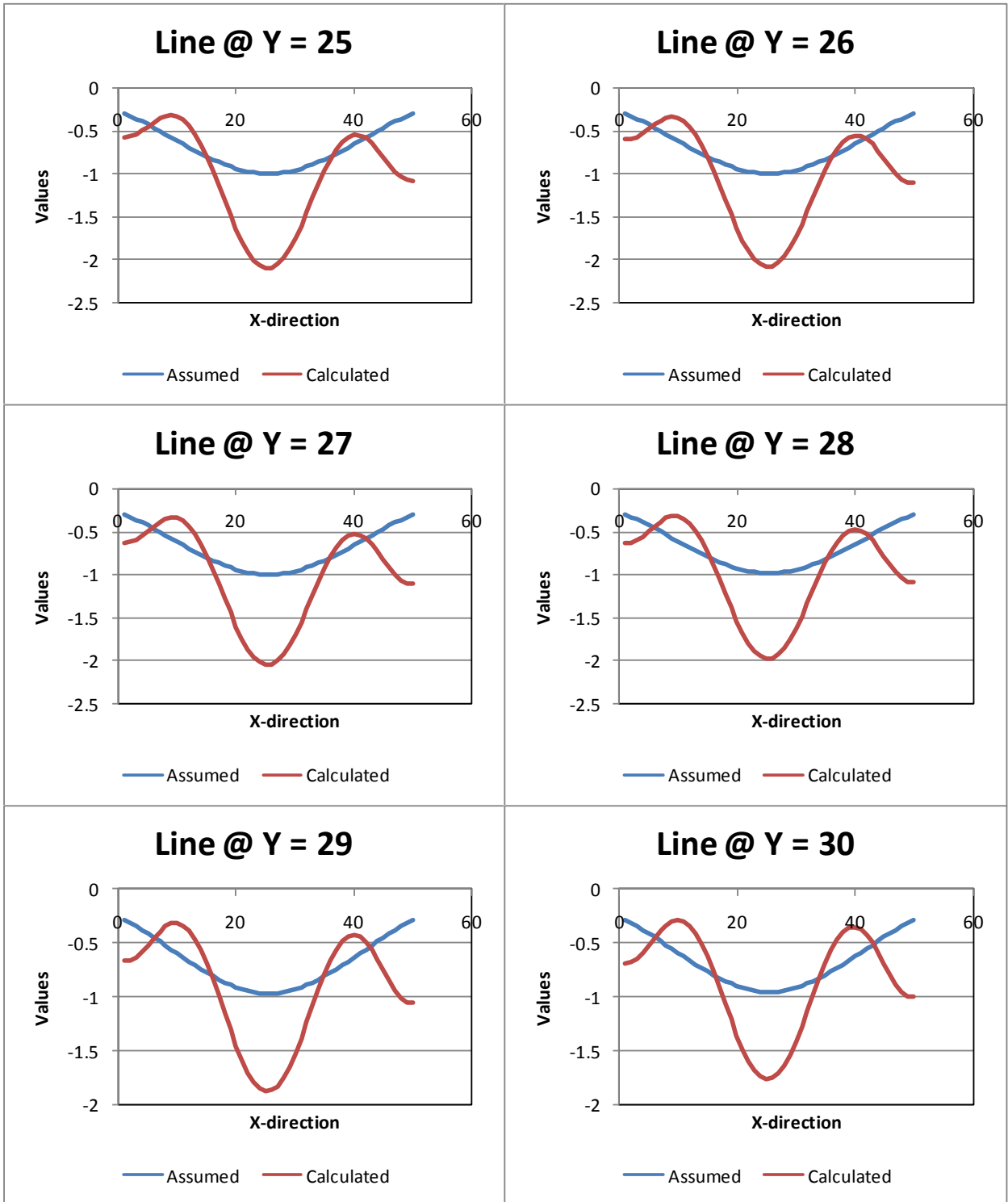
Figure 36: Δv for the rows 25 to 30 of the reservoir; Case 8.

As can be seen, adding only 0.5486 % of the maximum displacement value as error would completely change the results both in the shape of the volume distribution and also the magnitude of the values calculated. Displacements at observation points are therefore not suitable input data for solving the inverse ill-posed problem.

6.5.2 The effect of the error present in tilt measurements on the resolution of the ill-posed problem

6.5.2.1 Case 9: tilts1+2 with 3 % error

The geometry of the reservoir and the initial distribution of the volume changes are identical to those in the previous cases. With respect to the observation points, the entire deformation field considered was $-500 \leq x, y \leq 1000$. Tilts1+2 from each observation point were used as input data. As shown in previous sections, tilts1+2 result in the best resolution. The maximum value of the tilt in the deformation field was calculated to be

$$tilt_{max} = 3.73 * 10^{-4}$$

A value for random error was introduced in the following manner:

$$0 \leq error \leq 3\% * tilt_{max}$$

This random error was then added to each data set from each observation point

$$tilt1_{i_{error}} = random\ error + tilt1_i$$

$$tilt2_{i_{error}} = random\ error + tilt2_i$$

These data were then used as input for the back-calculations. The volume changes calculated were plotted along with the initial assumed volume changes and are shown in Appendix III.

6.5.2.2 Case 10: tilts1+2 with 6 % error

In case 10, 6 % of the maximum value of the tilts was added as the random error. The changes in volume calculated were plotted along with the initial assumed changes in volume and are shown in Appendix III.

6.5.2.3 Case 11: Tilts1+2 with 9 % error

The volume changes calculated were plotted along with the initial assumed changes in volume and are shown in Appendix III.

Case 12, using 10% error; case 13, using 12% error; case 14, using 15% error; case15, using 15% error, and case16, using 20% error were also modeled. The results from these cases are summarized in Figure 37.
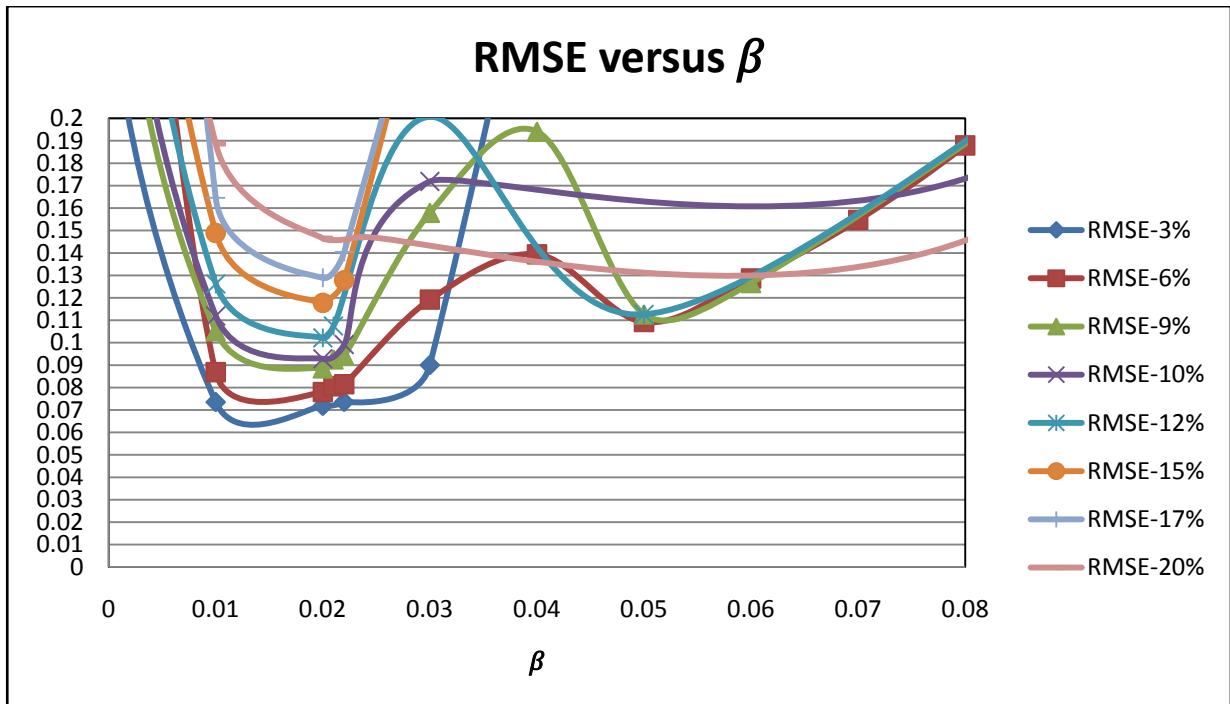
Figure 37: Results of RMSE from the inverse solution of different cases using tilt1+tilt2 with error plotted against β.

As can be seen, increasing the error results in an increase in the minimum standard deviation, and the general trend is almost identical in all cases. The solutions thus deviate farther from the exact solution.

The above chart can be summarized in Table 11.

Table 11: Minimum MSE for different error percentages used as input

Tilt1+tilt2 used as input data			
Case	% error of the maximum tilt value added	MSE_{min}	$RMSE_{min}$
9	3%	0.005156	0.071804
10	6%	0.006081	0.07798
11	9%	0.007841	0.088552
12	10%	0.008614	0.092814
13	12%	0.010438	0.102166
14	15%	0.008614	0.092814
15	17%	0.016622	0.128927
16	20%	0.021447	0.146448

The resulting volume changes compared to the initial assumed volume changes across each row in the reservoir for the first six rows and also for rows 25 to 30 are illustrated in Figure 38 and 39.
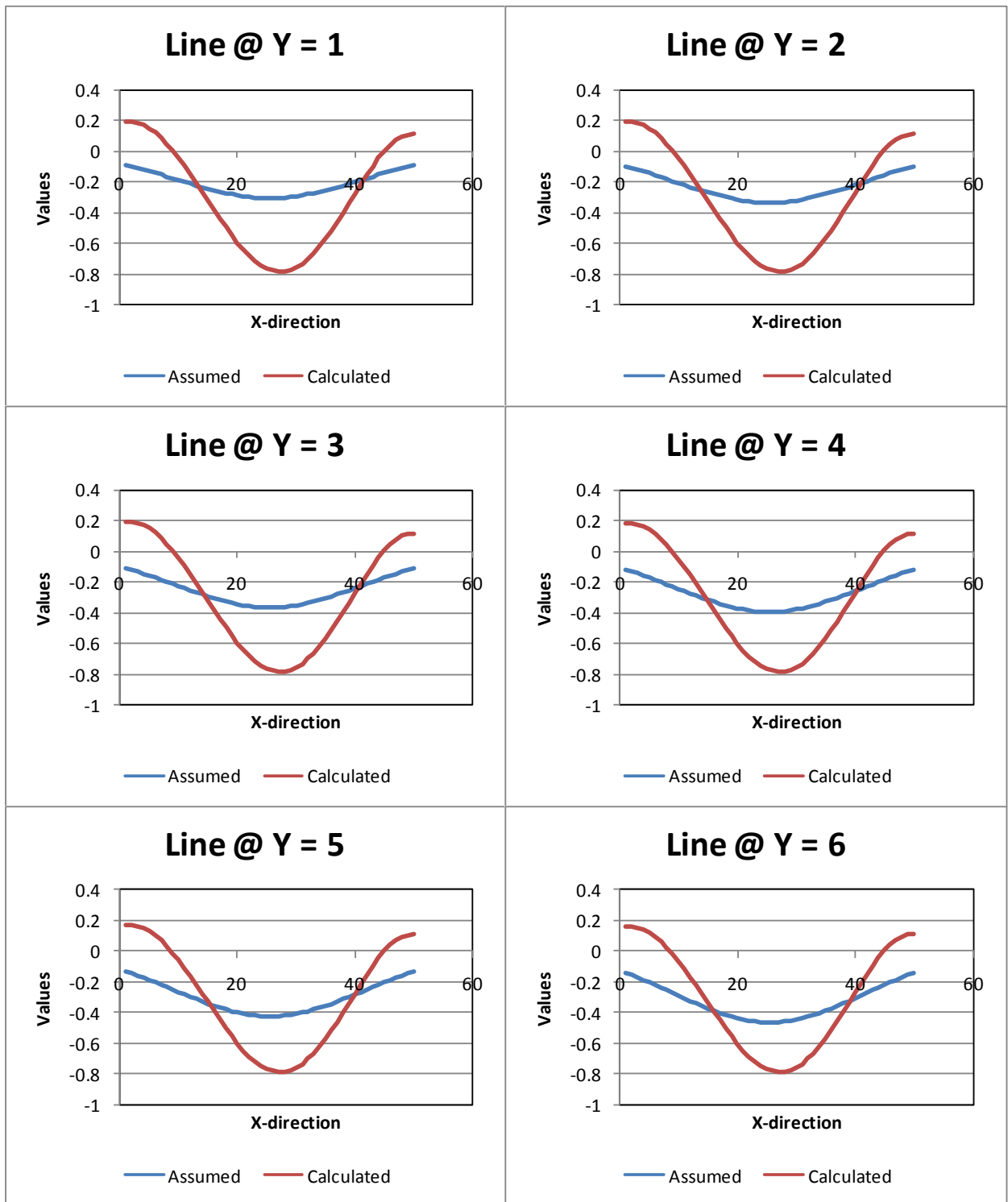
Figure 38: Δv for the first six rows of the reservoir; Case 16.
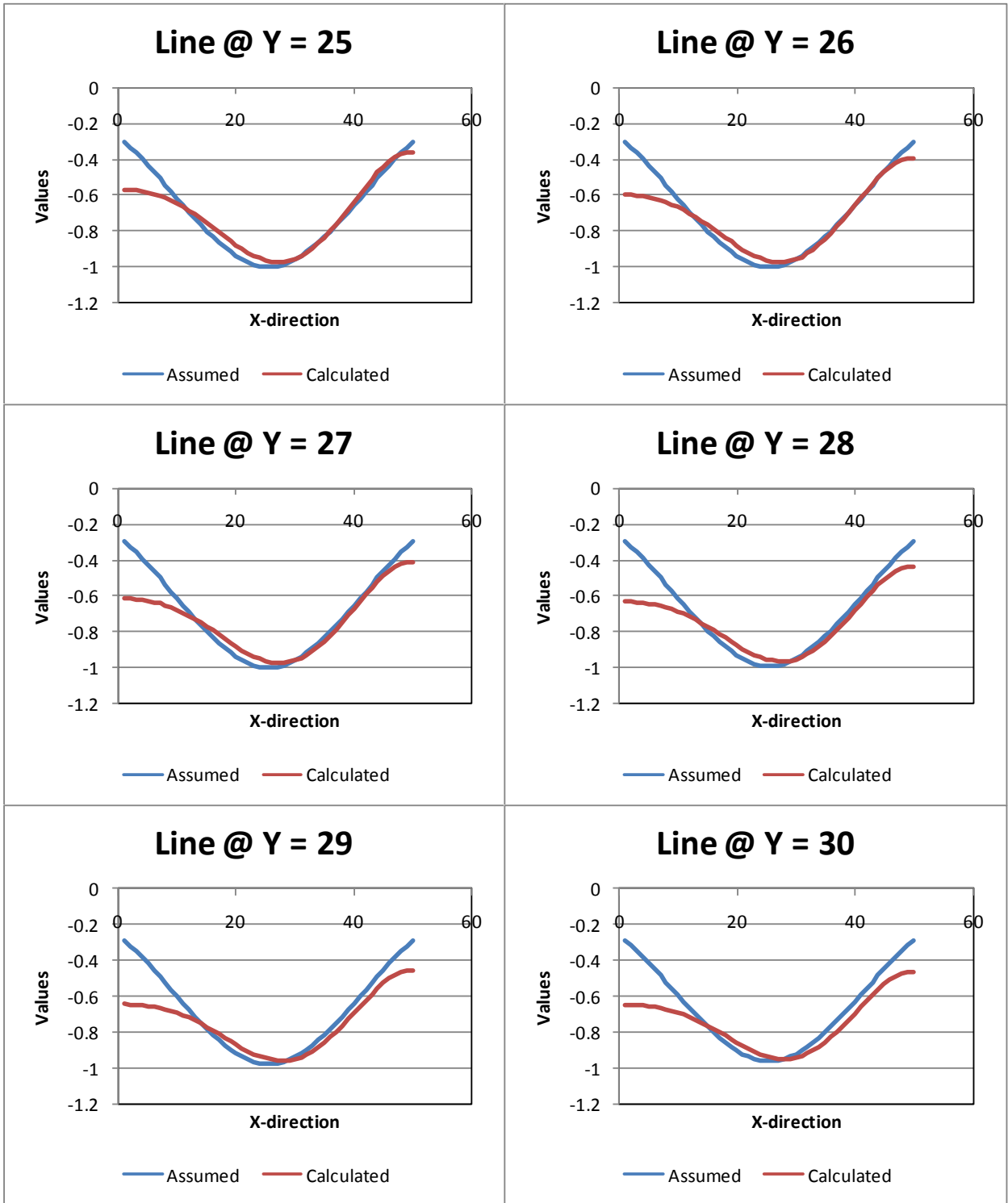
Figure 39: Δv for the rows 25 to 30 of the reservoir; Case 16.

From the above charts, it can be seen that using tilts1+2 as input data for the back-calculations, even when up to 20 % of the maximum value of recorded tilts is incorporated as error, would result in a volume change distribution calculated close to what expected with a good resolution.

6.5.3 The effect of error present in vertical displacement + tilts1+2 on the resolution of the ill-posed problem

6.5.3.1 Case 17: using vertical displacement + tilts1+2 with 1 % error present in all three sets of data

The geometry of the reservoir, volume change distribution and the total number of observation points are the same as those in the previous cases. The observation grid is extended over the reservoir to include the following range:

$$-500 \leq X_{obser}, Y_{obser} \leq 1000$$

With respect to the input for the back-calculations, tilts1+2 + the vertical displacement from each observation point were used. To enable all the data to be used together, as mentioned in the previous section, the values were normalized and then divided by the maximum value in the data set so that all three sets of data would be in the same range. With respect to the error, only 1 % of the maximum value was considered as random error, and the procedure used is as follows:

$$0 \leq random\ error_{tilt} \leq 1\% * tilt_{max}$$

$$0 \leq random\ error_{displacement} \leq 1\% * displacement_{max}$$

$$Tilt1_{error\ i} = Random\ error_{tilt\ 1} + tilt1_i$$

$$Tilt2_{error\ i} = Random\ error_{tilt\ 2} + tilt2_i$$

$$displacement_{error\ i} = Random\ error_{displacement} + displacement_i$$

For the back-calculations, these data incorporating the error were used as the input data from each observation point. The results are shown in Figure 40.
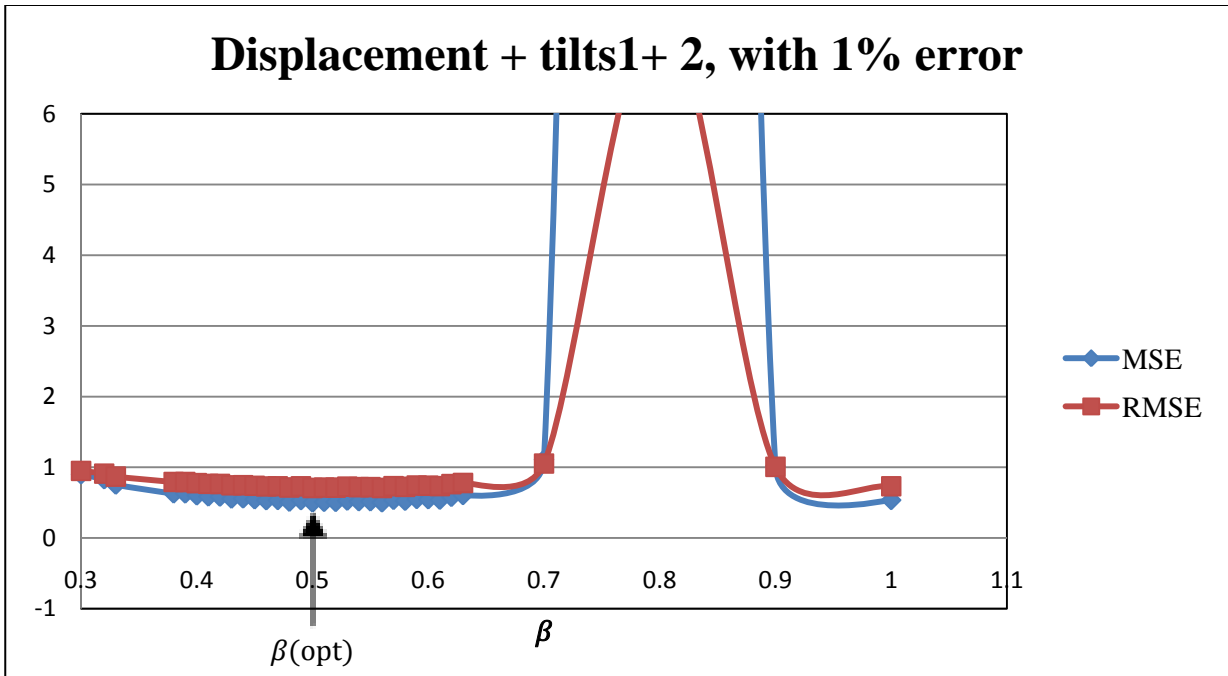
Figure 40: MSE and RMSE plotted against β: Case 17

The following should be noted: $\beta_{opt} = 0.5$, $MSE_{min} = 0.501324$, $RMSE_{min} = 0.708043$. The resulting volume changes compared to the initial assumed volume changes across each row in the reservoir for the first six rows and also for rows 25 to 30 are illustrated in Figure 41 and 42.
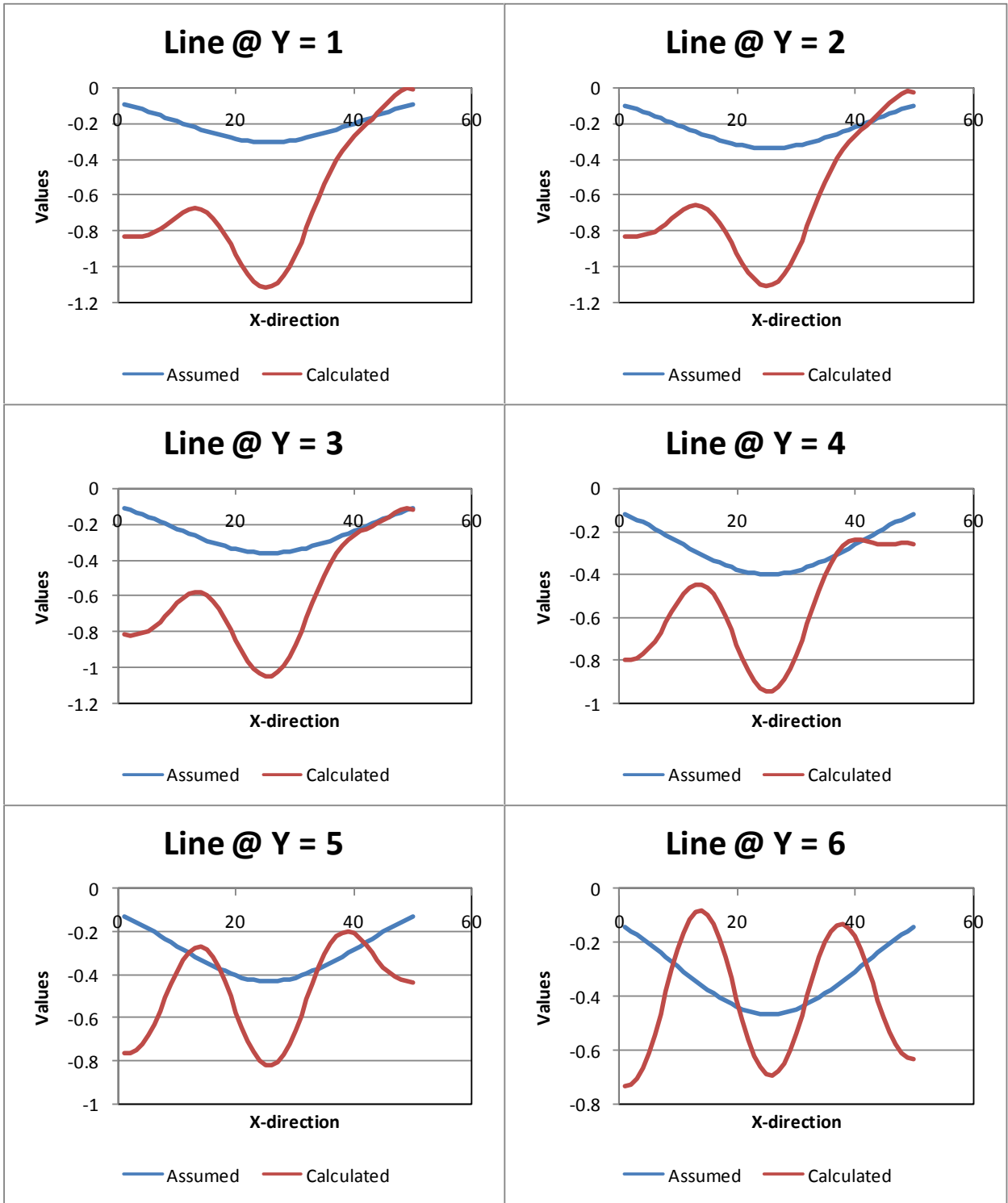
Figure 41: Δv for the first six rows of the reservoir; Case 17.
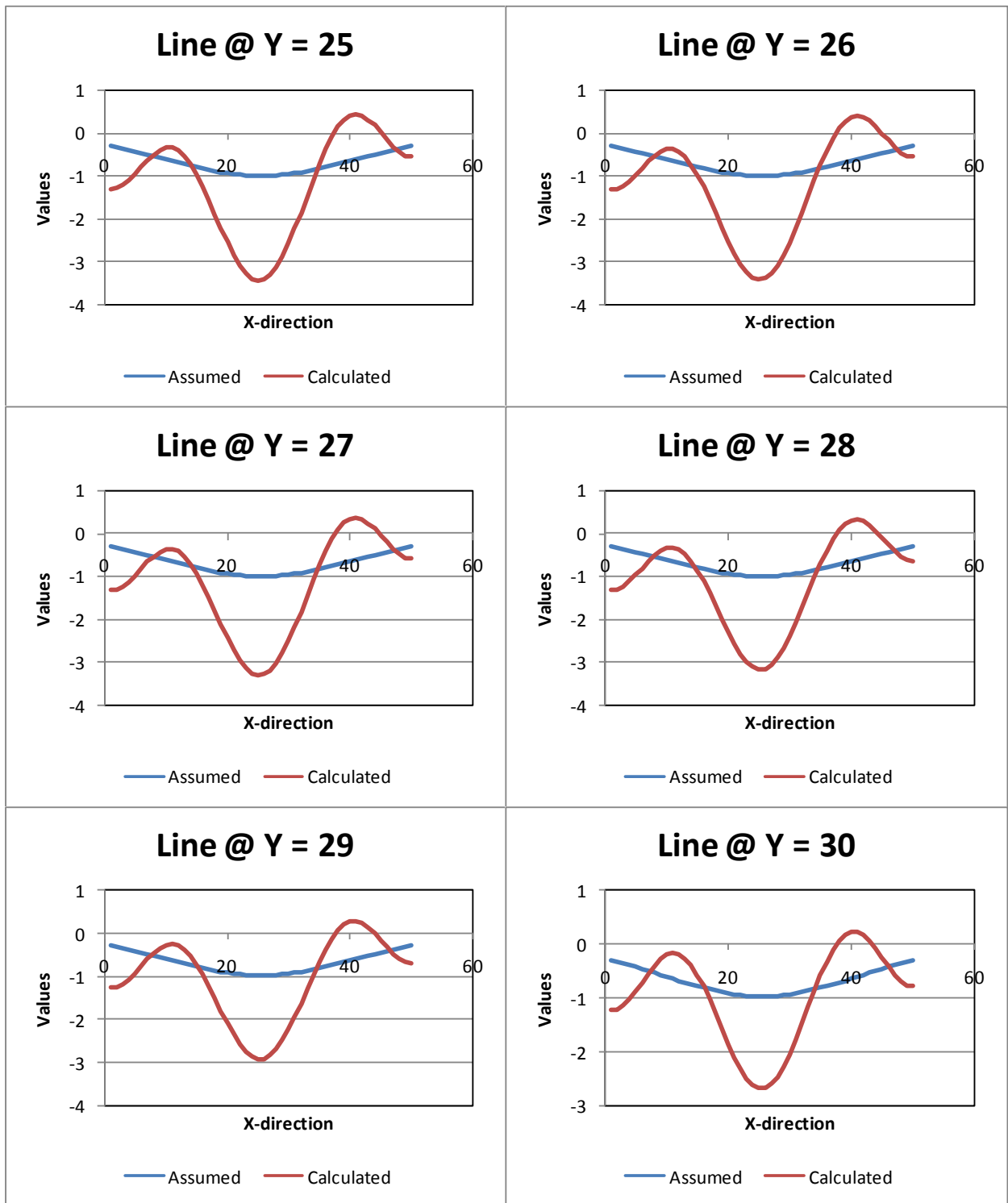
Figure 42: Δv for the rows 25 to 30 of the reservoir; Case 17.

As can be seen, adding only 1 % of the maximum values as error significantly affects the solution; the volume change distribution and the associated values are not at all close to the initial assumed distributions and values.

Table 12 summarizes the effect of error present in the observation data taken from the surface deformation field on the solution of the inverse problem and the resulting back-calculated volume change distributions.

Table 12: Results summarized to show the effect of error in the observation data.

Case	input data	% error	β_{Opt}	MSE_{min}	$RMSE_{min}$
2	displacement	0%	0.1000001	0.000768	0.027707
8	displacement	0.55%	0.2	0.141099	0.375631
6	displacements+Tilt1+2	0%	0.38	0.000433	0.020809
5	Tilt1+Tilt2	0%	0.000001	0.000408	0.020199
9	Tilt1+Tilt2	3%	0.02	0.005156	0.071804
10	Tilt1+Tilt2	6%	0.02	0.006081	0.07798
11	Tilt1+Tilt2	9%	0.02	0.007841	0.088552
12	Tilt1+Tilt2	10%	0.02	0.008614	0.092814
13	Tilt1+Tilt2	12%	0.02	0.010438	0.102166
14	Tilt1+Tilt2	15%	0.02	0.008614	0.092814
15	Tilt1+Tilt2	17%	0.02	0.016622	0.128927
16	Tilt1+Tilt2	20%	0.02	0.021447	0.146448
17	displacements+Tilt1+2	1%	0.5	0.501324	0.708043

6.6 Effect of the number of observation points on the inverse resolution

The number of observation points is another important factor in every monitoring and controlling project. The higher the number of observation points, the more devices must be used for observing and recording data, which for this study is the displacement data and tilts. Moreover, more time and energy would be required for the installation, monitoring and maintenance of the additional devices. On the other hand, the more observation points that are used, the more data that can be acquired from the deformation field, which would result in better resolution. Determining the optimum number of observation points would therefore be helpful for obtaining the desired resolution economically.

For the cases described so far, 2704 benchmarks were used, which is, in fact, an impractical number of observation points and would never actually be used. The number was chosen for the previous cases based on the number of reservoir elements. The reservoir was divided into grids with 50*50 elements, or 2500 overall. Thus the number of unknown volume changes to be solved for from the inverse case in this case was 2500. Based on that number, 2704 observation points were used, and the number of available data sets or known parameters was thus 2704. To study the sensitivity of the resolution to the number of observation points, some observation points were randomly omitted for each case. The percentage of the points omitted was based on the number of unknowns to be solved for, or the reservoir elements: 2500. This method was used in order to generalize the problem and so that the results would be applicable to a variety of cases.

To determine the sensitivity of the calculations to the number of observation points, the general model used in the previous cases with the same geometry and initial volume change distribution was applied here as well. The following cases were studied:

6.6.1 Omitting random points using tilt1+ 2 + displacement with 0 % error as input

All three data sets from each observation point, assuming that the data contains 0 % error and that the values are the exact actual values, were used as input for the cases presented in this section.

6.6.1.1 Case 18: omitting 4 % of the observation points

For case 18, 96 % of the number of reservoir elements, or 2400 points, were used as observation points. The MSE and RMSE plotted against β for the results are shown in Figure 43.

$$\beta_{opt} = 0.54, MSE = 0.000547, RMSE = 0.023385$$
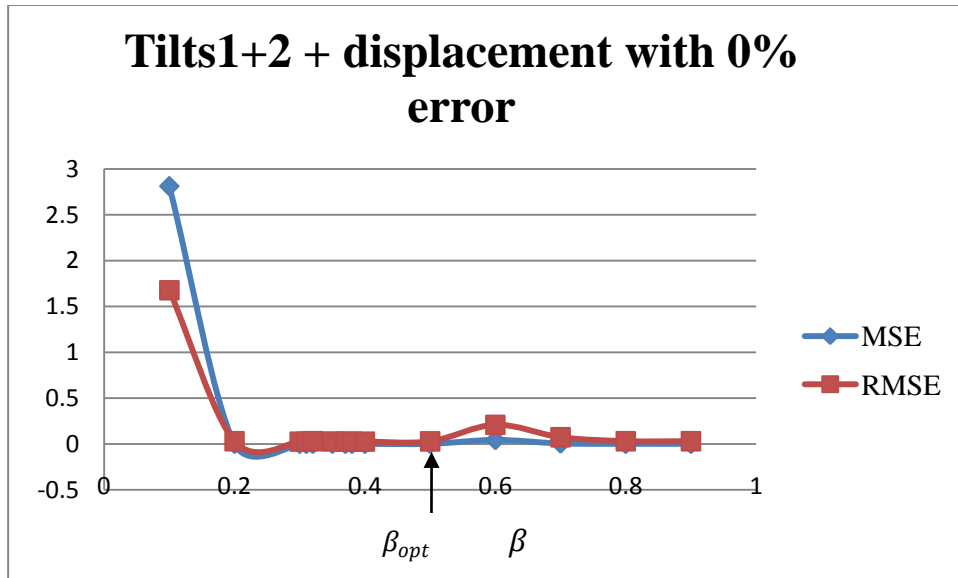
Figure 43: MSE and RMSE plotted against β: Case 18.

6.6.1.2 Case 19

In case 19, 90 % of the unknowns were used as the number of observation points. The results for 2250 observation points are shown in Figure 44.

$$\beta_{opt} = 0.37, MSE = 0.000579, RMSE = 0.024057$$
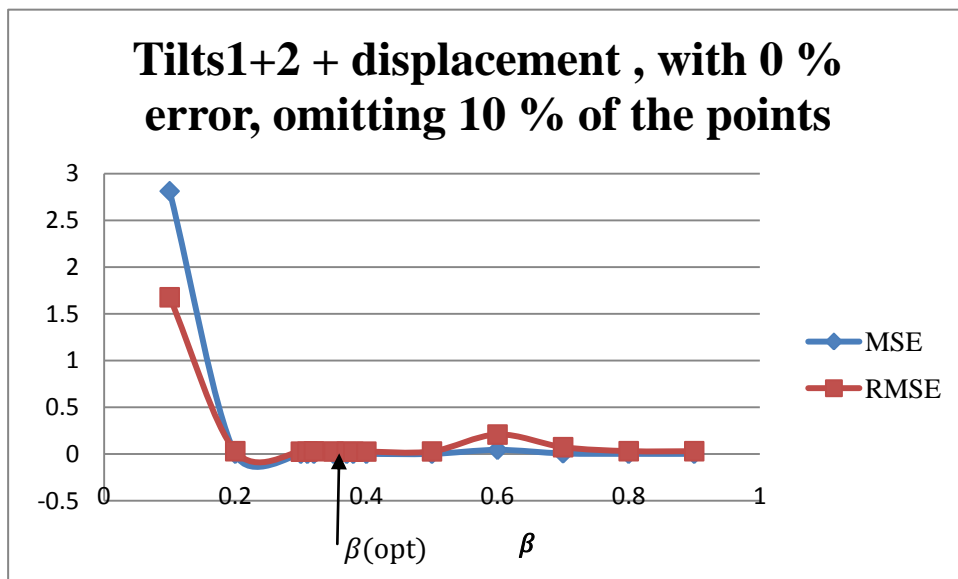
Figure 44: MSE and RMSE plotted against β: Case 19.

6.6.1.3 Case 20

For case 20, 20% of the total number of elements were randomly omitted from the benchmarks. Thus the calculations were performed using 2000 observation points. The results can be seen in Figure 45.

$$\beta_{opt} = 0.38, MSE = 0.000601, RMSE = 0.024514$$
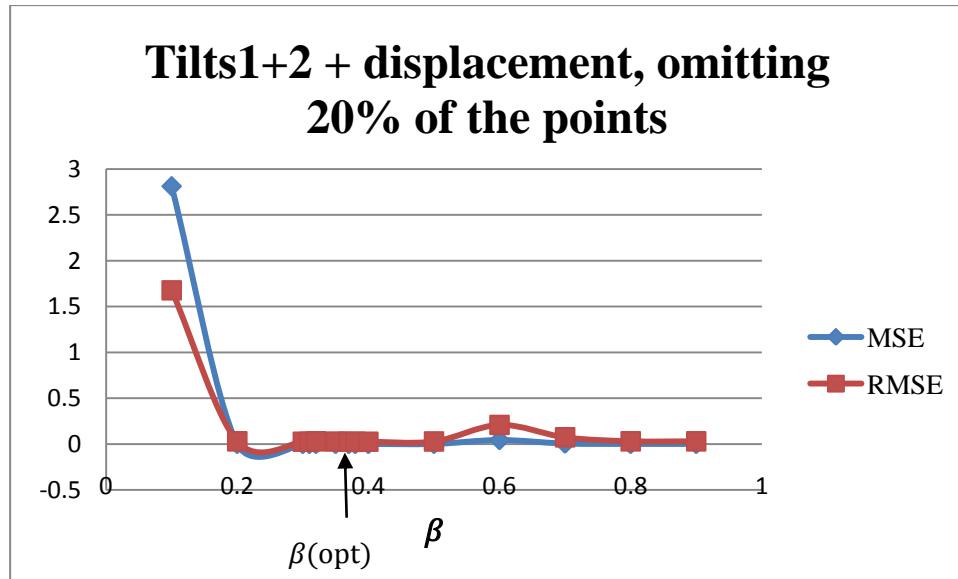
Figure 45: MSE and RMSE plotted against β: Case 20

6.6.1.4 Case 21

For case 21, 40% *2500 of the observation points were randomly omitted, and the results using 1500 points, as shown in Figure 46, were calculated as follows:

$$\beta_{opt} = 0.2, MSE = 0.000844, RMSE = 0.029051$$
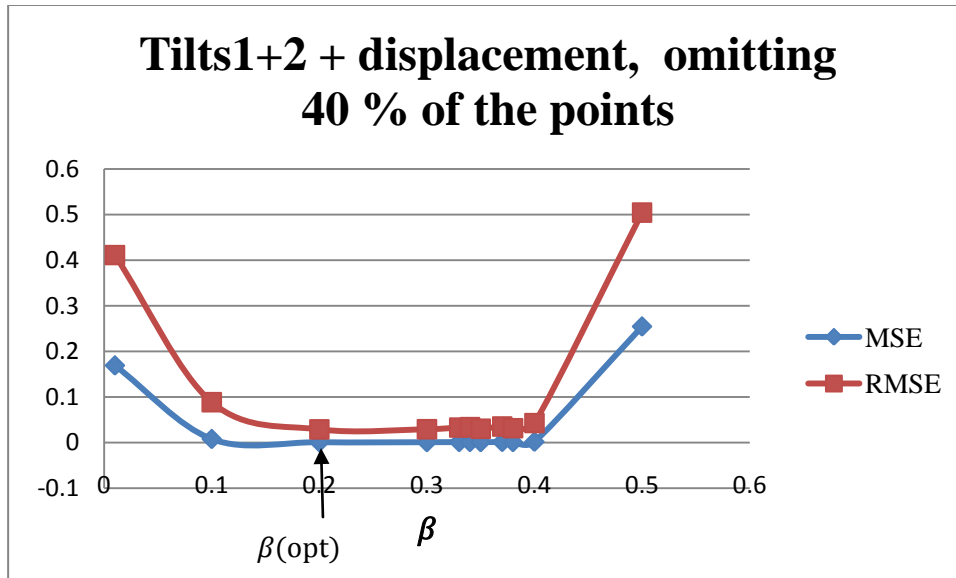
Figure 46: MSE and RMSE plotted against β: Case 21

6.6.1.5 Case 22

For case 22, 60%*2500 of the observation points were randomly omitted. Using 1000 points, the results of the MSE and RMSE were plotted against β, as shown in Figure 47, were as follows:

$$\beta_{opt} = 0.22, MSE = 0.000703, RMSE = 0.026517$$
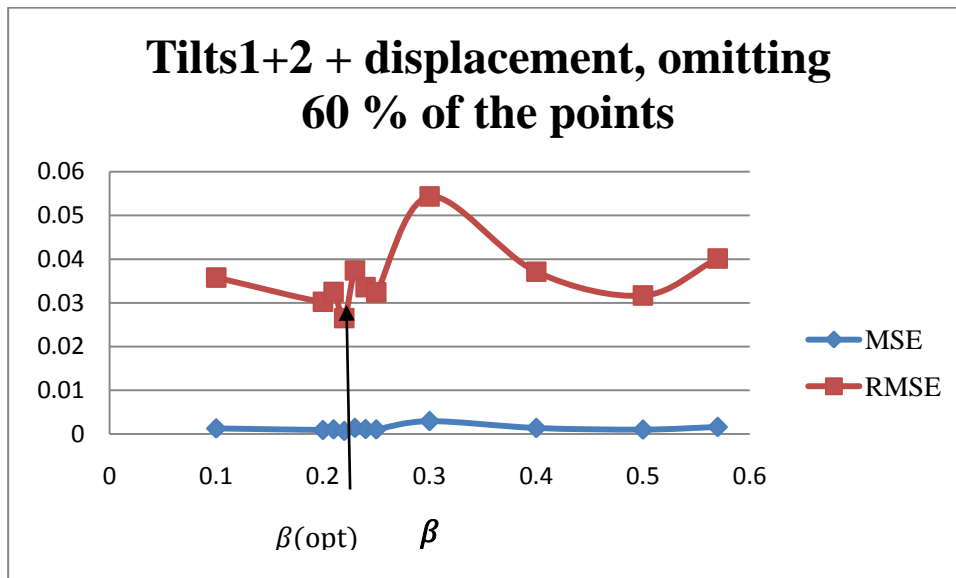
Figure 47: MSE and RMSE plotted against β: Case 22.

6.6.1.6 Case 23

For case 23, 80%*2500 of the data points were randomly omitted, and 500 random points were used. The results of MSE and RMSE plotted against β were as shown in Figure 48.

$$\beta_{opt} = 0.1, MSE = 0.000666, RMSE = 0.025801$$
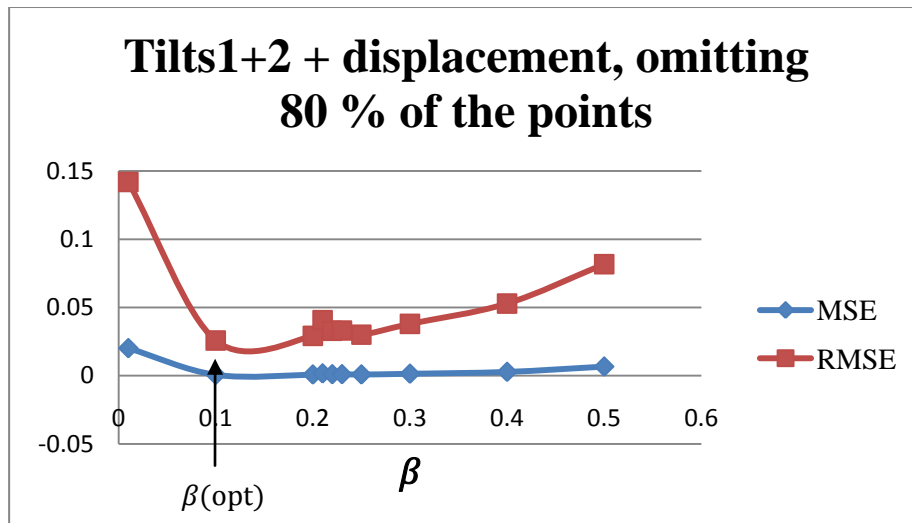
Figure 48: MSE and RMSE plotted against β: Case 23.

6.6.1.7 Case 24

For case 24, when 90%*2500 of the observation points were omitted, 250 points were used. The resulting MSE and RMSE were plotted against, as shown in Figure 49.

$$\beta_{opt} = 0.78, MSE = 0.001742, RMSE = 0.041741$$
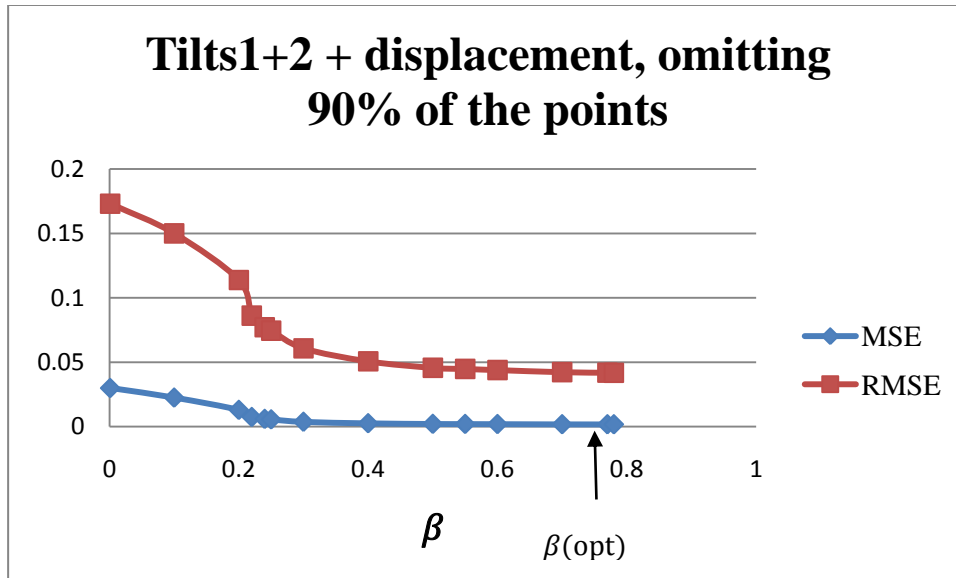
Figure 49: MSE and RMSE plotted against β: Case 24.

6.6.1.8 Case 25

For case 25, 96%*2500 of the observation points were randomly deleted, and 100 points were used as observation points. The results were as shown in Figure 50.

$$\beta_{opt} = 0.78, MSE = 0.001742, RMSE = 0.041741$$
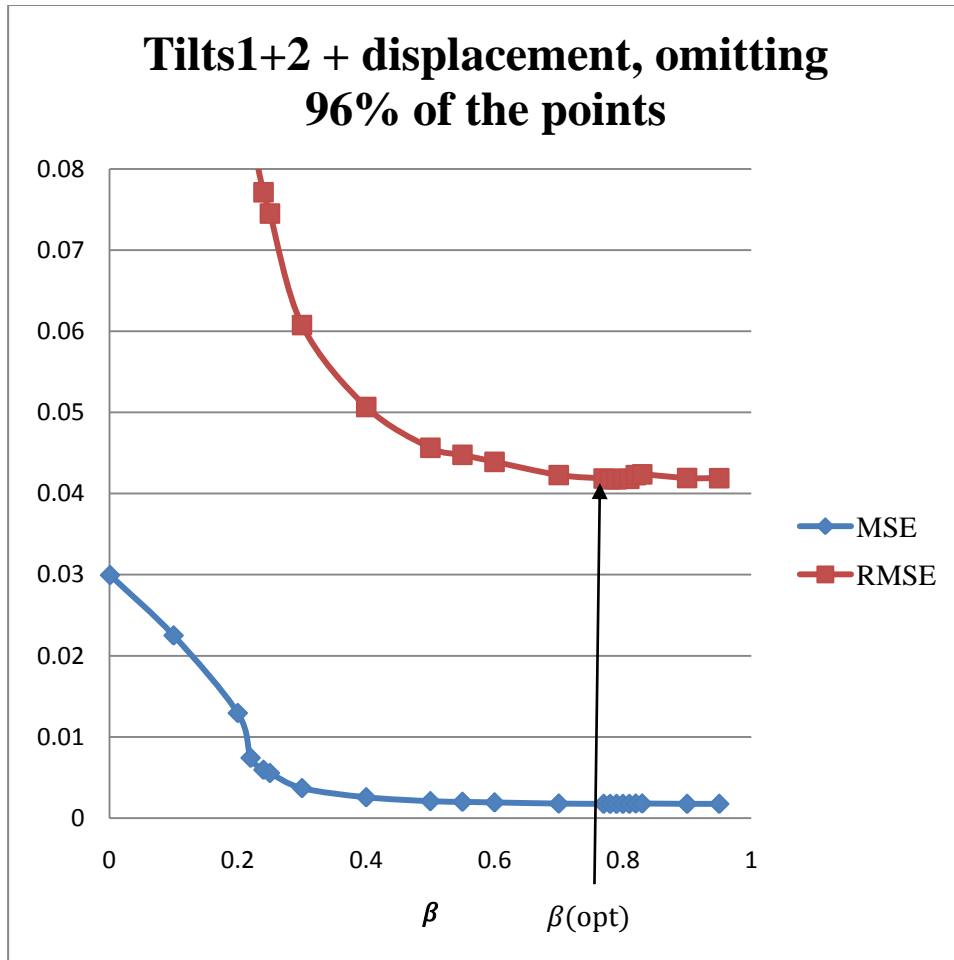
Figure 50: MSE and RMSE plotted against β: Case 25.

6.6.1.9 Case 26

For case 26, about 98% of the observation points were omitted, and 50 points were used as observation points. The results can be seen in Figure 51.

$$\beta_{opt} = 0.3, MSE = 0.001764, \text{RMSE} = 0.042006$$
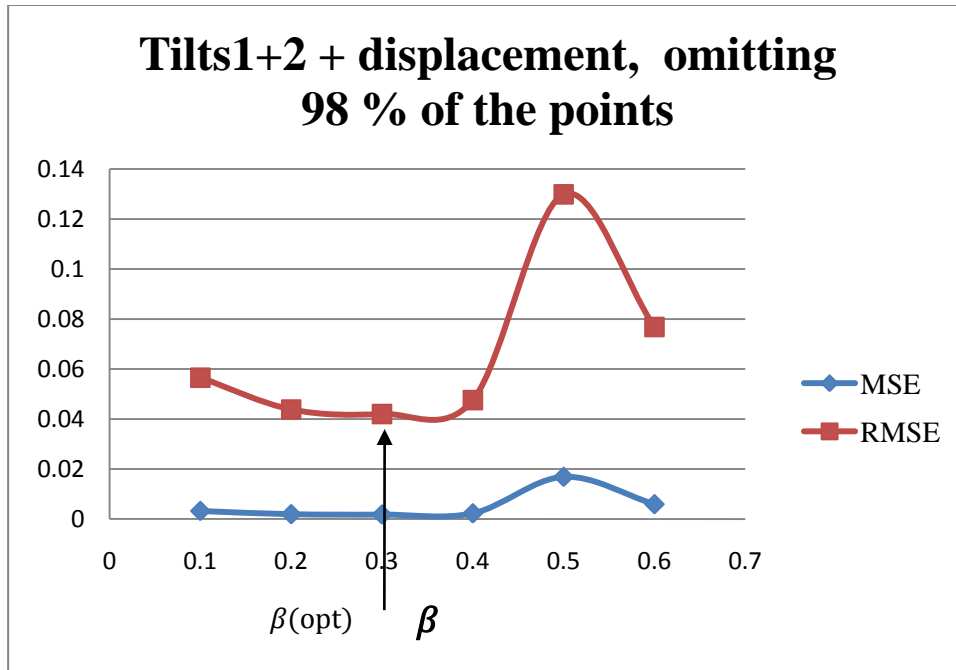
Figure 51: MSE and RMSE plotted against β: Case 26.

6.6.1.10 Case 27

Only 10 random points were chosen as observation points for case 27. The resulting MSE and RMSE were plotted against β, as shown in Figure 52.

$$\beta_{opt} = 0.8, MSE = 0.005009, RMSE = 0.070773$$
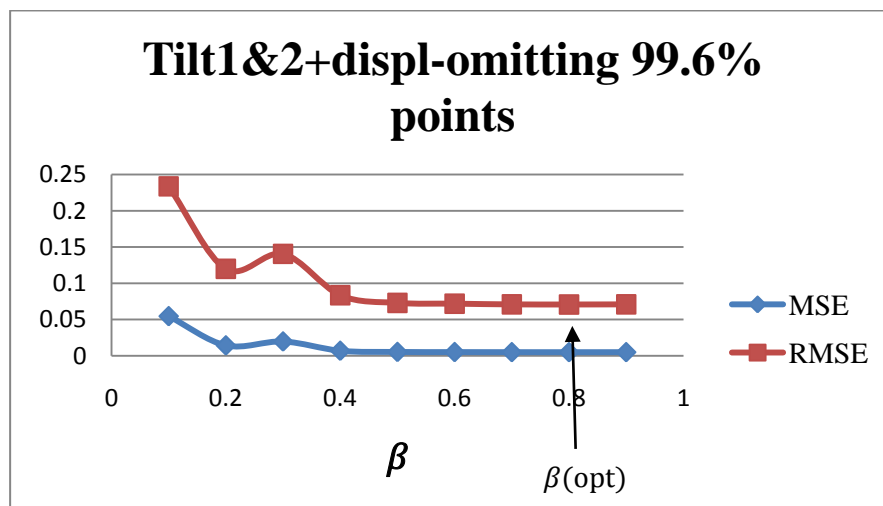
Figure 52: MSE and RMSE plotted against β: Case 27.

Table 13 provides a summary and comparison of the results of the above cases, and Figure 53 shows the RMSE plotted against the number of observation points used.

Table 13: Comparison of results to show the effect of the number of observation points.

Case	Data used for input	% error	Number of observation points used	% of the initial observation points randomly omitted	β_{Opt}	MSE_{min}	$RMSE_{min}$
6	tilt1+2+displacement	0%	2704	0%	0.38	0.000433	0.020809
18	tilt1+2+displacement	0%	2400	4%	0.54	0.000547	0.023385
19	tilt1+2+displacement	0%	2250	10%	0.37	0.000579	0.024057
20	tilt1+2+displacement	0%	2000	20%	0.38	0.000601	0.024514
21	tilt1+2+displacement	0%	1500	40%	0.2	0.000844	0.029051
22	tilt1+2+displacement	0%	1000	60%	0.22	0.000703	0.026517
23	tilt1+2+displacement	0%	500	80%	0.1	0.000666	0.025801
24	tilt1+2+displacement	0%	250	90%	0.1	0.001311	0.036212
25	tilt1+2+displacement	0%	100	96%	0.78	0.001742	0.041741
26	tilt1+2+displacement	0%	50	98%	0.3	0.001764	0.042006
27	tilt1+2+displacement	0%	10	99.60%	0.8	0.005009	0.070773
28	tilt1+2+displacement	0%	1	99.96%	0.12	0.05674	0.238201
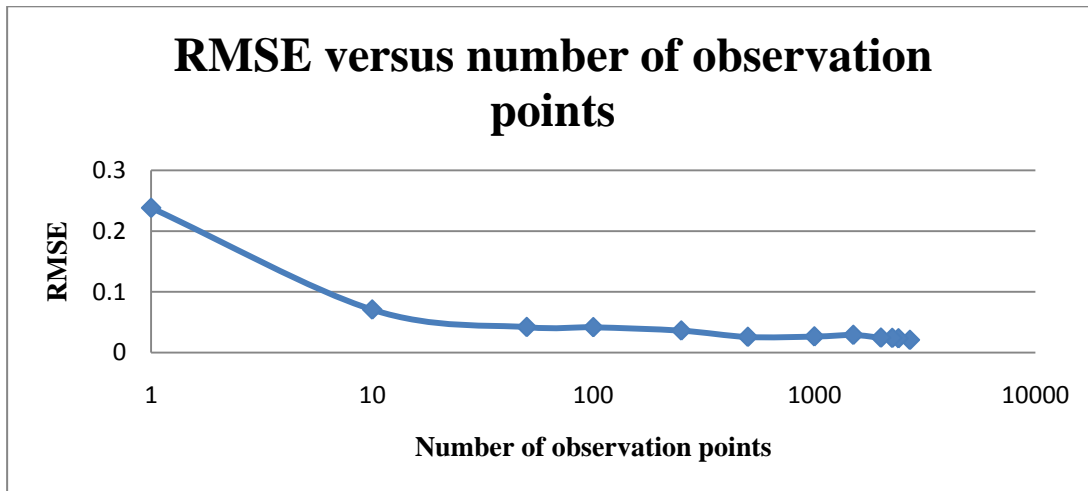
Figure 53: RMSE plotted against the number of observation points.

The results of the volume change calculations in each case, along with the initial assigned volume changes, were plotted in graphs for each block of the reservoir. The graphs are provided in Appendix IV.

As expected, it can be seen that omitting more points and thus using a lower number of observation benchmarks generally causes the RMSE to increase, which translates into a less accurate solution. However, from the graphs plotted and included in Appendix IV, it can be seen that if the error in the observation data is assumed to be 0, using only 10 points, or 99.6% of the number of reservoir elements, and thus having only 10 known data would result in an acceptable resolution. A closer examination of the results of the cases presented in Table 13 reveals that the RMSE does not change significantly with the omission of a large number of observation points, and thus a large amount of data. Using 2400 points resulted in a MSE of 0.000547 whereas, when 1900 points were omitted and only 500 used, the MSE increased only to 0.000666. Therefore, using a large number of benchmarks does not necessarily mean a much better resolution when a combination of tilts is used as input data. Thus, the resolution is not very sensitive to the number of observation points if the error in the observed data is considered to be zero.

From Table 13, it can be seen that for cases 22 and 23, omitting observation points leads to a slight decrease in the MSE. This effect could be due to the use of random points as observation data; thus, although the number of points used in these cases is lower, the composition of the grid of these points has a better distribution, and thus, the data gathered results in better resolution. The following sections present an examination of the effect of the distribution of the observation points on the resolution.

6.7 The effect of the distribution of the observation points on the resolution of the inverse problem

In the above cases, it was seen that the number of observation points does not need to be equal to the number of reservoir elements, which is the number of unknowns, and points can thus be omitted. However, for the above cases the points were randomly chosen for omission. In actual cases, however, it is practical to have a specific routine for choosing the distribution of the benchmarks because the observation process would be more convenient and easier to install, observe, and monitor. Moreover, the most important point is that the deformation field can be

reconstructed more effectively if an appropriate pattern is chosen for the distribution of the benchmarks.

To observe the sensitivity of the inverse case resolution to the distribution of the benchmarks chosen for collecting data on the surface above the reservoir, a number of cases scenarios were studied, and the results are presented in this section.

6.7.1 0% error present in the observation data

Data for tilts1+2 + displacements were used as input for the following cases, meaning that all three data sets from each observation point were used. A 0% error was assumed for the input data, and thus the exact calculated displacements and tilts were used for the calculations. The geometry of the reservoir and the initial volume change distribution were the same as in the previous cases. The number of observation points used was 100.

6.7.1.1 Case 29

The 100 benchmarks for case 29 were distributed in two rows, one vertical and one horizontal, that meet at a corner directly above the reservoir:

$$\begin{cases} X_{obser} = 5 \\ 5 \leq Y_{obser} \leq 495 \end{cases}$$

$$\text{and} \begin{cases} Y_{obser} = 5 \\ 5 \leq X_{obser} \leq 495 \end{cases}$$

The plan of the observation points placed above the reservoir is shown in the Figure 54. As can be seen, two rows of observation points, with 50 points in each row, are shown as crosses in two outside reservoir element rows that meet at a corner.
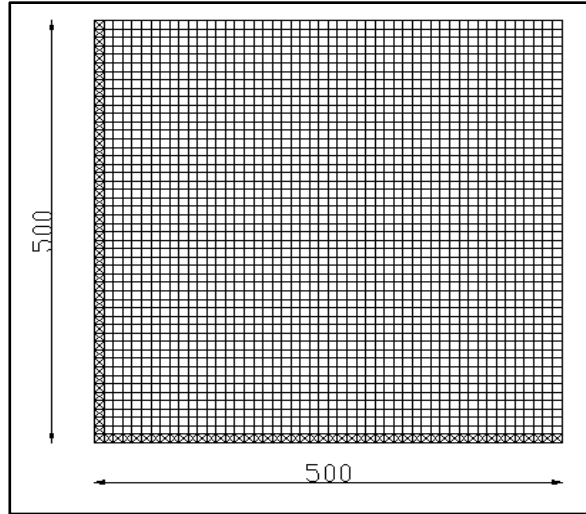
Figure 54: Plan of reservoir with observation points distributed in two rows, one vertical and one horizontal, which meet at the corner above the reservoir.

The resulting MSE and RMSE plotted against β were as shown in Figure 55.

$$\beta_{opt} = 0.1, MSE = 0.0024587, \text{RMSE} = 0.04958528$$
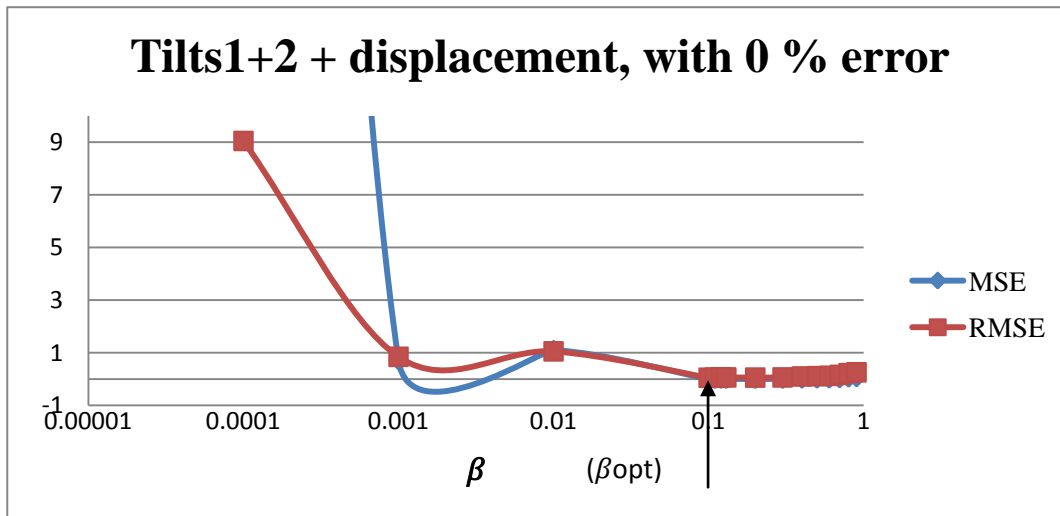
Figure 55: MSE and RMSE for different values of βs: Case 29

6.7.1.2 Case 30

For case 30, the 100 observation points were distributed in two rows, one vertical and one horizontal, which cross above the mid-point of the reservoir:

135

$$\begin{cases} X_{obser} = 250 \\ 5 \le Y_{obser} \le 495 \end{cases}$$

$$\text{And} \begin{cases} Y_{obser} = 250 \\ 5 \le X_{obser} \le 495 \end{cases}$$

The plan of the observation points placed above the reservoir is shown in Figure 56.
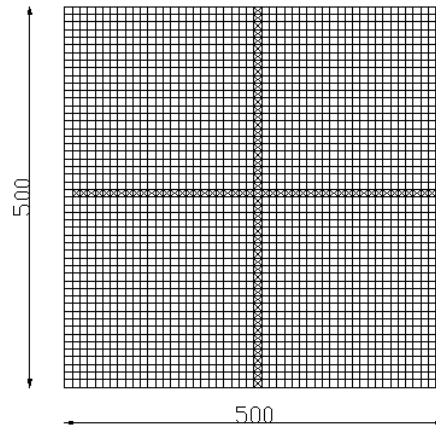
Figure 56: Plan of reservoir with observation points distributed in two rows, one horizontal and one vertical, which cross at the centre of the reservoir.

The results of MSE and RMSE plotted against β were as shown in Figure 57.

$$\beta_{opt} = 0.6, MSE = 0.0017898, \text{RMSE} = 0.042306028$$
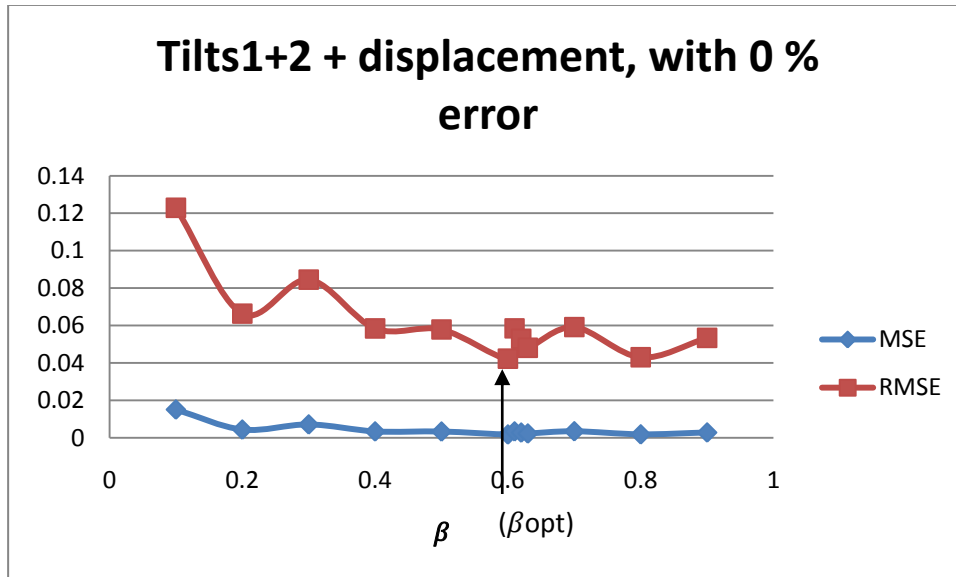
Figure 57: MSE and RMSE plotted against β: Case 30.

136

6.7.1.3 Case31:

In case 31, the 100 points extend from -500 to 1000, in two rows placed at the centre of the reservoir:

$$\begin{cases} X_{obser} = 250 \\ -500 \le Y_{obser} \le 1000 \end{cases}$$

$$\text{And} \begin{cases} Y_{obser} = 250 \\ -500 \le X_{obser} \le 1000 \end{cases}$$

The results were as shown in Figure 58.

$$\beta_{opt} = 0.92, MSE = 0.00192145, \text{RMSE} = 0.043834347$$
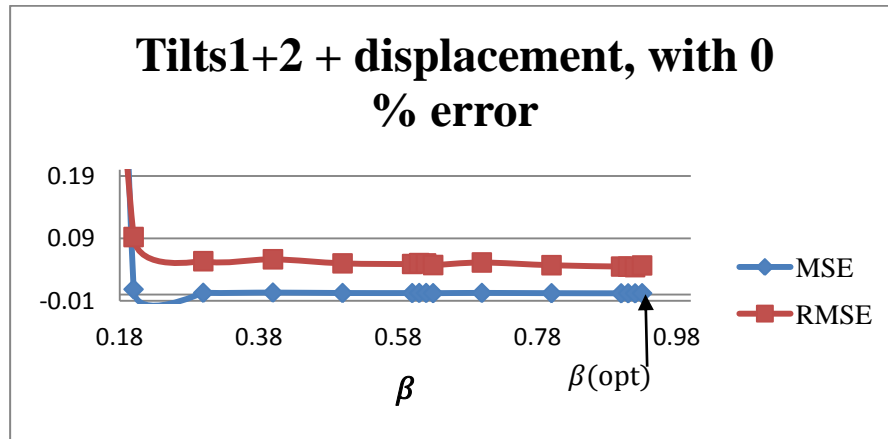
Figure 58: MSE and RMSE plotted against β: Case 31.

Table 14 provides a comparison of the results from the above three cases.

Table 14: Comparison of the results showing the effect of the distribution of observation points.

Case	No. Of observation points	Distribution of 100 points in two rows, one vertical and one horizontal	$beta_{opt}$	MSE_{min}	$RMSE_{min}$
29	100	2 rows meeting at the corner of the reservoir	0.1	0.002459	0.049585
30	100	2 rows crossing at the centre of the reservoir	0.6	0.00179	0.042306
31	100	2 rows extending from -500 to 1000 at the centre of the reservoir	0.92	0.001921	0.043834

It can be seen that the best for selecting benchmarks is from the centre line of the reservoir in both directions. Expanding the points to a wider area and using the same number of points but with larger spacing does not necessarily result in a better resolution.

6.7.1.4 Case 32

In case 32, 50 points are used in two rows, one vertical and one horizontal, with 25 points in each row, placed so that they cross at the centre of the reservoir:

$$\begin{cases} X_{obser} = 250 \\ 10 \leq Y_{obser} \leq 490 \end{cases}$$

$$\text{and} \begin{cases} Y_{obser} = 250 \\ 10 \leq X_{obser} \leq 490 \end{cases}$$

The resulting MSE and RMSE plotted against β were as shown in Figure 59.

$$\beta_{opt} = 0.4, MSE = 0.00187119, RMSE = 0.043257254$$
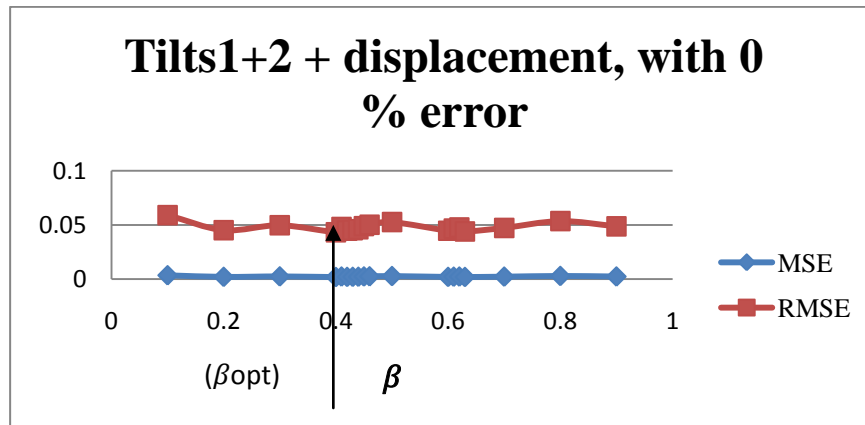
Figure 59: MSE and RMSE plotted against β: Case 32

6.7.1.5 Case 33

For case 33, only 10 points were used as observation points distributed in two rows, one horizontal and one vertical, crossing at the centre of the reservoir:

$$\begin{cases} X_{obser} = 250 \\ 50 \leq Y_{obser} \leq 450 \end{cases}$$

$$\text{and} \begin{cases} Y_{obser} = 250 \\ 50 \leq X_{obser} \leq 450 \end{cases}$$

138

The resulting of MSE and RMSE plotted against β were as shown in Figure 60.

$$\beta_{opt} = 0.3, MSE = 0.00224744, \text{RMSE} = 0.04740717$$
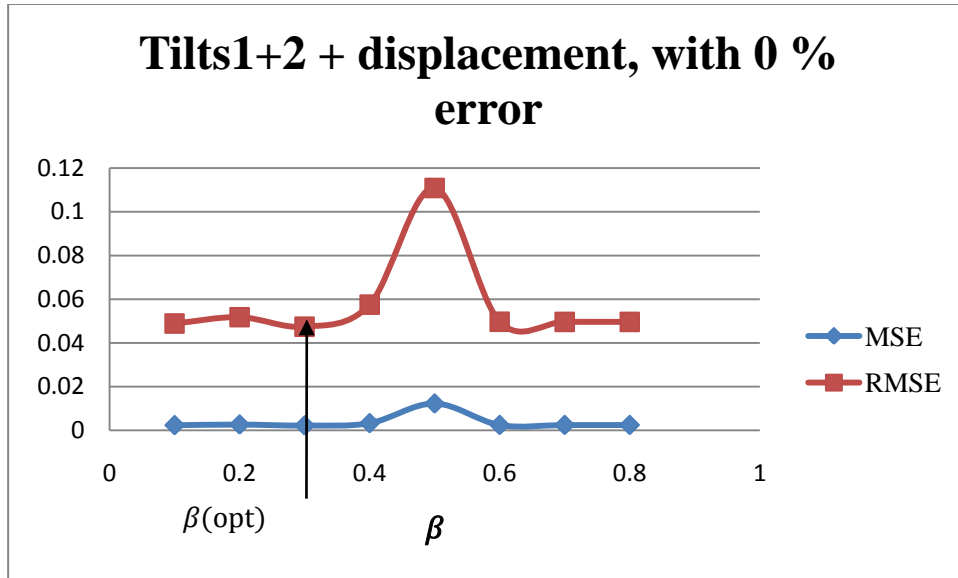
Figure 60: MSE and RMSE for different values of βs: Case33.

Table 15 summarises the results of cases 30, 32, and 33, which have the same geometry and benchmark distribution in 2 rows crossing at the centre of the reservoir, but differ with respect to the number of points.

Table 15: Comparison of the results of cases 30, 32,and 33.

Case	%error	No. of observation points	Distribution of points in two rows	β_{opt}	MSE_{min}	$RMSE_{min}$
30	0%	100	2 rows crossing at the centre of the reservoir	0.6	0.00179	0.042306
32	0%	50	2 rows crossing at the centre of the reservoir	0.4	0.001871	0.043257
33	0%	10	2 rows crossing at the centre of the reservoir	0.3	0.002247	0.047407

As expected, using more points would result in a better resolution.

6.8 The effect of the presence of error in the data combined with the omission of observation points

Thus far, error and the omission of a number of observation points, which limits the input data, have been examined separately in order to determine the separate effect of each of these factors on the resolution. In this section the effect of the combination of error and also data limitation is studied.

6.8.1 Error of 10 %

For the following cases, tilts1+2 from each observation point were used as input data and a random error of 10 % of the maximum tilt value that was calculated in the observation grid was added to each input data set for the back-calculation. The results using different distributions of the benchmarks are also presented in this section.

6.8.1.1 Case 34:

For case 34, 1000 points were distributed in two rows crossing at the centre of the reservoir in the following range:

$$\begin{cases} X_{obser} = 250 \\ -500 \leq Y_{obser} \leq 1000 \end{cases}$$

$$\text{and} \begin{cases} Y_{obser} = 250 \\ -500 \leq X_{obser} \leq 1000 \end{cases}$$

The results were as shown in Figure 61.

$$\beta_{opt} = 0.9, MSE = 0.10127, \text{RMSE} = 0.318229$$
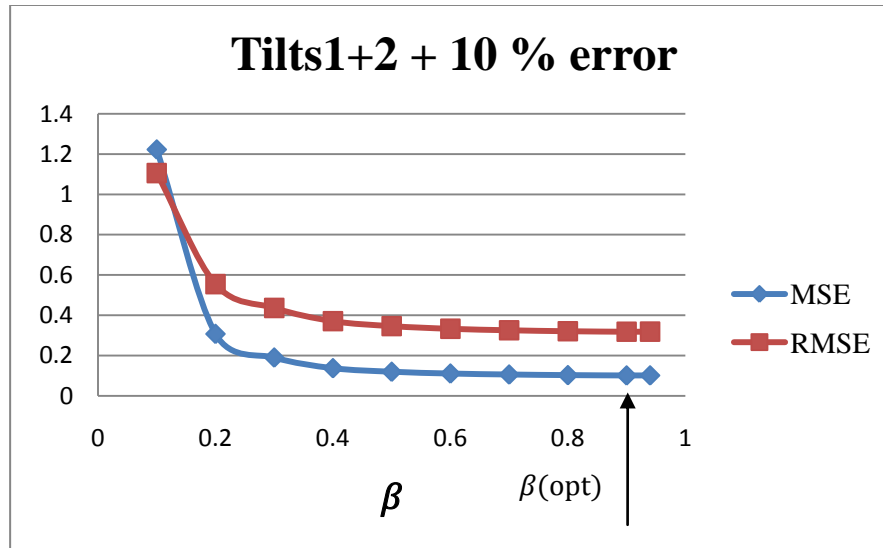
Figure 61: MSE and RMSE plotted against β: Case 34.

6.8.1.2 Case 35

For case 35, 300 points were distributed in two rows crossing at the centre of the reservoir in the following range:

$$\begin{cases} X_{obser} = 250 \\ -500 \leq Y_{obser} \leq 1000 \end{cases}$$

$$\text{and} \begin{cases} Y_{obser} = 250 \\ -500 \leq X_{obser} \leq 1000 \end{cases}$$

The results of the inverse solution can be seen in Figure 62.

$$\beta_{opt} = 0.8, MSE = 0.108702, \text{RMSE} = 0.3297$$
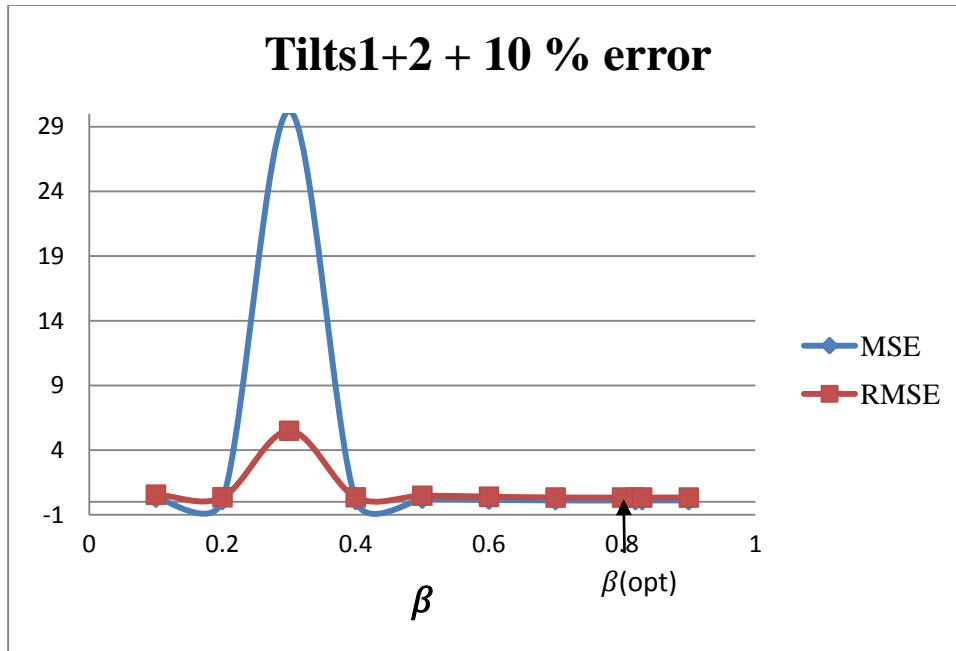
Figure 62: MSE and RMSE for different values of βs: Case 35.

6.8.1.3 Case 36

For case 36, 300 benchmark points are distributed in the area above the reservoir at

$$\begin{cases} X_{obser} = 250 \\ 0 \leq Y_{obser} \leq 500 \end{cases}$$

$$\text{and} \begin{cases} Y_{obser} = 250 \\ 0 \leq X_{obser} \leq 500 \end{cases}$$

The resulting MSE and RMSE plotted against β were as shown in Figure 63.

$$\beta_{opt} = 0.2, MSE = 0.107622, RMSE = 0.328058$$
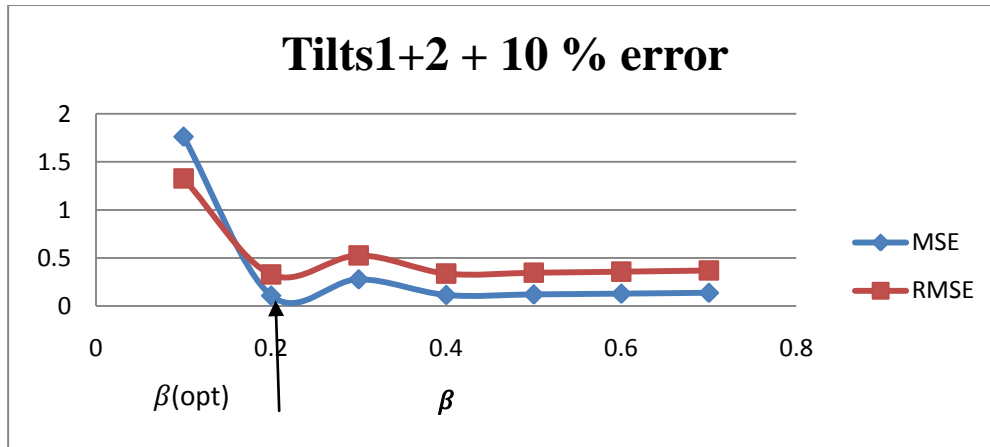
Figure 63: MSE and RMSE for different values of βs: Case36.

6.8.1.4 Case 37

Thus far only one distribution geometry has been considered for the observation points. In case 37, the 300 observation points are distributed in six rows: three vertical and three horizontal, crossing above the centre of the reservoir. Each row has 50 points, one at the centre of each reservoir element in each row. The plan of the observation points above the reservoir elements is shown in Figure 64. The spacing between each row of observation points is 10 metres.
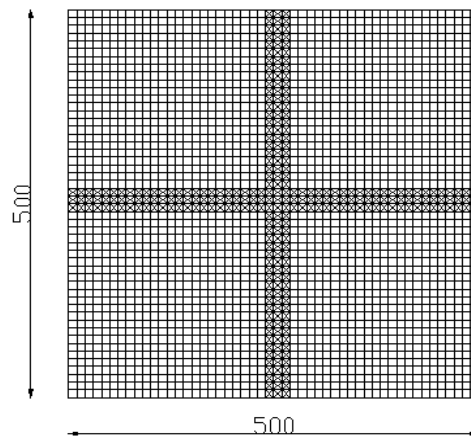
Figure 64: Plan of the reservoir with observation points distributed in three vertical and three horizontal rows crossing above the centre of the reservoir.

The resulting MSE and RMSE plotted against β are shown in Figure 65.

$$\beta_{opt} = 0.1, MSE = 0.084998, RMSE = 0.291543$$
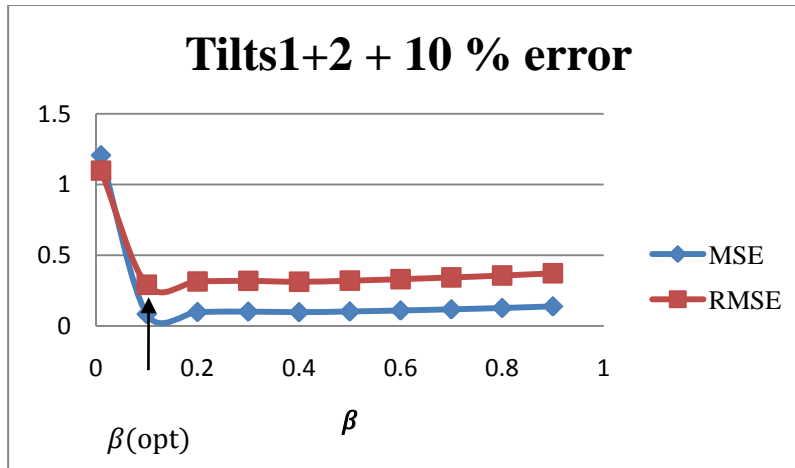
Figure 65: MSE and RMSE for different values of βs: Case 36.

6.8.1.5 Case 38

The same distribution used in case 37 was used for case 38 as well, with the exception that the distance between the rows of observation points was chosen as 100 metres. The observation data are thus spread out further than in the previous case, as shown in Figure 66.
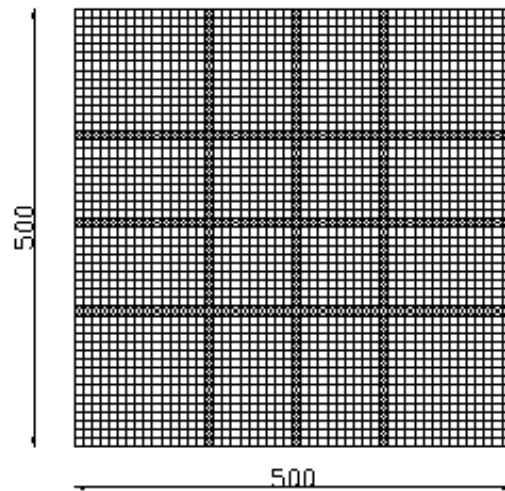
Figure 66: Plan of the reservoir with the observation points distributed in three vertical and three horizontal rows above the reservoir.

The results were as shown in Figure 67.

$$\beta_{opt} = 0.1, MSE = 0.115387, \text{RMSE} = 0.339687$$
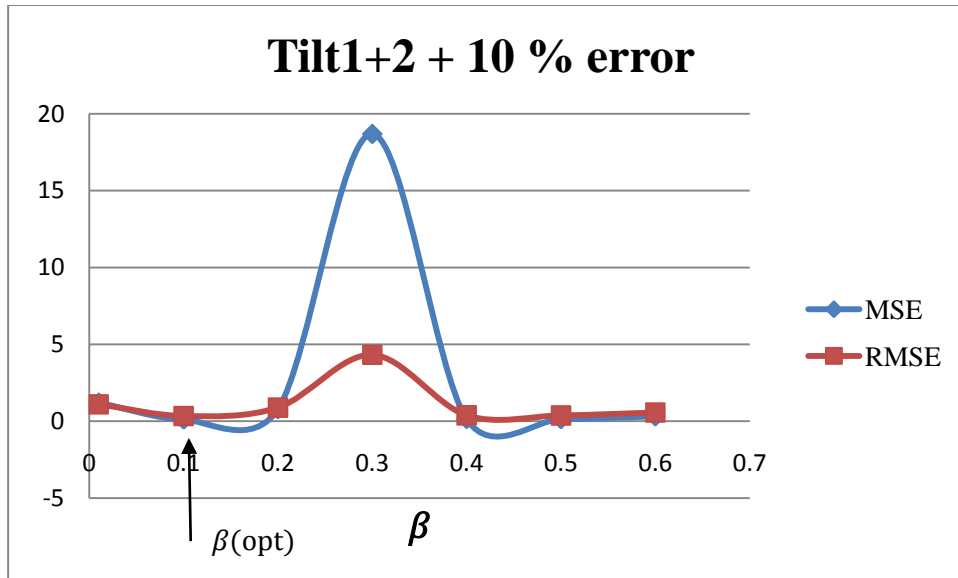
Figure 67: MSE and RMSE for different values of βs: Case 38

6.8.1.6 Case 39

For this case, 300 observation points were distributed in 6 vertical rows, with 50 points in each row. The plan of the observation points is shown in Figure 68.
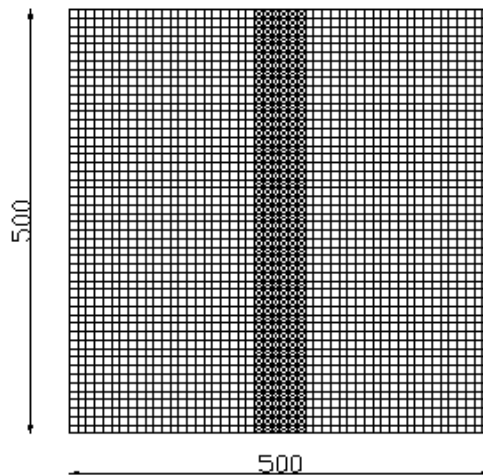
Figure 68: Plan of the reservoir with observation points distributed in six vertical rows above the centre of the reservoir.

The results can be seen in Figure 69.

$$\beta_{opt} = 0.2, MSE = 0.04971, \text{RMSE} = 0.222957$$
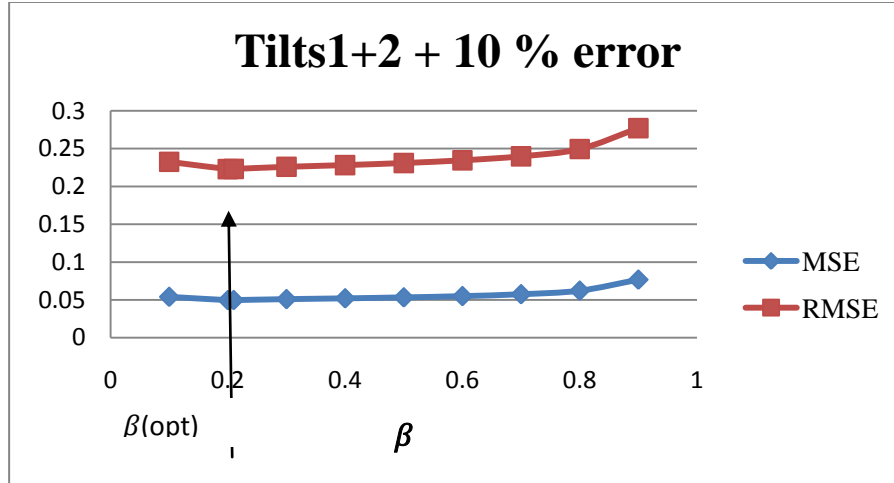
Figure 69: MSE and RMSE for different values of βs: Case 39.

6.8.1.7 Case 40

For this case, 300 observation points were chosen in two vertical rows as shown in Figure 70:

$$\begin{cases} X_{obser} = 245 \\ 0 \leq Y_{obser} \leq 500 \end{cases}$$

$$\text{and} \begin{cases} X_{obser} = 255 \\ 0 \leq Y_{obser} \leq 500 \end{cases}$$
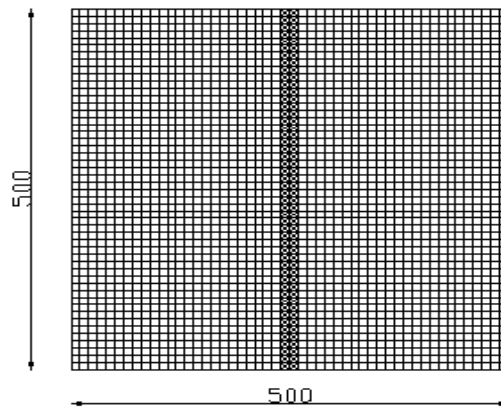
Figure 70: Plan of the reservoir with observation points distributed in two vertical rows above the centre of the reservoir.

The results are shown in Figure 71.

$$\beta_{opt} = 0.3, MSE = 0.073705, RMSE = 0.271487$$

146
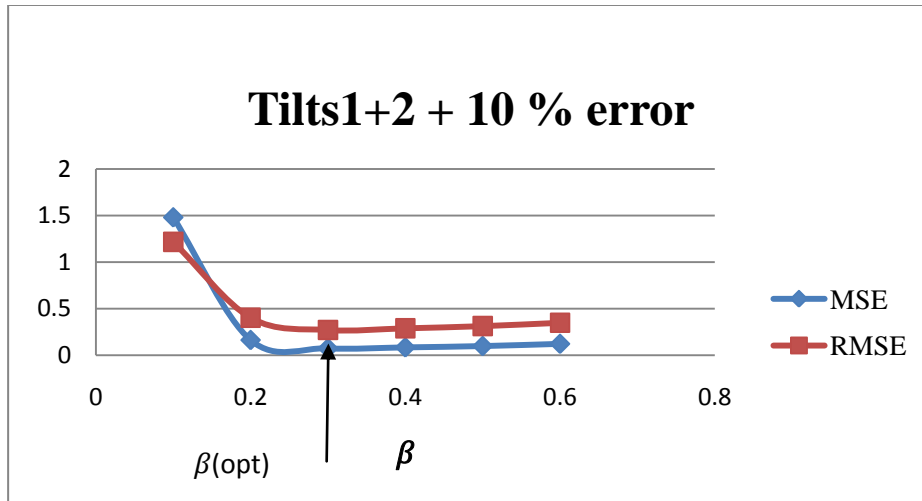
Figure 71: MSE and RMSE for different values of βs: Case 40.

6.8.1.8 Case 41:

In case, 100 points were used as observation points in two rows, with 50 horizontal and 50 vertical points. The results can be seen in Figure 72.

$$\beta_{opt} = 0.2, MSE = 0.140679, \text{RMSE} = 0.375072$$
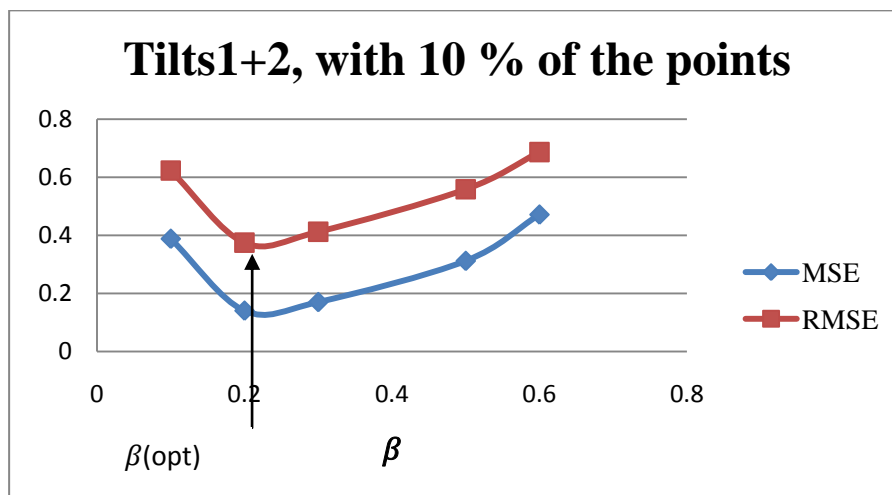
Figure 72: MSE and RMSE plotted against β: Case 41.

As a basis of comparison, the results of the cases considered in this section, with 10% error, are summarised in Table 16.

Table 16: Summary of results with respect to the effect of the number and distribution of observation points along with the error present in the observation data.

		Tilt1+tilt2+10% error			
Case	No. Of observation points	bench mark distribution	β_{opt}	MSE_{min}	$RMSE_{min}$
34	1000	2 rows, 1 vertical, 1 horizontal-500,1000	0.9	0.10127	0.318229
35	300	2 rows, 1 vertical, 1 horizontal-500,1000	0.8	0.108702	0.3297
36	300	2 rows, 1 vertical, 1 horizontal - 0,500	0.2	0.107622	0.328058
37	300	6 rows, 3 vertical, 3 horizontal, 10 m spacing between rows - 0,500	0.1	0.084998	0.291543
38	300	6 rows, 3 vertical, 3 horizontal, 100 m spacing between rows -,0,500	0.1	0.115387	0.339687
39	300	6 vertical rows, 10 m spacing between rows - 0,500	0.2	0.04971	0.222957
40	300	2 vertical rows, 10 m spacing between rows -,0,500	0.3	0.073705	0.271487
41	100	2 rows, 1 vertical, 1 horizontal - 0,500	0.2	0.140679	0.375072

As can be seen, using 300 points, in case 39, results in a much better resolution than does using 1000 points in case 34. The importance of the geometry of the benchmarks chosen can be seen by comparing the results presented in Table 16.

If cases 35 and 36 are compared, the MSE in case 35 is a bit higher than in case 36 but still very close. However, volume change distribution graphs (Appendix V includes the complete graphs) for the two cases show totally different results. The graphs for Case 35 are better approximation of the initial volume (Figure 73).

The MSE or RMSE alone are not sufficient factors for evaluating the solutions. Another shape factor thus must be developed in order to describe the differences in the graphs of the inverse solutions.
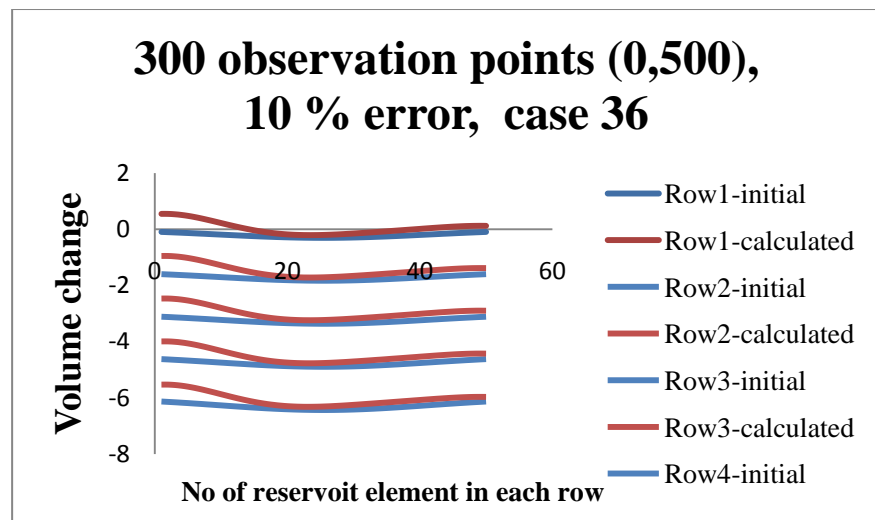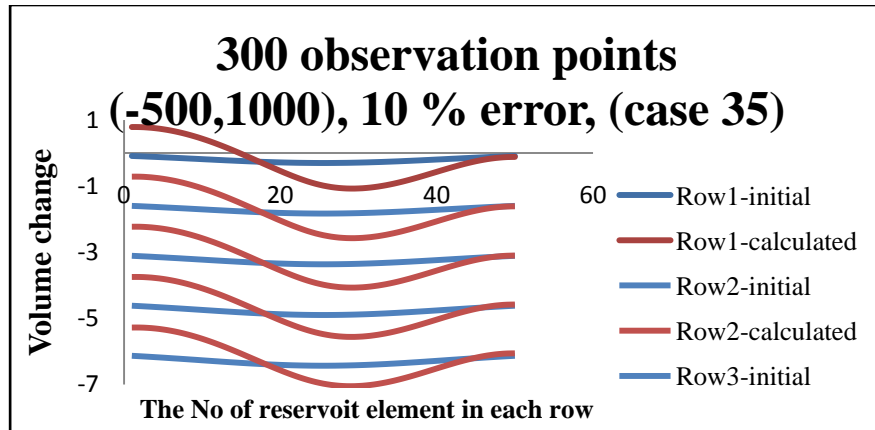
Figure 73: It can be seen although MSE being very close, the distribution is totally different.

6.8.2 Case of 5% error

6.8.2.1 Case 42

As can be seen from Table 16, it can be concluded that the best distribution of observation points is vertical placement in one direction, which in this study was the case that with 6 vertical rows of benchmarks, each row being placed above the centre of the reservoir elements, with distances equal to the sizes of the reservoir elements. This distribution was therefore considered for case 42 as well, and 300 observation points with the same reservoir geometry and initial volume changes were assumed. The error considered was 5 % of the maximum value of the calculated tilt, and this error was added to tilts. This data was then used as input for the back-calculations. The results are as shown in Figure 74.

$$\beta_{opt} = 0.1, MSE = 0.013457, \text{RMSE} = 0.116004$$
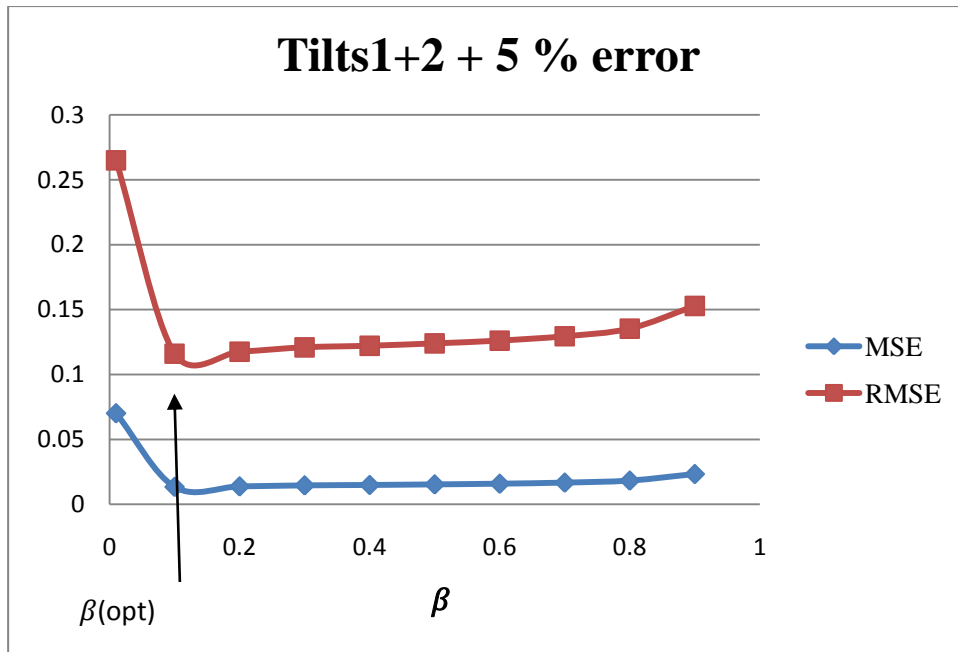
Figure 74: MSE and RMSE for different values of βs: Case 42.

6.8.3 Case of 3 % error

6.8.3.1 Case 43

All input and geometry are identical to those for case 42. Only a 3 % random error is added to the tilts at each observation point. The results of the inverse solution can be seen in Figure 75.

$$\beta_{opt} = 0.2, MSE = 0.006455, \text{RMSE} = 0.080343$$
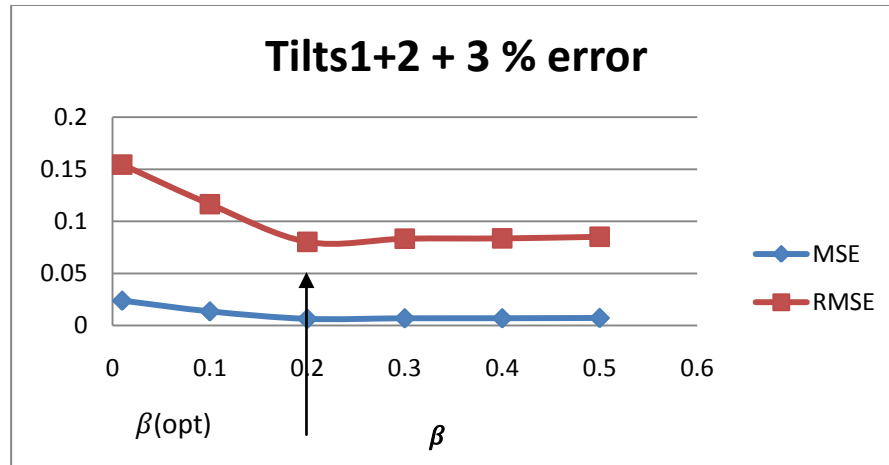
Figure 75: MSE and RMSE plotted aginst β: Case 43.

Table 17 provides a summary and comparison of the results of investigating the sensitivity of the calculation to error with a limited number of observation points. The number of observation points chosen was 300, which is only 12 % of the unknowns to be solved for. The results are listed for different percentage of error.

Table 17: Comparison of results: the effect of error for the best benchmark distribution

Case	Error	Number of observation points	Benchmark distribution	β_{opt}	MSE_{min}	$RMSE_{min}$
39	**10%**	300	6 vertical rows, distance between rows 10 m- 0,500	0.2	0.04971	0.222957
42	**5%**	300	6 vertical rows, distance between rows 10 m- 0,500	0.1	0.013457	0.116004
43	**3%**	300	6 vertical rows, distance between rows 10 m- 0,500	0.2	0.006455	0.080343

From Table 17 and a comparison of the graphs of the cases provided in the Appendix V, it can be seen that in the case with an error of 10 % for 300 benchmarks (12% of the number of unknown values), the results of the calculations vary significantly relative to the actual assigned values. In the case with an error of 5 %, however, the graphs show better calculated values compared to those for the 10 % error. With respect to the 3 % error, the results are quite acceptable, and the graphs show a suitable distribution of the changes in volume.

6.8.4 20 observation points with 1 % error: case 44

In reality, using 300 points as observation points, which means using 300 tilt meters to observe the deformations using tilts, is not practical. Therefore, in this section, 20 observation points were chosen, placed in 4 rows of 5 with a spacing of 20 m and located in the mid-section of the reservoir, as shown in Figure 76.
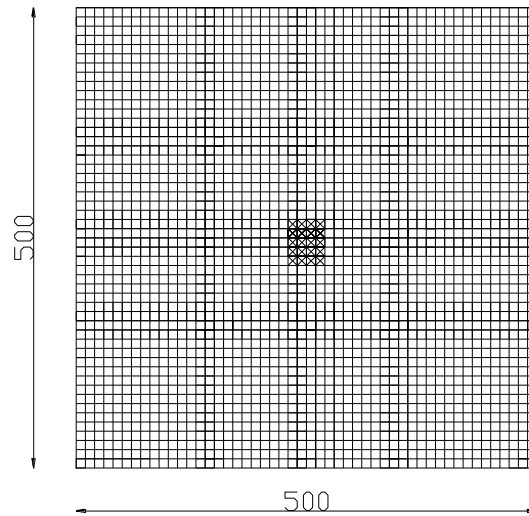
Figure 76: Observation grid of 20 points.

The resulting volume changes compared to the initial assumed volume changes across each row in the reservoir for the first six rows and also for rows 25 to 30 are illustrated in Figure 77 and 78.
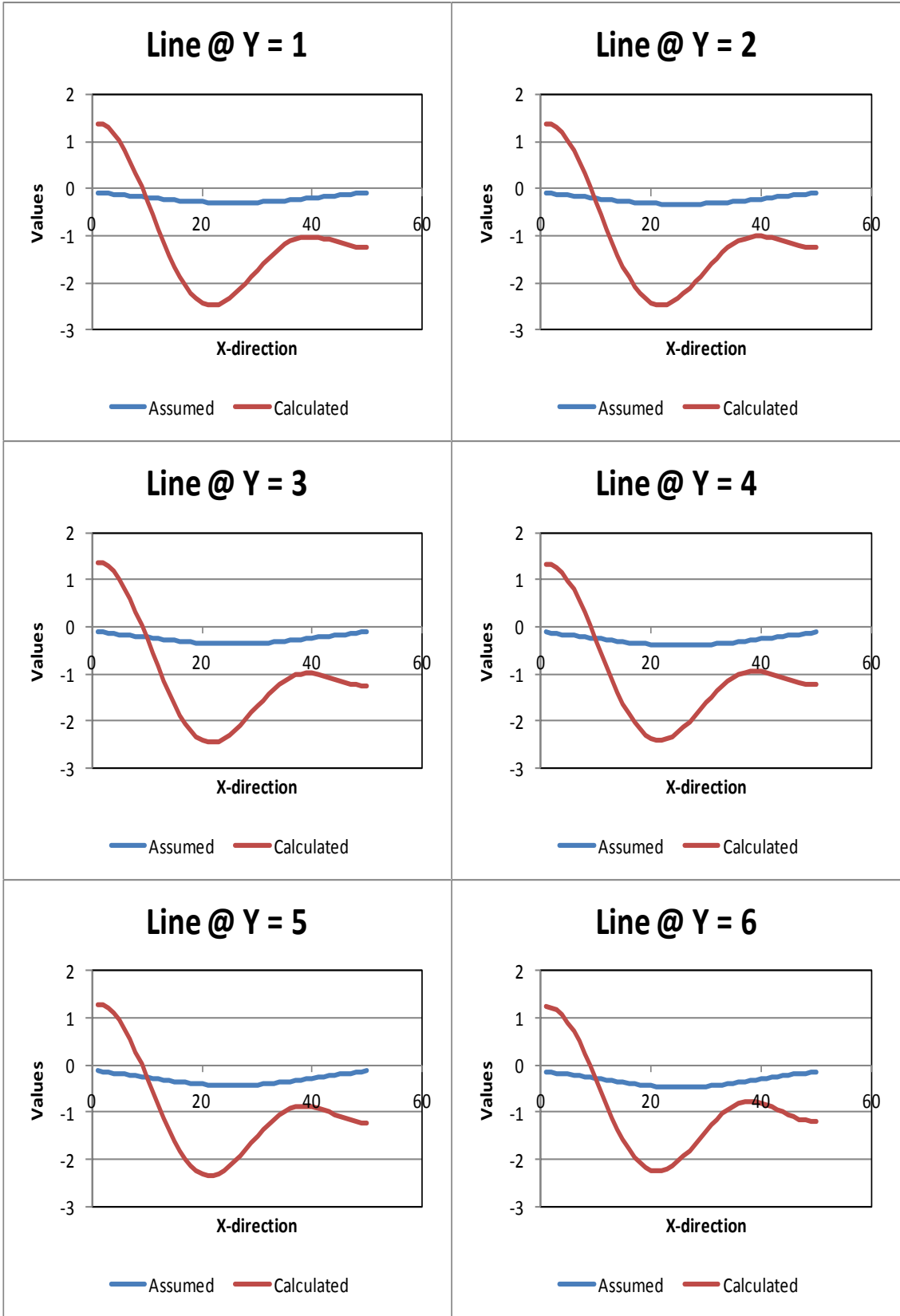
Figure 77: Δv for the first six rows of the reservoir; Case 44.

153
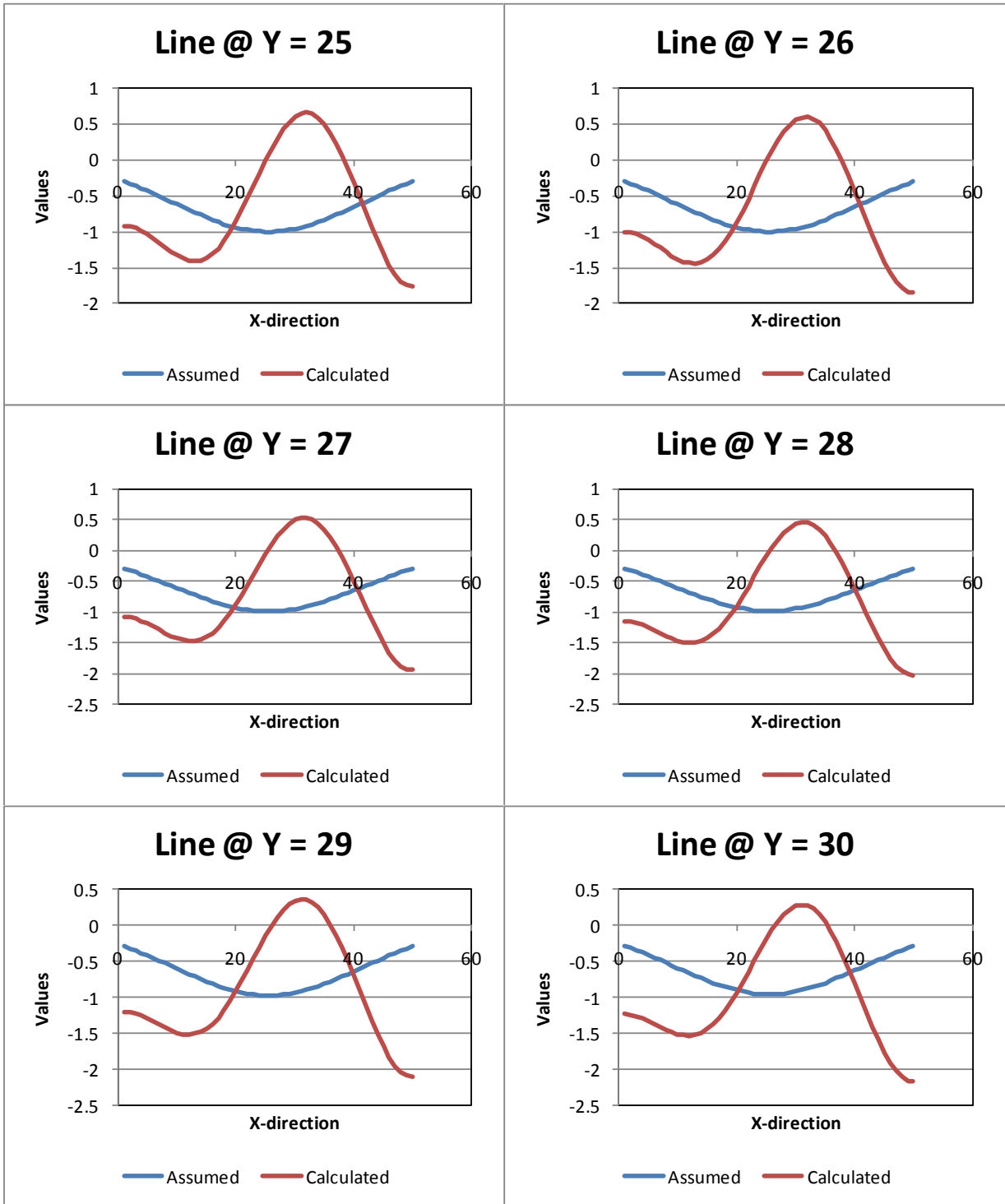
Figure 78: Δv for the rows 25 to 30 of the reservoir; Case 44.

It could be seen that using 20 points with only a 1 % error would not result in an acceptable remodelling. Therefore, since errors are always present in data, the number of observation points affects the results of the reconstructed values more significantly.

7.0 Conclusions

A numerical model for calculating surface deformations due to volumetric changes in a reservoir has been developed as the first part of this study. However, the main focus is on the solution of the inverse case, for which a computer code has been developed in C++ (1080 lines).

The computer codes written for the direct and the inverse cases have been verified. The direct case was verified using a checklist of numerical calculations as presented by Okada (1985). With respect to the inverse case, the results from the inversion of the direct solutions with 0 % error are used for the reconstruction of volume changes.

The calculations for these models are all based on generic subsurface changes in volume; the results can thus be applied to a variety of applications and types of reservoirs (e.g., hydrocarbon, underground water, geysers, waste reinjection projects, steam injection). The following summary and conclusions from the cases investigated are valid for all types of reservoirs:

- The RMSE of back-calculated changes in volume compared to the initial assumed values plotted for different reservoir elements shows fluctuations at some reservoir points and not at other points. The RMSE is much higher for the corner rows than for the middle rows. Thus, the inverse solution is poor for corner elements.
- For the case of the parameter $\beta=0$ (no regularization), the greater the depth of the reservoir, the more ill-conditioned the problem becomes Thus, for very shallow depths, the problem tends to be well-posed.
- Tilt measurements are more effective than vertical displacement measurements for inverting reservoir volumetric changes in the reservoir that occur at different depths.
  - ➢ For the case of tilt measurements with no errors, the computed RMSE value is smaller than the computed value for vertical displacements (by about 12 % in the case studied).
  - ➢ The presence of small errors in the measured displacement data (<0.55 % of the maximum surface displacement) generates significant deviations in the solution from the actual value. However, for tilt measurements with errors of up to 20 %

of the maximum tilt value, a reasonable reconstruction of the original volume changes is possible. It should be noted that an error of 10 % is considered reasonable for tilt measurements. Therefore, it is recommended that tilt measurements rather than vertical displacements be used as input data.

➢ The required area of observation can be reduced if tilt measurements are used, which would make the setup process for collecting experimental data more convenient.

- The predictions of changes in volume when tilt1(dz/dx) is used as input versus those generated when tilt2(dz/dy) is used as input for an identical case are almost identical.

- The best deformation data to be used as input were found to be Tilt1+Tilt2 together.

- Based on sensitivity analysis, when used as input data, displacement data were found to be much more sensitive to error than tilts are.

- For an error of zero, when tilts are used, very good resolution is obtainable using only 0.4 % of the number of unknowns as the number of benchmarks. That is, using only 10 observation points in the case of solving for a reservoir with 2500 elements (2500 unknowns to be solved) resulted in an acceptable reconstruction.

- Errors in the input data are more influential than the number of observation points for inverse solutions.

- The distribution of benchmark points significantly affects the results. The best distribution of benchmarks was found to be a parallel set of rows. The optimal spacing resulting in the solution with the highest resolution was found to be equal to the sizes of the elements in the reservoir.

- In some cases, although the RMSE of the results are very similar, the plots of the changes in volume change are different. Thus, it is of great importance to analyze the distribution of volume changes in order to provide an understanding of the behaviour of the reservoir during reinjection or production projects.

8. Future work and recommendations

- The consolidation of soils and the development of deformations usually takes time. How long is required for the entire deformation to be transferred to the surface depends on the overburden material, the history of the formation, and other factors. Thus the induced subsidence or upheaval observed on the surface and recorded might not represent the entire extent of the deformation. Therefore, using this data as input for the inverse problem can result in a misleading reconstruction and modeling of the inverse case. For future work, it is suggested that the time factor be considered and investigated for use in the inverse modeling.

- For the numerical modeling in this and most studies, one of the basic assumptions is that the media is isotropic and homogeneous. In reality, this is not the case. For future research, it is recommended that the effect of layering on models and the inverse ill-posed solution be considered and examined.

- Subsurface volume changes can be used to predict earthquakes. Surface deformation data can be recorded for areas above active faults and in zones that have the potential for earthquakes and can then be used to monitor changes in volume that occur in active zones. These changes in volume could possibly be converted to factors that could be helpful in predicting earthquakes.

- The inverse problem in the case of the presence of more than one source of subsurface deformation is also recommended as an area for further study.

References

Allis, R. G. (2000). Review of Subsidence at Wairakei Field, NewZealand. *Geothermics* , 455-478.

Amyx, J. W., Bass, D. M., & Whiting, R. L. (1960). *Petroleum Reservoir Engineering Physical Properties.*

Bilak, R. A. (1989). *Analysis of Surface Deformation Above Hydrocarbon Producing Reservoirs.* Waterloo.

Biot, M. A. (1956). *Appl. phys, 27,240* .

Bruno, M. S., & Bovberg, C. A. (1992). *Reservoir Compaction and Surface Subsidence Above the Lost Hills Field, California,* The 33th U.S. Symposium on Rock Mechanics, 92-0263.

Bruno, M. S., & Co, C. O. (1990). Subsidence-Induced Well Failure. *SPE* , 383-390.

Calhoun, J. (1917). *Fundamentals of Reservoir Engineering.* Norman, University of Oklahoma Press c1960 .

Carnec, C., & Fabriol, H. (1999). Monitoring and Modeling Land Subsidence at the Cerro Prieto Geothermal Field, Baja California, Mexico, Using SAR Interferometry. *Geophysical Research letters*, VOL. 26, NO. 9, Pages 1211-1214, MAY 1, 1999.

Chan, A. W., & Zoback, M. D. (2007). The Role of Hydrocarbon Production on Land Subsidence and Fault Reactivation in the Louisiana Coastal Zone. *Journal of Coastal Research* , 771–786.

Chen, C.-T., Hu, J.-C., Lu, C.-Y., Lee, J.-C., & Chan, Y.-C. (2007). Thirty-Year Land Elevation Change from Subsidence to Uplift Following the Termination of Groundwater Pumping and its Geological Implications in the Metropolitan Taipei Basin, Northern Taiwan. *Engineering Geology* , 30-47.

Chin, L., Boade, R. R., Prevost, J. H., & Landa, G. H. (1993). Numerical Simulation of Shear-Induced Compaction in the Ekofisk Reservoir. *Int. J. Rock Mech. Min. Sci. & Geomech* , 1193-1200.

Cosse, R. (1993). *Oil and Gas Field Development Techniques: Basics of Reservoir Engineering.* Paris.

Das, B. M. (Sixth Edition,2006). *Principles of Geotechnical Engineering.* California.

Du, J., & Olson, J. E. (2001). A Poroelastic Reservoir Model for Predicting Subsidence and Mapping Subsurface Pressure Fronts. *Journal of Petroleum Science and Engineering* , 181–197.

Dusseault, M. B., & Rothenburg, L. (2002). Analysis of Deformation Measurements for Reservoir Management. *Oil & Gas Science and Technology* , 539-554.

Dusseault, M. B., Bilak, R. A., & Rothenburg, L. (1993). Inversion of Surface Displacements to Monitor In Situ Processes. *lnL J. Rock Mech. Min. Sci, & Geomech* , 1219-1222.

Engl, H. W., & Groetsch, C. W. (1987). *Inverse and Ill-posed Problems.* London: Academic Press, INC.

Ferretti, A., Novali, F., & Vasco, D. W. (2008). Reservoir Monitoring and Characterization Using Satellite Geodetic Data: Interferometric Synthetic Aperture Radar Observations from the Krechba field, Algeria. *GEOPHYSICS,VOL. 73* , 113–122.

Galloway, D. L., Hudnut, K. W., Ingebritsen, S. E., Phillips, S. P., Peltzer, G., Rogez, F., et al. (1998). Detection of Aquifer System Compaction and Land Subsidence Using Interferometric Synthetic Aperture Radar, Antelope Valley, Mojave Desert, California. *Water Resources Research* , 2573-2585.

Gambolati, G. (1975). Numerical Models in Land Subsidence Control. *Cmputer Methods in Applied Mechanics and Engineering*, 227-237.

Geertsma, J. (1957). A Remark on the Analogy Between Thermoelasticityand the Elasticity of Saturated Porous Media. *Journal of the Mechanics and Physics of Solids* , 13-16.

Geertsma, J. (1973). Land Subsidence Above Compacting Oil and Gas Reservoirs. *JOURNAL OF PETROLEUM TECHNOLOGY* , 734-744.

Geertsma, J. (1957). The Effect of Fluid Pressure Decline on Volumetric Changes of Porous Rocks. Trans. AIME, 210, 331–340.

Glowacka, E., Gonzalez, J., & Fabriol, H. (1999). Recent Vertical Deformation in Mexicali Valley and its Relationship with Tectonics, Seismicity, and the Exploitation of the Cerro Prieto Geothermal Field, Mexico. *Pure appl. geophys* , 591-614.

Gurevich, A. E., & Chilingarian, G. V. (1993). Subsidence Over Producing Oil and Gas Fields, and Gas Leakage to the Surface. *Journal of Petroleum Science and Engineering* , 239-250.

Hermansen, H., Landa, G. H., Sylte, J. E., & Thomas, L. K. (2000). Experiences After 10 Years of Waterflooding the Ekofisk Field,Norway. *Journal of Petroleum Science and Engineering* , 11-18.

Hu, R. L., Yue, Z. Q., Wang, L. C., & Wang, S. J. (2004). Review on Current Status and Challenging Issues of Land Subsidence in China. *Engineering Geology* , 65– 77.

J. Carlos Santamaria, D. F. (2005). *Discrete Signals and Inverse Problems.*

Kroon, I. C., Nguyen, B. L., Fokker, P. A., Muntendam-Bos, A. G., & Lange, G. d. (2008). Disentangling Shallow and Deep Processes Causing Surface Movement. *International Association for Mathematical Geosciences* .

Nagel, N. B. (2001). Compaction and Subsidence Issues Within the Petroleum Industry: From Wilmington to Ekofisk and Beyond. *Phys. Chem. Earth* , Vol. 26, No. 1-2, pp. 3-14.

Okada, Y. (1985). Surface Deformation Due to Shear and Tensile Faults in a Half-Space. *Bulletin of the Seismological Society of America* , Vol. 75, No. 4, pp. 1135-1154.

Press, W. H., Teukolsky, S. A., Vetterling, W. T., & Flannery, B. P. (1988). *Numerical Recipes in C.* Press Syndicate of university of Cambridge.

Rothenburg, L., Dusseault, M. B., Bilak, R. A., & Bruno, M. S. (1994). Waste Disposal Monitoring Using the Surface Displacement Field. *Society of Petroleum Engineers* , 29-31.

Segall, P. (1985). Stress and Subsidence Resulting from Subsurface Fluid Withdrawal in the Epicentral Region of the 1983 Coalinga Earthquake. J. Geophys. Res., 90, 6801– 6816.

Tikhonov, A. N., & Arsenin, V. Y. (1977). *Solutions of Ill-posed Problems.*

Vardoulakis, I., Vairaktaris, E., & Papamicho, E. (2004). Subsidence Diffusion– Convection: I. The Direct Problem. *Comput. Methods Appl. Mech. Engrg* , 2745–2760.

Vasco, D. W. (2004). Estimation of Flow Properties Using Surface Deformation and Head Data: A Trajectory-Based Approach. *Water Resources Research*, VOL. 40.

Vasco, D. W., Wicks, C. J., Karasaki, K., & Marques, O. (2002). Geodetic Imaging: Reservoir Monitoring Using Satellite Interferometry. *Geophys. J. Int* , 555–571.

Appendix

Appendix I: Calculating the L matrix

Calculating the L matrix

As mentioned in the previous section the problem of solving the ill-posed equation of calculating reservoir volume changes based on surface deformation data came to solving the following equation:

$$[K - \beta L]_{N*N} * [\Delta v \; or \; the \; unknown\;]_{N*1} = [U \; or \; The \; Answer \; matrix]_{N*1}$$

K matrix was described in detail in section4.6. β also is a number chosen between zero and one. Δv the unknown matrix and U is the known matrix from surface deformation data as mentioned in section4.6. In this section calculating the L matrix is of intention. The reservoir can be assumed to be very thin, thus we can deal with the problem as two dimensional. Thus the surface deformation can be written as:

$$\frac{dZ}{ds} = \frac{\partial^2 Ev}{\partial x^2} + \frac{\partial^2 Ev}{\partial y^2}$$

If looking at a one dimensional case, thus the partial derivative would be as follows:

$$\frac{\partial u}{\partial x} = \frac{(u_{i+1} - u_i) - (u_i - u_{i-1})}{\Delta x} = \frac{u_{i+1} + u_{i-1} - 2u_i}{\Delta x}$$

In our case, u_i represents the volume change in the ith reservoir element.

The second derivative with respect to Δx would thus be:

$$\frac{\partial^2 u}{\partial x^2} = \frac{u_{i+1} + u_{i-1} - 2u_i}{\Delta x} * \frac{1}{\Delta x} = \frac{u_{i+1} + u_{i-1} - 2u_i}{\Delta x^2}$$

As for our case which is a two dimensional problem we would have:

$$\frac{\partial^2 u}{\partial x^2} + \frac{\partial^2 u}{\partial y^2} = \frac{u_{i+1,j} + u_{i-1,j} - 2u_{i,j}}{\Delta x^2} + \frac{u_{j+1,i} + u_{j-1,i} - 2u_{j,i}}{\Delta y^2} = 0$$

We are looking at a reservoir grid, where $\Delta x \; and \; \Delta y$ is the grid spacing is two directions. A representative part of reservoir grid is shown as follows:
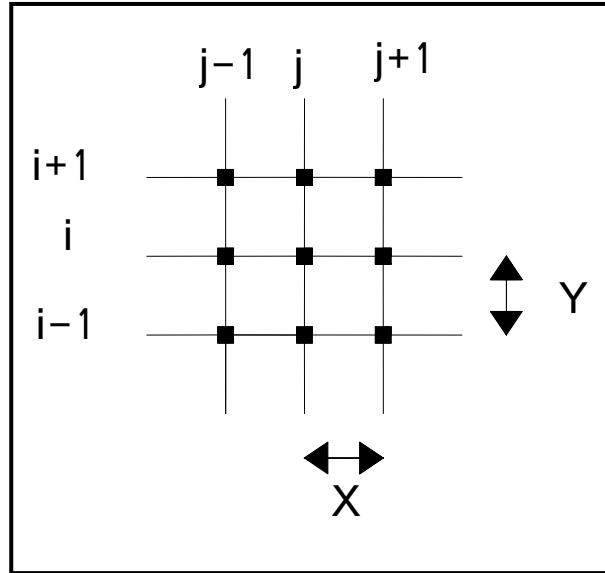
As for a specific case we consider $\Delta x = \Delta y = h$.

For the mid reservoir elements the second derivative can be easily explained using the above equation. For the elements on the corner of the reservoir, we assume that we do have a row of data points outside the grid and their volume changes are assumed to be equal to that of the inside row. See the following example:

A 4*4 reservoir element (N=16) is used to show the procedures of constructing a Laplacian matrix to solve for the inverse ill-posed problem:

163
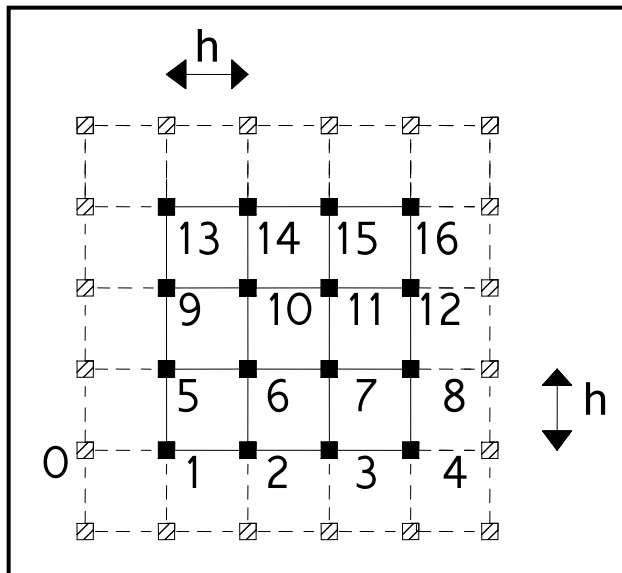
Each point represents a reservoir element's volume change. The dotted rows all around the reservoir grid is the imaginary row of elements with the same volume changes as the one right across and inside. For point 0 for instance, $V_{10} = V_{12}$.

For 1st and 2nd rows the elements for the Laplacian matrix are calculated as follows:

$$For\ point\ 1 = -\frac{v_{15} + v_{15} + v_{12} + v_{12} - 4 * v_{11}}{h^2} = -\frac{2v_{15} + 2v_{12} - 4v_{11}}{h^2}$$

$$For\ point\ 2 = -\frac{v_{21} + v_{23} + v_{26} + v_{26} - 4 * v_{22}}{h^2} = -\frac{v_{21} + v_{23} + 2v_{26} - 4v_{22}}{h^2}$$

$$For\ point\ 3 = -\frac{v_{32} + v_{34} + v_{37} + v_{37} - 4 * v_{33}}{h^2} = -\frac{v_{32} + v_{34} + 2v_{37} - 4v_{33}}{h^2}$$

$$For\ point\ 4 = -\frac{2v_{43} + 2v_{48} - 4v_{44}}{h^2}$$

$$For\ point\ 5 = -\frac{v_{51} + v_{59} + 2v_{56} - 4 * v_{55}}{h^2}$$

$$For\ point\ 6 = -\frac{v_{65} + v_{67} + v_{610} + v_{62} - 4 * v_{66}}{h^2}$$

....

The L matrix formed for a 4*4 reservoir with 16 elements is as follows using the abovementioned procedure. The elements with no numbers have all zero values.

$$[L]_{16*16} =$$

	1	2	3	4	5	6	7	8	9	10	11	12	13	14	15	16
1	$\frac{4}{h^2}$	$-\frac{2}{h^2}$			$-\frac{2}{h^2}$											
2	$-\frac{1}{h^2}$	$\frac{4}{h^2}$	$-\frac{1}{h^2}$			$-\frac{2}{h^2}$										
3		$-\frac{1}{h^2}$	$\frac{4}{h^2}$	$-\frac{1}{h^2}$			$-\frac{2}{h^2}$									
4			$-\frac{2}{h^2}$	$\frac{4}{h^2}$				$-\frac{2}{h^2}$								
5	$-\frac{1}{h^2}$				$\frac{4}{h^2}$	$-\frac{2}{h^2}$			$-\frac{1}{h^2}$							
6		$-\frac{1}{h^2}$			$-\frac{1}{h^2}$	$\frac{4}{h^2}$	$-\frac{1}{h^2}$			$-\frac{1}{h^2}$						
7			$-\frac{1}{h^2}$			$-\frac{1}{h^2}$	$\frac{4}{h^2}$	$-\frac{1}{h^2}$			$-\frac{1}{h^2}$					
8				$-\frac{1}{h^2}$			$-\frac{2}{h^2}$	$\frac{4}{h^2}$				$-\frac{1}{h^2}$				
9					$-\frac{1}{h^2}$				$\frac{4}{h^2}$	$-\frac{2}{h^2}$			$-\frac{1}{h^2}$			
10						$-\frac{1}{h^2}$			$-\frac{1}{h^2}$	$\frac{4}{h^2}$	$-\frac{1}{h^2}$			$-\frac{1}{h^2}$		
11							$-\frac{1}{h^2}$		$-\frac{1}{h^2}$		$\frac{4}{h^2}$	$-\frac{1}{h^2}$			$-\frac{1}{h^2}$	
12								$-\frac{1}{h^2}$			$-\frac{2}{h^2}$	$\frac{4}{h^2}$				$-\frac{1}{h^2}$
13									$-\frac{2}{h^2}$				$\frac{4}{h^2}$	$-\frac{2}{h^2}$		
14										$-\frac{2}{h^2}$			$-\frac{1}{h^2}$	$\frac{4}{h^2}$	$-\frac{1}{h^2}$	
15											$-\frac{2}{h^2}$			$-\frac{1}{h^2}$	$\frac{4}{h^2}$	$-\frac{1}{h^2}$
16												$-\frac{2}{h^2}$		$-\frac{2}{h^2}$	$-\frac{2}{h^2}$	$\frac{4}{h^2}$

Appendix II: Graphs: limiting observation area

Case4, using tilt2, β=0.0000003, RMSE=0.02436, -500<X,Y<1000
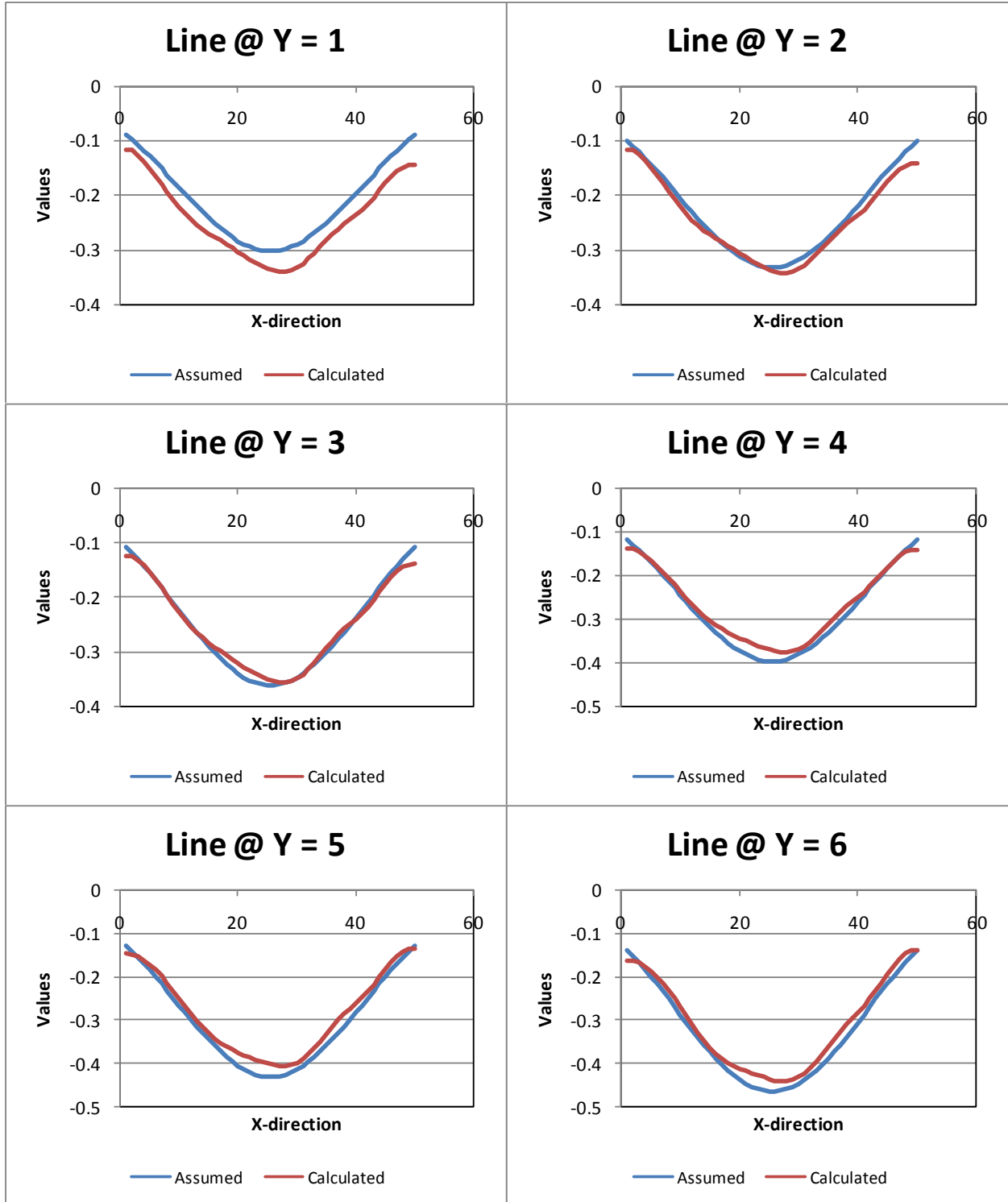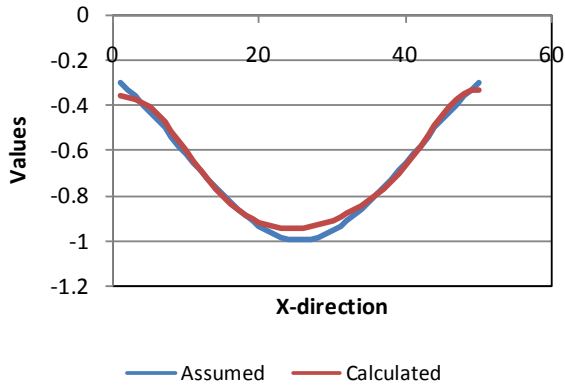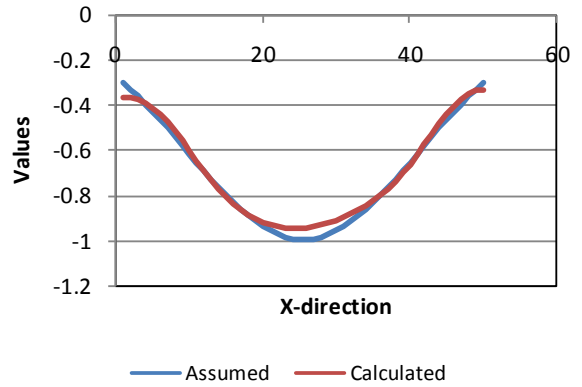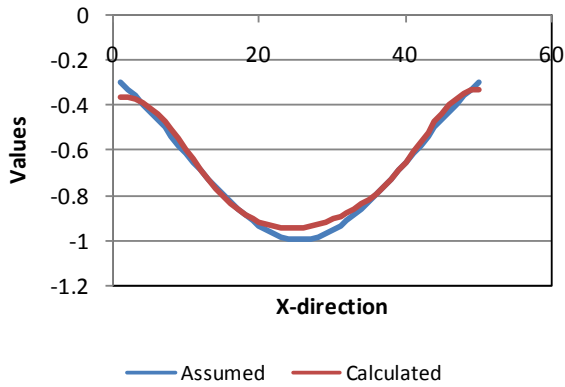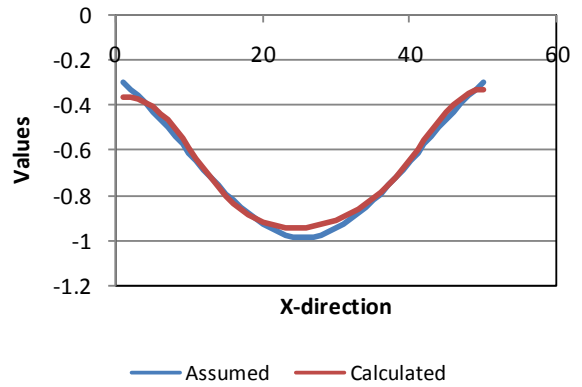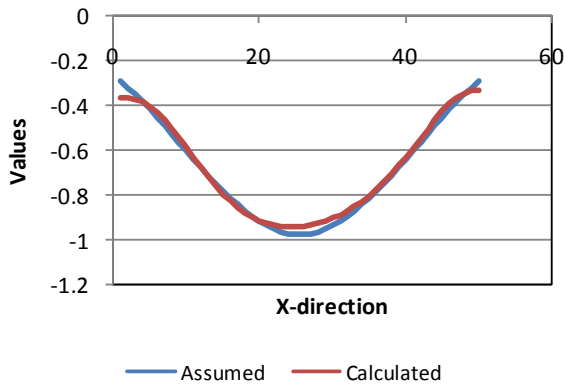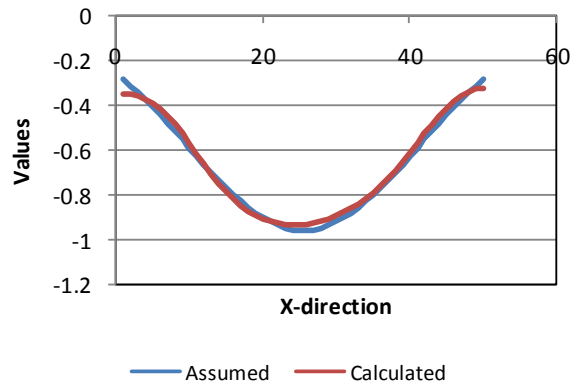
Case7: Using tilt2 as input, 0% error, $-5 \le X_{obser}, Y_{obser} \le 505$
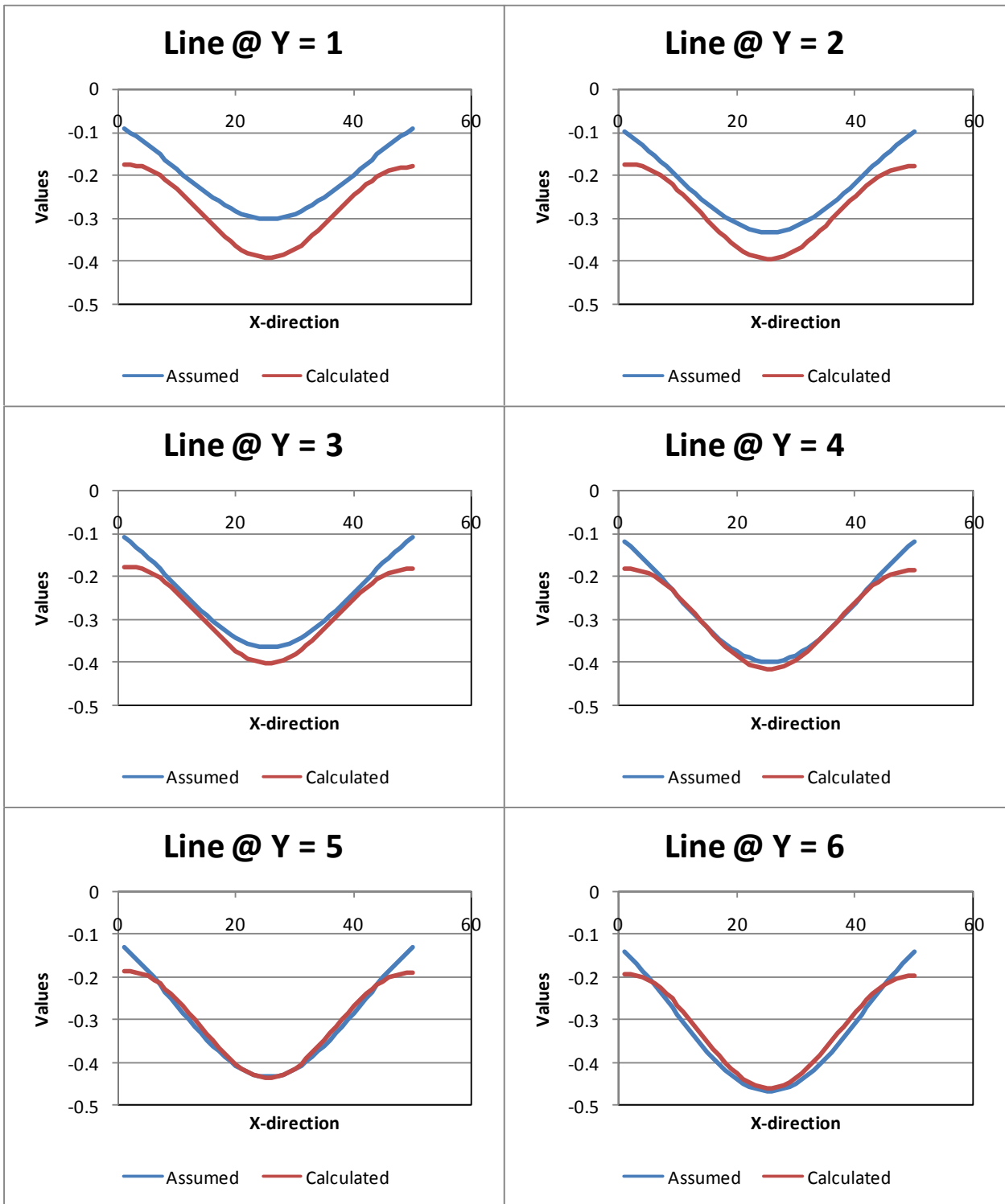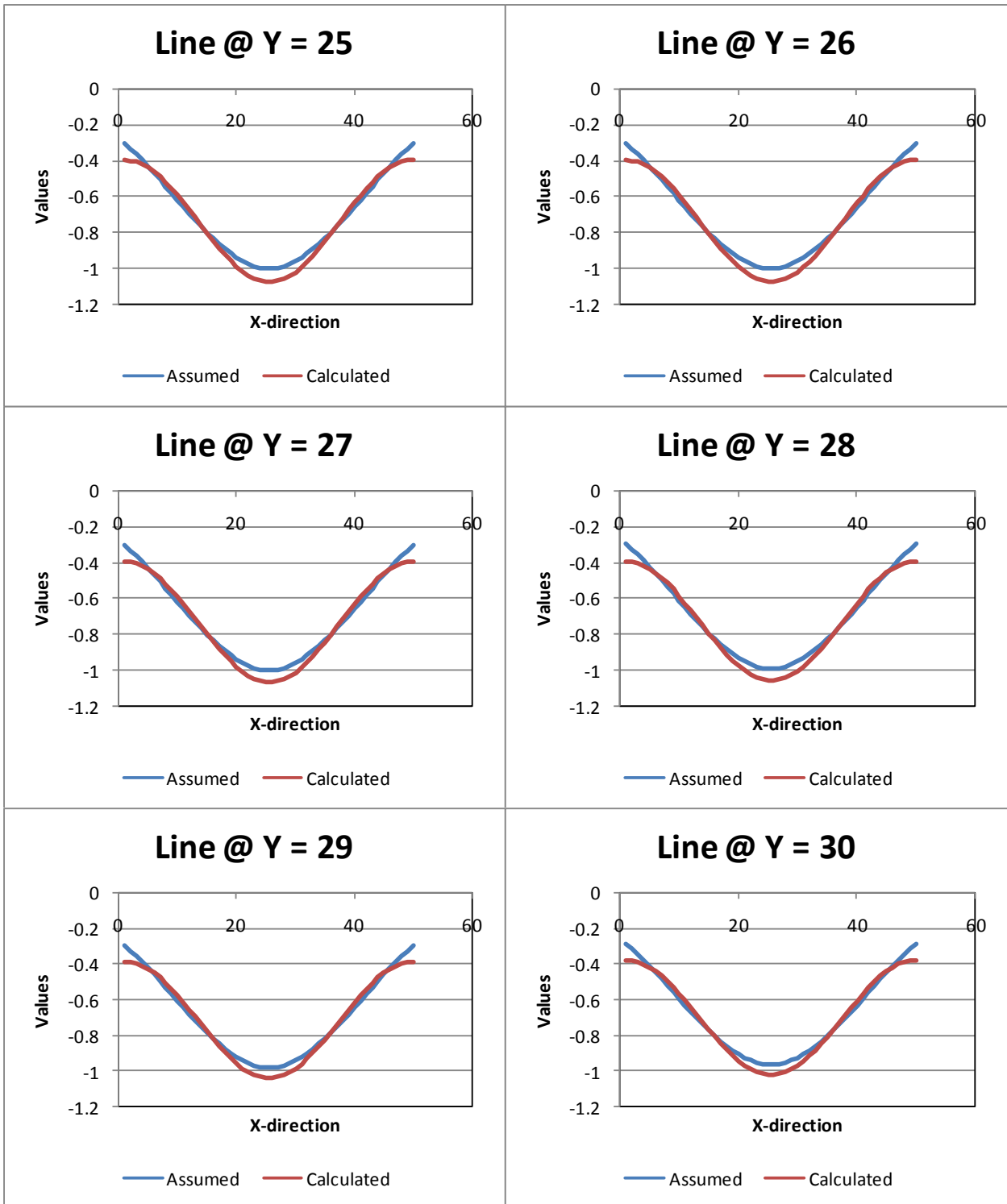
Appendix III: Graphs; error in input data

Case9: Tilt1+2 with 3% error, RMSE=0.26796
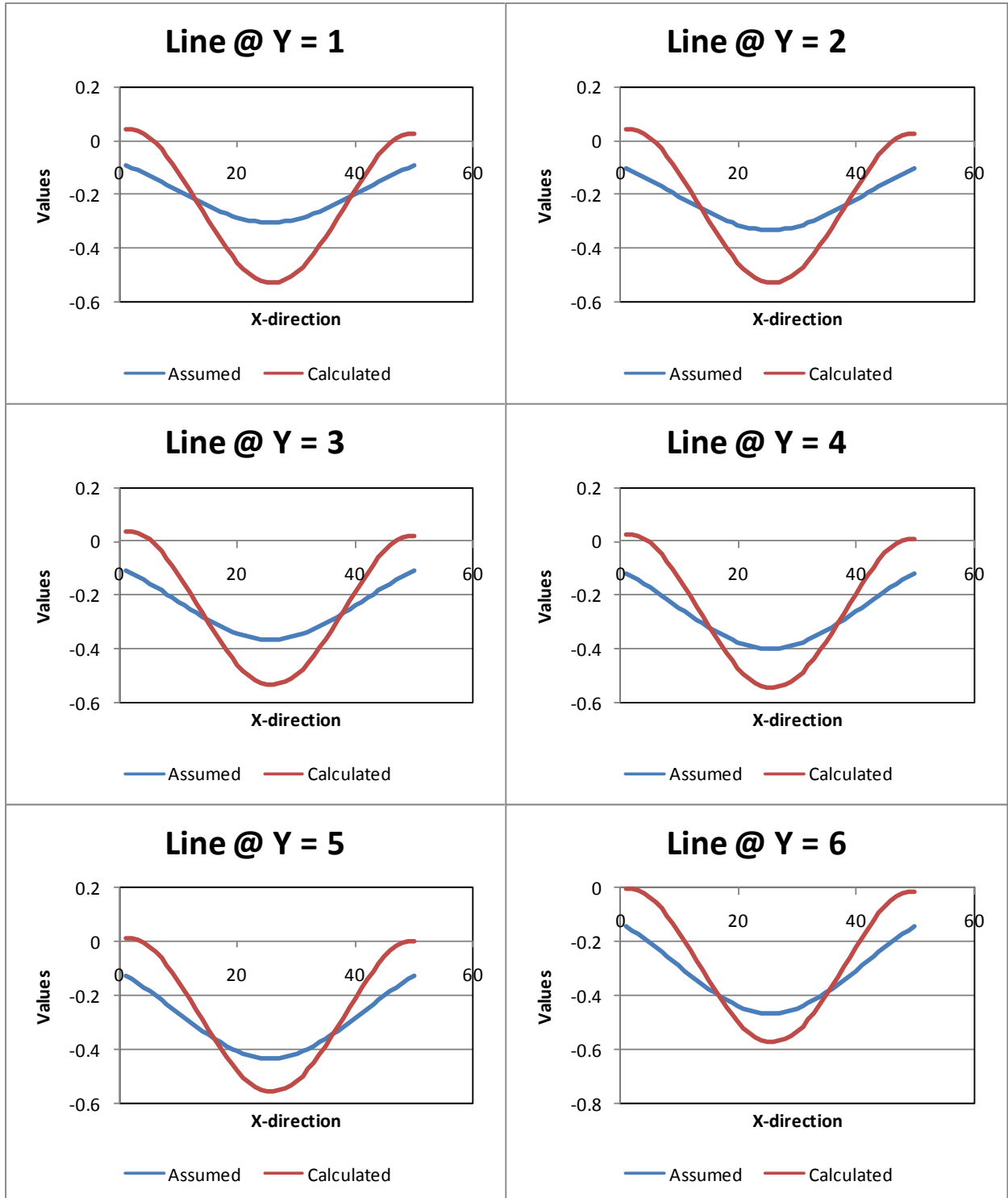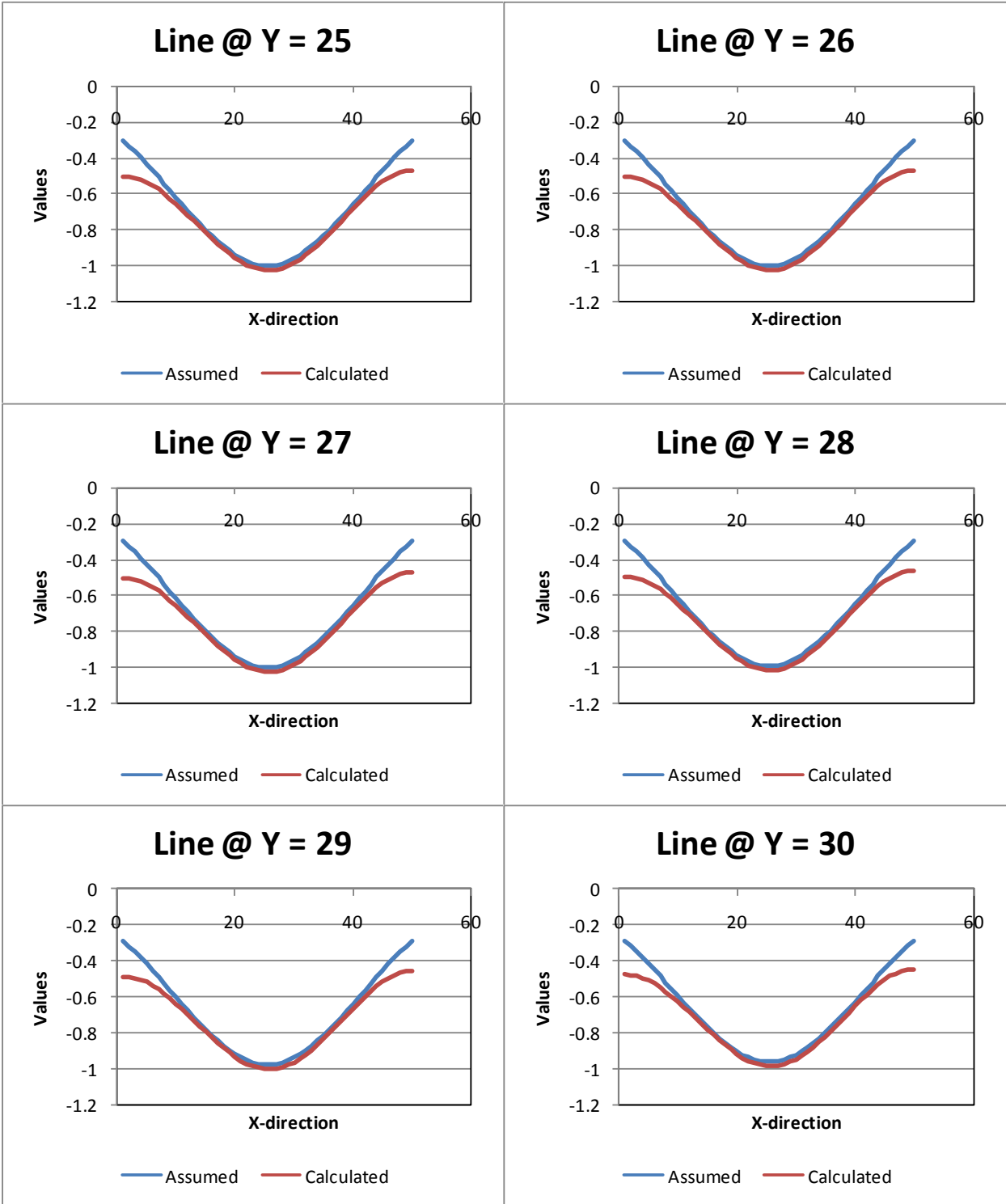
Case10:

Tilt 1&2 with maximum error of 6%   RMSE= 0.0779796
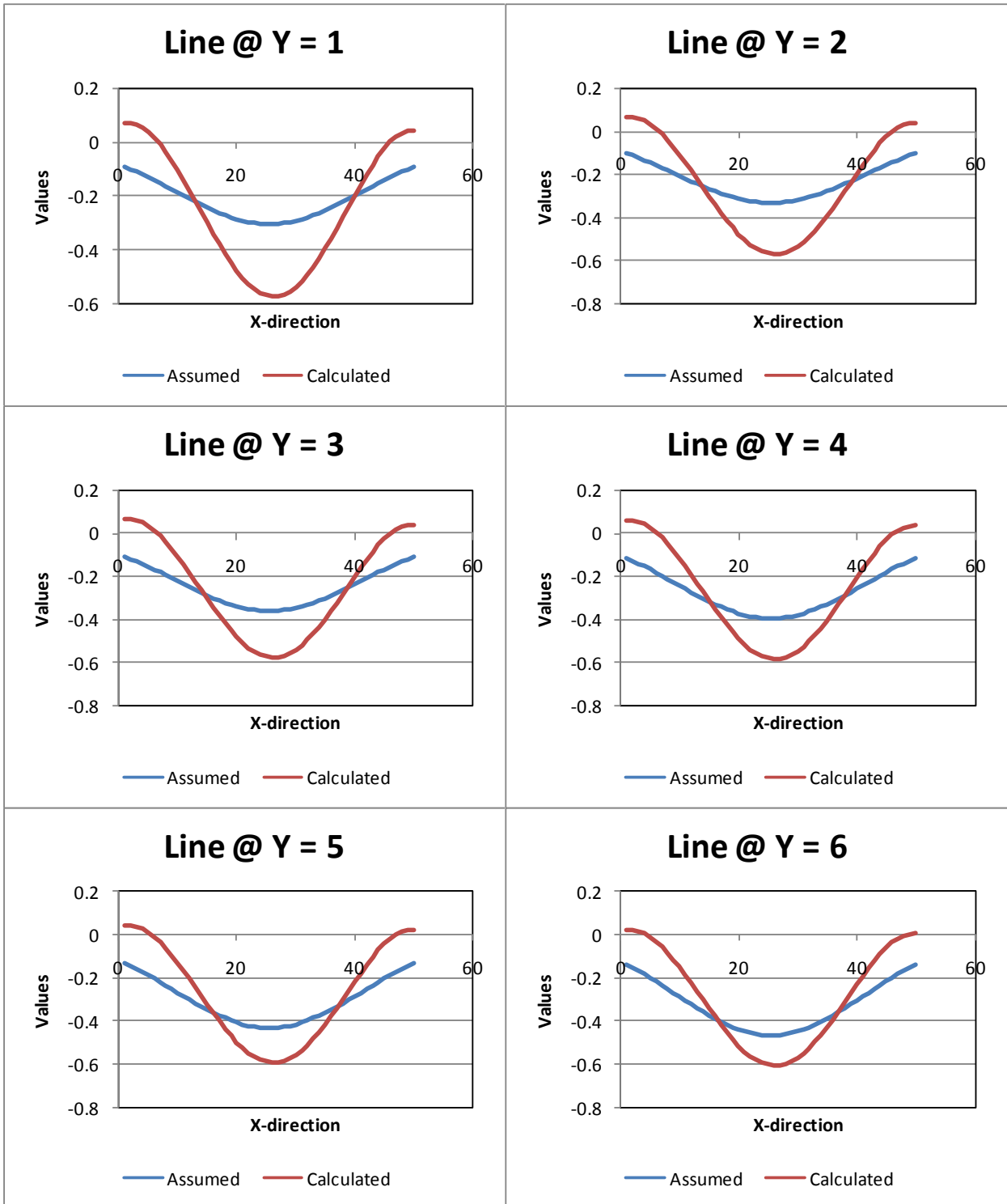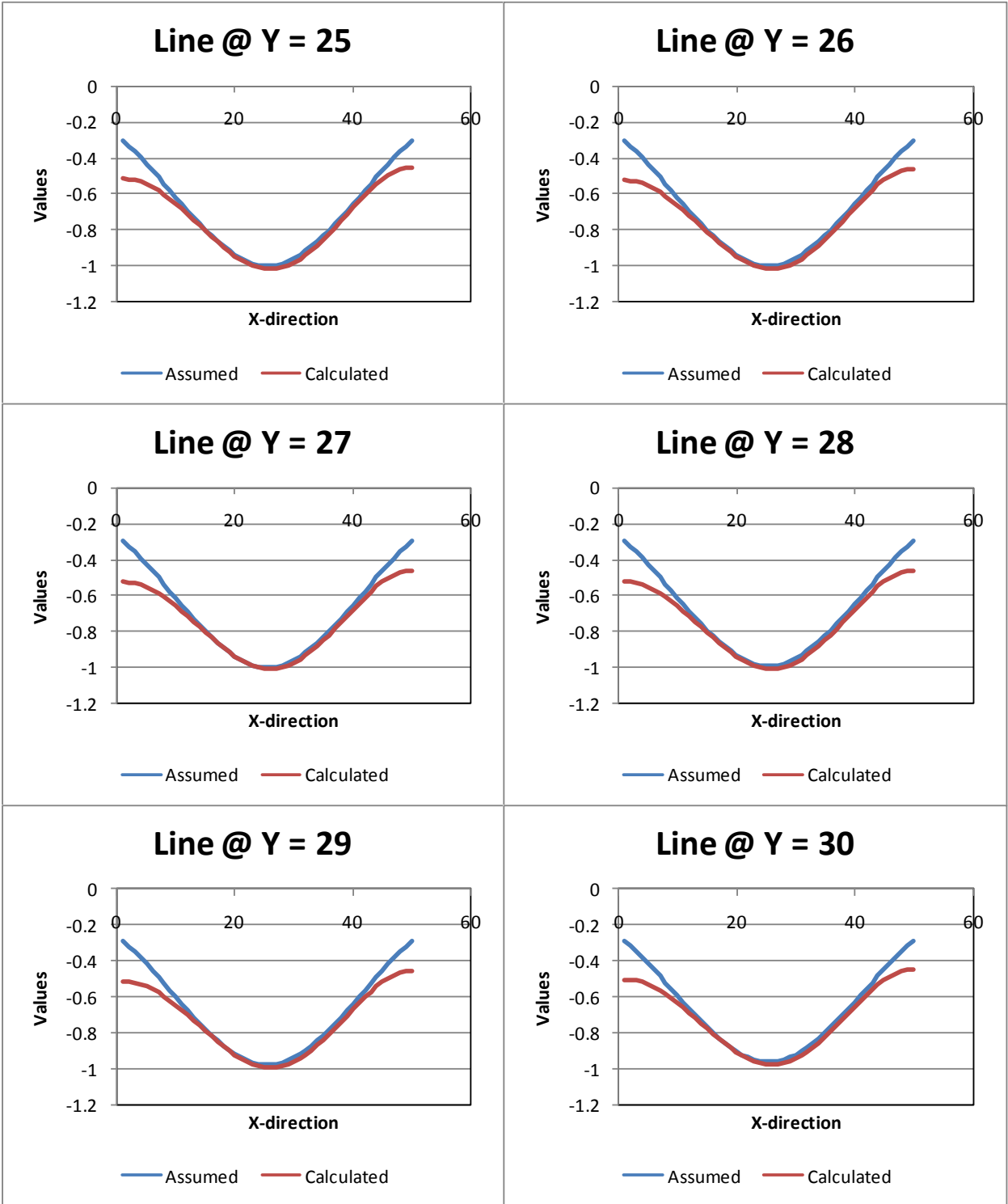
Case11:

Tilt 1&2 with maximum error of 9%   RMSE= 0.0885516
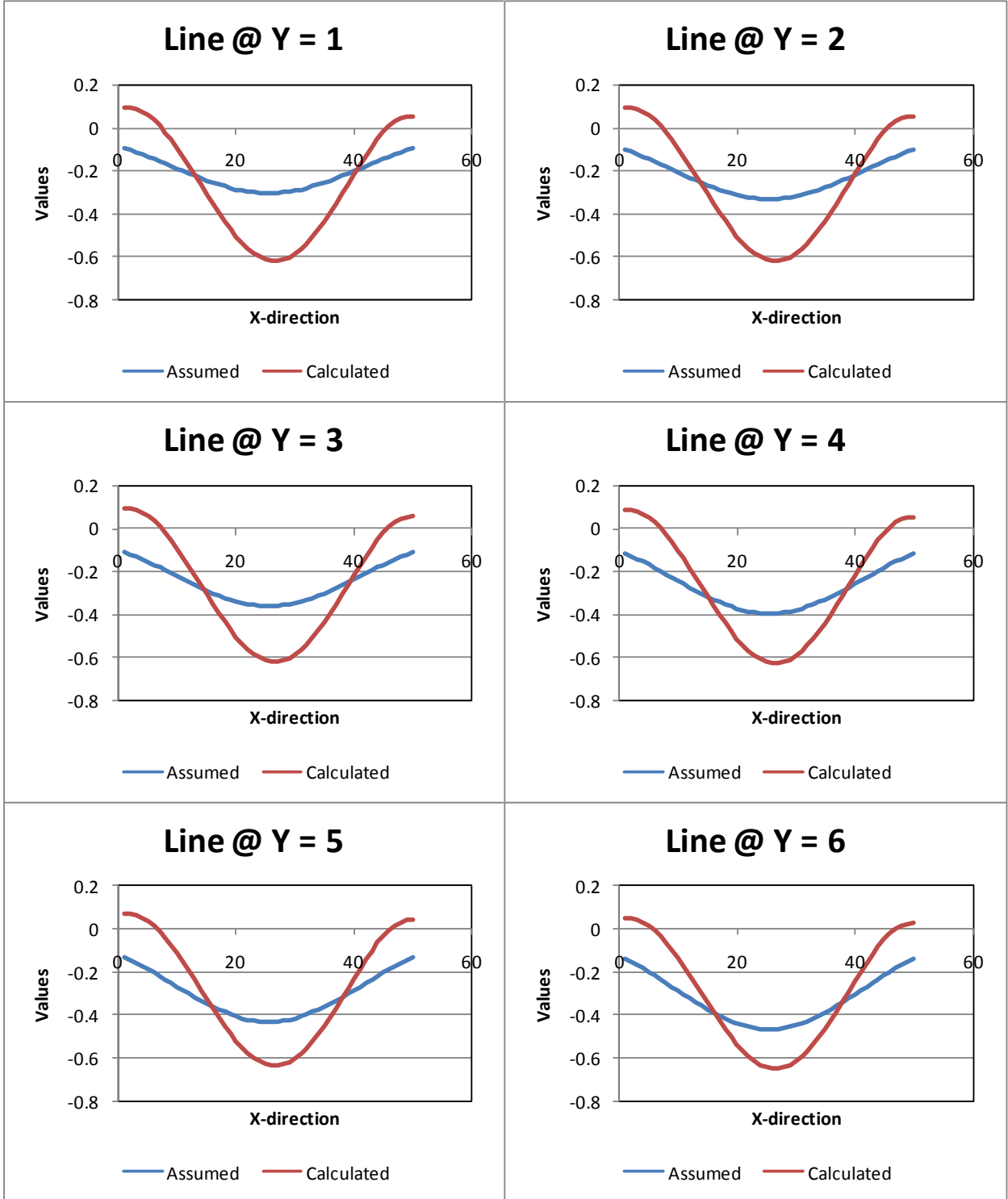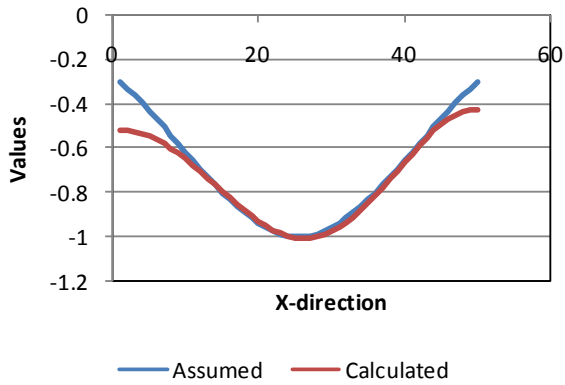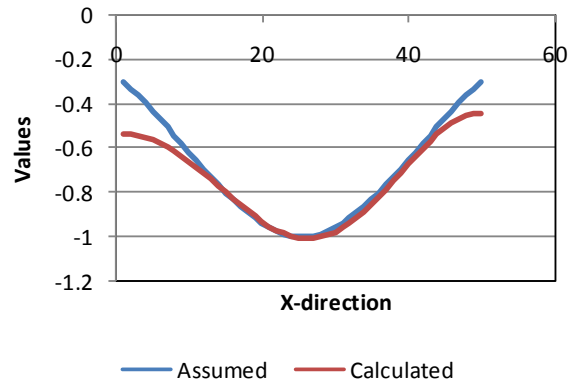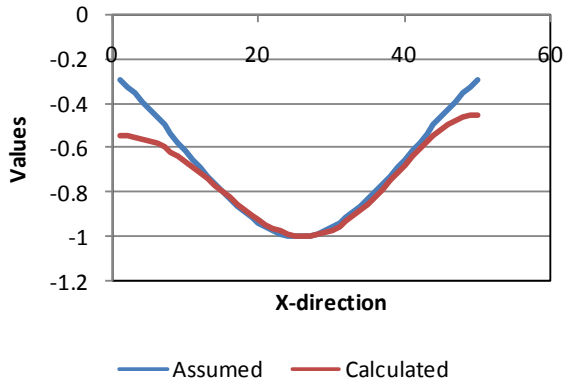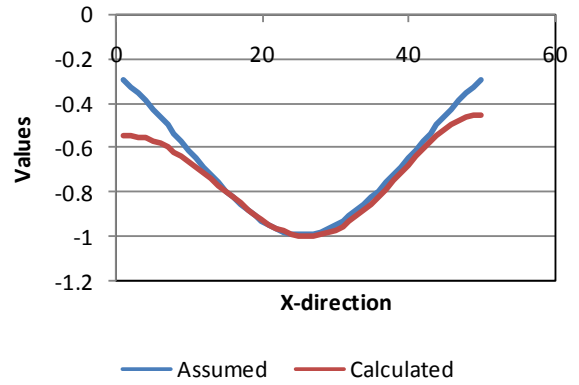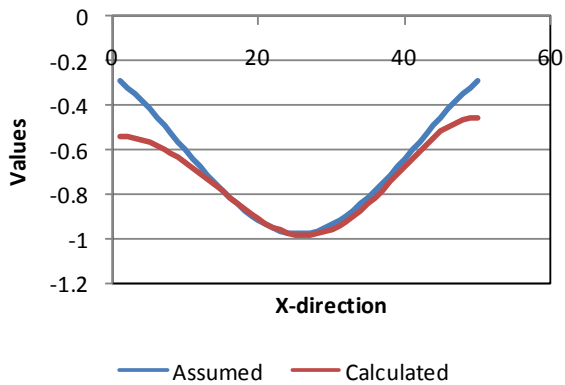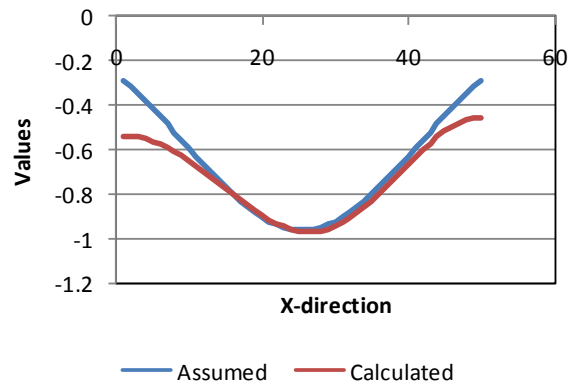
Appendix IV: Graphs; volume change calculations; omitting points:

Case18: Tilt1+2+Displacement, 0% err   omitting 4% data points (100)
RMSE=0.0233846
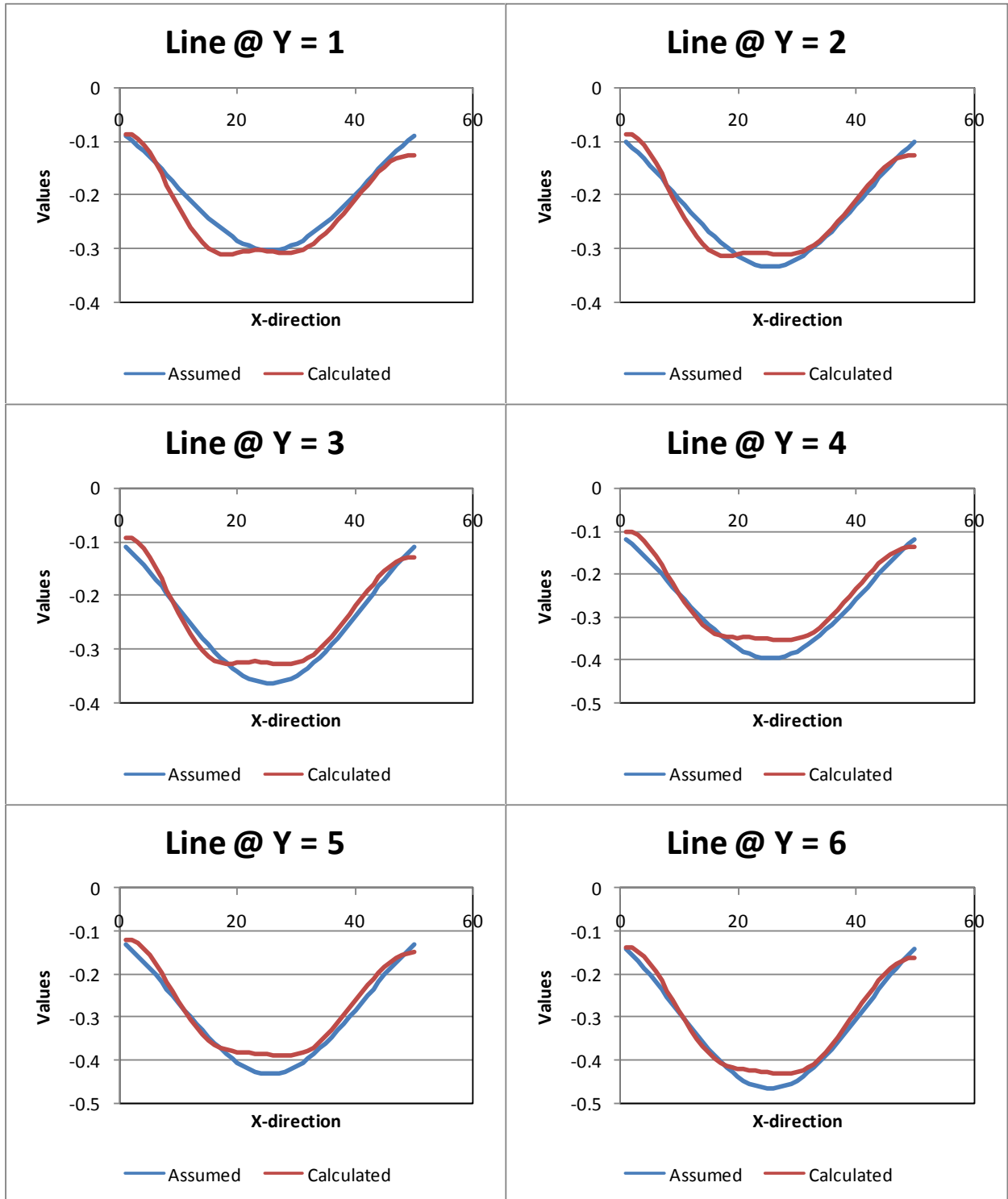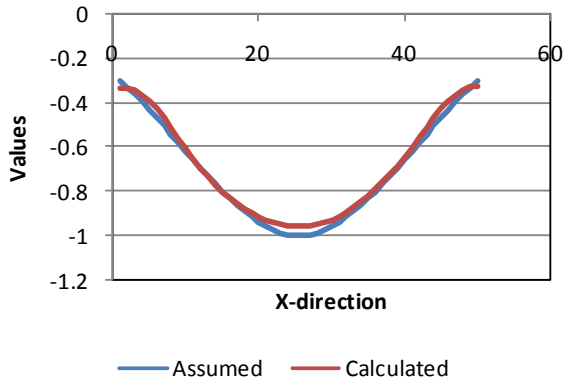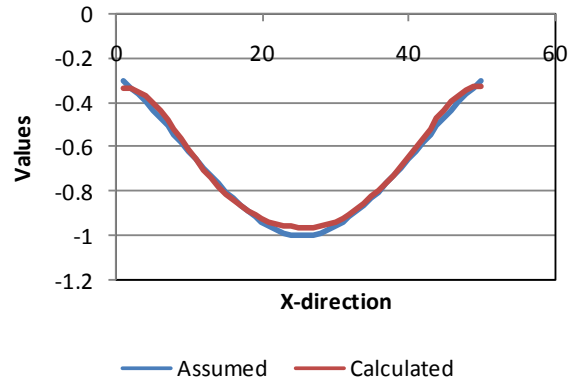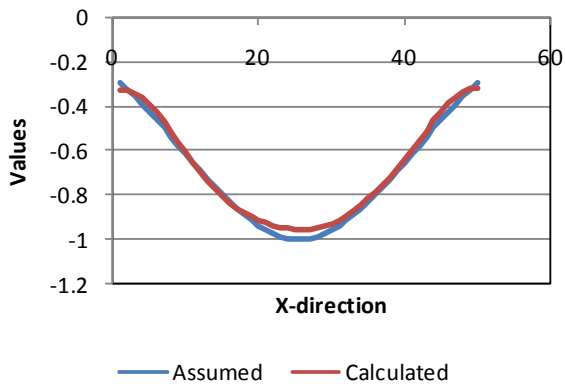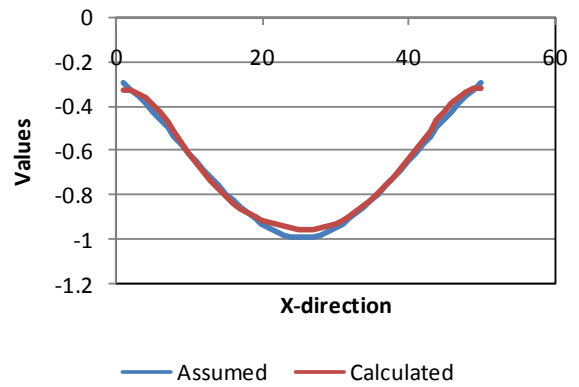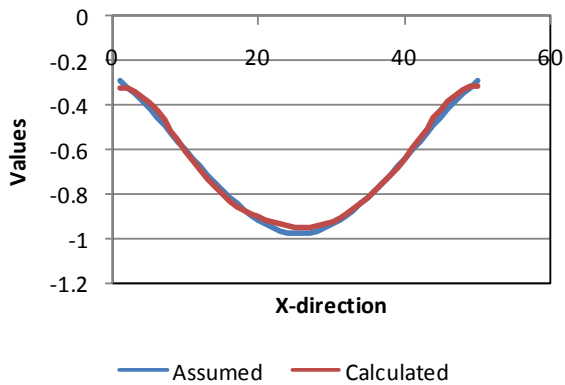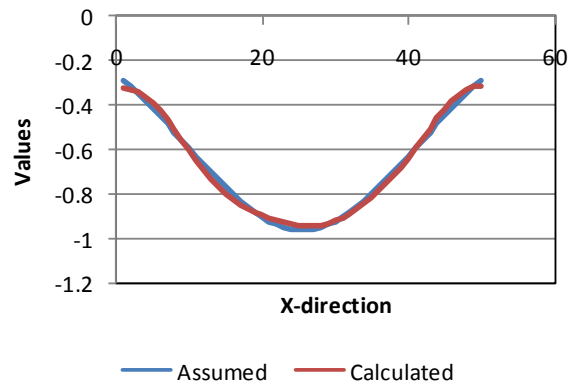
Cas19:

Tilt1+2+Displacement, 0%err   Omitting 9.2% of points (250)   RMSE=0.024057
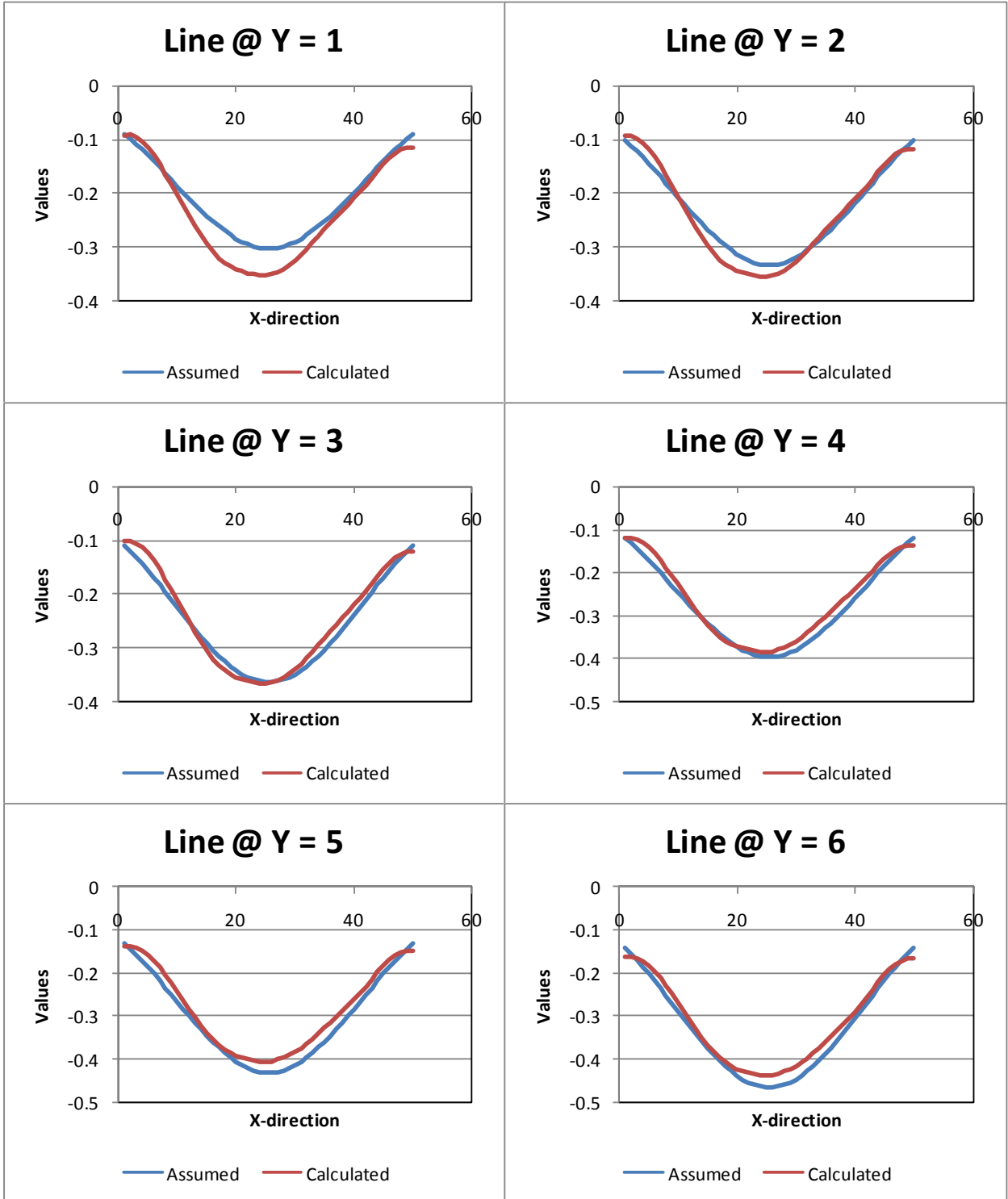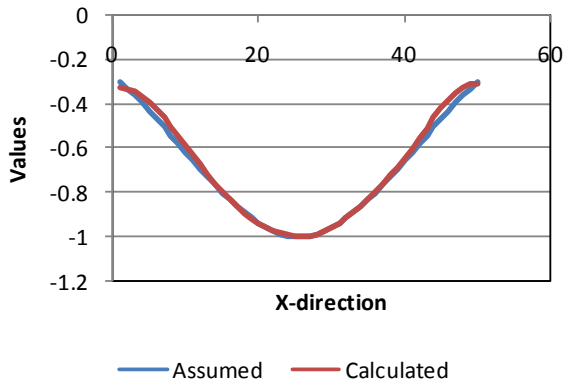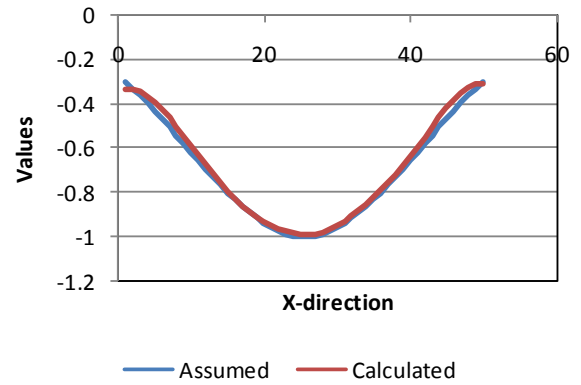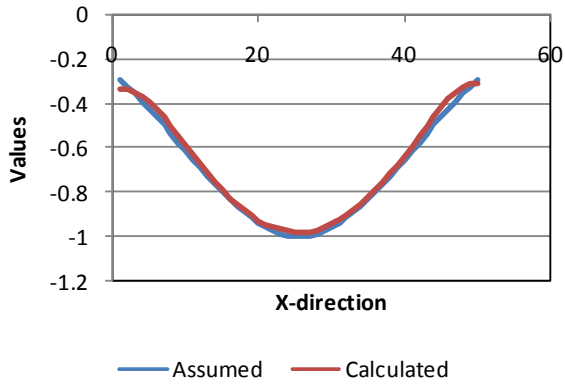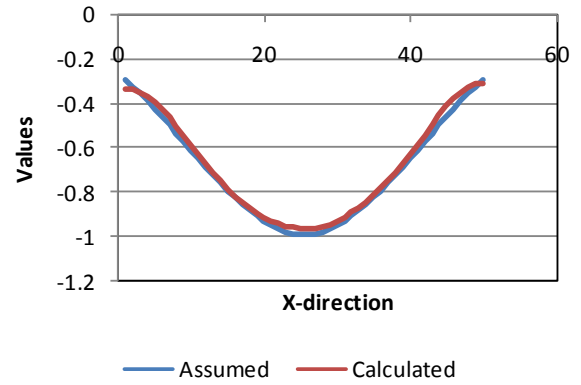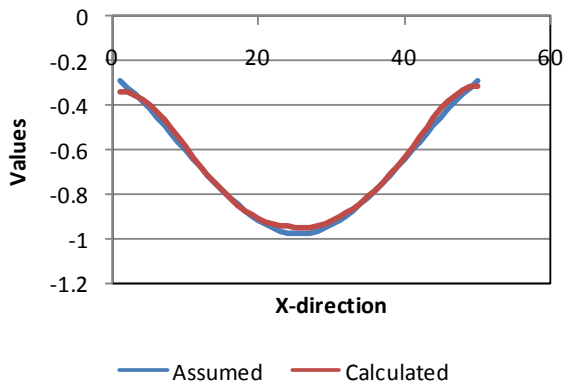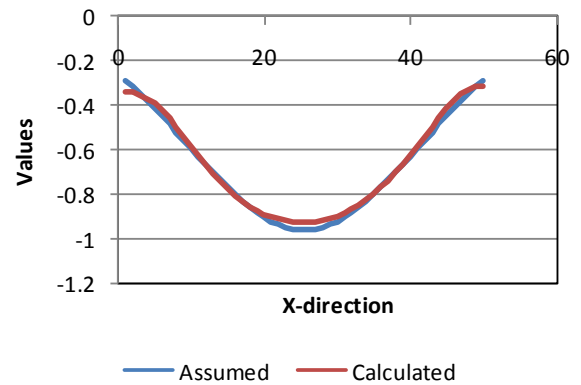
Case20:

Tilit1+2+displacement,0%err   Omitting 18.5% of points(500)
RMSE=0.024514
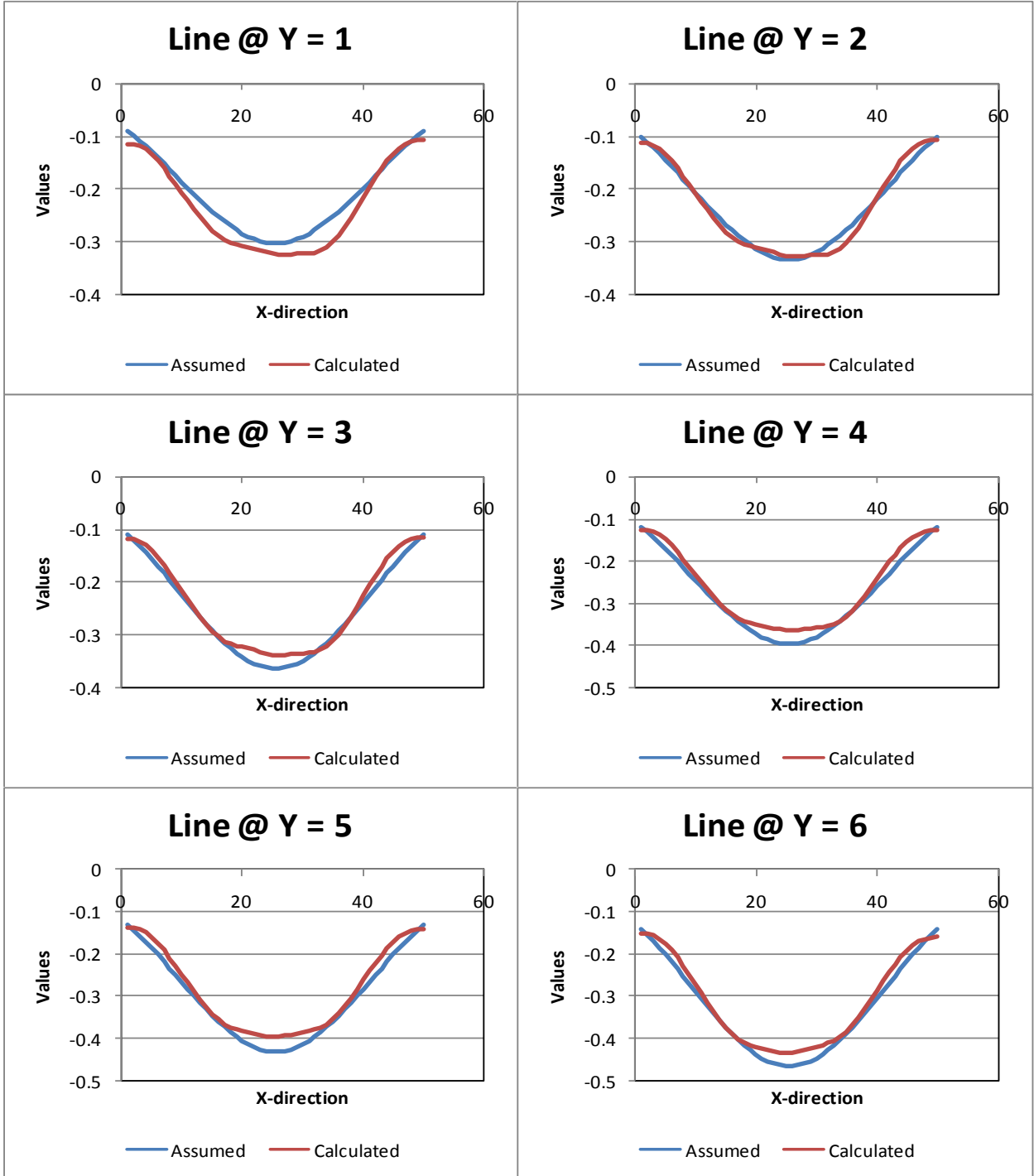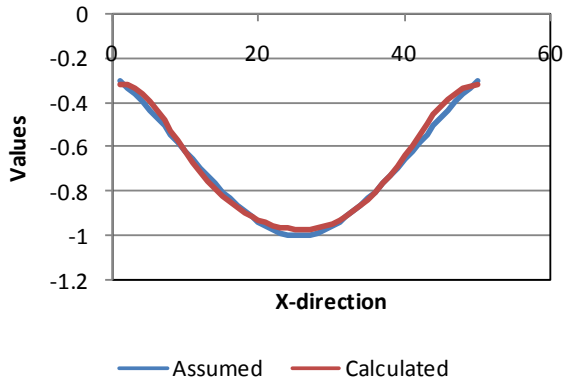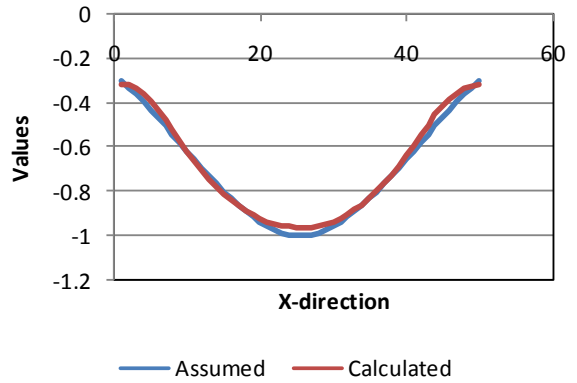
Line @ Y = 25
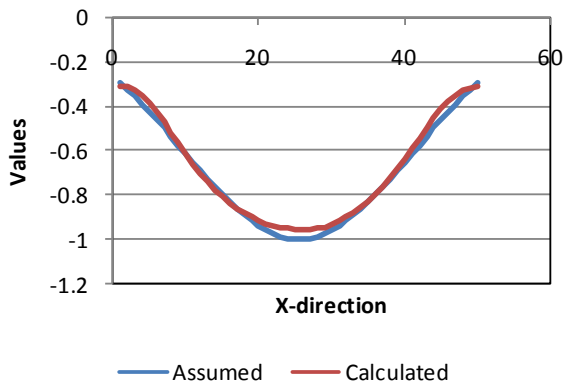
Line @ Y = 26
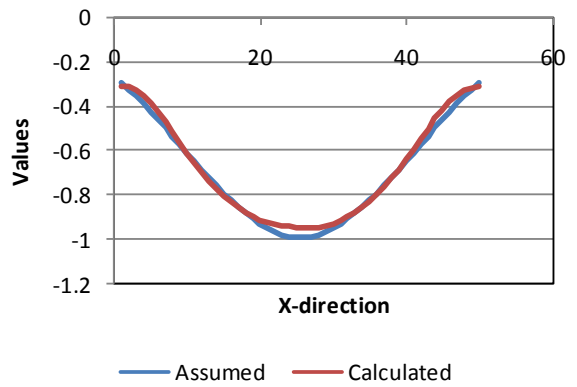
Line @ Y = 27
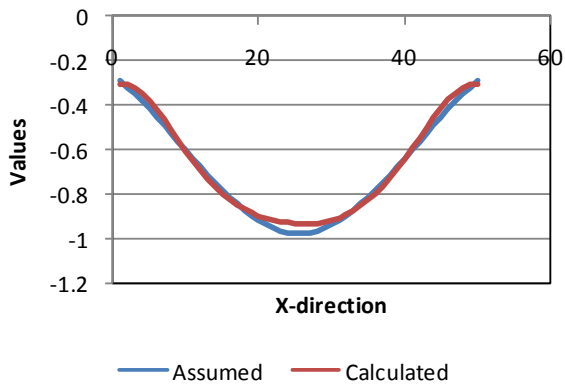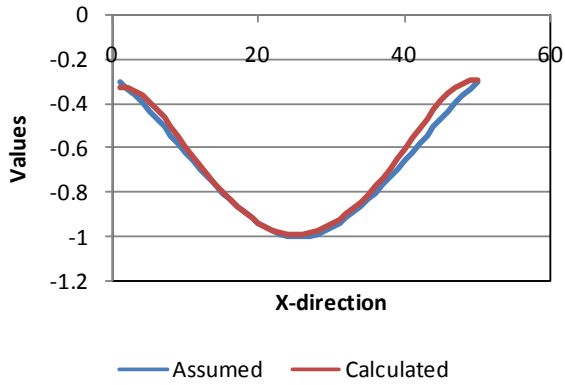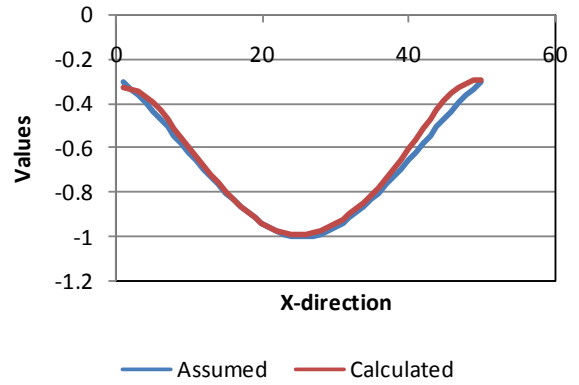
Line @ Y = 28
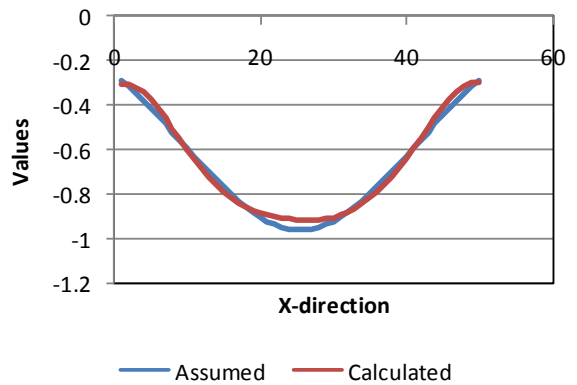
Line @ Y = 29

Line @ Y = 30

Case21:

Tilt1+2+displacement,0%err   omitting 37% of points(1000)
RMSE=0.029051
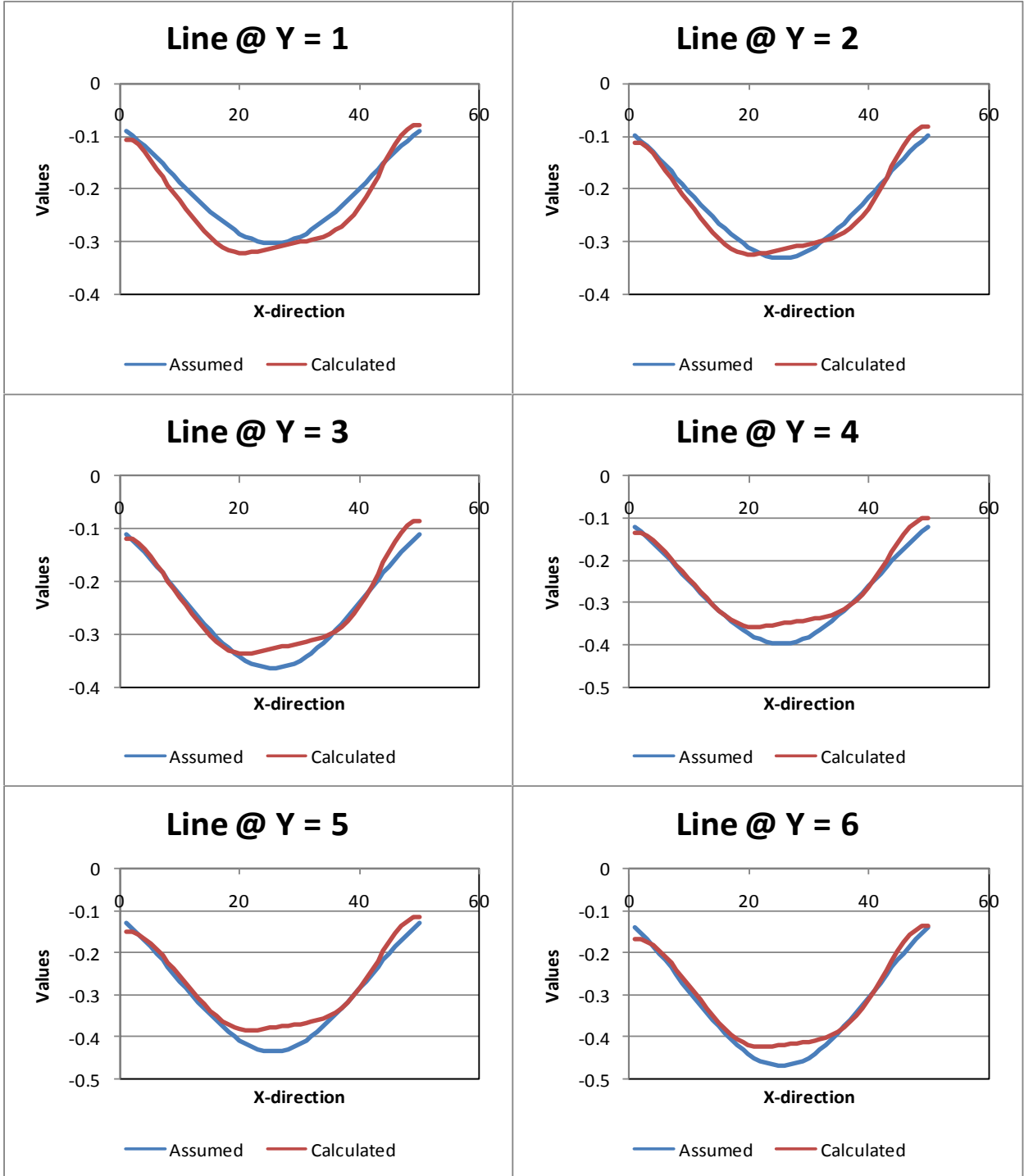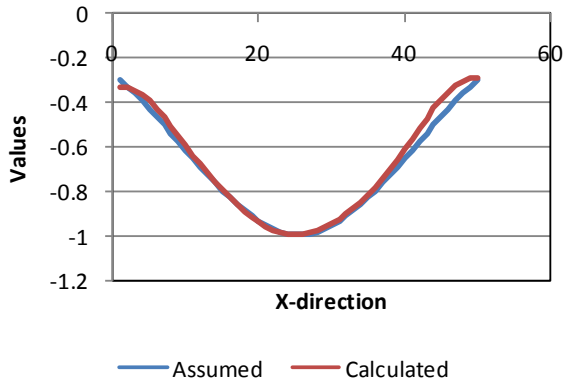
Case 22

Tilit1+2+displacement,0%err   omitting 55.5% of points(1500)
RMSE=0.026517

Case 23:

Tilt1+2+displacement,0%err   omitting 74% of points(2000)   RMSE=0.025801
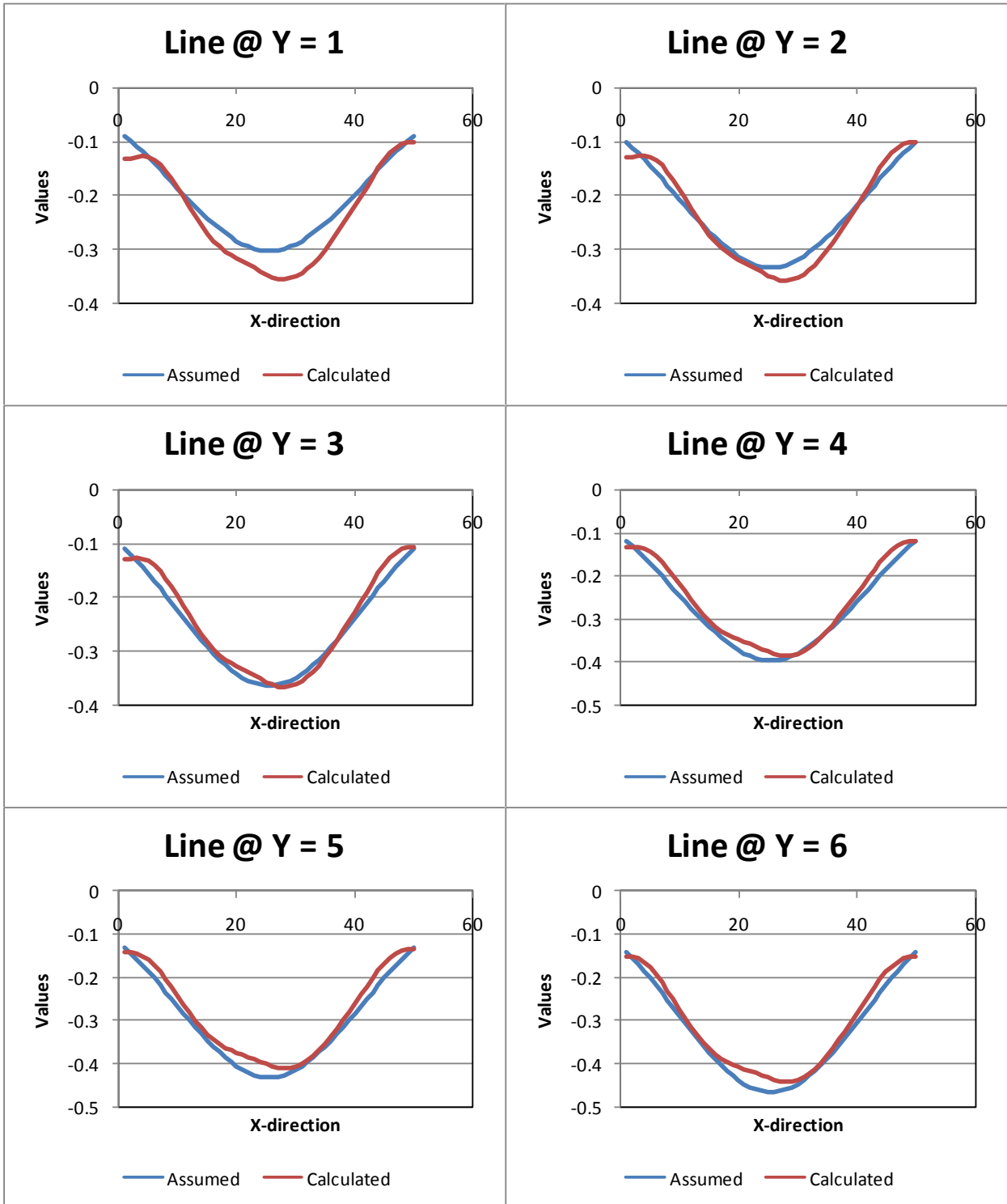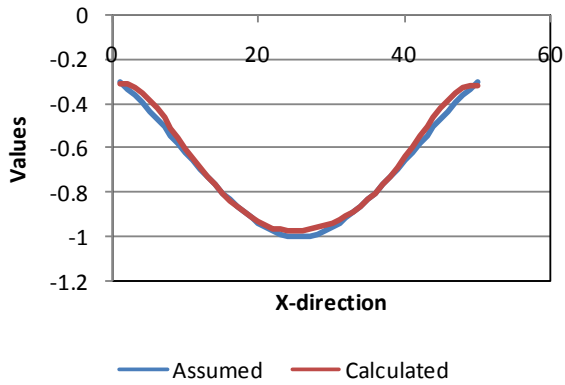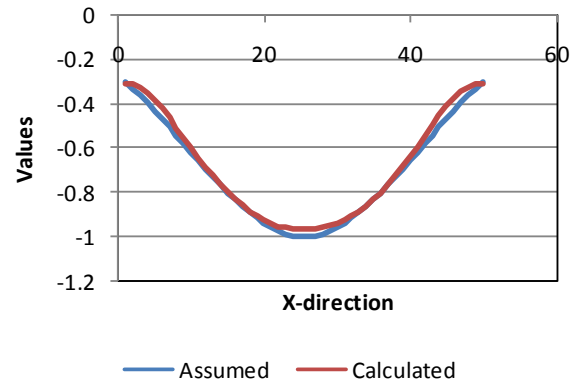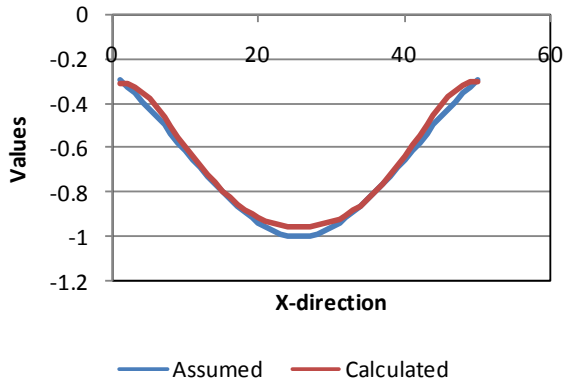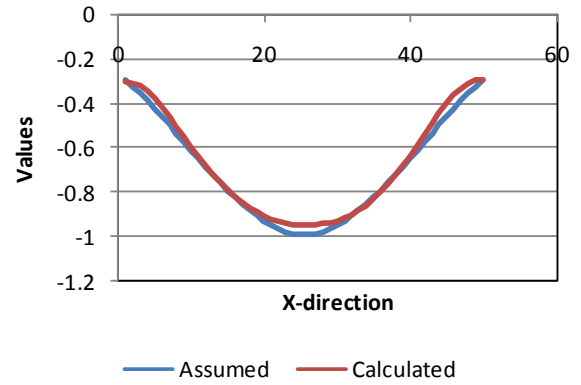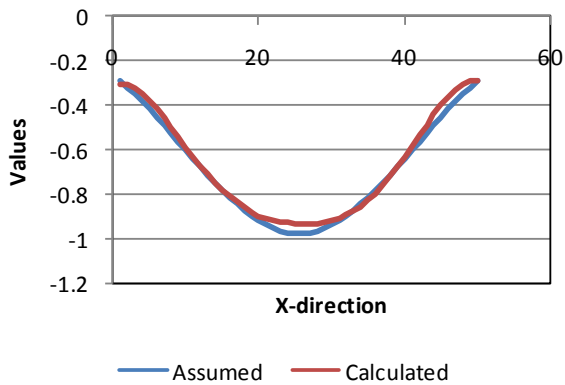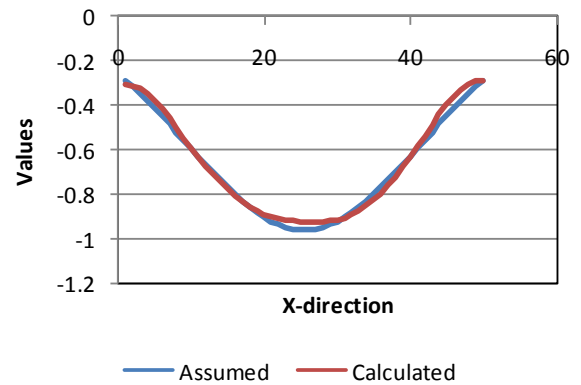
Case 24:

Tilts1+2+Displacements,0%err   Omitting 83% of points(2250)   RMSE=0.036212
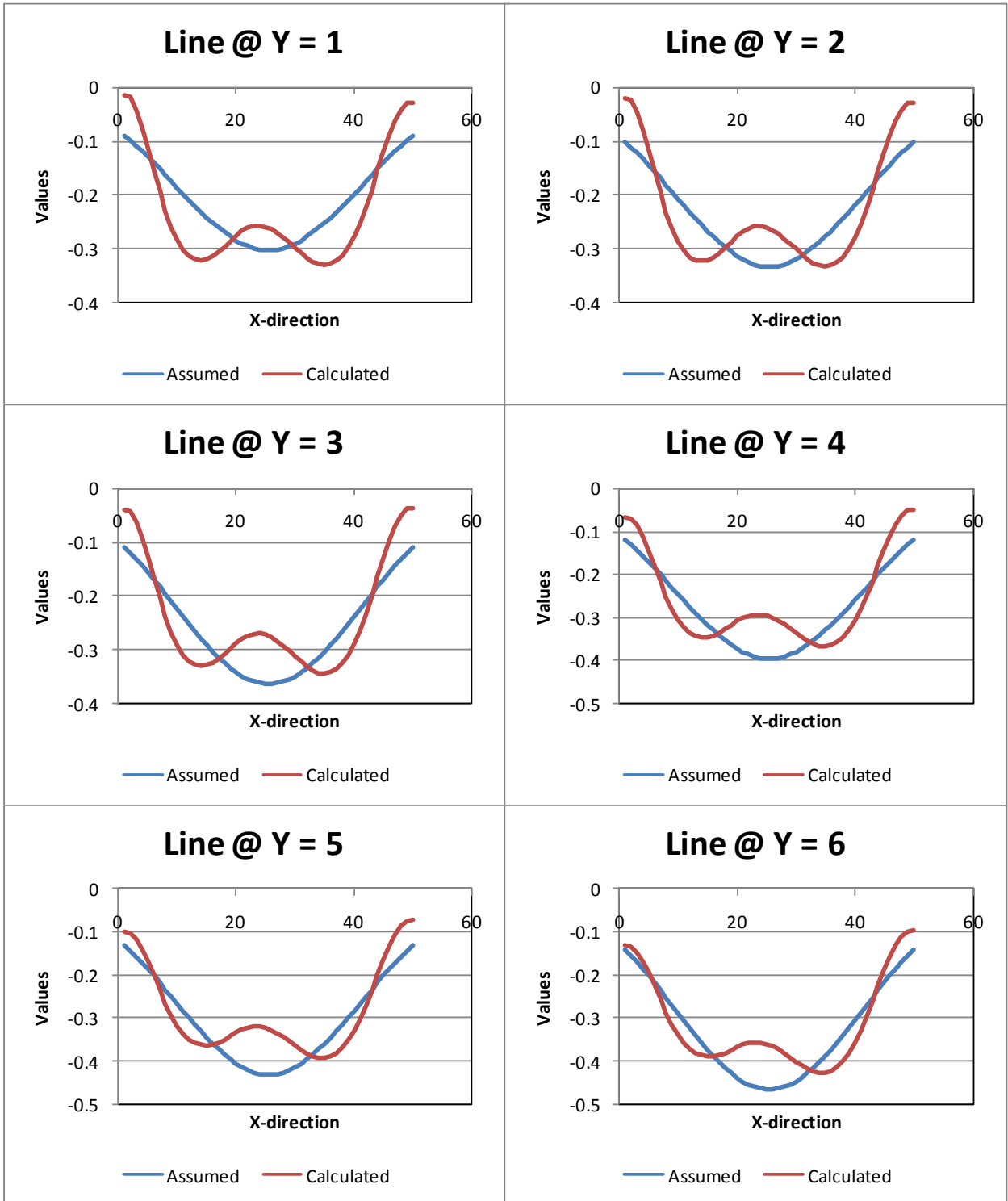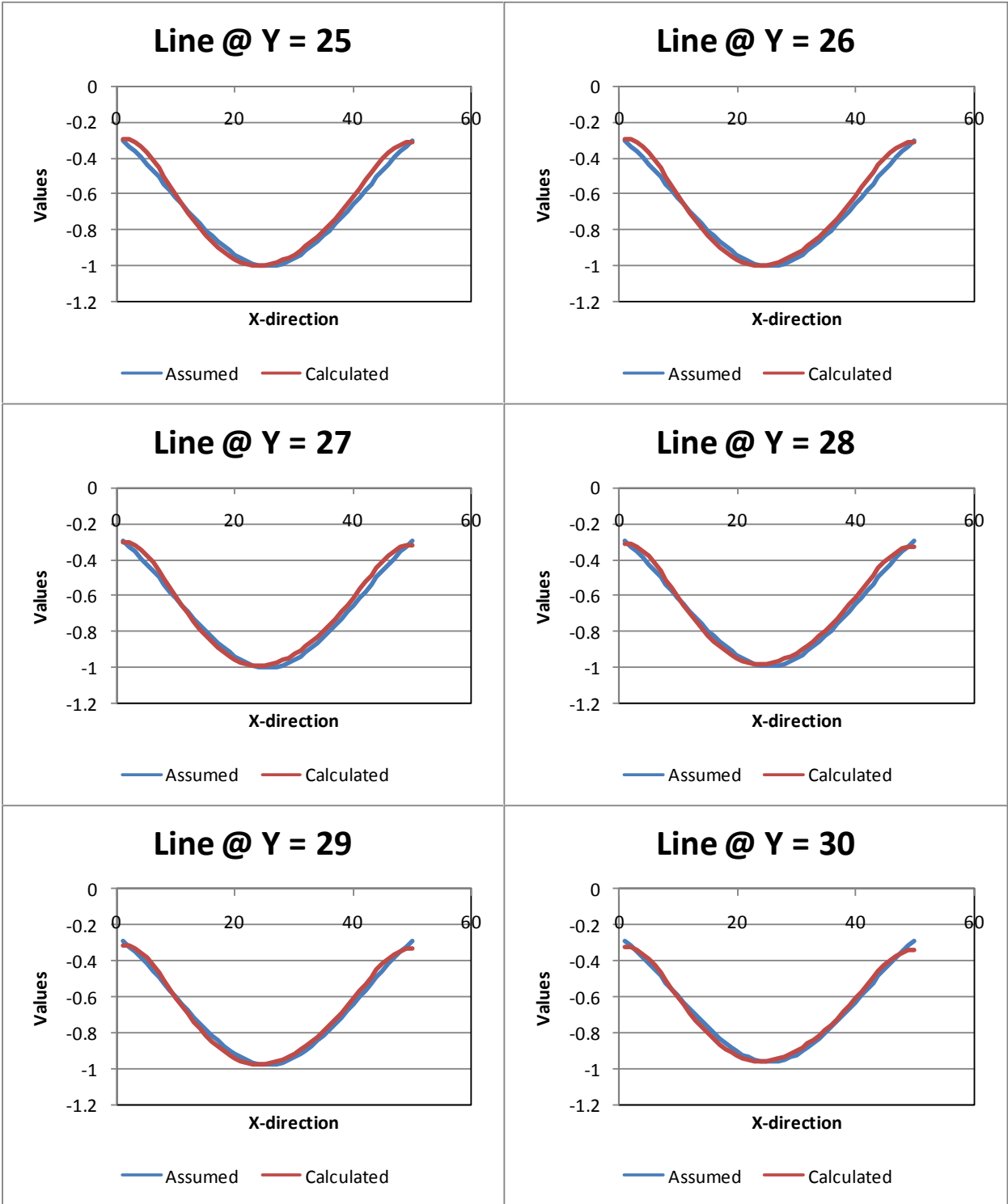
Case 25:

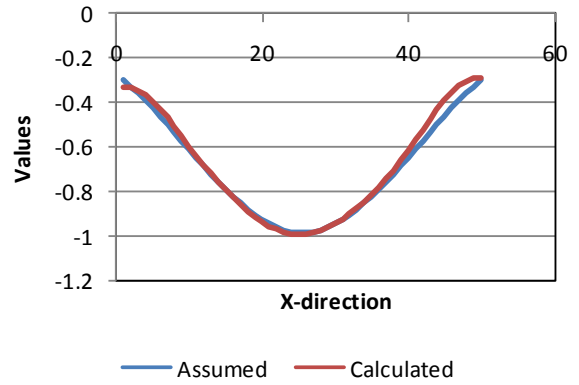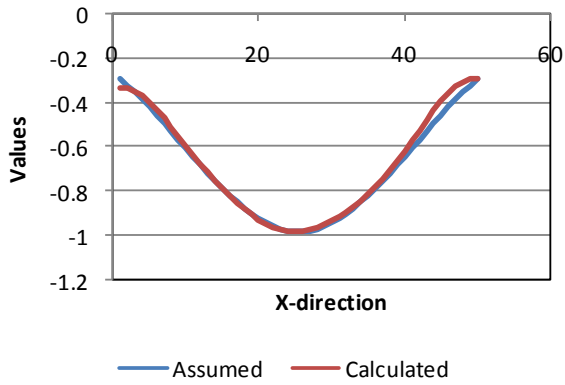Tilt1+2+displacement,0%err   omitting 89% of points(2400)   RMSE=0.041741
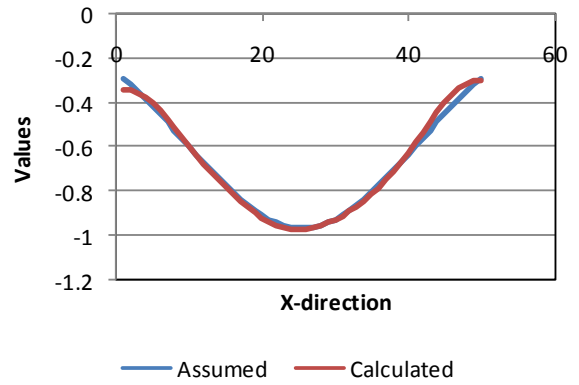
Line @ Y = 25

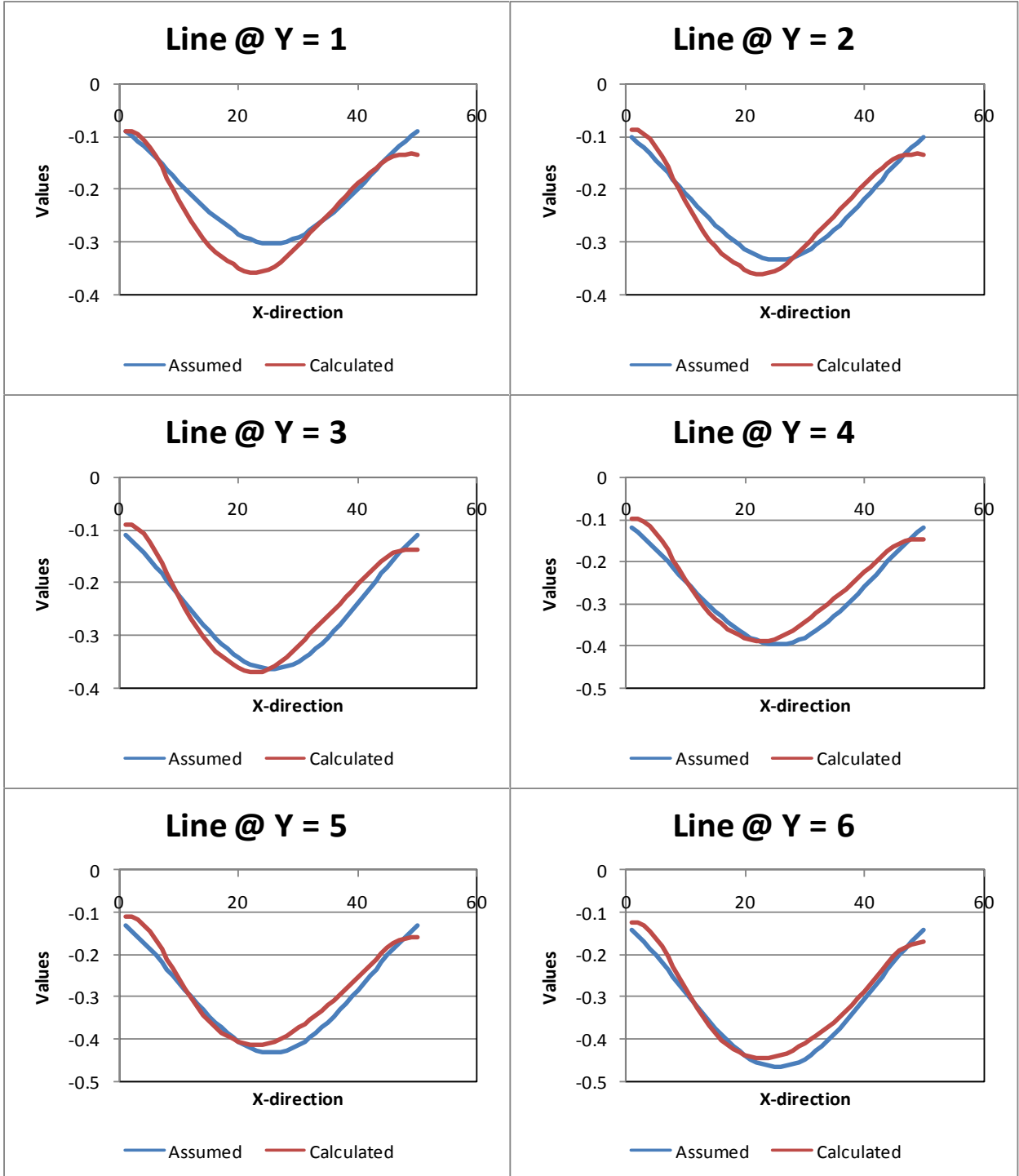Line @ Y = 26

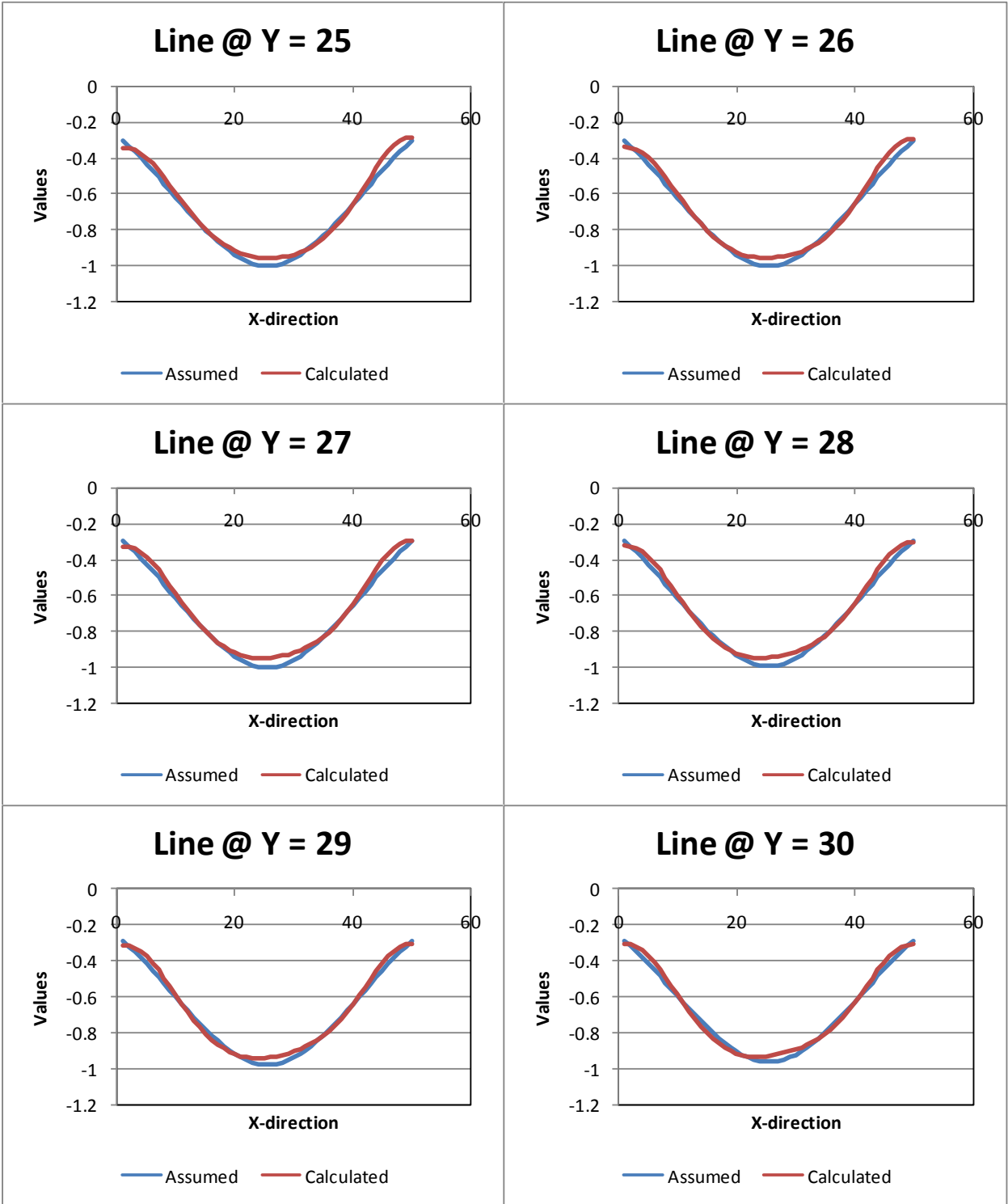Line @ Y = 27

Line @ Y = 28
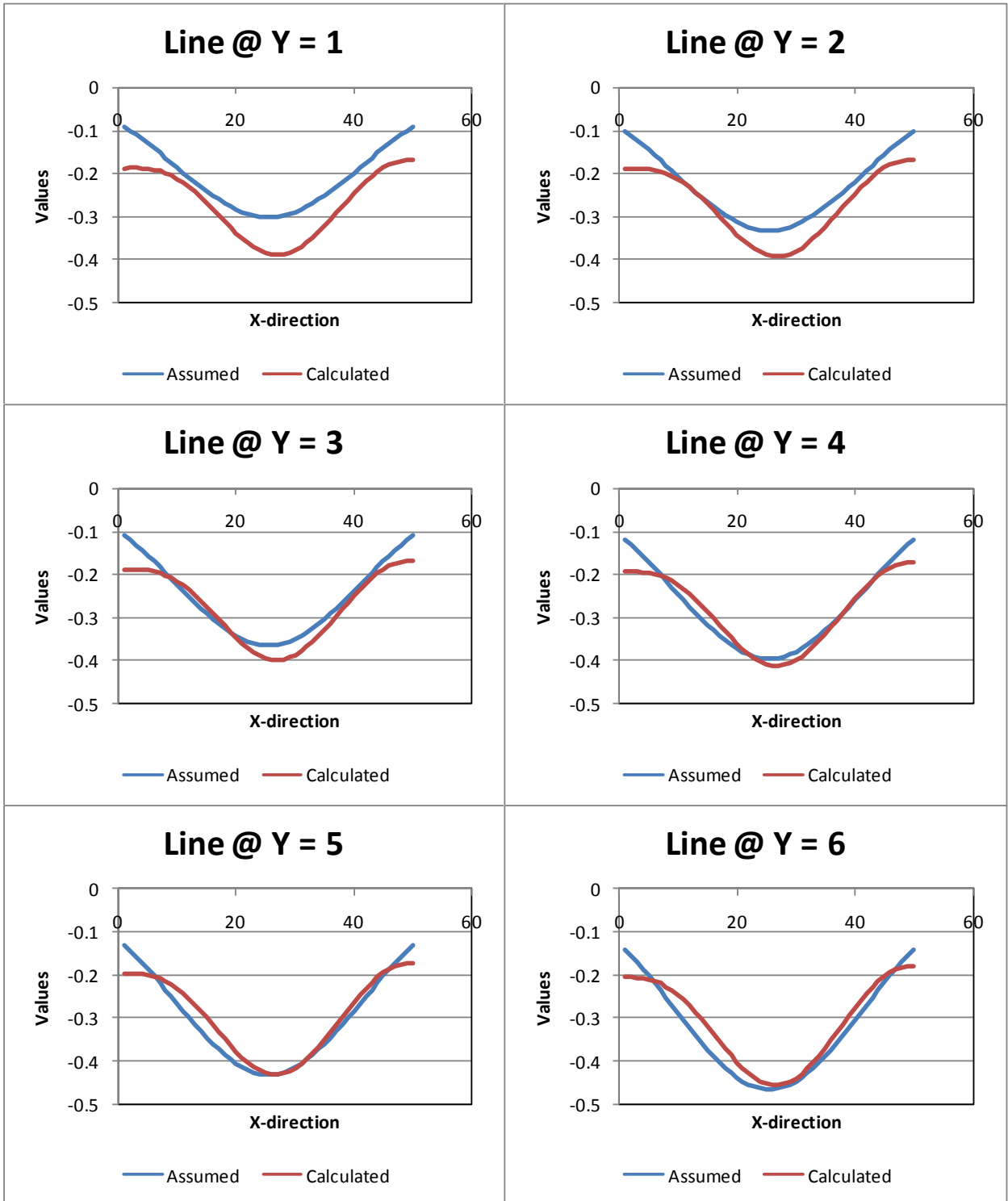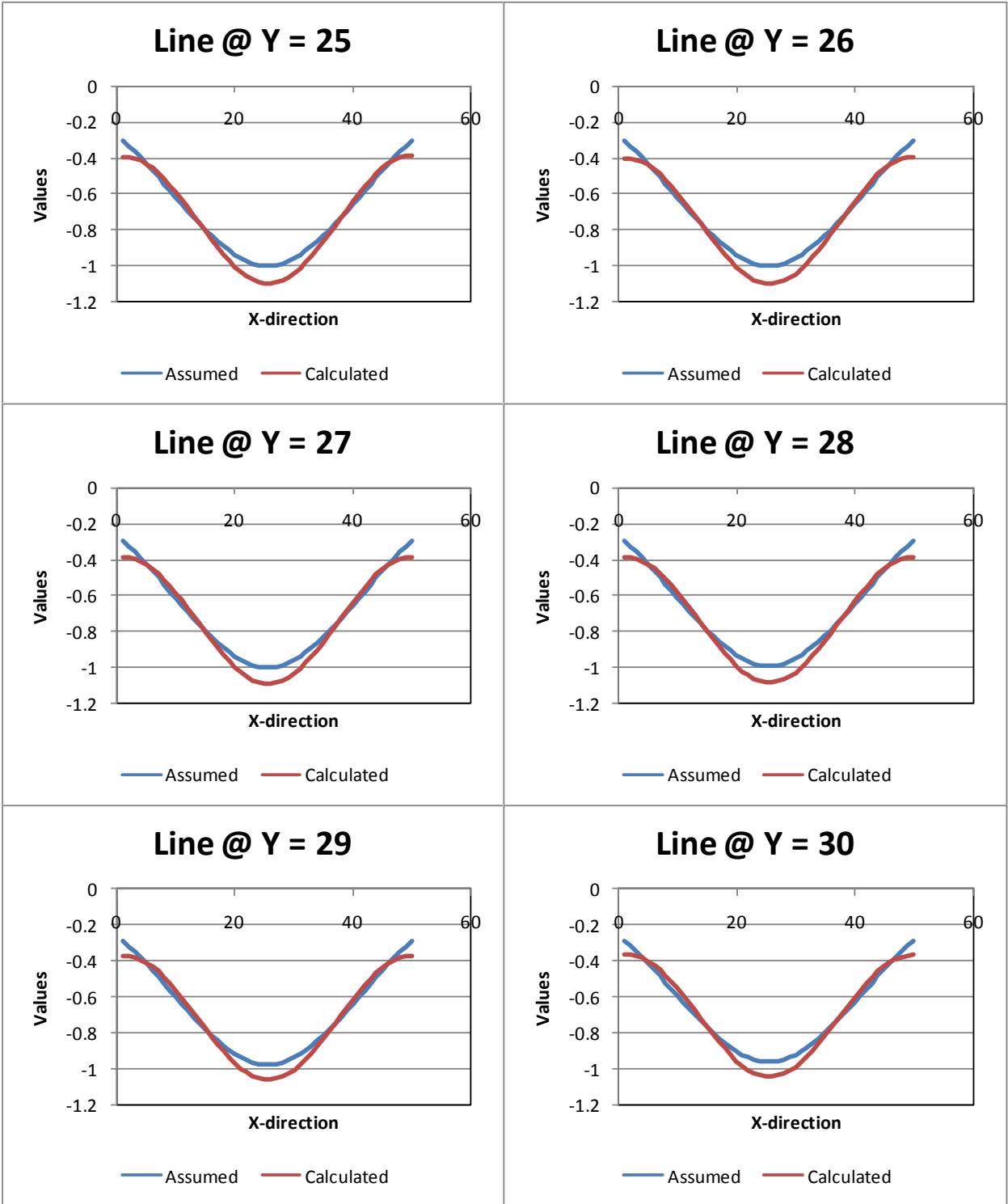
Line @ Y = 29

Line @ Y = 30

Case 26:

Tilt1+2+Displacement, 0%err   omitting 90.6% of data points (2450)   RMSE=0.042006
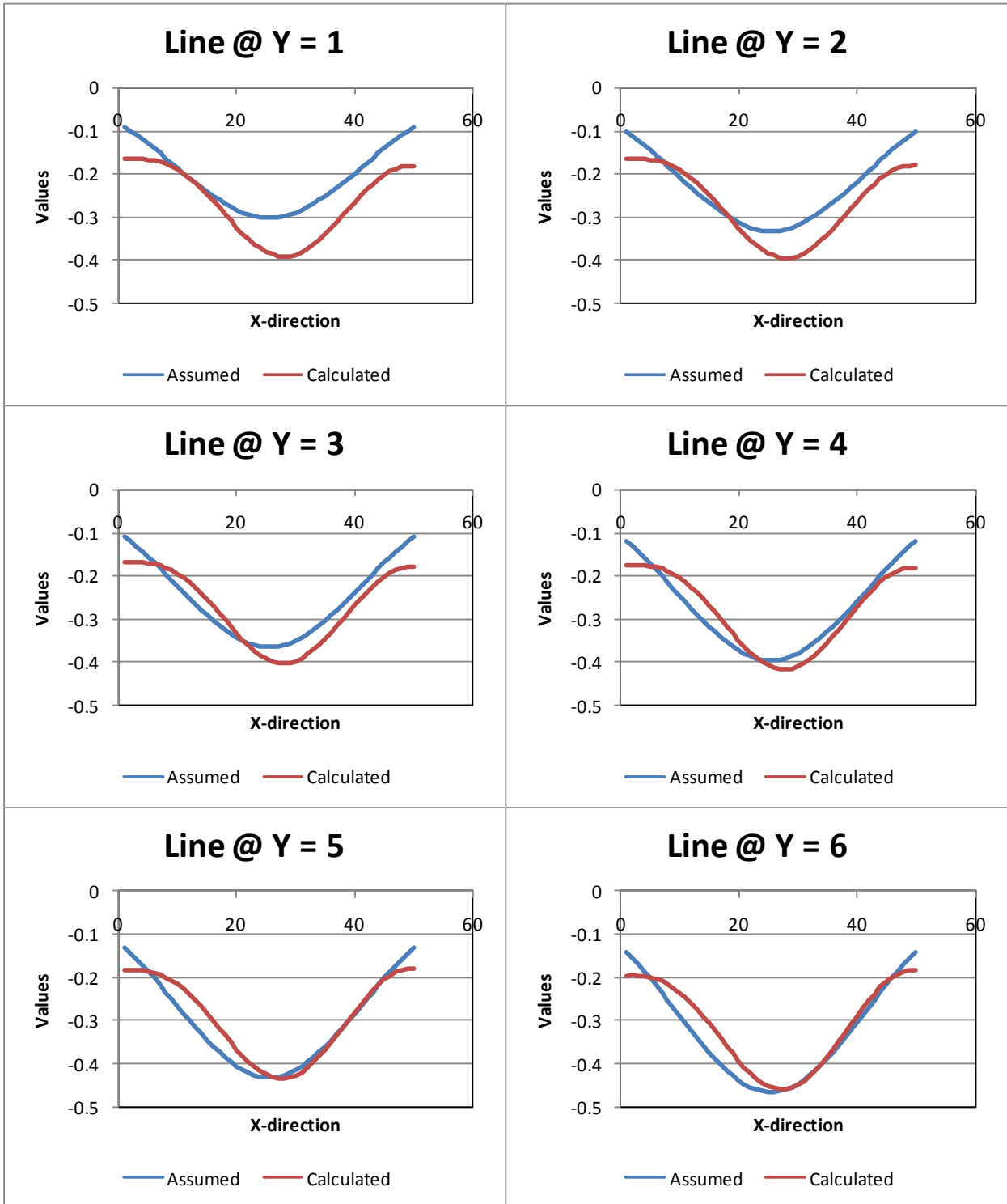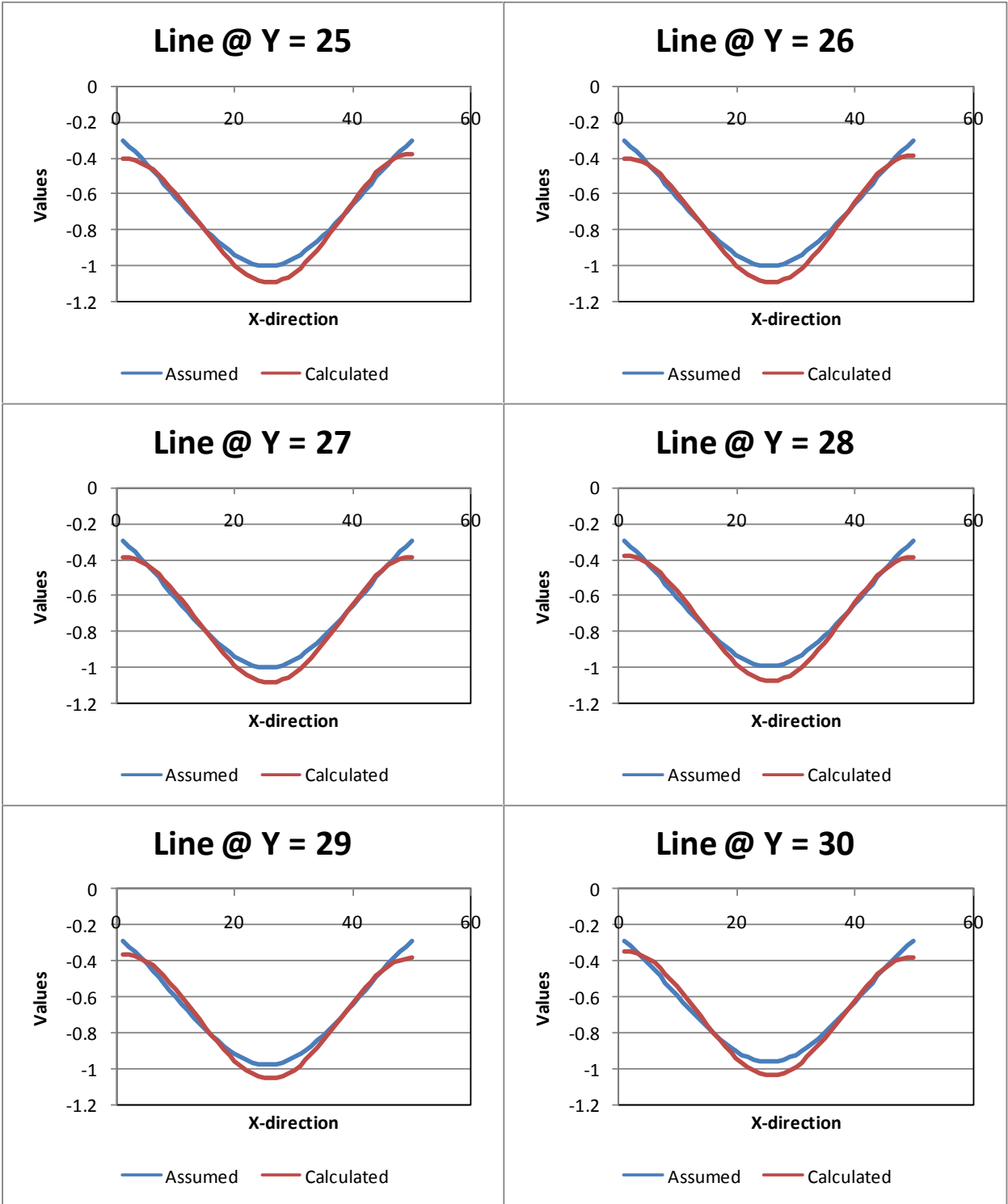
Case 27:

Tilt1+2+Displacement, 0%error   omitting 99.6% of data points (using only 10 random points)
RMSE=0.070773
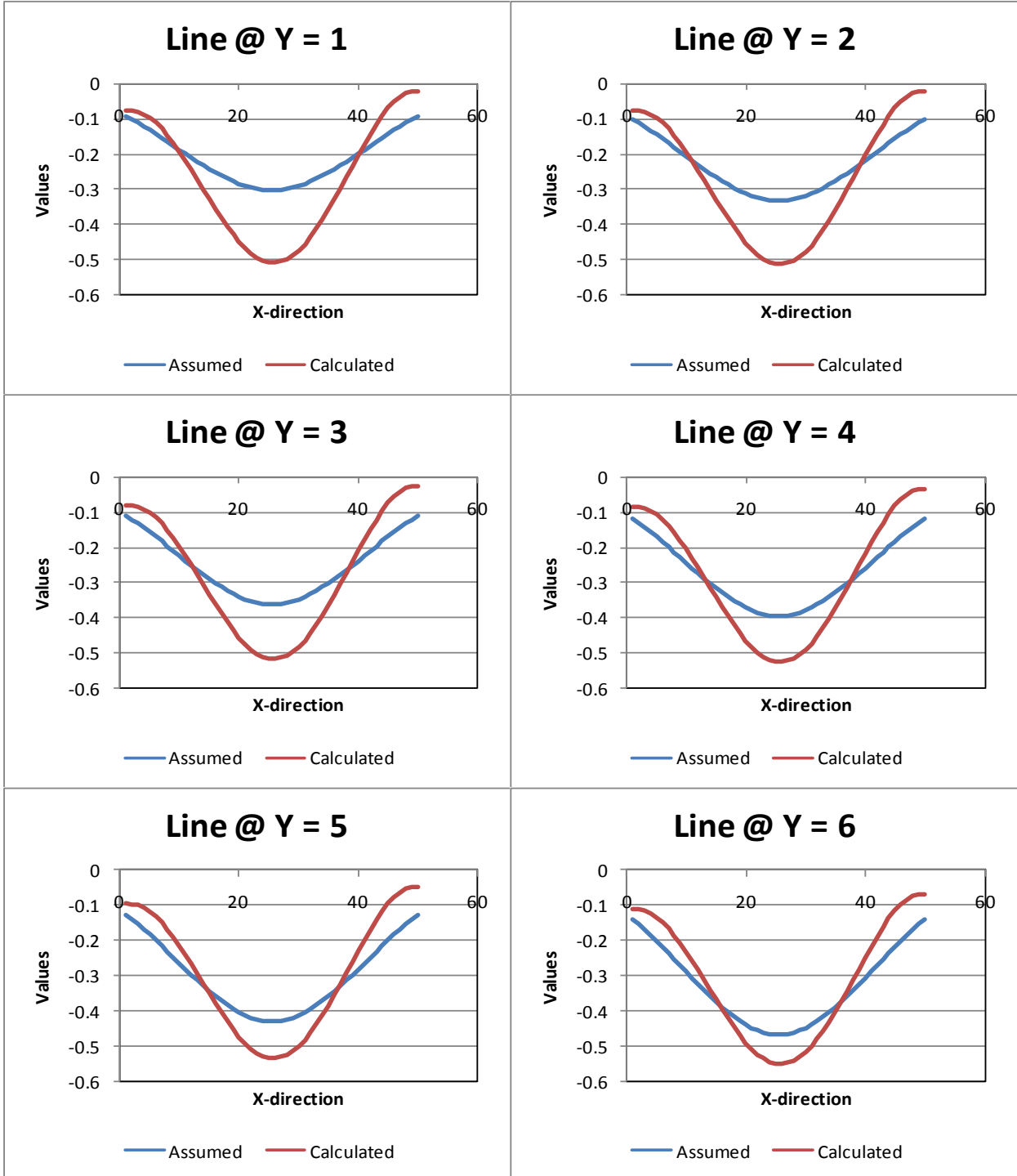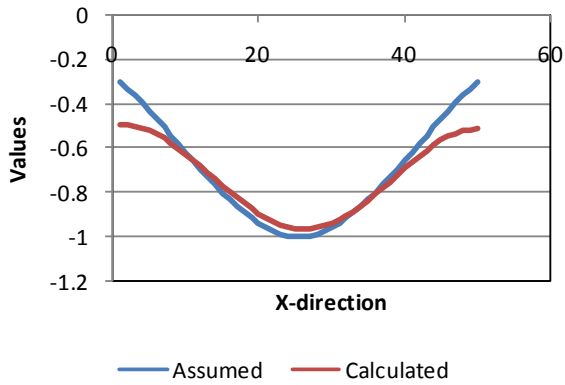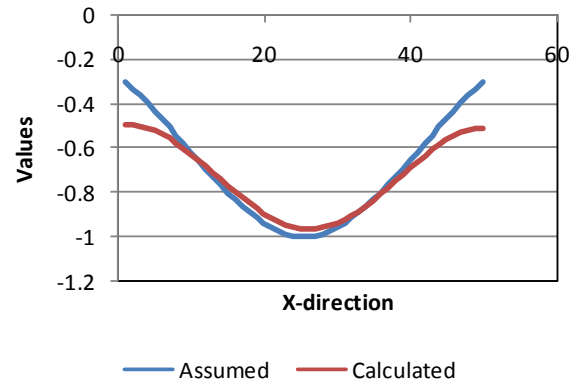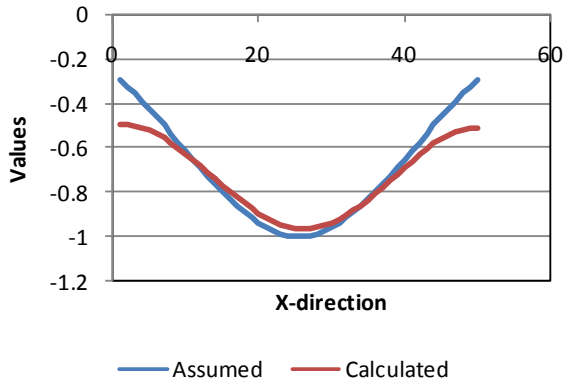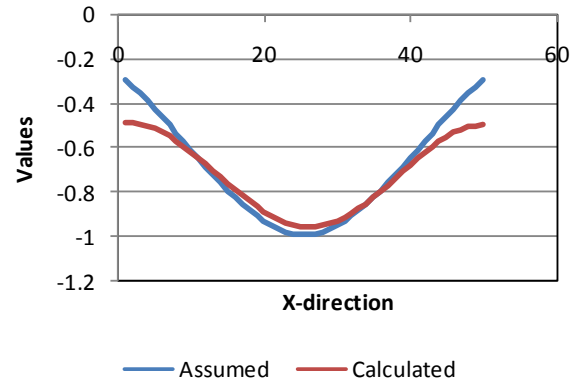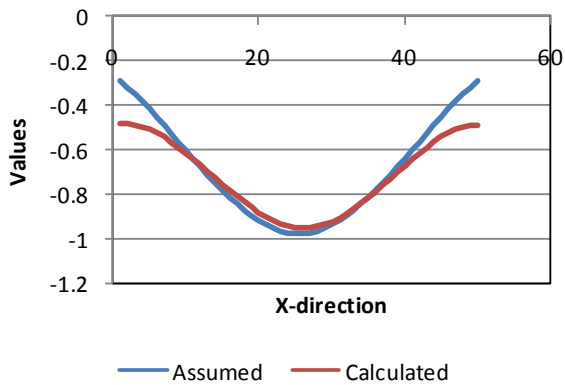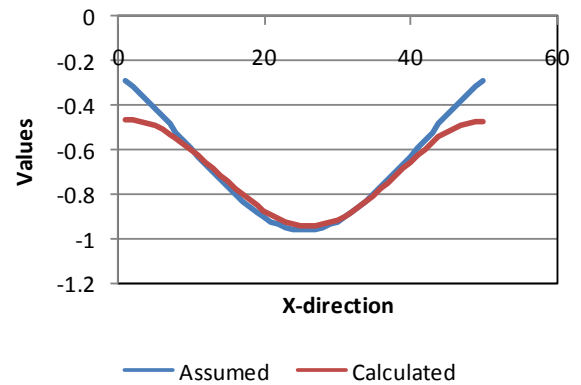
Case28:

Tilt1+2+Displacements, 0% err   Using 1 point outside the grid   RMSE=0.238201
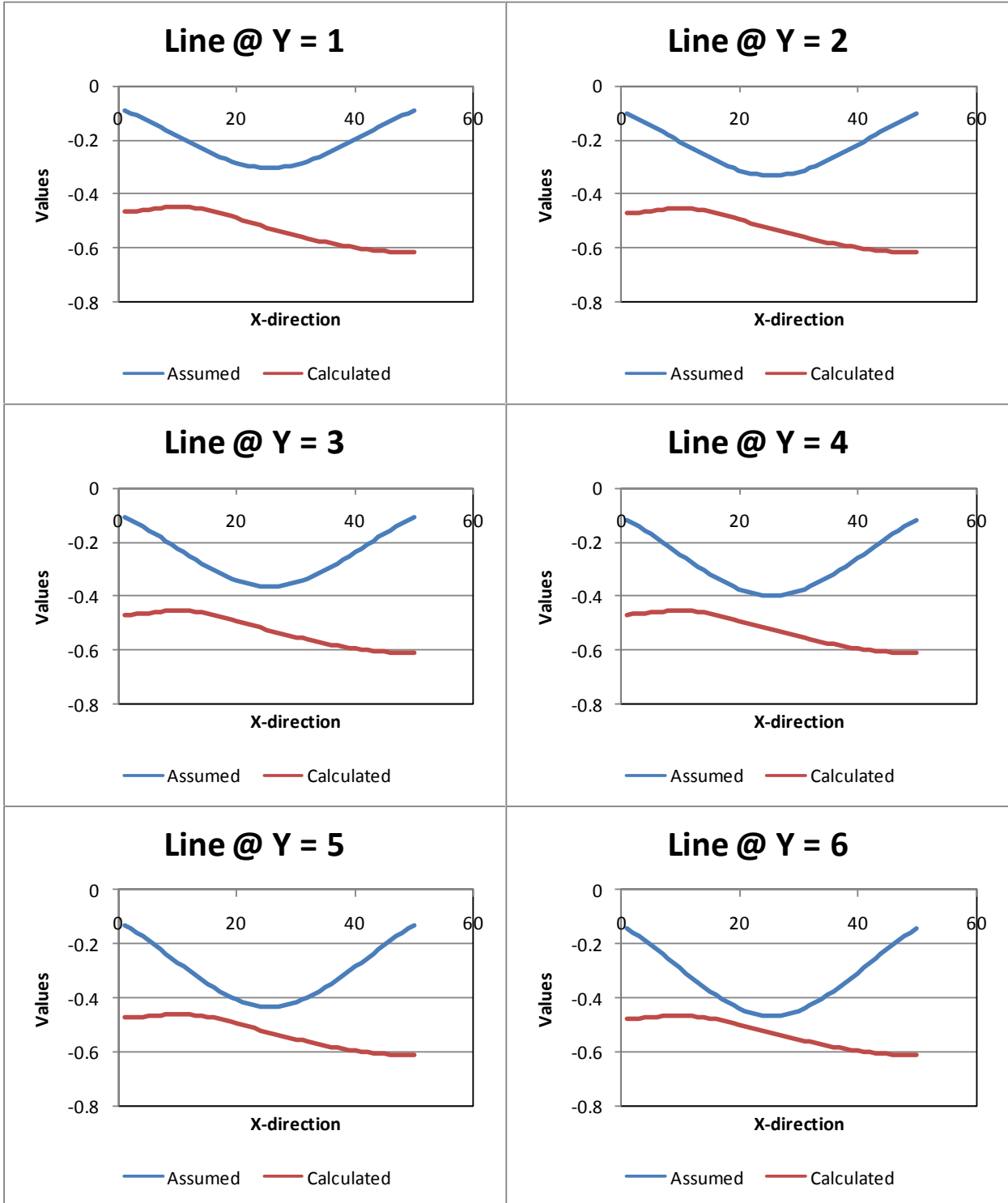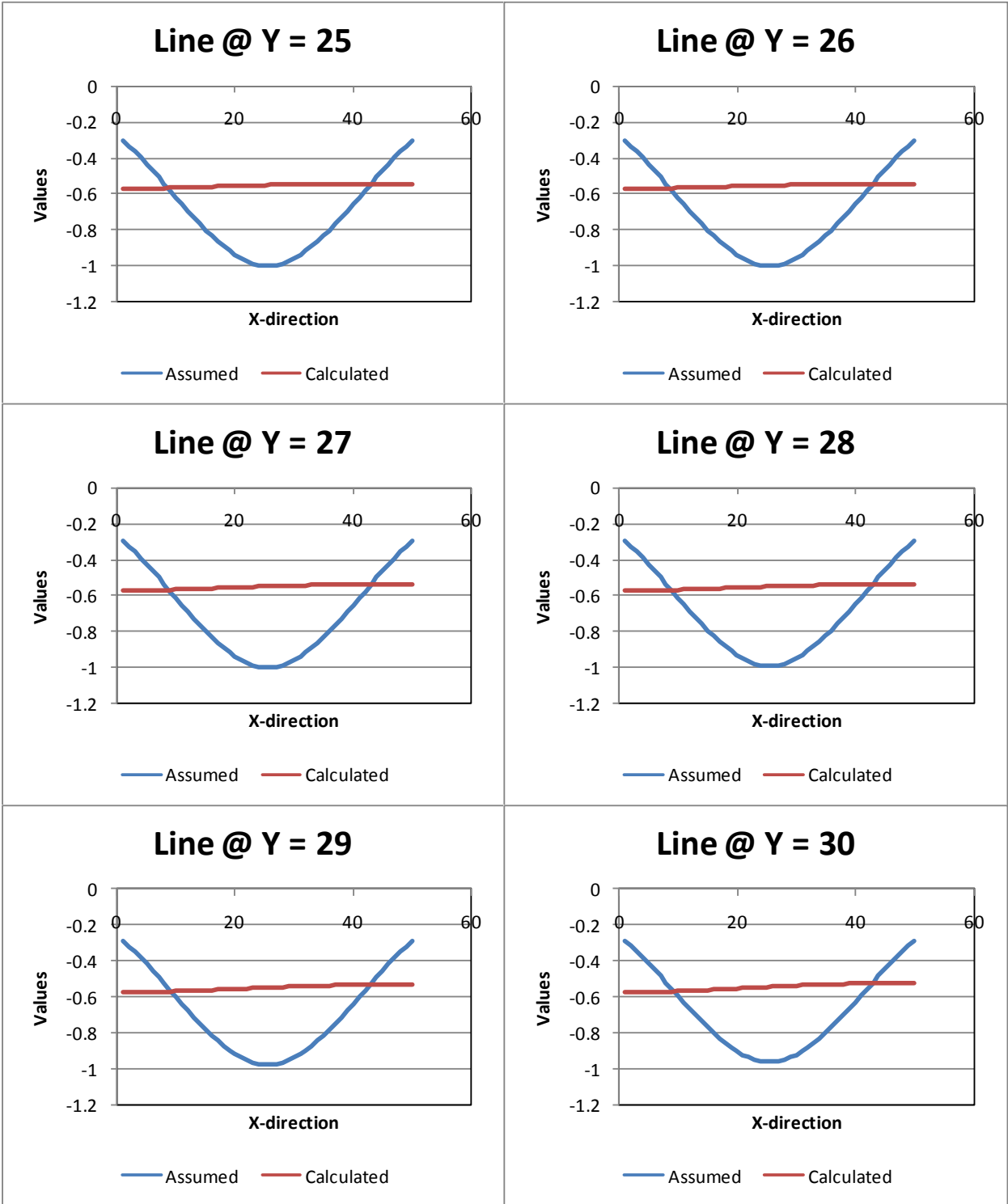
Appendix V: Graphs; studying the effect of observation distribution

Case29: Tilt1+2+Displ,0%err, using 100points at 1 vertical and 1horizontal rows at corners of grid: X,Y=5   5<X,Y<495   RMSE=0.04958528
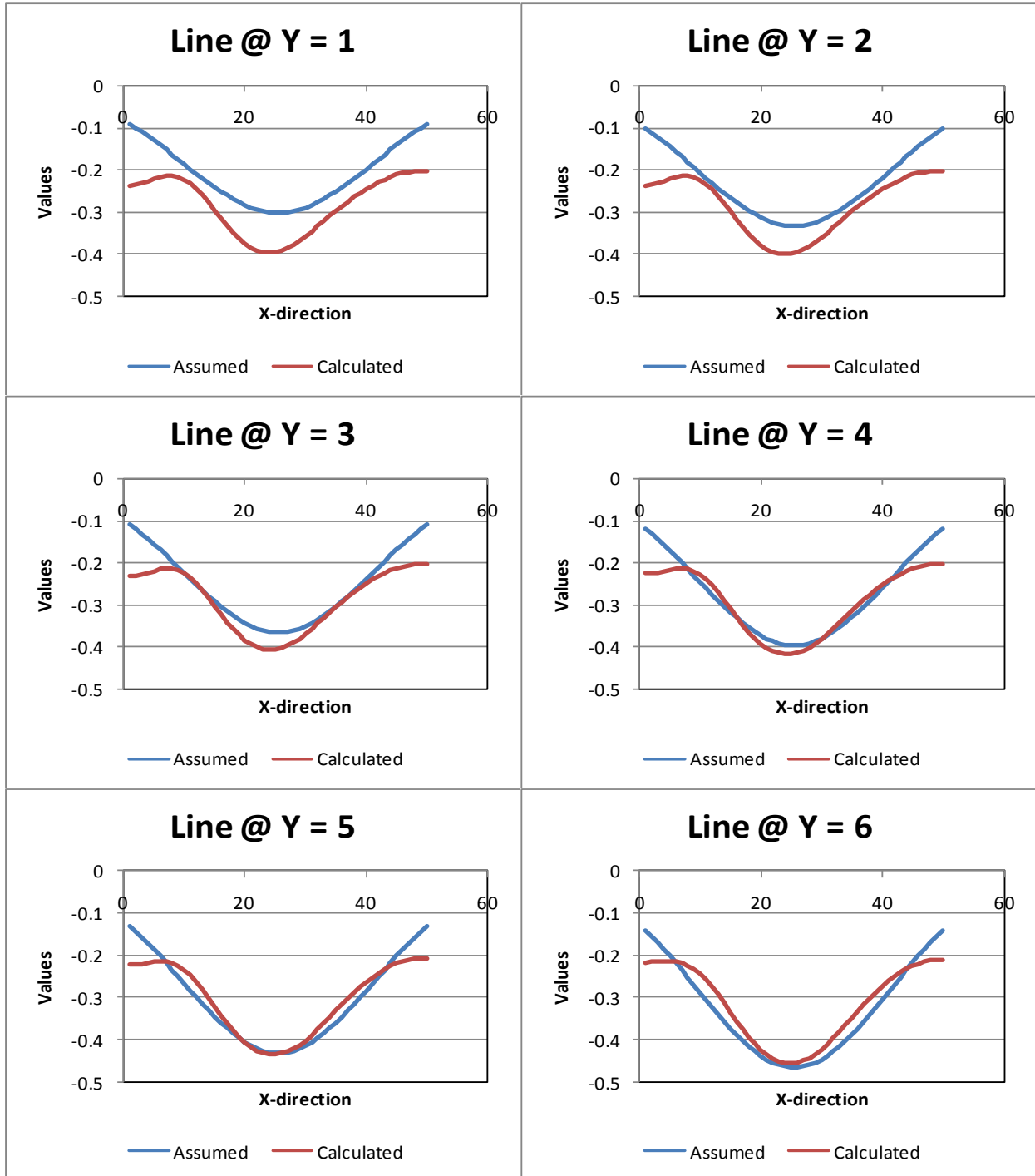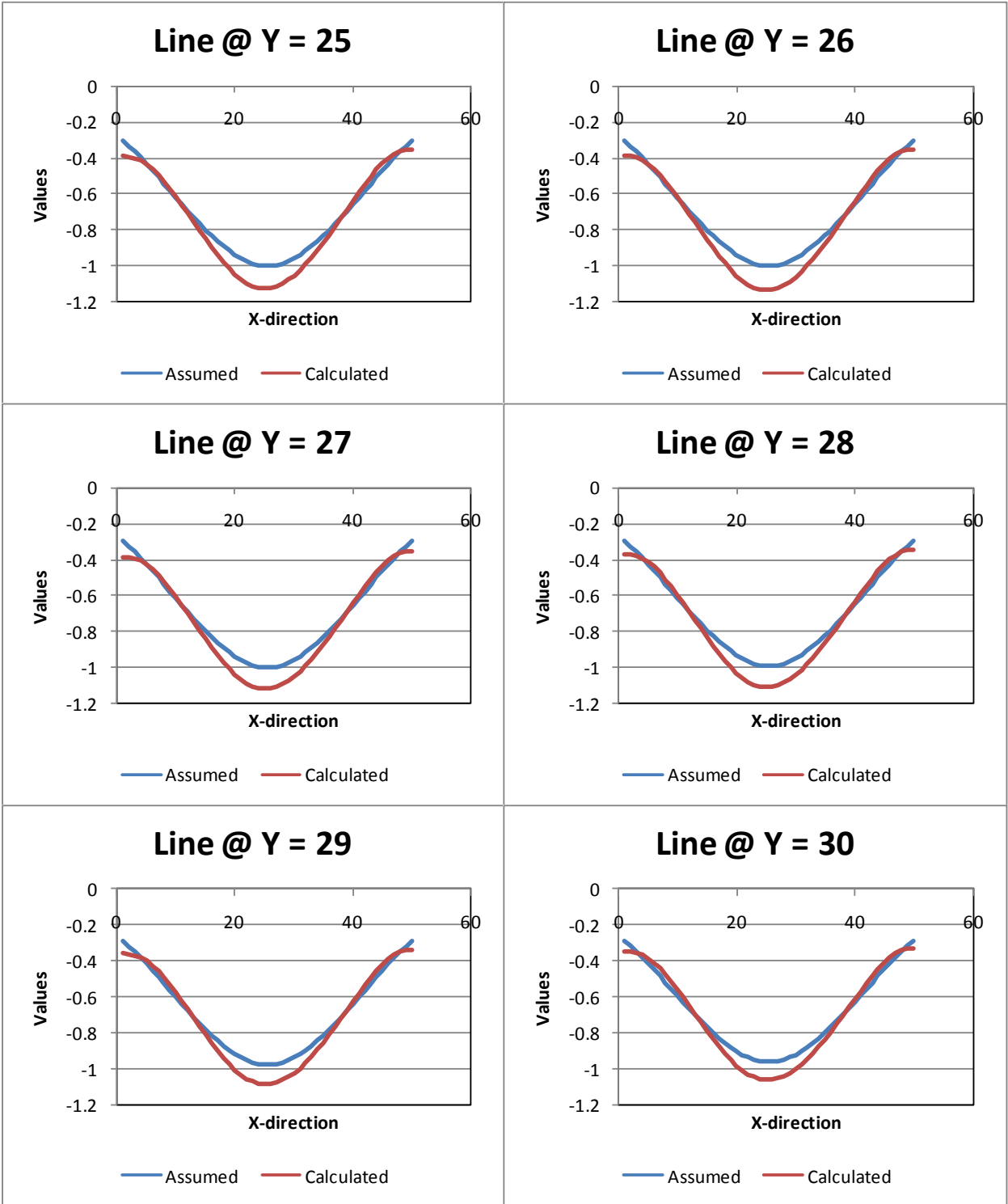
Case30:

Tilt1+2+displ,0% err, Using 100 points in 1horizontal and 1 vertical rows in the mid grid,
x,y=250
5<x,y<495   RMSE=0.042306028
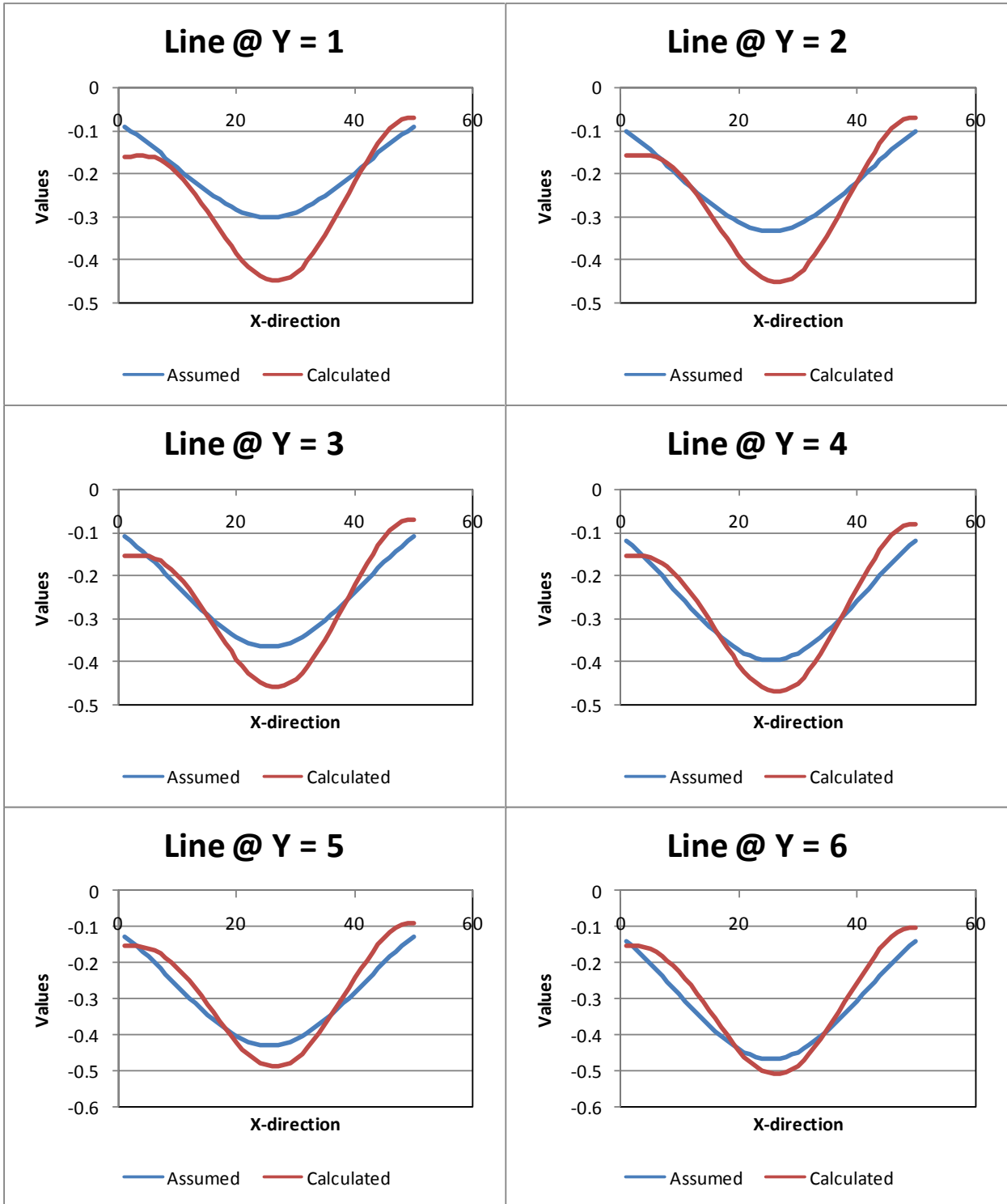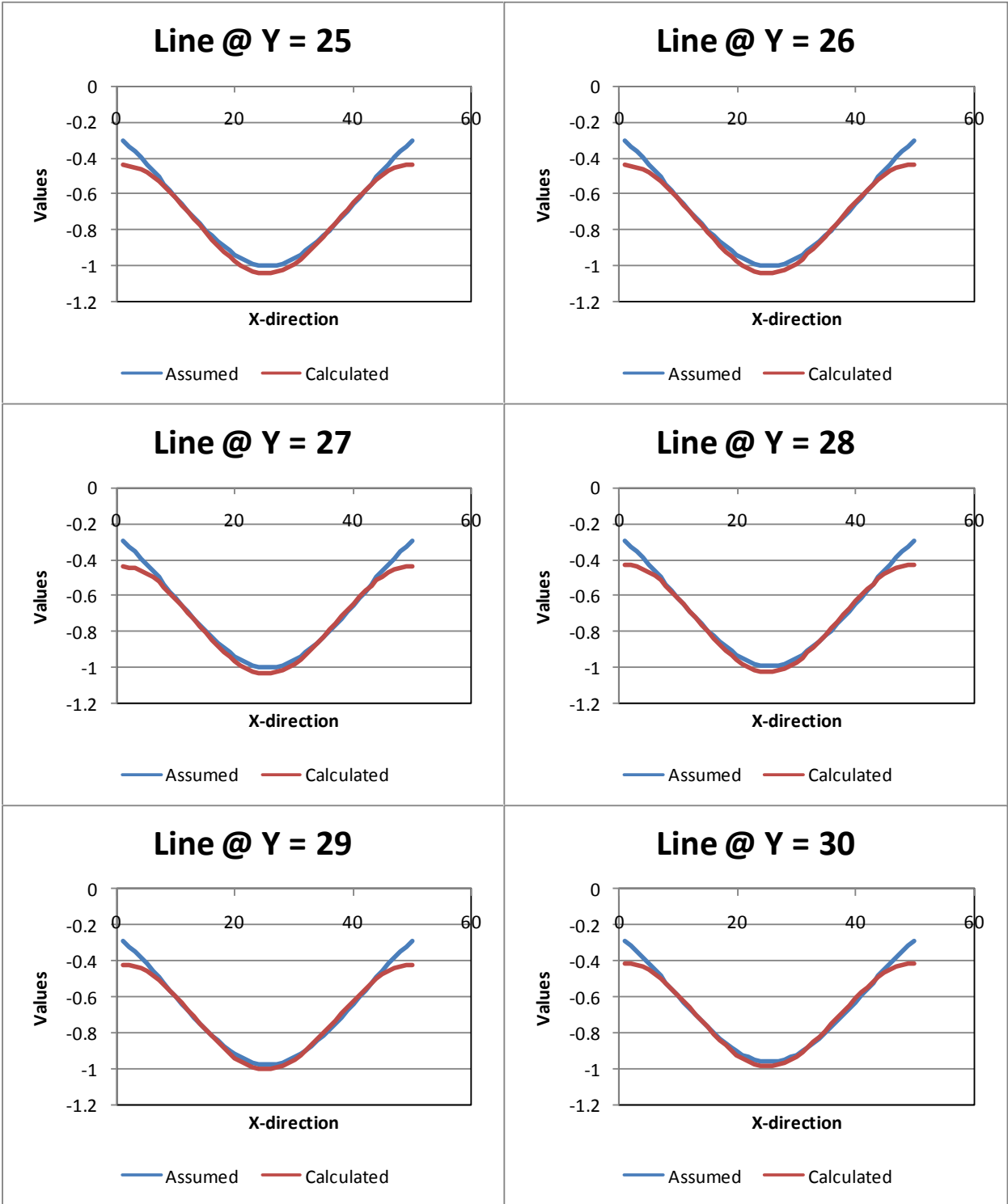
Case31:

Tilt1+2+displ,0%err,Using 100 extended points(-500<x,y<1000) in 1vertical and 1 horizontal
rows in the mid grid(X,Y=250)   RMSE=0.043834347
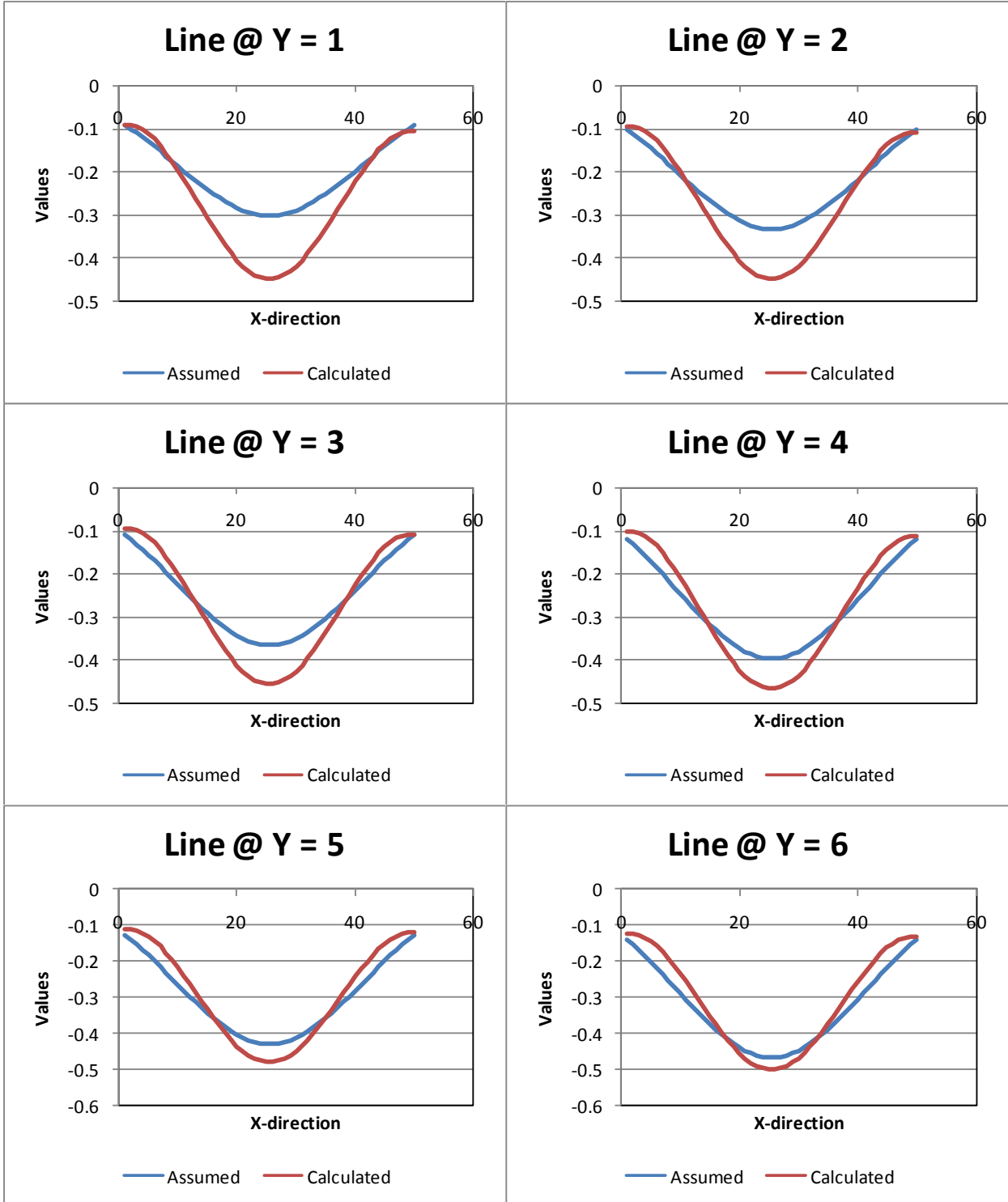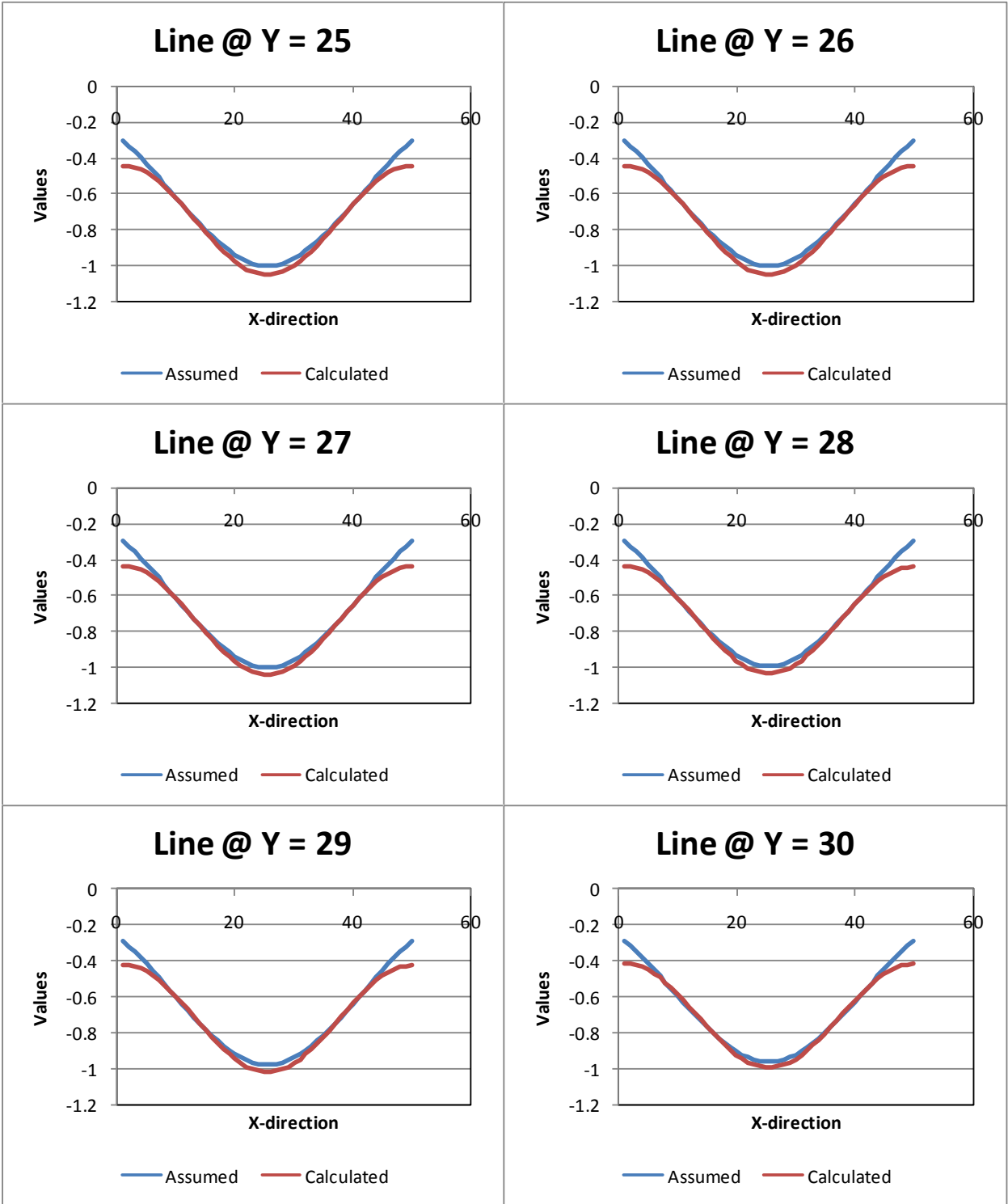
Case32:

Tilt1+2+Displ,0%err, Using 50points in 1 vertical and 1 horizontal row, mid points, X,Y=250(points between 10-490)   RMSE=0.043257254
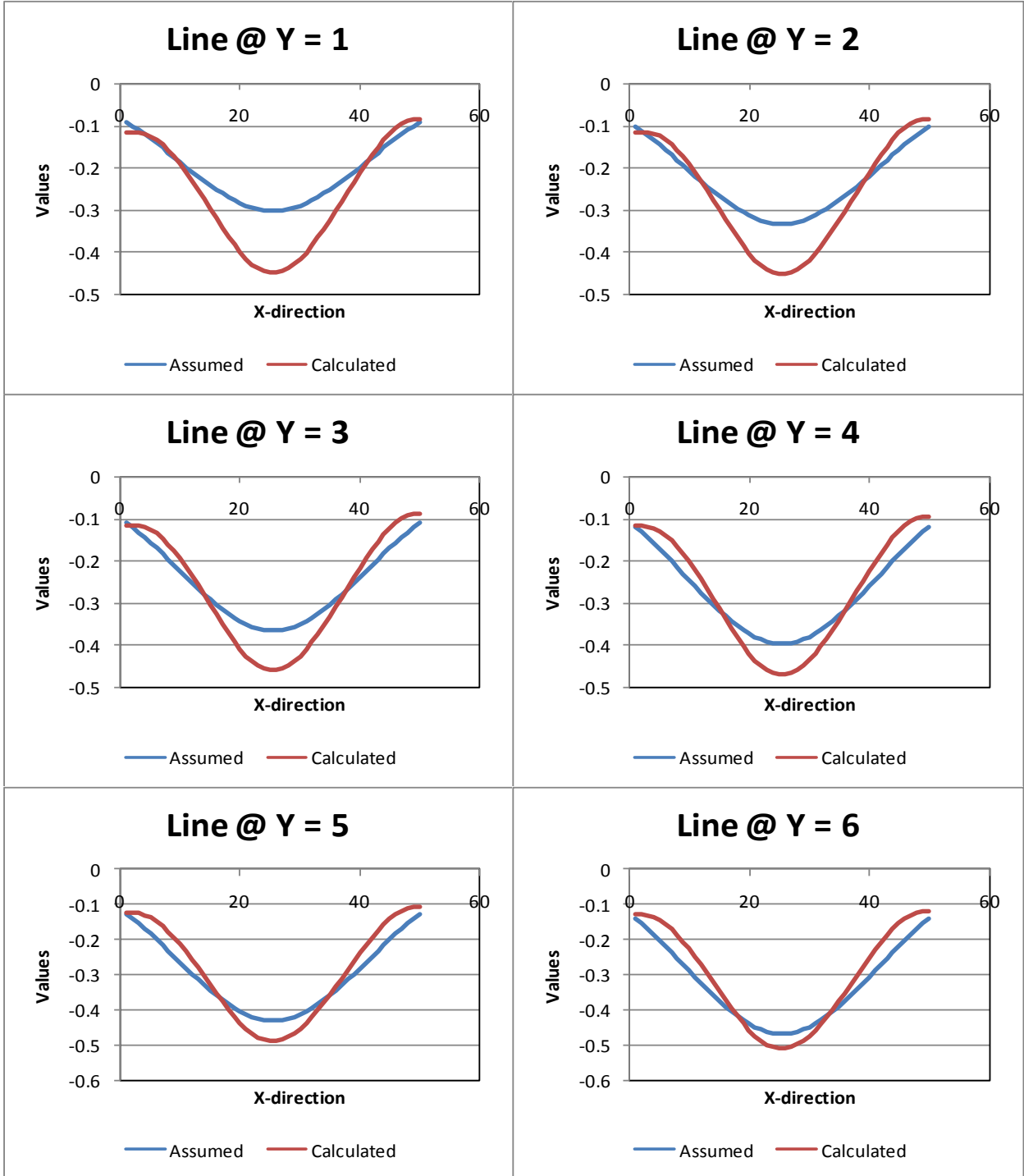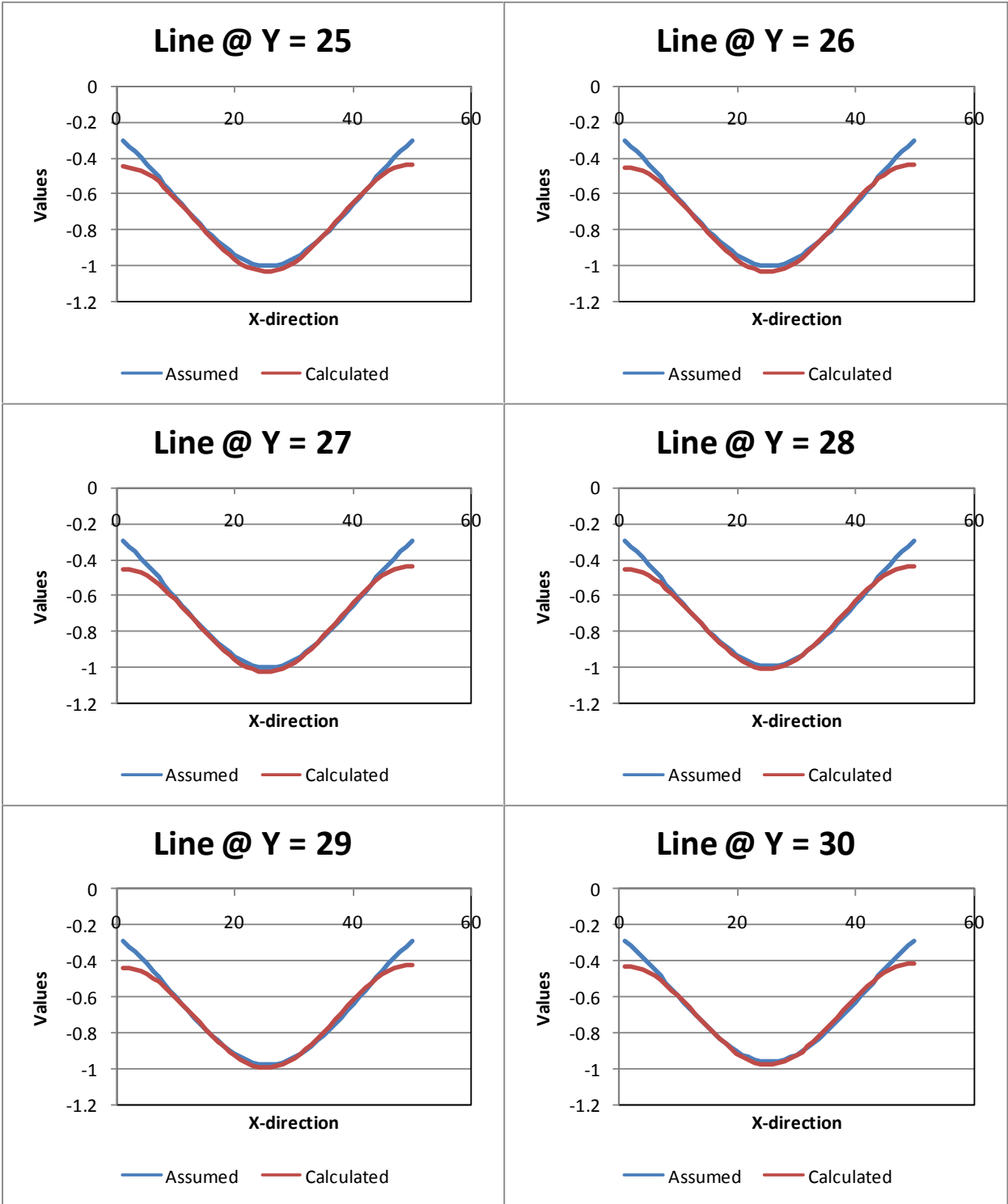
Case33:

Tilt1+2+displ, 0%err Using 10points in 1 vertical and 1 horizontal points, mid points of the grid X,Y=250
5<x,y<495   RMSE=0.047407172

207
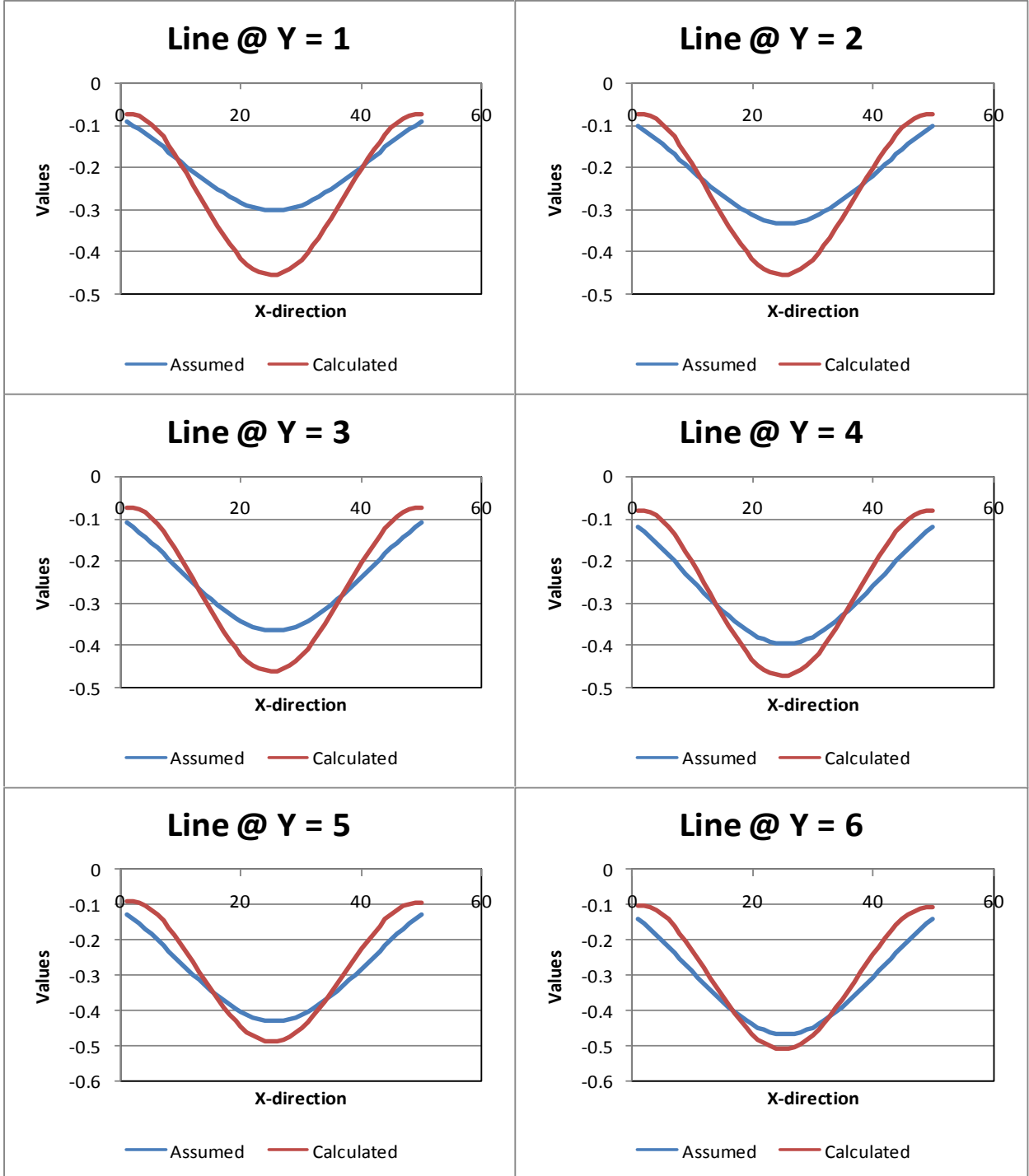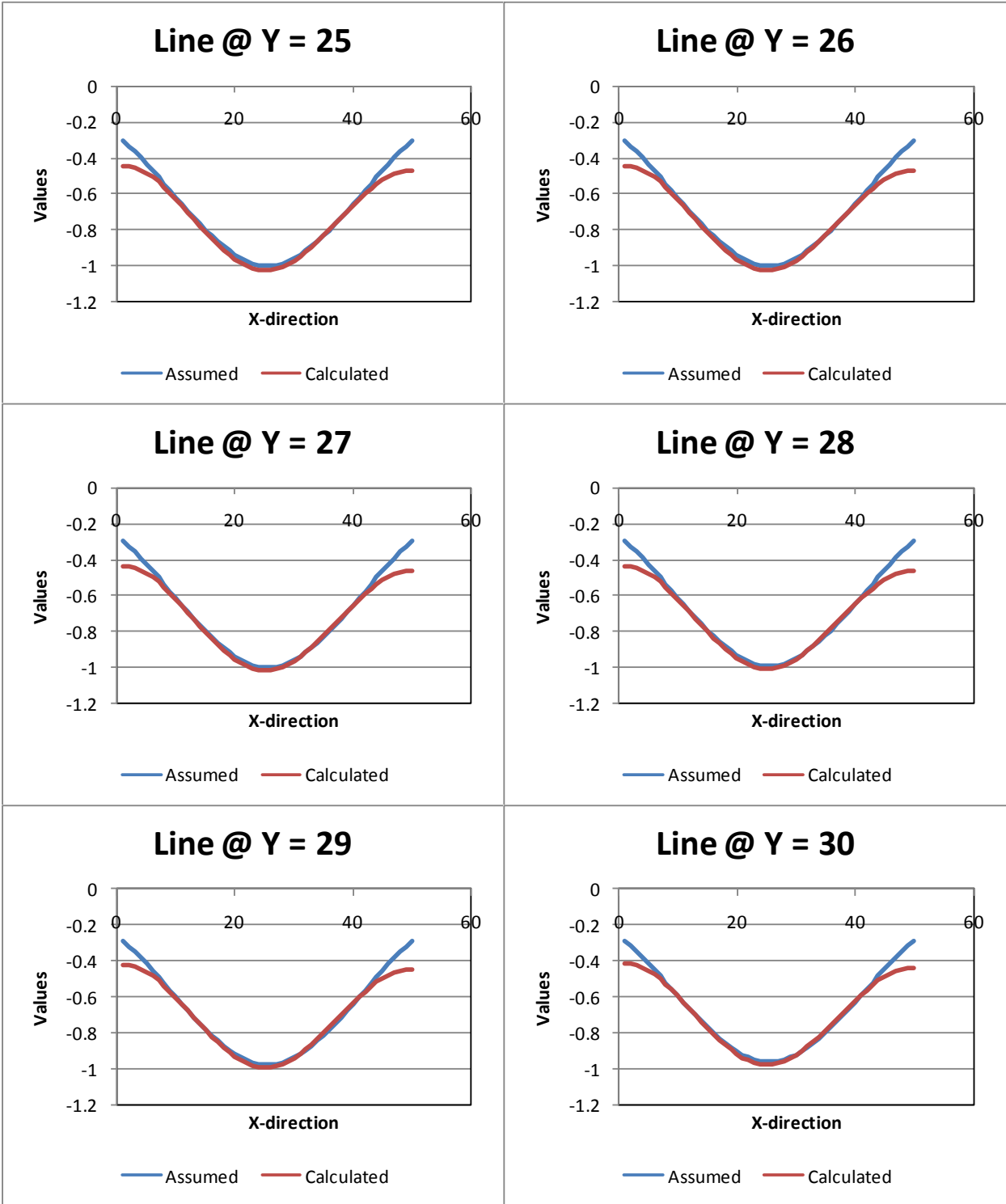
Case34:

Tilt1+2 10%err, Using1000 points in 1 vertical and 1 horizontal rows,-500<x,y<1000
RMSE=0.318229
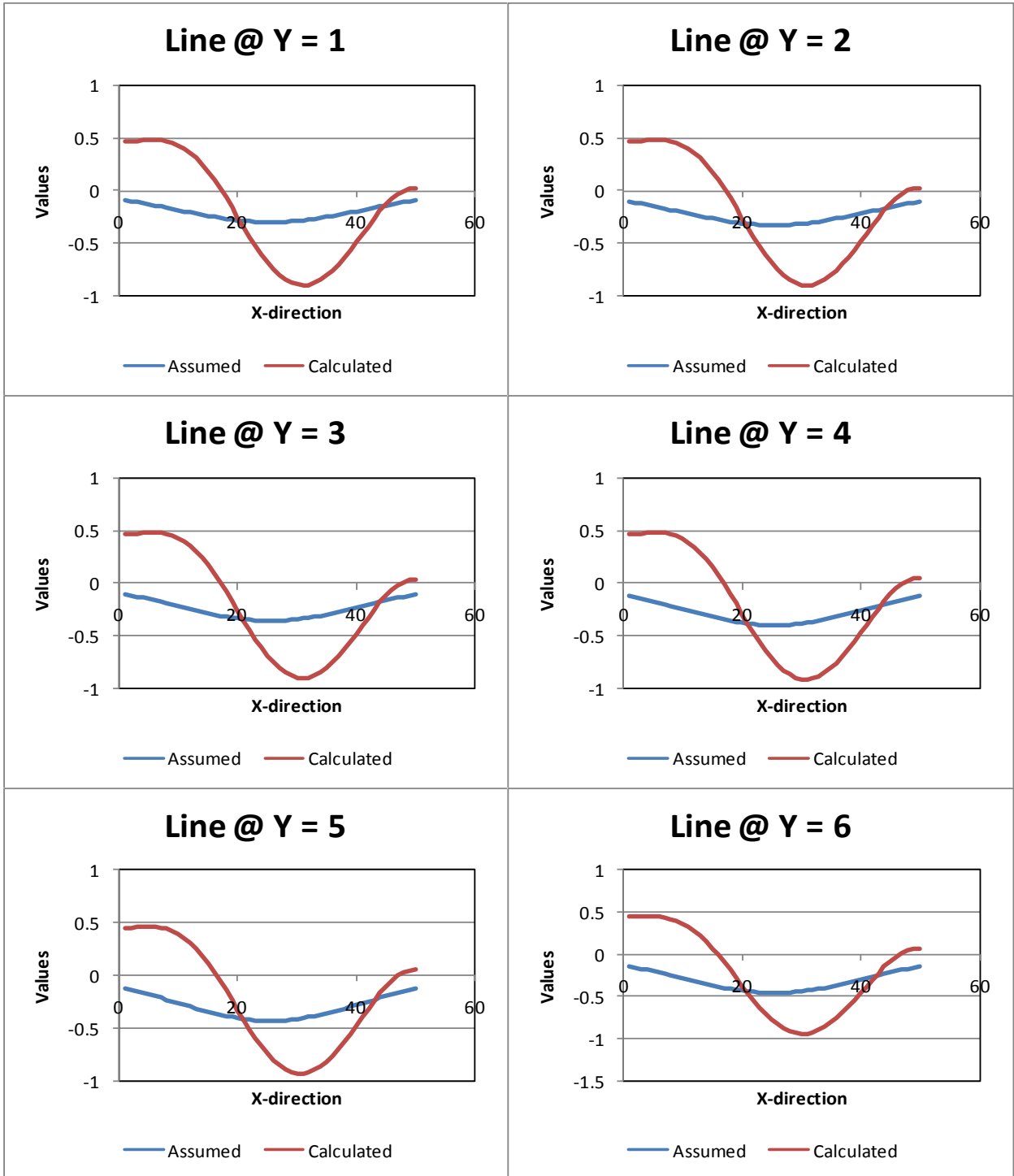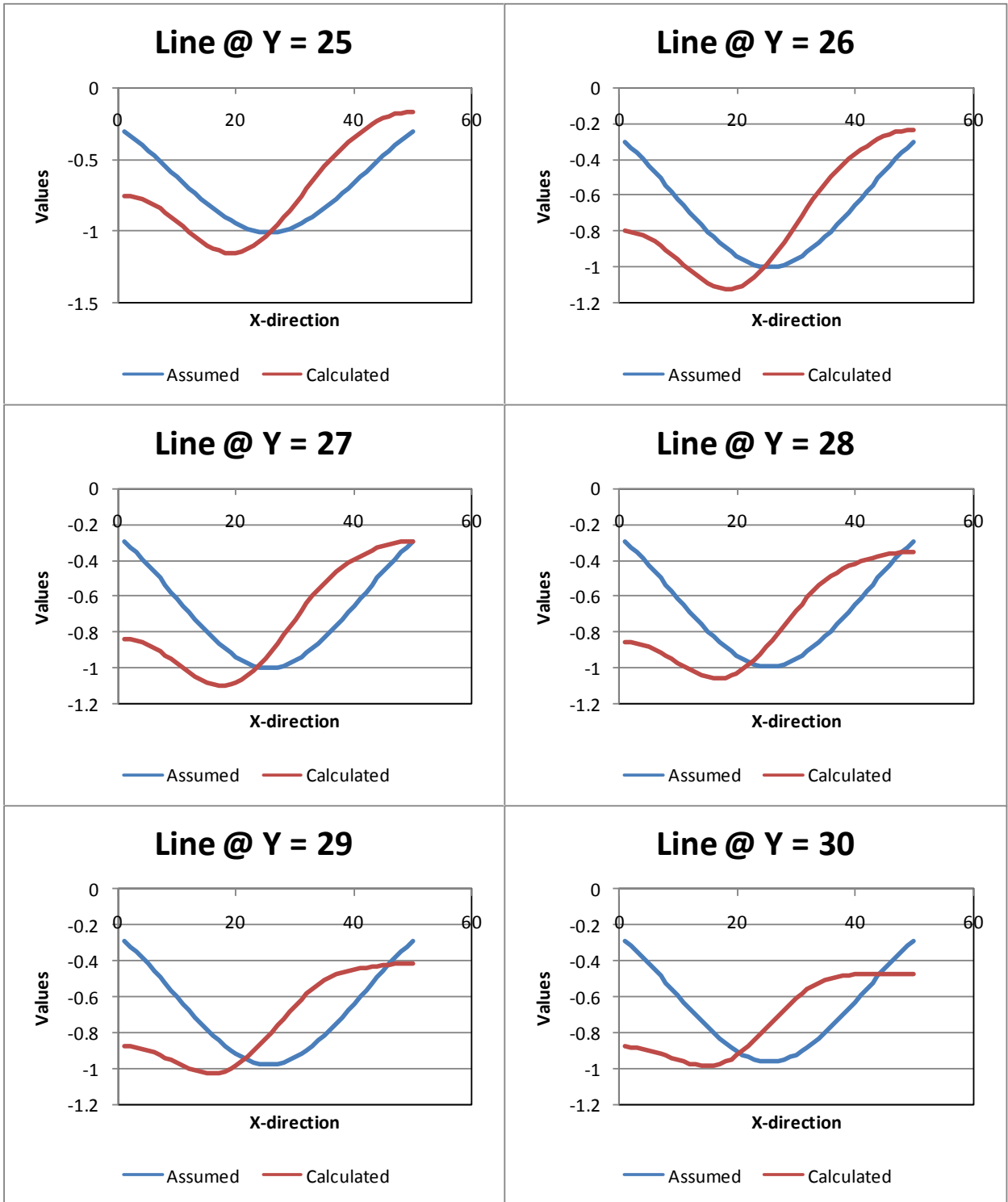
Case 35:

Tilt1+2,10% err, Using300 points in 1vertical and 1horizontal rows, -500<x,y<1000
RMSE=0.3297
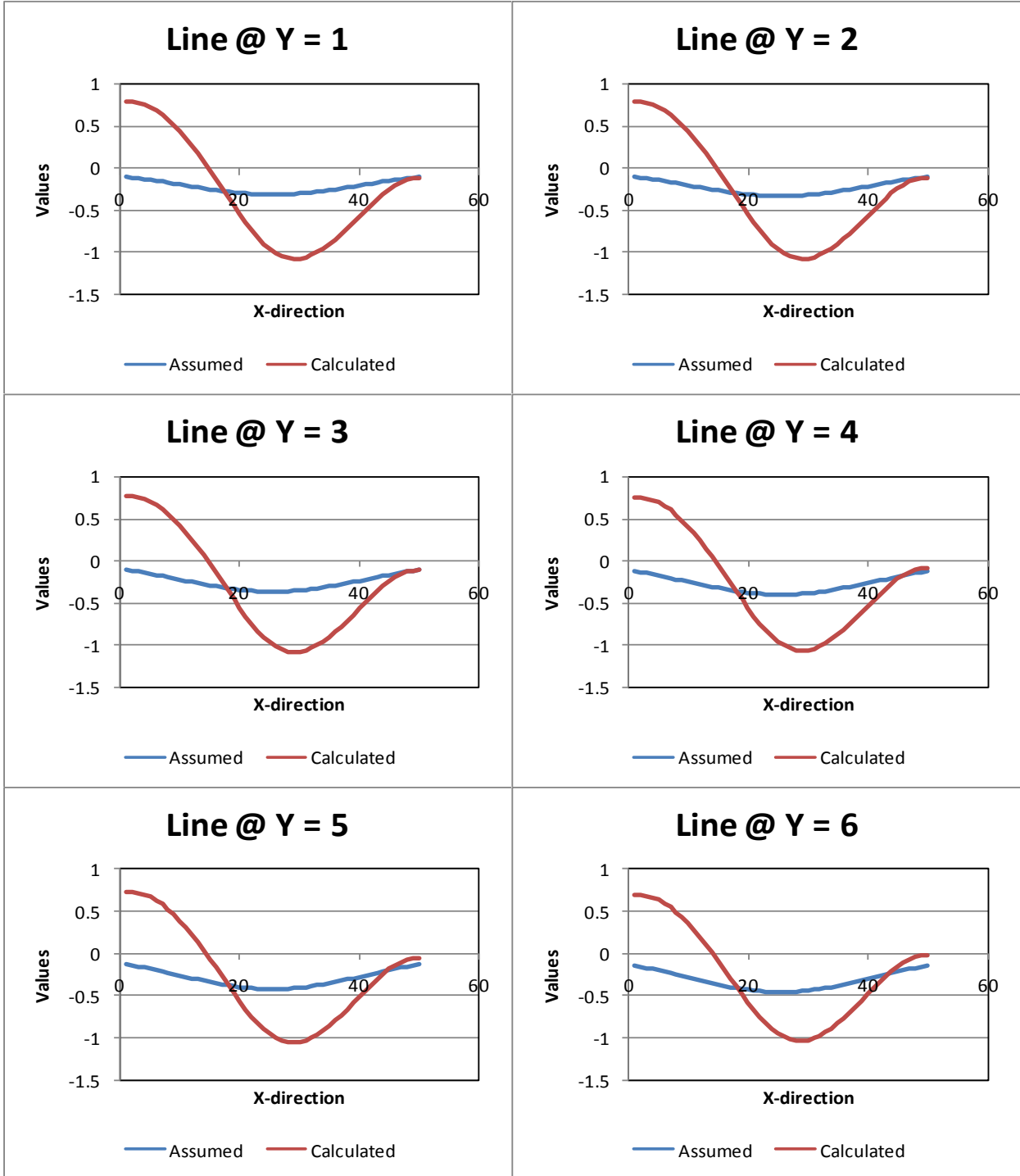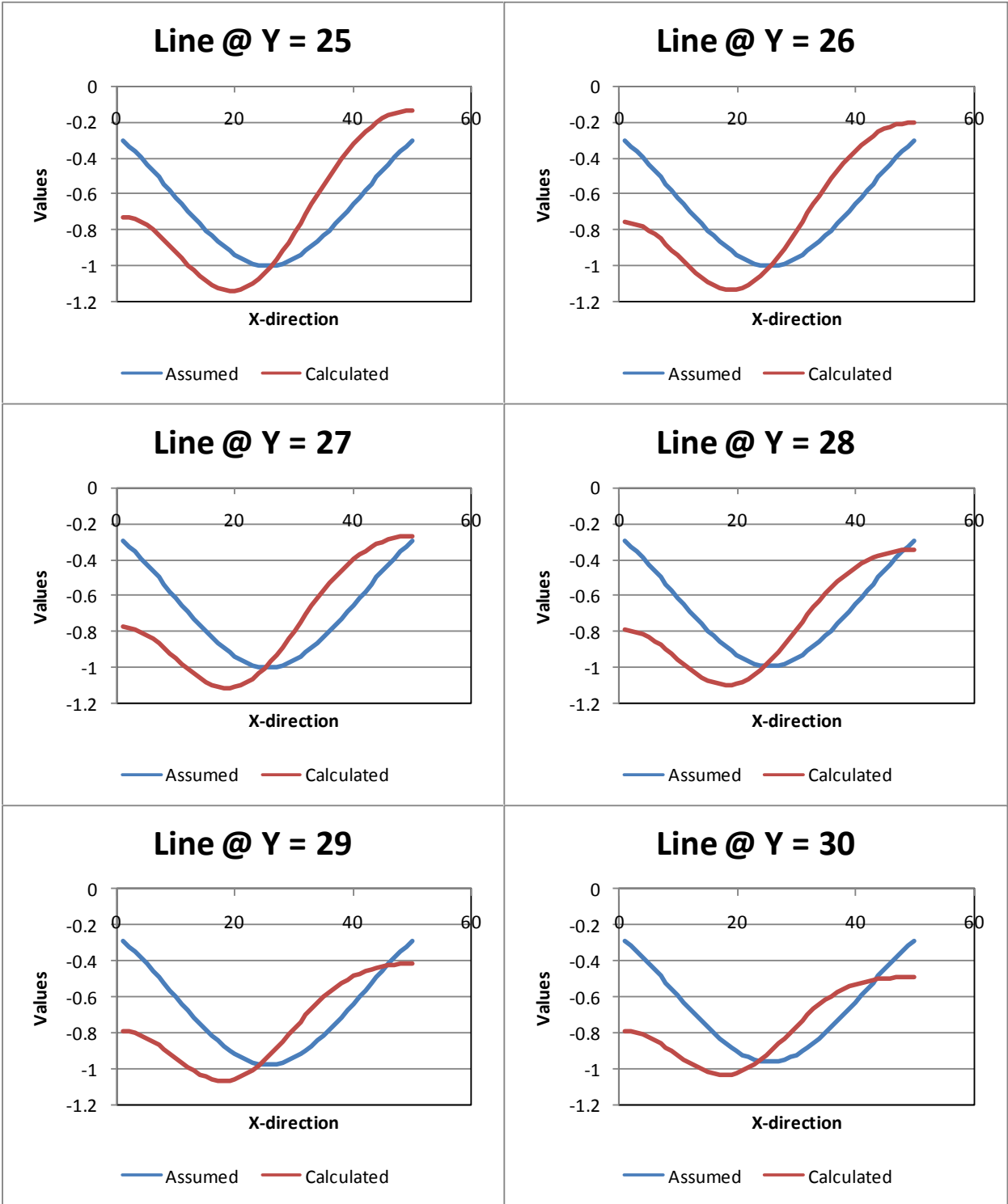
Case 36:

Tilt1+2, 10%err Using 300points in 1 horizontal & 1 vertical row   0<X,Y<500
RMSE=0.328058

213
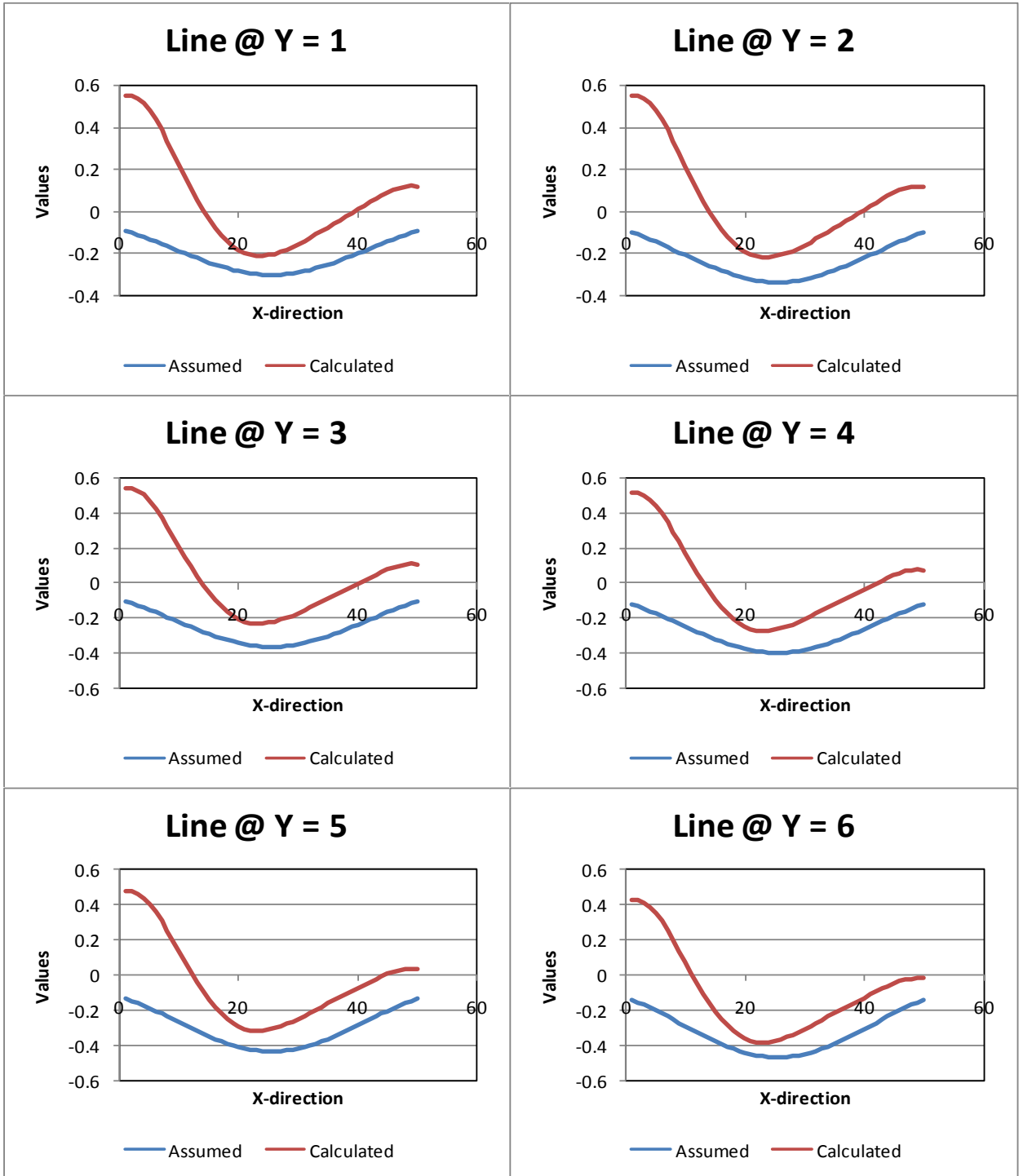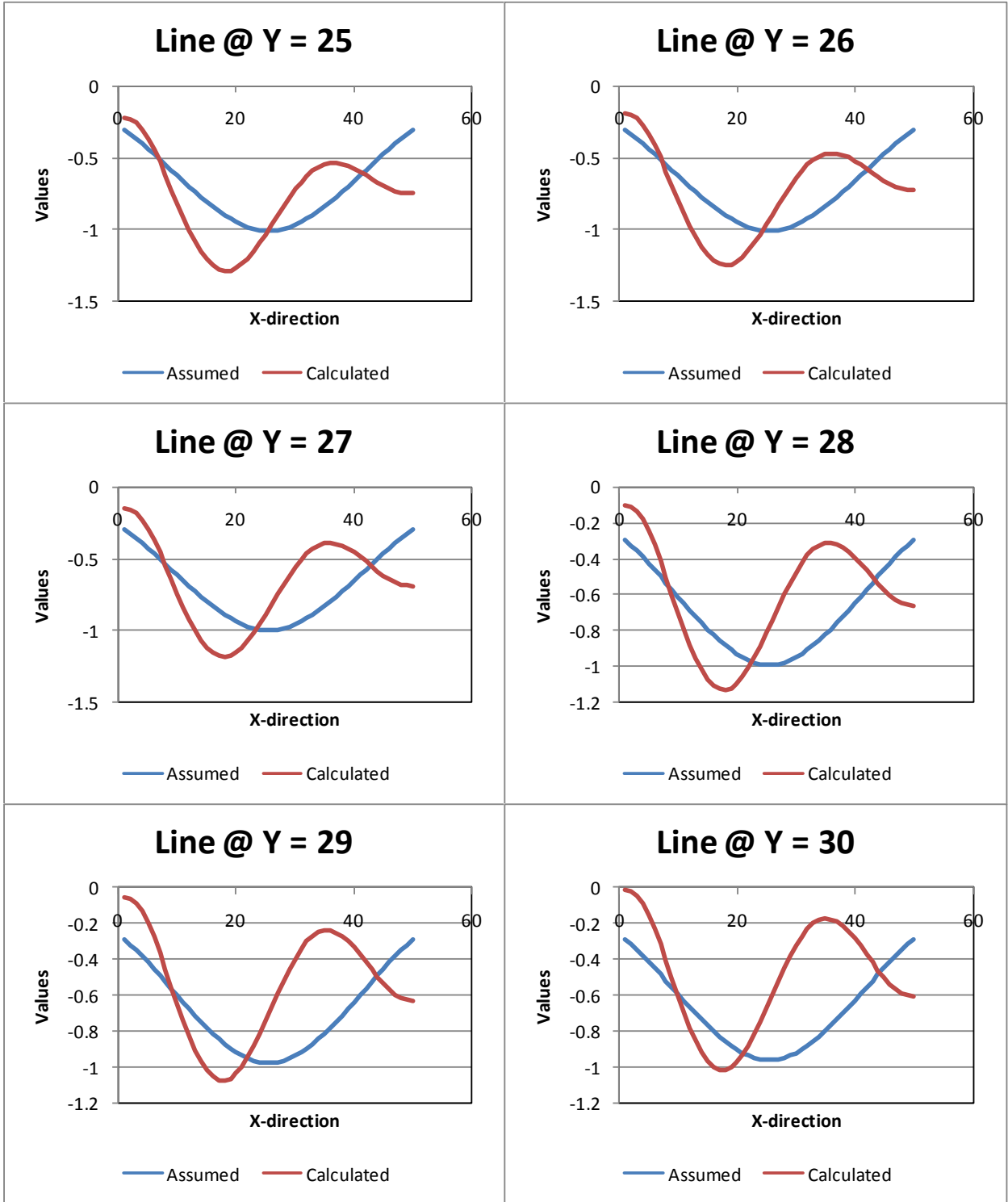
Case37:

Tilt1+2, 10%err   Using300points in 3 horizontal,3 vertical rows
RMSE=0.291543

Line @ Y = 25

Line @ Y = 26

Line @ Y = 27

Line @ Y = 28

Line @ Y = 29

Line @ Y = 30
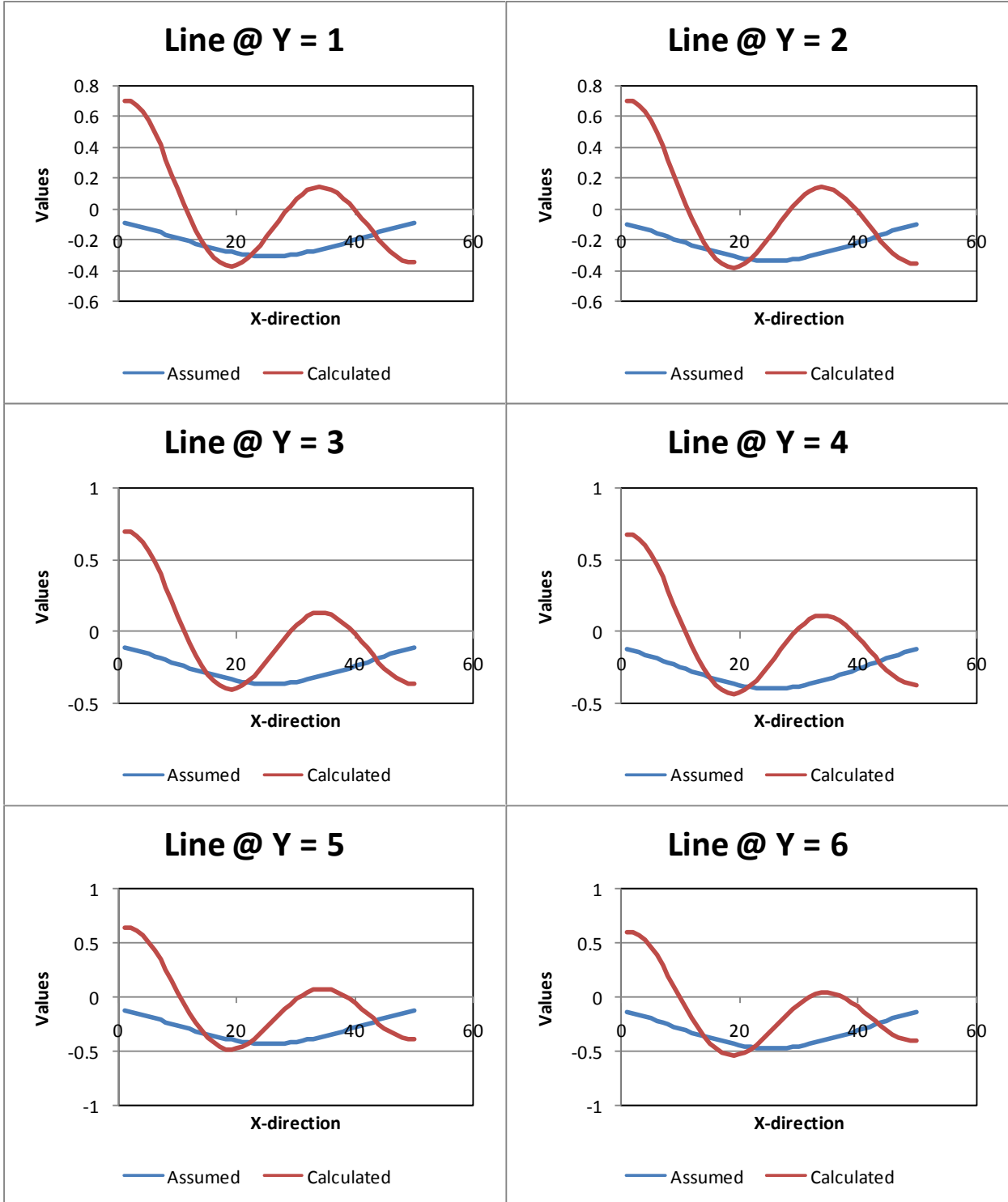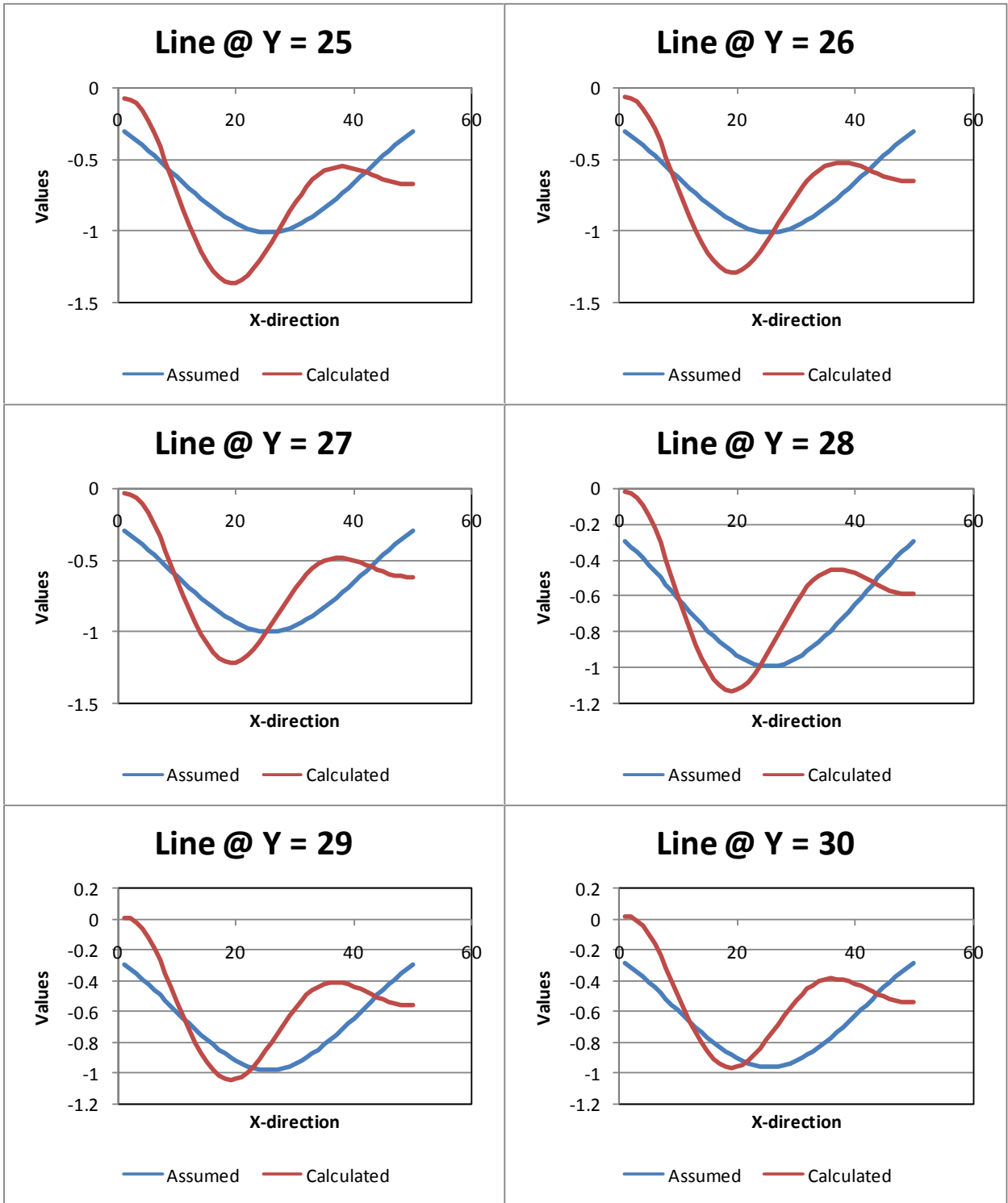
Case38:

300points,3 vertical,3 horizontal rows,100m spacing between rows,10% err
RMSE=0.339687
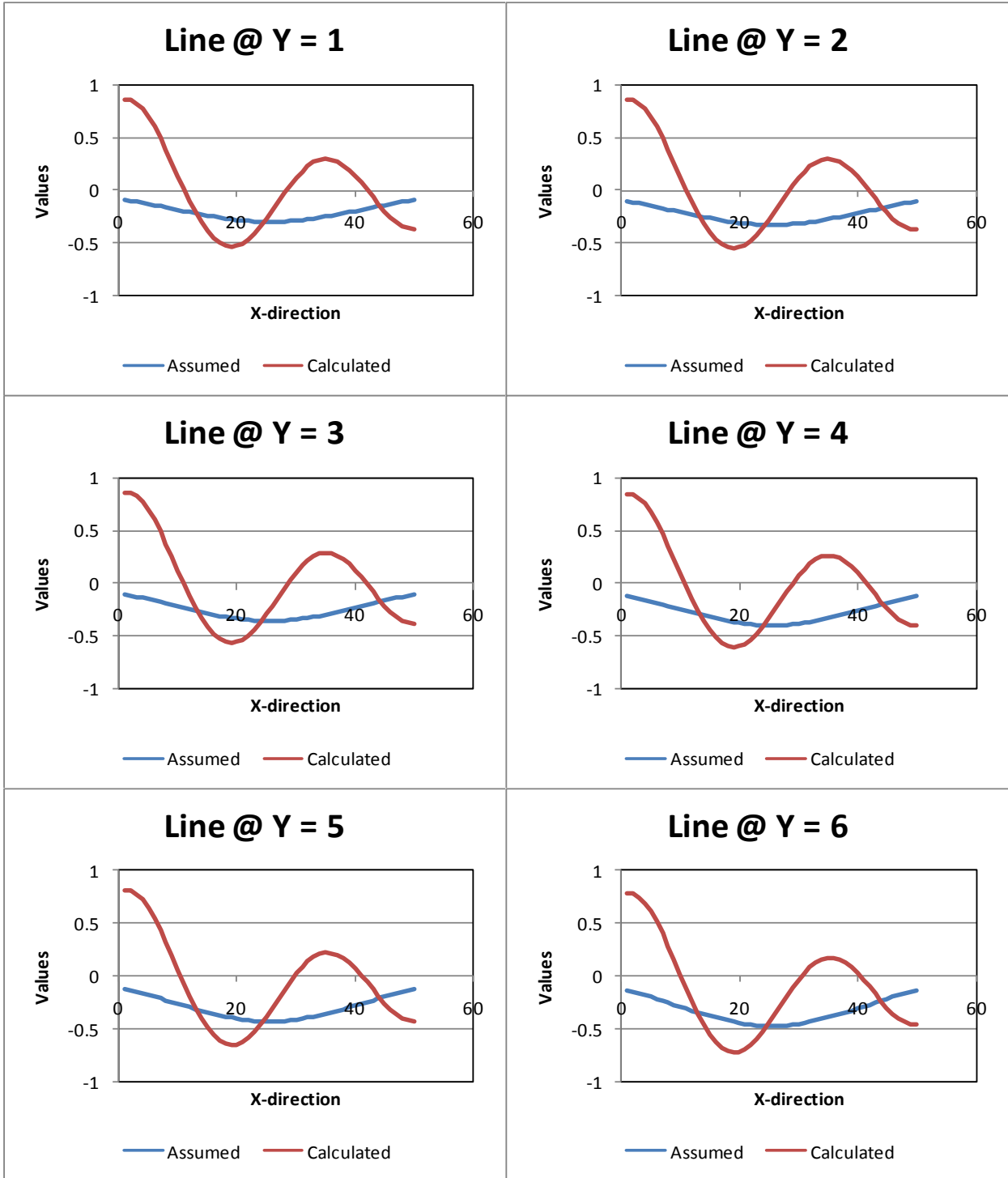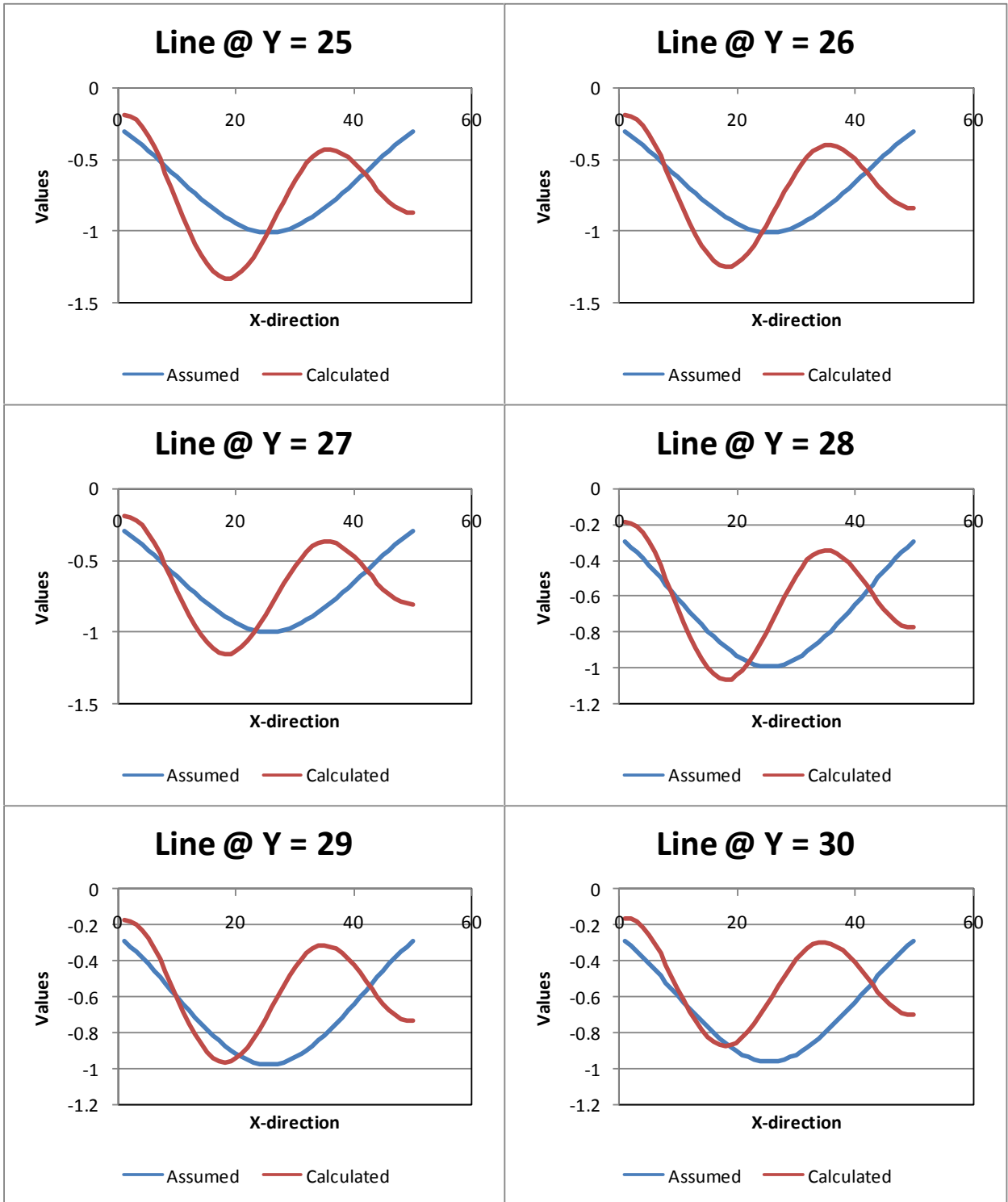
Case39:

300 points 6Vertical rows of 50, 10% err, Tilt1+2   RMSE=0.222957

Line @ Y = 25

Line @ Y = 26

Line @ Y = 27

Line @ Y = 28
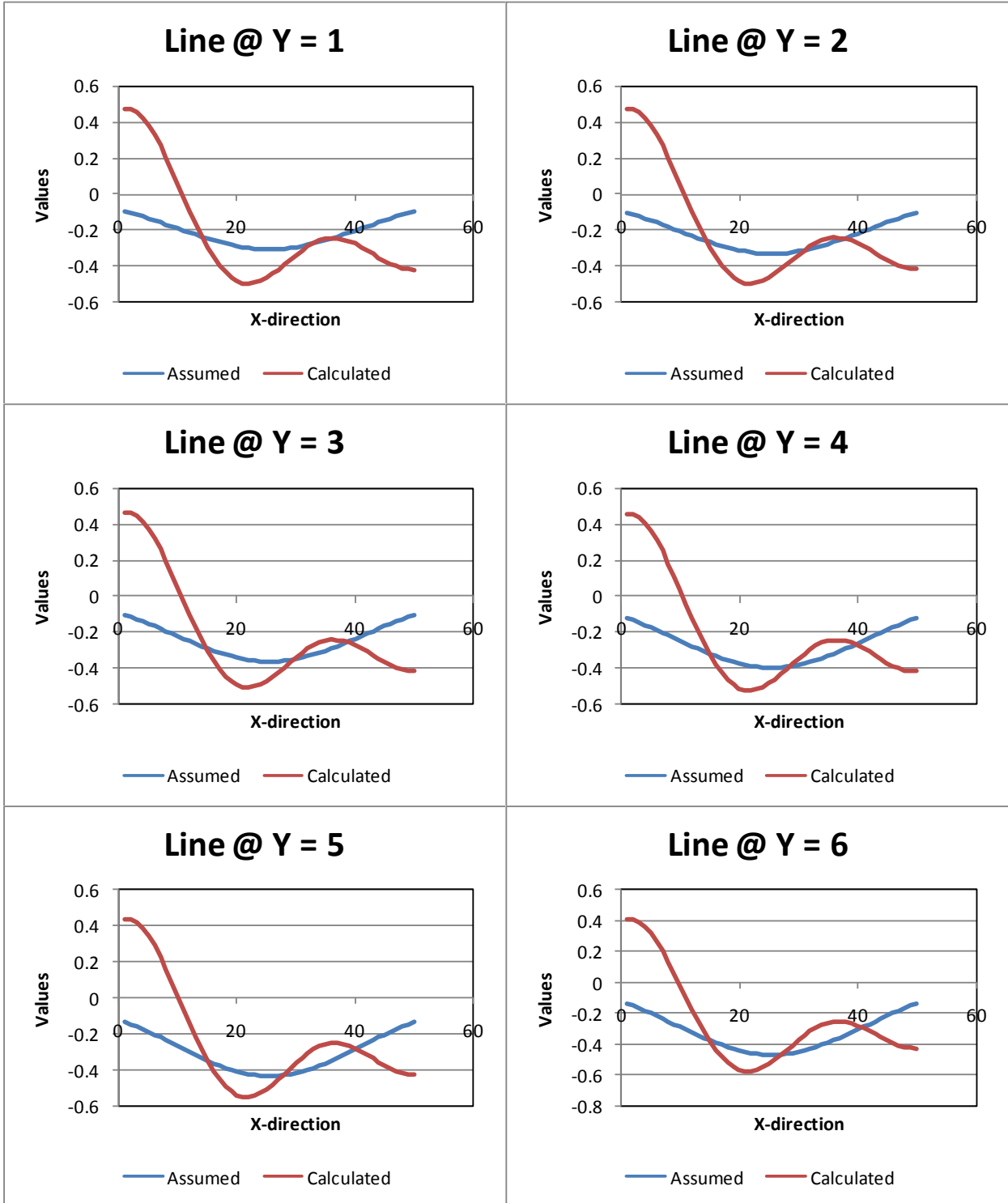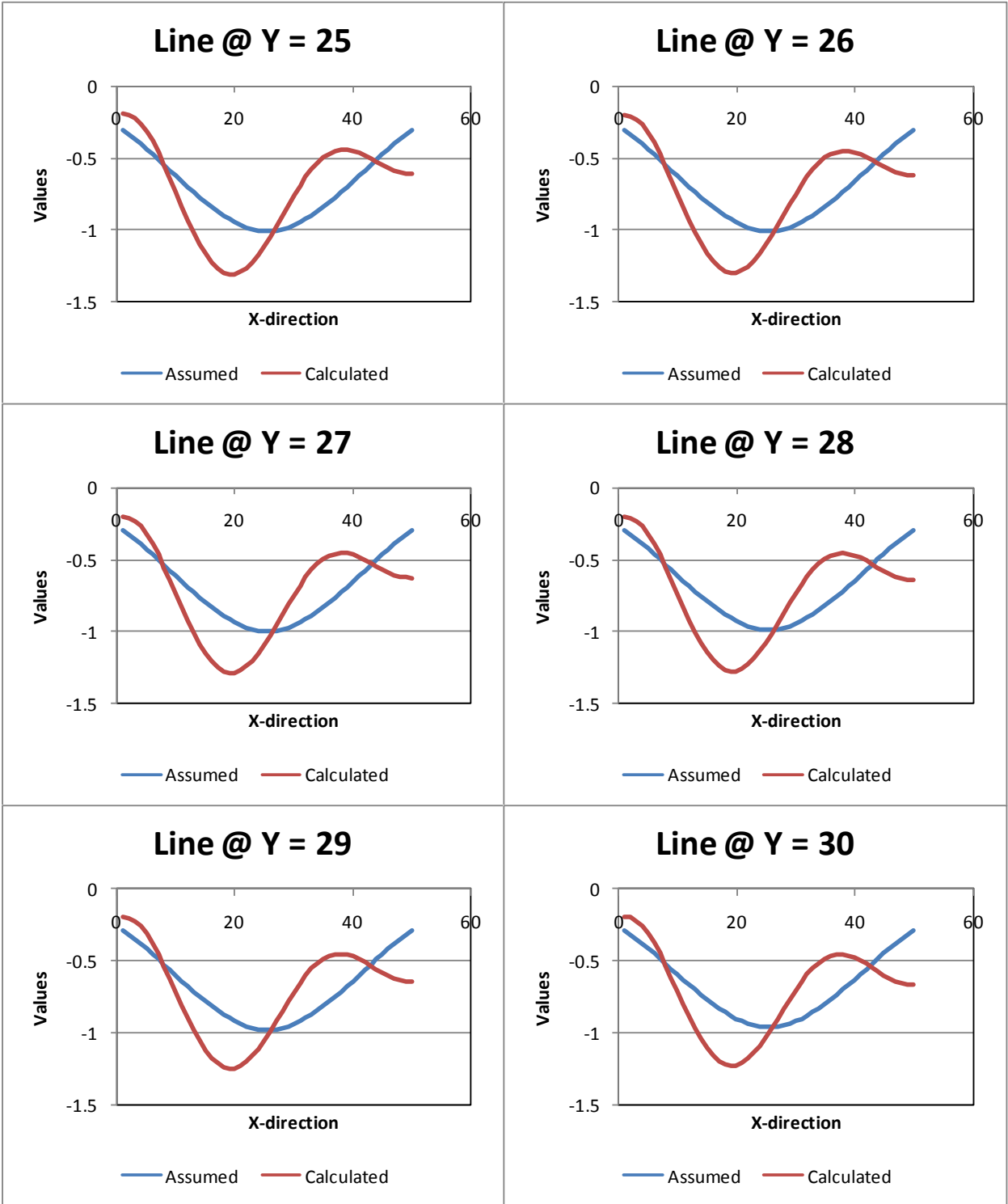
Line @ Y = 29

Line @ Y = 30

Case 40:

Tilt1+2 , 10%err   Using 300 points in 2 vertical rows 0<x,y<500   RMSE=0.271487
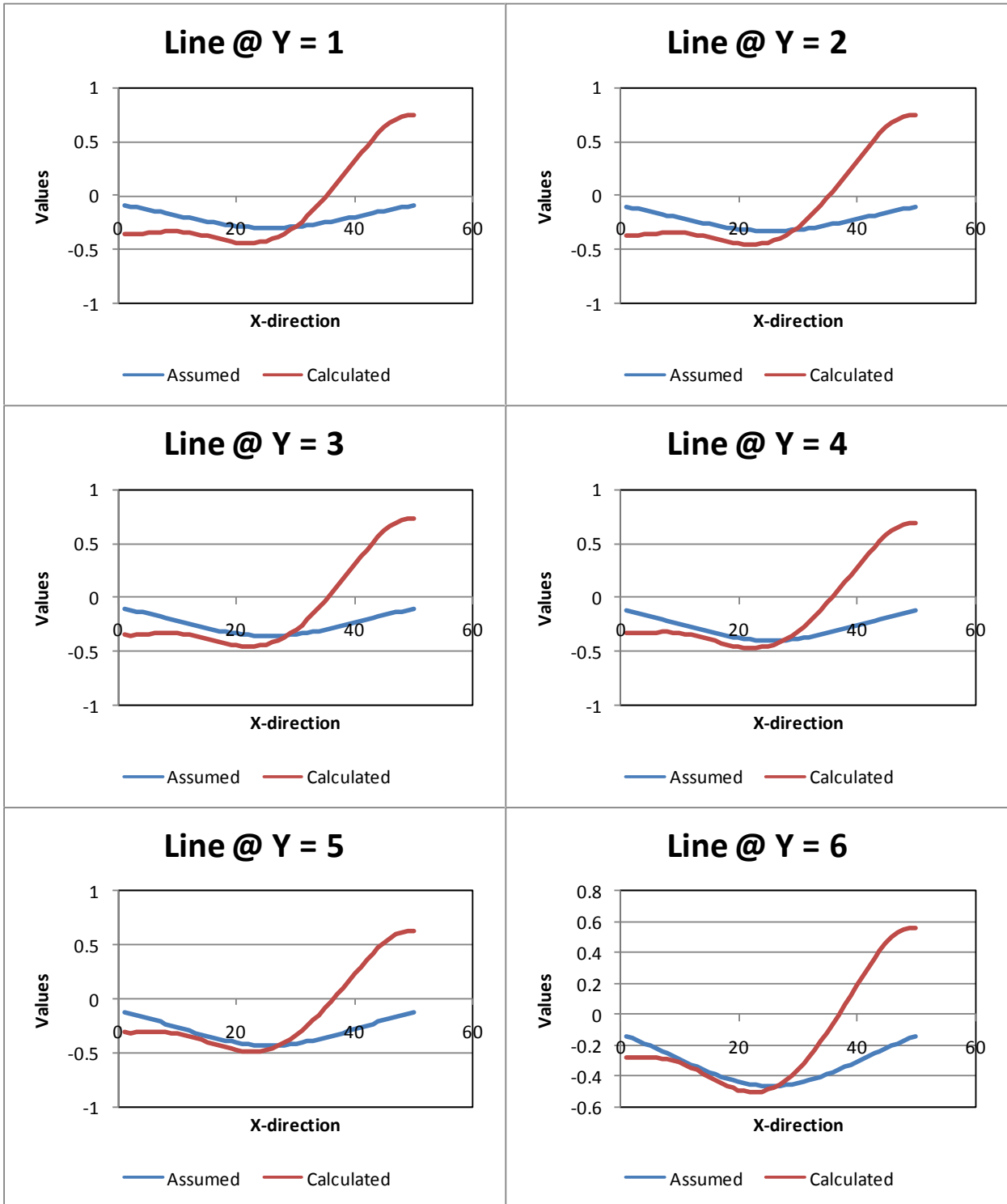
Line @ Y = 25
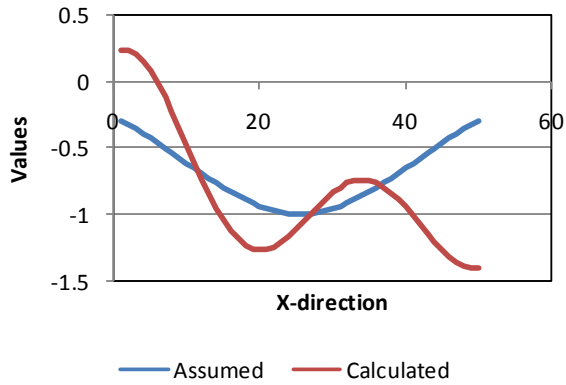
Line @ Y = 26
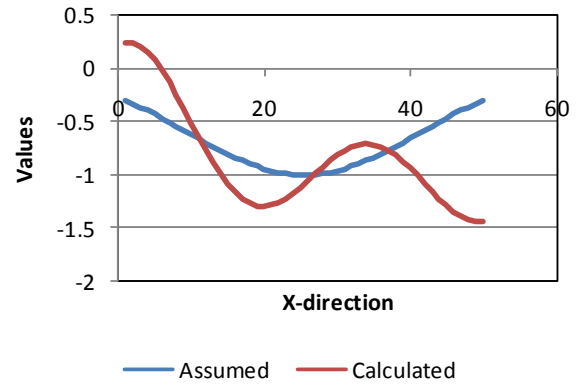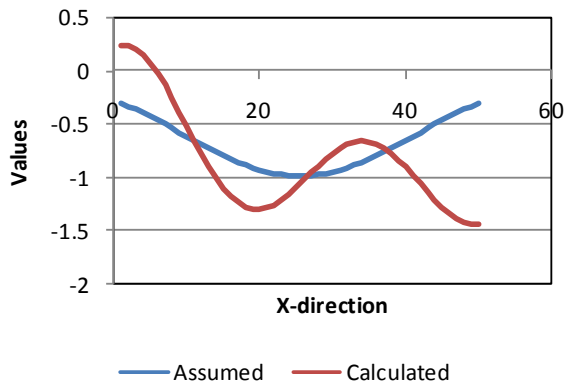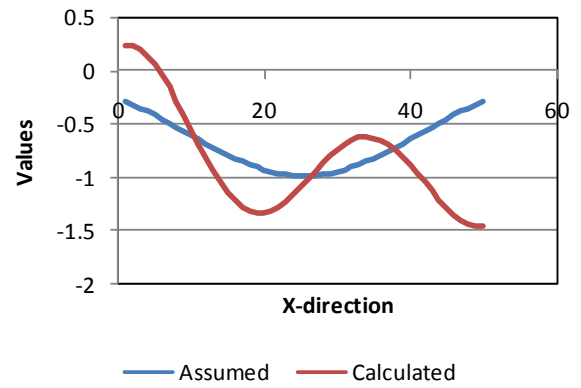
Line @ Y = 27
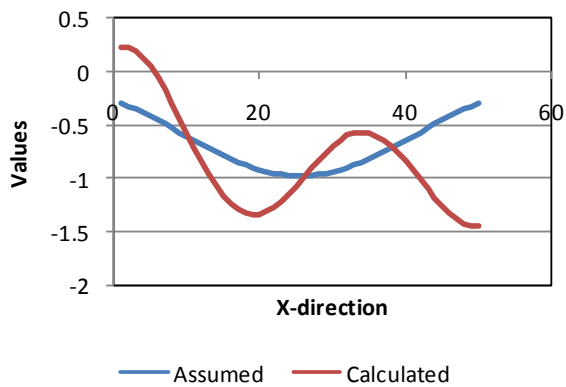
Line @ Y = 28

Line @ Y = 29

Line @ Y = 30
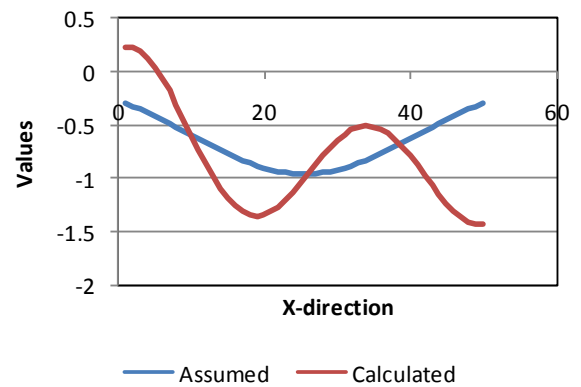
Case41:

Tilt1+2,10%err, Using 100 points in 1 horizontal and 1 vertical row 0<x,y<500
RMSE=0.375072
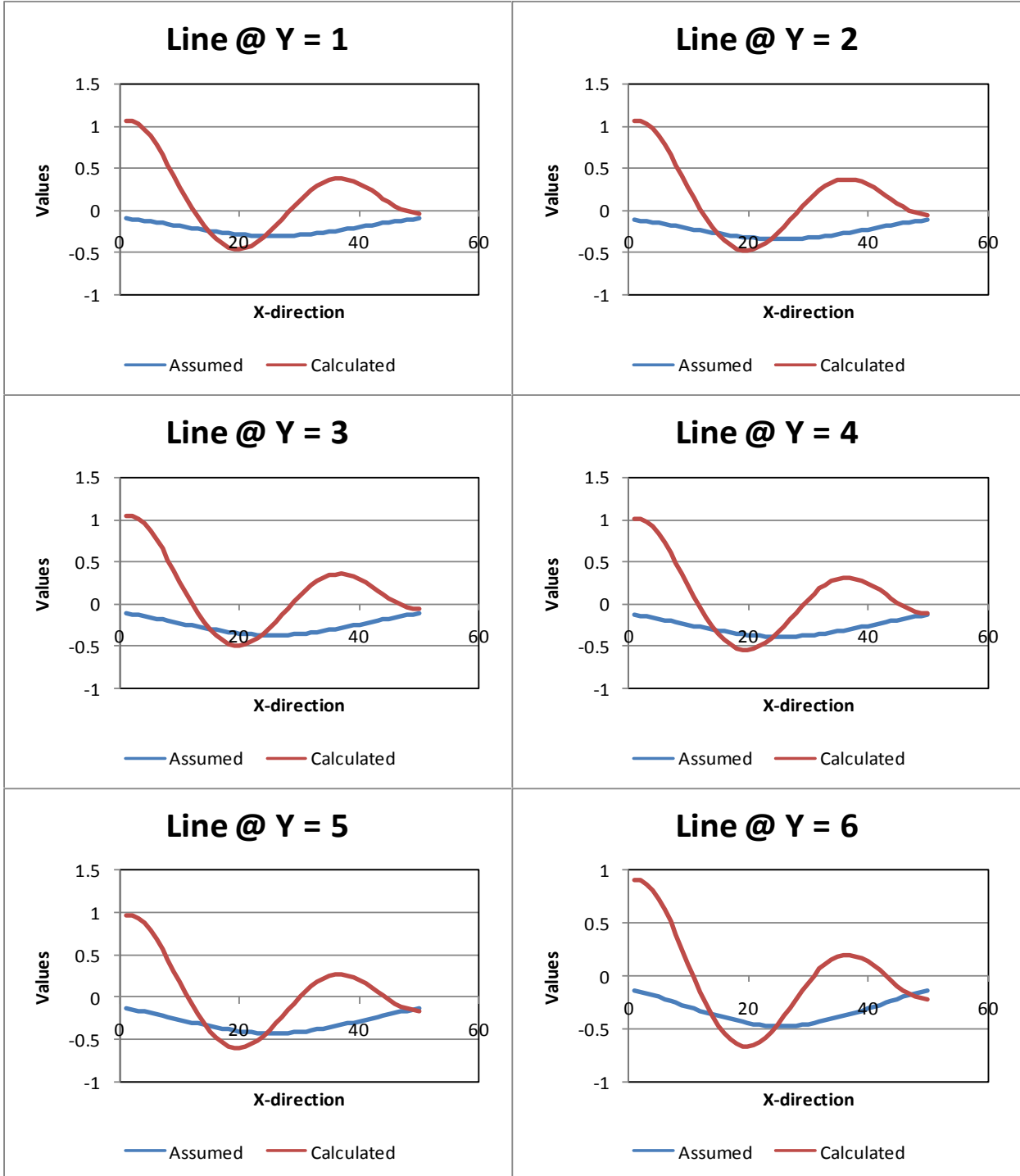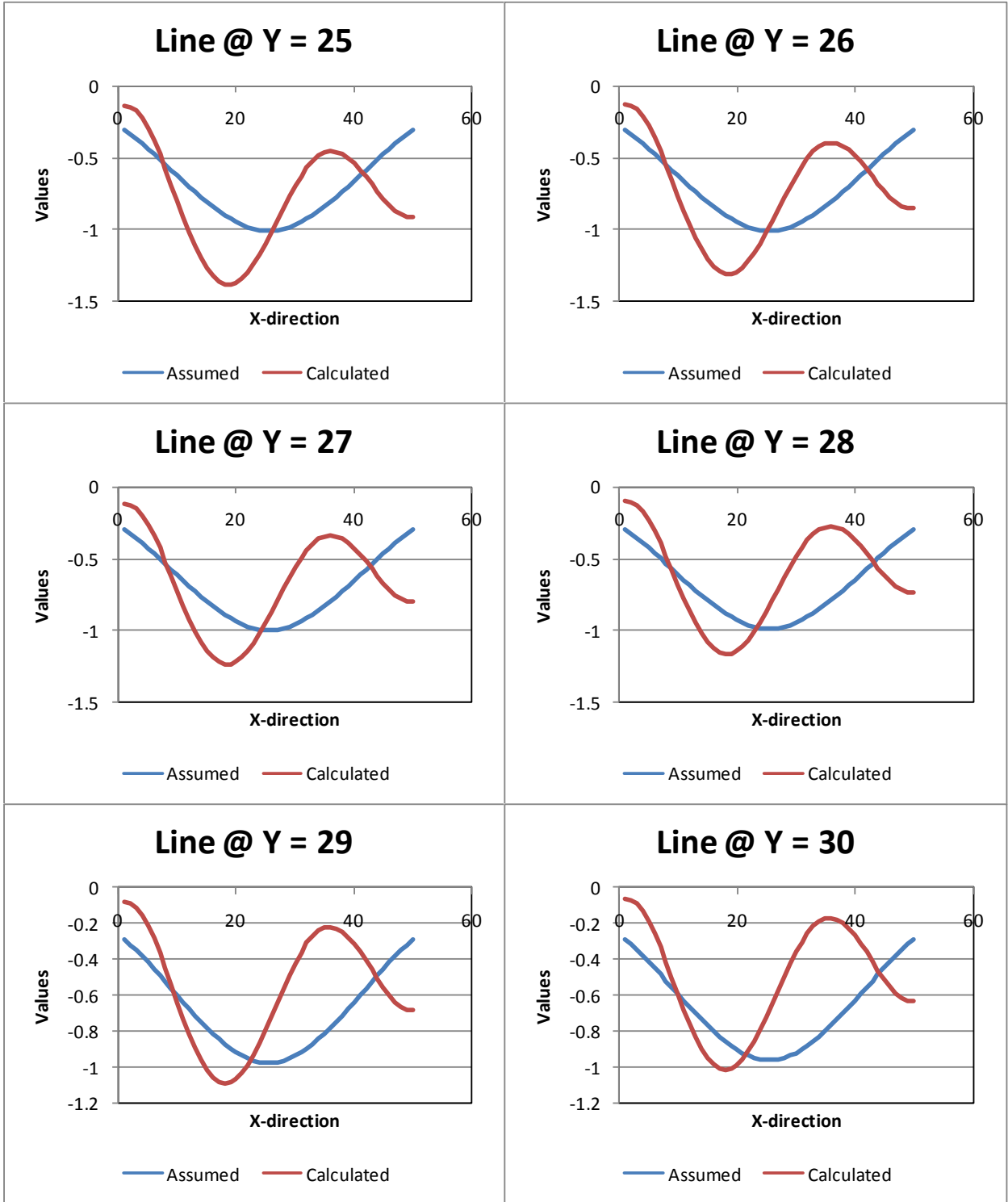
Case42:

Tilt1+2, 5%err   Using300 points in 6 rows   RMSE=0.116004

Line @ Y = 1

Line @ Y = 2

Line @ Y = 3

Line @ Y = 4
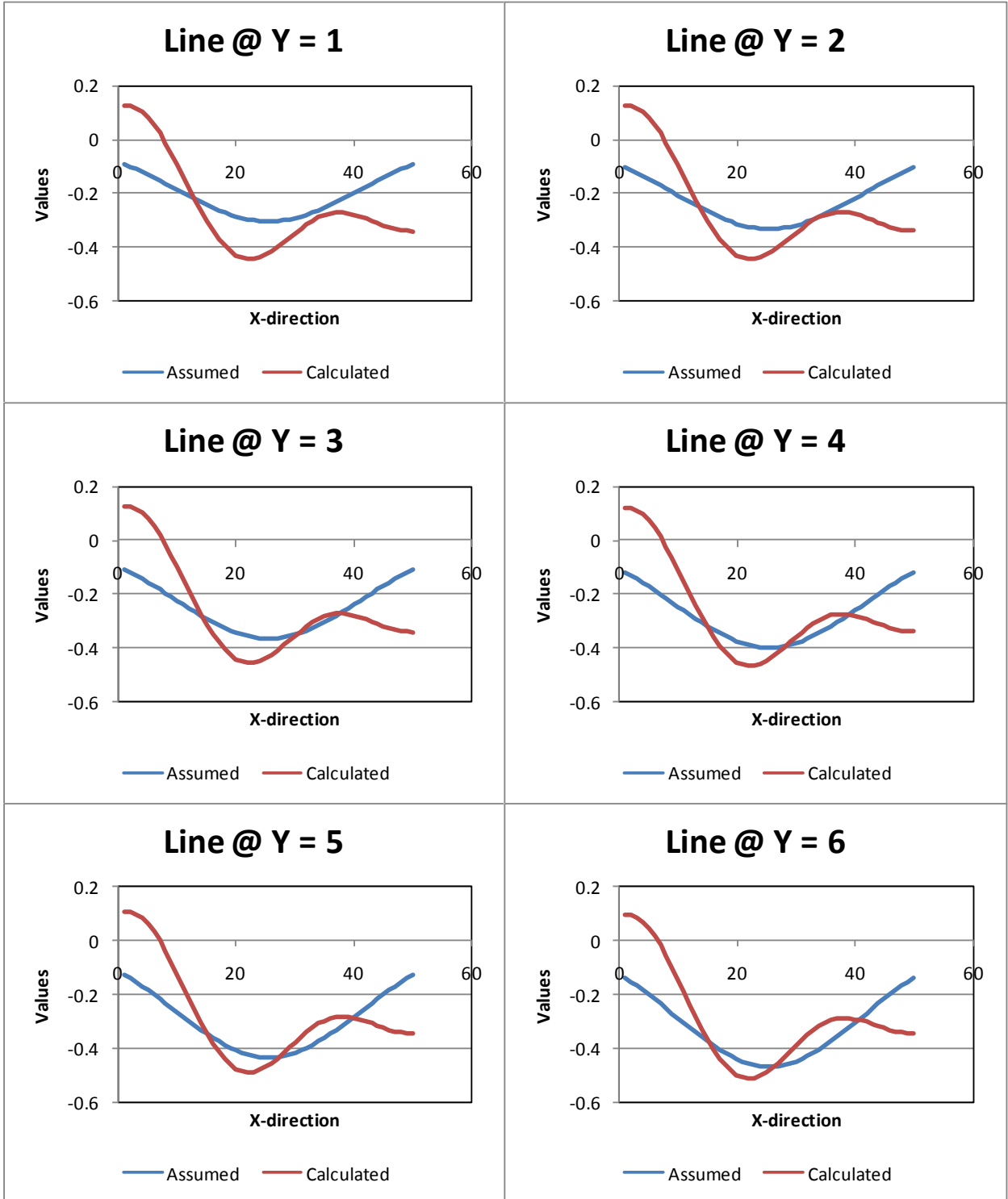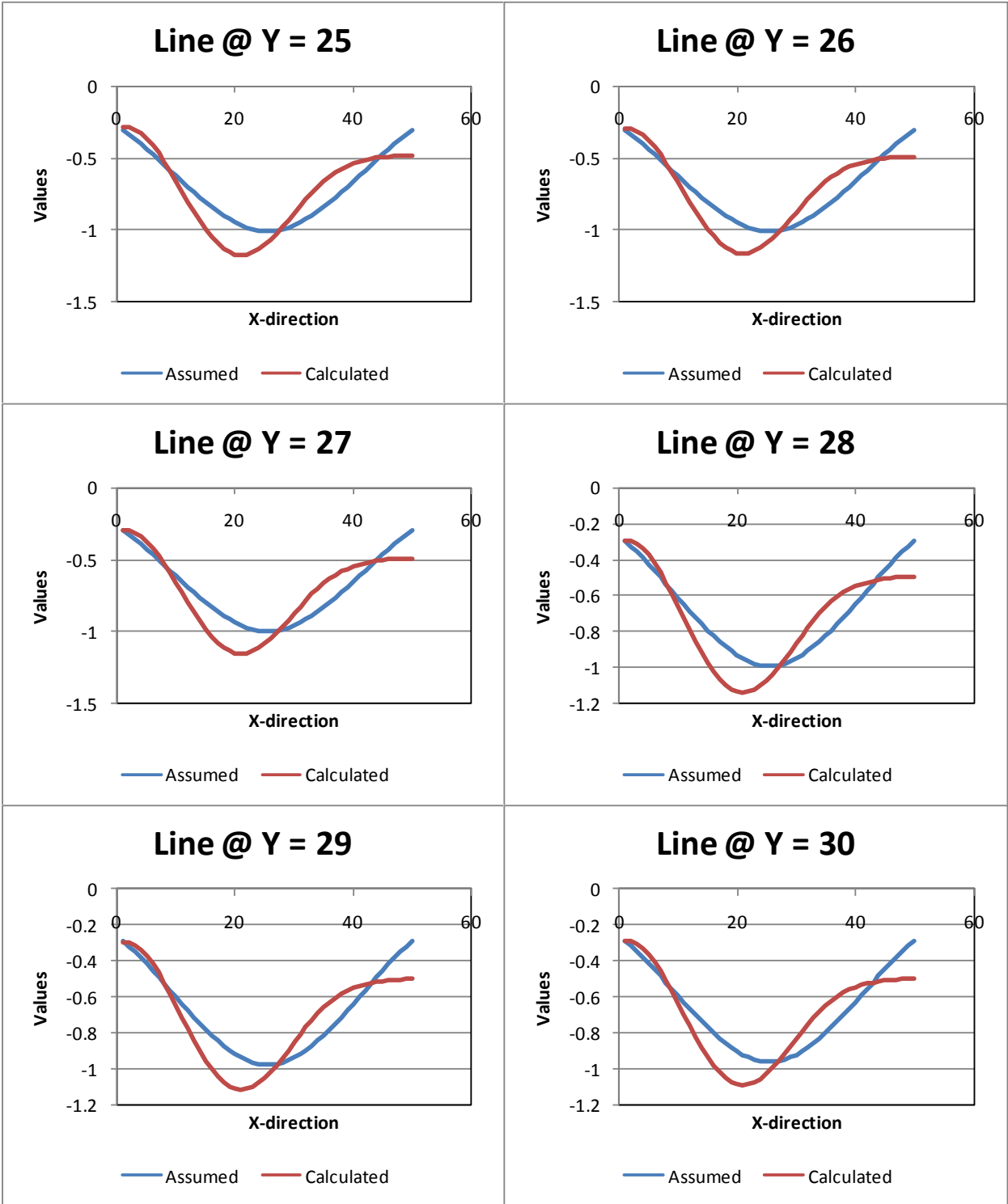
Line @ Y = 5

Line @ Y = 6

Case43:

Tilt1+2-3%err   Using 300points at 6 vertical rows   RMSE=0.080343
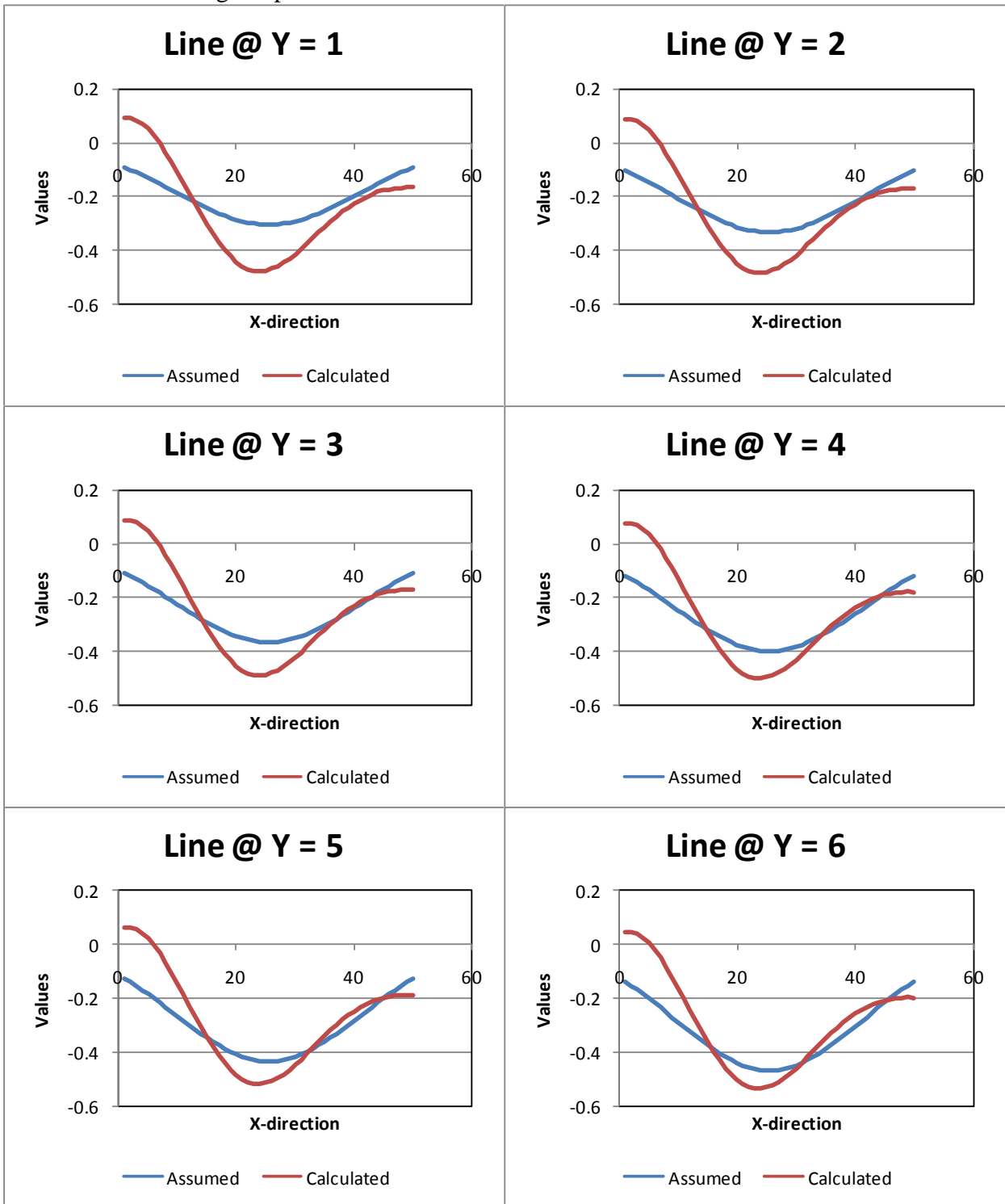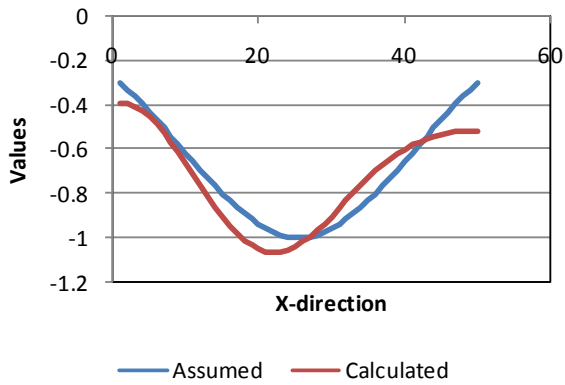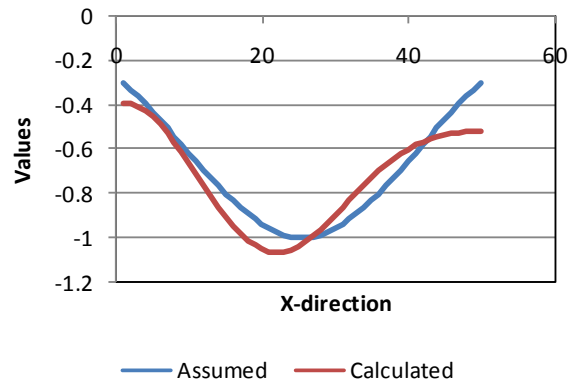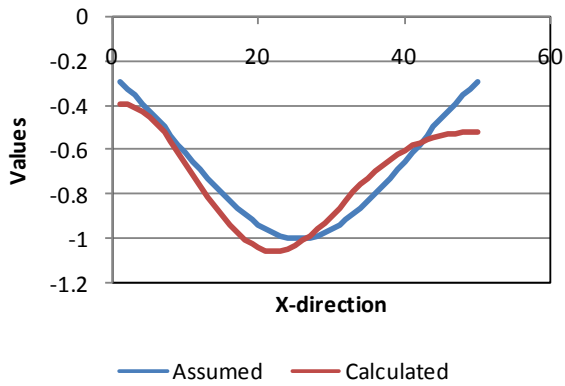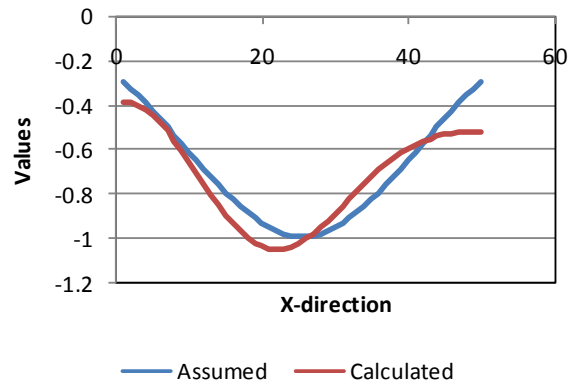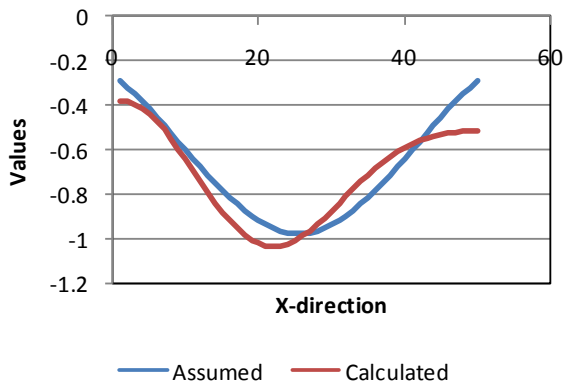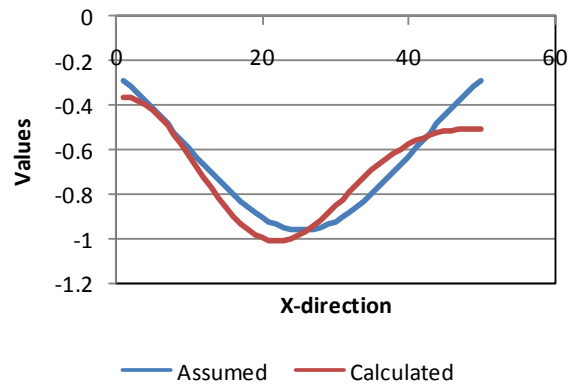
Appendix VI: the numerical modeling of the inverse solution in C++

The Coding of the direct and inverse solution:

```cpp
#include<iostream>
#include<fstream>
#include<iomanip>
#include<cstdio>
#include<math.h>
#include<time.h>
#include <stdio.h>
using namespace std;
void okadadisp(double x,double y,double z,double e,double d,double dip,double sn,double cs,double prt, double
a[3]);
void okadatilt(double x,double y,double z,double e,double d,double dip,double sn,double cs,double prt,double
tss[5],double tds[5],double tts[5]);
void calculation(double ,double ,double ,double ,double ,double ,double ,double , double ,double ,double ,double ,
double* ,double* ,double* ,double* ,double* ,double*,double*);
void laplace(double dx,double N,int nx,int ny,double **lap,double **L);
void SVDcmp(int,int,double **KL,float **u,float **s,float **vT,float w[3600],float **v);
void svbksb(float **u,float w[3600],float **v,int m,int n,float b[3600],float x[3600]);
void main()
{
        double dx,dy,FL,FW,XF4,YF4,disS[4],disD[4],disT[4],Tstrike[4],Tdip[4],Ttensile[4];
        double disstrike,disdip,distensile,TStrike[4],TDip[4],TT[4];
        double l,W,Dx,Dy,XO,YO,depth, dip,asim, depthr,dtr,umd4,ums4,umv4,Xmin,Xmax,Ymin,Ymax;
        int i,j,nx,ny,k,m,Nx,Ny,El;
        double U1[3600],U2[3600];
        int obser,el,o,F;
        double β;
        int NX,NY;
        float **u,**s,**vT,**v;
        float w[3600],Answer[3600],volume[3600];
        int NO;
        double UMV[3600],Err[3600],std,Var;
        double kk[4];
        double KK[4];
        double Xobser[3000],Yobser[3000];
        double Aa;
        double TTerror1[2],TTerror2[2];
        double RR;

    time_t start, stop;
    clock_t ticks; long count;

    time(&start);

        double ** K1,**K2,**L,**lap,**A,**KL;
                K1 = new double*[3600];
        for (i=0;i<=3600;i++)
                K1[i]=new double[3600];
        K2 = new double*[3600];
        for (i=0;i<=3600;i++)
                K2[i]=new double[3600];
        L = new double*[3600];
```

```
for (i=0;i<=3600;i++)
        L[i]=new double[3600];
lap = new double*[3600];
for (i=0;i<=3600;i++)
        lap[i]=new double[3600];
A = new double*[3600];
for (i=0;i<=3600;i++)
        A[i]=new double[3600];
        KL = new double*[3600];
for (i=0;i<=3600;i++)
        KL[i]=new double[3600];
u = new float*[3600];
for (i=0;i<=3600;i++)
        u[i]=new float[3600];
s = new float*[3600];
for (i=0;i<=3600;i++)
        s[i]=new float[3600];
vT = new float*[3600];
for (i=0;i<=3600;i++)
        vT[i]=new float[3600];
v = new float*[3600];
for (i=0;i<=3600;i++)
        v[i]=new float[3600];


β=0.0000001;      ///β is the calibration factor for invers
dtr = 3.1415926/180;
umd4=0;
ums4=0;
umv4=-1;

nx=51;   //No of reservior nodes
ny=51;
FL=500;
FW=500;
depth=500;
dip=0;
asim =0;
dx=FL/(nx-1);
dy=FW/(ny-1);
//reservior elements
El=(nx-1)*(ny-1);
NX=nx-1;   ///No of reservior elements in X direction
NY=ny-1;   ///No of reservior elements in Y direction
Nx=50;     //No of observation points in x direction
Ny=50;
//Dx=10;
//Dy=10;
//Dx=(Xmax-Xmin)/(Nx-1);
//Dy=(Ymax-Ymin)/(Ny-1);
disstrike=0;
TT[1]=0;
TT[2]=0;
disdip=0;
distensile=0;
TStrike[1]=0;
```

```
        TStrike[2]=0;
        TDip[1]=0;
        TDip[2]=0;

//////////   OBSERVATION POINTS//////

        ofstream fout;
        fout.open("test.txt");

        o=Nx*Ny;
        obser=0;
        el=0;
        Aa=1+depth/(FL/2);
        //////////////for observation points grid with respect to depth//////
        Xobser[0]=Aa*(0-FL/2)+FL/2;
        Yobser[0]=Aa*(0-FL/2)+FL/2;
        Xobser[Nx+1]=Aa*(FL-FL/2)+FL/2;
        Yobser[Ny+1]=Aa*(FL-FL/2)+FL/2;

        for(i=1;i<=2500;++i){
                XF4=(i-1)*dx+dx/2;              //RESERVIOR POINTS
                YF4=(i-1)*dy*cos(dip*dtr)+dy/2;
                Xobser[i]=Aa*(XF4-FL/2)+FL/2;
                Yobser[i]=Aa*(YF4-FL/2)+FL/2;
            cout<<"OBSERVATION POINT"<<Xobser[i]<<"    "<<Yobser[i]<<"\n";}
    fout<<"OBSERVATION POINT:    "<<"\n";
        for(k=0;k<=Nx+1;++k)
        {
                for(m=0;m<=Ny+1;++m)
                {
                        NO=0;
obser=obser+1;
                        el=0;
                        //XO=Xmin+(k-1)*Dx;
                        //YO=Ymin+(m-1)*Dy;
          XO=Xobser[k];
                    YO=Yobser[m];
                    disstrike=0;
            TT[1]=0;
            TT[2]=0;
            disdip=0;
            distensile=0;
            TStrike[1]=0;
            TStrike[2]=0;
            TDip[1]=0;
            TDip[2]=0;
                cout<<"OBSERVATION POINT:    "<<XO<<"    "<<YO<<"\n";
                for (i=1;i<=nx-1;++i)
                        {
                                for (j=1;j<=(ny-1);++j)

                                {

                                        NO=NO+1;
                        XF4=(i-1)*dx+dx/2;              //RESERVIOR POINTS
                                        YF4=(j-1)*dy*cos(dip*dtr);
```

230

```
                          depthr = depth - dy*(j-1)*sin(dip*dtr);
umv4=-exp(-(((XF4-FL/2)*(XF4-FL/2)+(YF4+dy/2-FW/2)*(YF4+dy/2-FW/2)))/(100*FL));
UMV[NO]=umv4;  Volume change assigned to each reservoir element:

calculation(XO,YO,XF4,YF4,dy,dx,depthr,dip,asim,umd4,ums4,umv4,disS,disD,disT,Tstrike,Tdip,Ttensile,KK);
                          disstrike=disS[1]+disstrike;
             disdip=disD[1]+disdip;
                          el=el+1;
             K1[obser][el]=KK[1];
                     K2[obser][el]=KK[2];
                          distensile=disT[1]+distensile;
             TStrike[1]=Tstrike[1]+TStrike[1];
                     TStrike[2]=Tstrike[2]+TStrike[2];
             TDip[1]=Tdip[1]+TDip[1];
                     TDip[2]=Tdip[2]+TDip[2];
                TT[1]=Ttensile[1]+TT[1];
             TT[2]=Ttensile[2]+TT[2];
          ///////////For random generator to consider error
RR=rand()%(10)+1;
                                     RR=6.341*0.00001*RR/10;
                                     TTerror1[1]=TT[1]+RR;
                                     TTerror2[1]=TT[2]+RR;
         ////for U tilt matrix: (input data with error for inverse solution)
                                     U1[obser]=TTerror1[1];
                                     U2[obser]=TTerror2[1];
                              }
                       }
       fout<<XO<<","<<YO<<","<<distensile<<"\n";
       fout<<"TILT1 of X Y with error and Tilt2=  "<<TTerror1[1]<<"          "<<TTerror2[1]<<"\n";
       cout<<"disp strike ="<<disstrike<<"\n";
       cout<<"disp dip    ="<<disdip<<"\n";
           cout<<"disp tilt   ="<<distensile<<"\n";
           cout<<"tilt S x ="<<TStrike[1]<<"\n";
           cout<<"tilt s y ="<<TStrike[2]<<"\n";
           cout<<"tilt D x ="<<TDip[1]<<"\n";
           cout<<"tilt D y ="<<TDip[2]<<"\n";
           cout<<"tilt t x ="<<TT[1]<<"\n";
           cout<<"tilt t y ="<<TT[2]<<"\n";
                 }
       }
       fout.close();
       fout.open("test2.txt");
       for (i=1;i<=El;i++)
               for (j=1;j<=El;j++)
                     A[i][j]=0;
                     for (i=1;i<=El;i++){
                           for (j=1;j<=El;j++){
                                 for (F=0;F<=o-1;F++){
                                       if (i<=j){

       A[i][j]=A[i][j]+K1[1+F][i]*K1[1+F][j]+K2[1+F][i]*K2[1+F][j];}
                                       else
                                            A[i][j]=A[j][i];}
                            }
                     }
```

```cpp
cout<<"//////////////////////////////////////////"<<"\n";
laplace(dx,El,NX,NY,lap,L);
for (i=1;i<=El;i++)
        {
        for(j=1;j<=El;j++)
                        {
                                KL[i][j]=A[i][j]-β*L[i][j];}
                }
                for (i=1;i<=El;i++){
                        Answer[i]=0;}
                for (i=1;i<=El;i++){
                        for (j=1;j<=o;j++){
                                Answer[i]+=K1[j][i]*U1[j]+K2[j][i]*U2[j];}
                }
                SVDcmp(El,El,KL,u,s,vT,w,v);
                ///for calculating volume
                svbksb(u,w,v,El,El,Answer,volume);
                cout<<"initial Volume="<<"\n";
                fout<<"initial Volume="<<"\n";
                for(i=1;i<=El;i++){
                        cout<<UMV[i]<<"\n";
                        fout<<UMV[i]<<"\n";
                }
                cout<<" Volume="<<"\n";
                fout<<" Volume="<<"\n";
                for(i=1;i<=El;i++){
                        cout<<volume[i]<<"\n";
                        fout<<volume[i]<<"\n";
                }

                cout<<"NO="<<NO<<"\n";
                fout<<"NO="<<NO<<"\n";

                ////////////error calculation:
    cout<<"Error%="<<"\n";
                fout<<"Error%="<<"\n";
                for(i=1;i<=El;i++){
                        Err[i]=(UMV[i]-volume[i])*100/UMV[i];
                        cout<<Err[i]<<"\n";
                        fout<<Err[i]<<"\n";
                }
                ////calculating MSE and RMSE:
                Var=0;
                for(i=1;i<=El;i++)
                {
                        Var=Var+(UMV[i]-volume[i])*(UMV[i]-volume[i]);
                }

                Var=Var/El;
                std=sqrt(Var);

                time(&stop);

                cout<<"MSE"<<Var<<"\n";
                cout<<"RMSE"<<std<<"\n";
                fout<<"MSE"<<Var<<"\n";
```

232

```
                    fout<<"RMSE"<<std<<"\n";


printf("Finished in about %.0f seconds. \n",        difftime(stop, start));

                         fout.close();


}

///////////////////////////////////////////////////////////////////////////////////////////////////

void calculation(double Xo4,double Yo4,double Xf,double Yf,double fw4,double fl4,double depth4, double dip4,
double asim4,double Umd,double Ums,double Umv, double SS[4],double DS[4],double TS[4],double t[3],double
td[3],double tilt[5],double KK[4])
{

        double pi,pi2,prt,dtr,asim,dip,d;
        double ca,sa,sn,cs,DX,DY,XL,YL,zi,zf,ei,ef,okd1[5],okd2[5],okd3[5],okd4[5];
        double ds1,ts1,ss1,disl,ss2,ss3,ss4,ds2,ds3,ds4,ts2,ts3,ts4;
        double
tss1[4],tss2[4],tss3[4],tss4[4],tds1[4],tds2[4],tds3[4],tds4[4],tts1[4],tts2[4],tts3[4],tts4[4],Tilt[4],pi2i,disp4;
        double kk[5];
        int i;

        prt=0.5;
        pi=3.141592654;
        pi2=pi*2;
        pi2i=1/pi2;
        dtr=pi2/360;   //for angle trans
        asim=asim4*dtr;
        dip=dip4*dtr;
        d=depth4;
        ca=cos(asim);
        sa=sin(asim);
        sn=sin(dip);
        cs=cos(dip);
        DX=Xo4-Xf;
        DY=Yo4-Yf;
        XL=DX*ca+DY*sa;
        YL=-DX*sa+DY*ca;
        zi=XL-0.5*fl4;
        zf=XL+0.5*fl4;
        ei=YL*cs+d*sn;
        ef=ei-fw4;
        okadadisp(XL,YL,zi,ei,d,dip,sn,cs,prt,okd1);
        ss1=okd1[1];
        ds1=okd1[2];
        ts1=okd1[3];
        okadadisp(XL,YL,zi,ef,d,dip,sn,cs,prt,okd2);
        ss2=okd2[1];
        ds2=okd2[2];
        ts2=okd2[3];
        okadadisp(XL,YL,zf,ei,d,dip,sn,cs,prt,okd3);
        ss3=okd3[1];
        ds3=okd3[2];
```

233

```
            ts3=okd3[3];
            okadadisp(XL,YL,zf,ef,d,dip,sn,cs,prt,okd4);
            ss4=okd4[1];
            ds4=okd4[2];
            ts4=okd4[3];
            disl=(ss1-ss2-ss3+ss4)*Ums;
            SS[1]=disl*pi2i;
            disl=disl+(ds1-ds2-ds3+ds4)*Umd;
            DS[1]=(ds1-ds2-ds3+ds4)*Umd*pi2i;
            disl=disl+(ts1-ts2-ts3+ts4)*Umv;
            TS[1]=(ts1-ts2-ts3+ts4)*Umv*pi2i;
            disp4=disl*pi2i;
            okadatilt(XL,YL,zi,ei,d,dip,sn,cs,prt,tss1,tds1,tts1);

            okadatilt(XL,YL,zi,ef,d,dip,sn,cs,prt,tss2,tds2,tts2);

            okadatilt(XL,YL,zf,ei,d,dip,sn,cs,prt,tss3,tds3,tts3);

            okadatilt(XL,YL,zf,ef,d,dip,sn,cs,prt,tss4,tds4,tts4);

            t[1]=(tss1[1]-tss2[1]-tss3[1]+tss4[1])*Ums/pi2;
            t[2]=(tss1[2]-tss2[2]-tss3[2]+tss4[2])*Ums/pi2;
            td[1]=(tds1[1]-tds2[1]-tds3[1]+tds4[1])*Umd/pi2;
            td[2]=(tds1[2]-tds2[2]-tds3[2]+tds4[2])*Umd/pi2;
            for(i=1;i<=2;++i){
                    Tilt[i]=(tss1[i]-tss2[i]-tss3[i]+tss4[i])*Ums;
                    Tilt[i]=Tilt[i]+(tds1[i]-tds2[i]-tds3[i]+tds4[i])*Umd;
                    Tilt[i]=Tilt[i]+(tts1[i]-tts2[i]-tts3[i]+tts4[i])*Umv;
                    kk[i]=tts1[i]-tts2[i]-tts3[i]+tts4[i];
            }
            KK[1]=(kk[1]*ca-kk[2]*sa)/pi2;
            KK[2]=(kk[1]*sa+kk[2]*ca)/pi2;
            tilt[1]=(Tilt[1]*ca-Tilt[2]*sa)/pi2;
            tilt[2]=(Tilt[1]*sa+Tilt[2]*ca)/pi2;

    }

void okadadisp(double x,double y,double z,double e,double d,double dip,double sn,double cs,double prt,double
a[3])
 {
        double q,dt,yt,rc,xc,rci,rce,rcz,tn,lgt,t4,tn5,td5,t5,tme,tmz,tmzr,tmer,ds,ts,ss;
        cs=cos(dip);
        sn=sin(dip);
        q=y*sn-d*cs;
        dt=e*sn-q*cs;
        yt=e*cs+q*sn;
        rc=sqrt(z*z+e*e+q*q);
        xc= sqrt(z*z+q*q);
        rci=1/rc;
        rce=rc+e;
        rcz=rc+z;

        if (abs(q)> 0.00001)
                tn=atan((z*e)/(q*rc));
        else
                tn=0;
```

```c
        if (abs(cs)>0.00001) {
                if (rce>0.00001)
                        lgt= log(rce);
                else
                        lgt=-log(rc-e);
                t4=prt*((log(rc+dt)-sn*lgt)/cs);
                if (abs(z)>0.00001)
                {
                        tn5=e*(xc+q*cs)+xc*(rc+xc)*sn;
                        td5=z*(rc+xc)*cs;
                        t5=prt*2*atan(tn5/td5)/cs;
                }
                else
                        t5=0;
        }
        if (abs(cs<0.00001)){
                t4=-prt*q/(rc+dt);
                t5=-prt*z*sn/(rc+dt);

        }

        if (abs(rce)>0.00001){
                tme=q/rce;}
        else
                tme=0;

        if (rcz!=0)
                tmz=q/rcz;
        else
                tmz=0;
        tmzr=tmz*rci;
        tmer=tme*rci;
        ss=-dt*tmer-(tme+t4)*sn;
        ds=-dt*tmzr-sn*tn+t5*sn*cs;
        ts=yt*tmzr+cs*(z*tmer-tn)-t5*sn*sn;
        a[1]=ss;
        a[2]=ds;
        a[3]=ts;

}
void okadatilt(double x,double y,double z,double e,double d,double dip,double sn,double cs,double prt,double
ss[4],double ds[4],double ts[4])

{

        double q,dt,yt,rc,xc,q2,z2,sn2,sncs,r3,re,rz,rd,az,qr3,rrz,rre,ae,trm;
        double tk1,tk2,tk3;

        cs=cos(dip);
        sn=sin(dip);
        q=y*sn-d*cs;
        dt=e*sn-q*cs;
        yt=e*cs+q*sn;
        rc=sqrt(z*z+e*e+q*q);
        xc= sqrt(z*z+q*q);
```

```
        q2=q*q;
        z2=z*z;
        sn2=sn*sn;
        sncs=sn*cs;
        r3=rc*rc*rc;
        re=rc+e;
        rz=rc+z;
        rd=rc+dt;
        az=(2*rc+z)/(r3*rz*rz);
        qr3=q/r3;
        rrz=rc*rz;
        rre=rc*re;
        if (re>0.00001){
                ae=(2*rc+e)/(r3*re*re);
                trm=sn/rre;
        }
        else{
                ae=0;
                trm=0;
        }
        if (abs(cs>0.00001)){
                tk1=prt*z*(1/(rc*rd)-sn/rre)/cs;
                tk3=prt*(q/rre-yt/(rc*rd))/cs;
                tk2=prt*(-sn/rc+q*cs/rre)-tk3;
        }
        else{
                tk1=prt*z*q/(rc*rd*rd);
                tk3=prt*sn/rd*(z2/(rc*rd)-1);
                tk2=prt*(-sn/rc)-tk3;
        }
        ss[1]=-z*q2*ae*cs+(z*qr3-tk1)*sn;
        ss[2]=dt*cs*qr3+(z2*q*ae*cs-sn/rc+yt*qr3-tk2)*sn;

        ds[1]=dt*qr3+q*trm+tk3*sncs;
        ds[2]=yt*dt*q*az-(2*dt/rrz+z*trm)*sn+tk1*sncs;

        ts[1]=-q2*sn/r3+q*q2*ae*cs-tk3*sn2;
        ts[2]=-(yt*sn+dt*cs)*q2*az-z*q2*ae*sncs+(2*q/rrz-tk1)*sn2;

        }
///for calculating Laplace operator:
void laplace(double h,double N,int nx,int ny,double **l,double **L)
{
        int i,j,F;
        //for array-matriz:
        int k;
        double hx,hy;
   //N No of reservior elements
   //M No of observation points


        //hx=1;
        for (i=1;i<=N;i++){
                for(j=1;j<=N;j++){
                        l[i][j]=0;}
```

236

```
}

for (i=1;i<=N;i++)
{
        for(j=1;j<=N;j++)

        {
                if(i==j)
                {l[i][j]=-4/(h*h);}
                else{
                        for (k=1;k<=ny-2;k++){         ///for mid points
                                if(i>(k*nx+1) && i<(k+1)*nx){
                        l[i][i-nx]=1/(h*h);
                        l[i][i-1]=1/(h*h);
                        l[i][i+1]=1/(h*h);
                        l[i][i+nx]=1/(h*h);}}

                        if (i==1){
                                l[i][i+1]=l[i][i+nx]=2/(h*h);}
                        if (i==nx){
                                l[i][i-1]=l[i][i+nx]=2/(h*h);}
                        if (i==nx*(ny-1)+1 ||i==N){
                                l[i][i+1]=l[i][i-nx]=2/(h*h);}
                        if (i==N){
                                l[i][i-1]=l[i][i-nx]=2/(h*h);
                        }
                }

                        if(1<i && i<nx){
                                l[i][i-1]=l[i][i+1]=1/(h*h);
                                l[i][i+nx]=2/(h*h);}
                        if((ny-1)*nx+1<i && i<N){
                                l[i][i-1]=l[i][i+1]=1/(h*h);
                                l[i][i-nx]=2/(h*h);}
                        for(k=1;k<ny-1;k++){
                                if(i==(k+1)*nx){
                                        l[i][i-1]=2/(h*h);
                                        l[i][i+nx]=l[i][i-nx]=1/(h*h);}

                                else
                                        if(i==k*nx+1){
                                        l[i][i+1]=2/(h*h);
                                        l[i][i+nx]=l[i][i-nx]=1/(h*h);}
                }


        }
}

for (i=1;i<=N;i++){
        for (j=1;j<=N;j++){
                L[i][j]=0;
        }
}
for (i=1;i<=N;i++)
{
```

```
                for (j=1;j<=N;j++)
                {
                        for (F=0;F<=N-1;F++)
                        {
                                if (i<=j){
                                        L[i][j]=L[i][j]+l[1+F][i]*l[1+F][j];}
                                else
                                        L[i][j]=L[j][i];
                        }
                }
        }

    }

///////////////////////////////////////////////////////
void SVDcmp(int m,int n,double **a,float **aa,float **S,float **vT,float w[3600],float **v)
{
        float pythag(float a,float b);
        int flag,i,its,j,jj,k,l,nm;
        float anorm,c,f,g,h,s,scale,x,y,z,rv1[3600],M;
        float **T,**A;


        T = new float*[3600];
        for (i=0;i<=3600;i++)
                T[i]=new float[3600];
        A = new float*[3600];
        for (i=0;i<=3600;i++)
                A[i]=new float[3600];
    g=0;
        scale=0;
        anorm=0;

        for (i=1;i<=n;i++){
                l=i+1;
                rv1[i]=scale*g;
                g=s=scale=0.0;
                if (i<=m){
                        for (k=i;k<=m;k++)
                                scale+=fabs(a[k][i]);
                        if(scale){
                                for (k=i;k<=m;k++){
                                        a[k][i]/=scale;
                                        s+=a[k][i]*a[k][i];
                                }
                                f=a[i][i];
                                M=f/abs(f);
                                g=-1*abs(sqrt(s))*M;
                                h=f*g-s;
                                a[i][i]=f-g;
                                for (j=l;j<=n;j++){
                                        for (s=0.0,k=i;k<=m;k++)
                                                s+=a[k][i]*a[k][j];
                                        f=s/h;
                                        for (k=i;k<=m;k++)
                                                a[k][j]+=f*a[k][i];

                                                238
```

```
                                     }
                                     for (k=i;k<=m;k++)
                                            a[k][i]*=scale;
                              }
                       }
               w[i]=scale*g;
               g=s=scale=0.0;
               if(i<=m && i!=n){
                       for (k=l;k<=n;k++)
                              scale+=fabs(a[i][k]);
                       if (scale){
                              for (k=l;k<=n;k++){
                                     a[i][k]/=scale;
                                     s+=a[i][k]*a[i][k];
                              }
                              f=a[i][l];
                              //Replacement for -SIGN function
                                     M=f/abs(f);
                                     g=-1*abs(sqrt(s))*M;
                              h=f*g-s;
                              a[i][l]=f-g;
                              for (k=l;k<=n;k++)
                                     rv1[k]=a[i][k]/h;
                              for (j=l;j<=m;j++){
                                     for (s=0.0,k=l;k<=n;k++)
                                            s+=a[j][k]*a[i][k];
                                     for (k=l;k<=n;k++)
                                            a[j][k]+=s*rv1[k];
                              }
                              for (k=l;k<=n;k++)
                                     a[i][k]*=scale;
                       }
               }

               anorm=max(anorm,(fabs(w[i])+fabs(rv1[i])));
       }

       for(i=n;i>=1;i--){
               if (i<n){
                       if (g){
                              for (j=l;j<=n;j++)
                                     v[j][i]=(a[i][j]/a[i][l])/g;
                              for (j=l;j<=n;j++){
                                     for (s=0.0,k=l;k<=n;k++)
                                            s+=a[i][k]*v[k][j];
                                     for (k=l;k<=n;k++)
                                            v[k][j]+=s*v[k][i];
                              }
                       }
                       for (j=l;j<=n;j++)
                              v[i][j]=v[j][i]=0.0;
               }
               v[i][i]=1.0;
               g=rv1[i];
               l=i;
       }
```

```
//Accumulation of left-hand transformations.
for (i=min(m,n);i>=1;i--){
        l=i+1;
        g=w[i];
        for (j=l;j<=n;j++)
                a[i][j]=0.0;
        if(g){
                g=1/g;
                for(j=l;j<=n;j++){
                        for(s=0.0,k=l;k<=m;k++)
                                s+=a[k][i]*a[k][j];
                        f=(s/a[i][i])*g;
                        for (k=i;k<=m;k++)
                                a[k][j]+=f*a[k][i];
                }
                for (j=i;j<=m;j++)
                        a[j][i]*=g;
        }
        else for (j=i;j<=m;j++)
                a[j][i]=0.0;
        ++a[i][i];
}

//Diagonalization of the bidiagonal form:Loop over singular values,and over allowed iterations
for (k=n;k>=1;k--){
        for(its=1;its<=300;its++){
                flag=1;
                for(l=k;l>=1;l--){
                        nm=l-1;
                        if ((float)(fabs(rv1[l])+anorm)==anorm) {
                                flag=0;
                                break;
                        }
                        if ((float)(fabs(w[nm])+anorm)==anorm)
                                break;
                }
                if (flag){   //cancellation of rv1[l],if l>1
                        c=0.0;
                        s=1.0;
                        for (i=l;i<=k;i++){
                                f=s*rv1[i];
                                rv1[i]=c*rv1[i];
                                if((float)(fabs(f)+anorm)==anorm)
                                        break;
                                g=w[i];
                                h=pythag(f,g);
                                w[i]=h;
                                h=1/h;
                                c=g*h;
                                s=-f*h;
                                for (j=1;j<=m;j++){
                                        y=a[j][nm];
                                        z=a[j][i];
                                        a[j][nm]=y*c+z*s;
                                        a[j][i]=z*c-y*s;
```

```
                                       }
                            }
                  }

                  z=w[k];
                  if(l==k){
                            if(z<0.0){
                                       w[k]=-z;
                                       for (j=1;j<=n;j++)
                                                 v[j][k]=-v[j][k];
                            }
                            break;
                  }

                  if(its==300){ cout<<"not conver"<<"\n";
                            exit(1);
                  }
                            //nrerror("no convergence on 30 svdcmp iterations");
                  ///////shift from bottom 2-by-2 minor//////
                  x=w[l];
                  nm=k-1;
                  y=w[nm];
                  g=rv1[nm];
                  h=rv1[k];
                  f=((y-z)*(y+z)+(g-h)*(g+h))/(2*h*y);
                  g=pythag(f,1);
                  //Replacement for -SIGN function
                            M=f/abs(f);
                            g=abs(g)*M;
                  f=((x-z)*(x+z)+h*((y/(f+g))-h))/x;

                  c=s=1.0;
                  for (j=l;j<=nm;j++){
                            i=j+1;
                            g=rv1[i];
                            y=w[i];
                            h=s*g;
                            g=c*g;
                            z=pythag(f,h);
                            rv1[j]=z;
                            c=f/z;
                            s=h/z;
                            f=x*c+g*s;
                            g=g*c-x*s;
                            h=y*s;
                            y *=c;
                            for (jj=1;jj<=n;jj++){
                                       x=v[jj][j];
                                       z=v[jj][i];
                                       v[jj][j]=x*c+z*s;
                                       v[jj][i]=z*c-x*s;
                            }
                            z=pythag(f,h);
                            w[j]=z;
                            if (z){
                                       z=1/z;
```

```
                                                c=f*z;
                                                s=h*z;
                                  }
                          f=c*g+s*y;
                          x=c*y-s*g;
                          for (jj=1;jj<=m;jj++){
                                          y=a[jj][j];
                                          z=a[jj][i];
                                          a[jj][j]=y*c+z*s;
                                          a[jj][i]=z*c-y*s;
                                  }
                  }
          rv1[l]=0;
          rv1[k]=f;
          w[k]=x;
      }
}
for(k=1;k<=m;++k)
          {
                          for(j=1;j<=n;++j)
                          {
                                  aa[k][j]=a[k][j];}
}
for (i=1;i<=n;++i)
{
      for(k=1;k<=n;++k)
      {
              vT[i][k]=v[k][i];
      }
}
cout<<"w[]="<<"\n";
for (i=1;i<=n;i++){
      for(j=1;j<=n;j++){
              if(i!=j)
                      S[i][j]=0;
              else
                      S[i][j]=w[i];
      }
}
for (i=1;i<=m;i++){
      for(j=1;j<=n;j++){
              T[i][j]=0;

      }
}
for (i=1;i<=n;i++){
      for(j=1;j<=n;j++){
              for(k=1;k<=n;k++){
                      T[i][j]+=S[i][k]*vT[k][j];
              }
      }
}
for (i=1;i<=m;i++){
      for(j=1;j<=n;j++){
              A[i][j]=0;
      }
```

242

```
        }

        for(i=1;i<=m;i++){
                for(j=1;j<=n;j++){
                        for(k=1;k<=n;k++){
                                A[i][j]+=a[i][k]*T[k][j];
                        }
                }
        }

}


float pythag(float a,float b)
//computes (a^2+b^2)^0.5 without destructive underflow or overflow
{
        float absa,absb;
        absa=fabs(a);
        absb=fabs(b);
        if(absa>absb)
                return absa*sqrt(1+(absb/absa)*(absb/absa));
        else
                return (absb==0?0 : absb*sqrt(1+(absa/absb)*(absa/absb)));
}

//////////////////////////////////////////////////////////////////////void svbksb(float **u,float w[3600],float **v,int m,int n,float
b[3600],float x[3600])
{
        int jj,j,i;
        double s,tmp[3600];

        for (j=1;j<=n;j++){              ///calculate UT B
                s=0;
                if(w[j]){               ///Nonzero result only if wj is nonzero
                        for(i=1;i<=m;i++)
                                s+=u[i][j]*b[i];
                        s/=w[j];
                }
                tmp[j]=s;
        }
        for(j=1;j<=n;j++){
                s=0;                    ///Matrix multiply by V to get answer
                for(jj=1;jj<=n;jj++)
                        s+=v[j][jj]*tmp[jj];
                x[j]=s;
        }
}
```